Ultrasound cardiac therapy guided by elastography and ultrafast imaging

Wojciech Kwiecinski

Université Pierre et Marie Curie

Ecole doctorale : Sciences mécaniques, acoustique, électronique & robotique de Paris – ED SMAER 391

Institut Langevin / Equipe des Ondes Pour la Médecine

Ultrasound cardiac therapy guided by elastography and ultrafast imaging

Thérapies ultrasonores cardiaques guidées par élastographie et échographie ultrarapides

Par Wojciech Kwiecinski

Thèse de doctorat d'Acoustique Physique

Dirigée par Mickaël Tanter

Codirigée par Mathieu Pernot

Présentée et soutenue publiquement le 3 Juillet 2015

Devant un jury composé de :

M. Jan D'Hooge	Rapporteur
M. David Melodelima	Rapporteur
Mme. Lori Bridal	Membre du jury
M. Mathieu Pernot	Encadrant de thèse
M. Rémi Dubois	Membre du jury
M. Mickaël Tanter	Directeur de thèse

À Witold, son petit frère et leur maman

Acknowledgments

En tout premier lieu je voudrais remercier mes deux directeurs de thèse Mickaël Tanter et Mathieu Pernot. Mickaël, par un mélange de passion, enthousiasme, avec l'excellence scientifique et une vision claire réussit à créer un environnement très stimulant et formateur, dans lequel les sciences et l'envie de créer prennent la première place. Grâce à l'énergie qu'il déploie pour faire vivre et avancer toute l'Équipe des Ondes Pour la Médecine, sans oublier toutes personnes qui l'épaulent, un étudiant en thèse n'a plus qu'à faire des sciences pour récompenser le confort qu'on lui offre. Je le remercie de m'avoir accordé sa confiance pour tout ce travail.

Mathieu qui a été mon interlocuteur de tous les jours. Il a été un vrai exemple à suivre tant par son dynamisme, son efficacité, son côté humain que sa pertinence scientifique et expérimentale. Je le remercie de m'avoir pris en stage, par lequel toute l'aventure a commencé, puis de m'avoir fait confiance et accompagné durant ces années de thèse.

Je voudrais remercier les rapporteurs David Melodelima et Jan D'hooge pour avoir accepté de rapporter ma thèse, ainsi que Lori Bridal et Rémi Dubois pour avoir accepté de faire partie du jury.

Cette thèse a fait l'objet de plusieurs collaborations et aucun résultat n'est le fruit d'un seul groupe. Je souhaite remercier l'équipe du laboratoire LabTau de Lyon en particulier Elodie Constanciel, Francis Bessière, Cyril Lafon, W. Apoutou N'Djin avec lesquels j'ai pu travailler pour l'imagerie transoesophagienne. Le projet intracardiaque est tout d'abord le fruit d'un travail à Vermon par Mathieu Legros et son équipe, An Nguyen-Dinh et Rémi Dufait, qui ont été disponibles, enthousiastes et nous ont fourni de nombreux prototypes que nous avons pu joyeusement détruire. Merci à eux. Je remercie aussi l'équipe de l'Institut LYRIC de Bordeaux, Frédéric Sacher, Rémi Dubois, pour avoir été des acteurs importants des expérimentations intracardiaques animales.

Un grand merci à Antoine Mariani avec lequel j'ai pu mener mes premières expériences à l'hôpital et eu de nombreux échanges intéressants. Je souhaite remercier Olivier Villemain très enthousiaste, humain et vivant qui donne et à qui on veut donner.

Parce que l’Institut Langevin n’est pas constitué que de Mickaël et Mathieu, je voudrais remercier tous les membres de l’Institut, son ancien directeur Mathias Fink pour m’avoir accueilli et le directeur actuel, Arnaud Tourin, pour tout son engagement.

Merci à Patricia, Khadija, toute l’équipe POM, en particulier Jean, avec lequel j’ai pu apprendre plein de choses, Thomas qui a été d’un soutien important, Jean-Luc pour murmurer à l’oreille des machines, Olivier pour sa fraîcheur d’idées, Philippe pour ses conseils et son aide technique. Merci enfin à toute cette joyeuse troupe de l’équipe : Mafalda, Claudia, Justine, Simon, Heldmuth, Clément, Charlie, Mai, Bastien, Elodie, Wei-Ning, David, Martin, Miguel, Youliana, Laurent, Bruno… avec laquelle c’était très agréable de travailler au quotidien et de partager de nombreux moments de détente et soirées !

Un tout particulier merci à ma famille, mes parents, qui m’ont soutenu et protégé, le groupe de théâtre humanitaire SCRIBE, véritable source de vie. Enfin et surtout, merci à ma femme, Cécile, pour son soutien, pour donner de la joie tous les jours, pour Witold et son petit frère. Witold, pour ta joie et ton amour.

Abstract

Atrial fibrillation (AF) affects 2-3% of the European and North-American population, whereas ventricular tachyarrhythmia (VT) is related to an important risk of sudden death. AF and VT originate from dysfunctional electrical activity in cardiac tissues and can be treated with drug therapy, tissue ablation or a combination of both. Minimally-invasive approaches such as Radio-Frequency Catheter Ablation (RFCA) have revolutionized the treatment of these diseases; however the success rate of RFCA is currently limited by the lack of monitoring techniques to precisely control the extent of thermally ablated tissue.

The aim of this thesis is to propose novel ultrasound-based approaches for minimally invasive cardiac ablation under guidance of ultrasound imaging: a dual-mode imaging/therapy intracardiac approach, and a second approach based on transesophageal ultrasound-guided-High-Intensity-Focused-Ultrasound (USgHIFU) through a collaboration with LabTau (Inserm U1032).

In this thesis, we first validated the accuracy and clinical viability of Shear-Wave Elastography (SWE) as a real-time quantitative imaging modality for thermal ablation monitoring in vivo. An excellent sensitivity to detect the change of stiffness during the lesion formation was demonstrated during radiofrequency ablation of the liver on a large animal model. Second we implemented SWE on an intracardiac transducer and validated the feasibility of evaluating thermal ablation in vitro and in vivo on beating hearts of a large animal model. Myocardial stiffness maps were performed after RFCA demonstrating the sensitivity of intracardiac SWE to detect thermal lesions in the atrium and the ventricles. Two novel imaging techniques were also developed and assessed on cardiac tissues: ultrafast Doppler imaging to detect small vessels and ultrafast acoustoelectric imaging to map acousto-electrical properties of cardiac tissues. Third a dual mode intracardiac transducer was developed to perform both ultrasound therapy and imaging with the same elements, on the same device. SWE-controlled HIFU thermal lesions were successfully performed in vivo in the atria as well as in the ventricles of a large animal model. At last, SWE was implemented on a transesophageal ultrasound imaging and therapy device and the feasibility of transesophagial approach was demonstrated in vitro and in vivo. These novel approaches may lead to new clinical devices for a safer and controlled treatment of a wide variety of cardiac arrhythmias and diseases.

Keywords: Ultrasound, Medical imaging, Echography, Non-invasive therapies, Cardiac arrhythmias, Shear-Wave Elastography, High-Intensity-Focused Ultrasound, Thermal ablation monitoring, Intracardiac echocardiography, Transesophageal echocardiography, Ultrafast Doppler imaging, Acoustoelectric imaging

Résumé de la thèse

Chapitre 1 : Introduction

Les troubles du rythme cardiaque sont associés à des risques pour la santé à court et à long terme. La fibrillation atriale (AF), l'arythmie la plus fréquente, qui affecte 2-3% de la population européenne et nord-américaine[1], est associée à un risque accru 5 fois d'avoir un accident vasculaire-cérébral, à une incidence d'insuffisance cardiaque de 40% [2, 3] et en général à un taux de mortalité doublé [4, 5]. L'AF est causée par une activité électrique dysfonctionnelle qui survient autour des veines pulmonaires [6] ou dans les oreillettes [7]. Les tachycardies ventriculaires (VT) sont liées à un risque important de mort subite [2]. Les VT peuvent prendre origine dans des circuits de réentrées électriques autour de cicatrices du myocarde ou des points d'activation précoce dans le muscle ventriculaire [8]. Alors que les VT nécessitent souvent d'implanter un défibrillateur automatique implantable, l'AF et les VT peuvent être traitées avec des médicaments, de l'ablation tissulaire ou une combinaison des deux.

Les approches minimalement invasives comme l'Ablation par Cathéter Radiofréquence (RFCA) ont révolutionné le traitement de l'AF et représentent une nouvelle possibilité pour les traitements des VT. La RFCA consiste à isoler les sources de réentrées communes [6, 9] ou des foyers locaux [10, 11] par le biais d'une coagulation thermique des tissus réalisée avec un cathéter radiofréquence (RF) intracardiaque. Cependant, malgré l'utilisation de différentes techniques de guidage et d'imagerie, la RFCA souffre du manque d'une imagerie de suivi d'ablation précise pour évaluer la transmuralité des lésions thermiques [8, 12] qui constitue un aspect crucial pour l'efficacité des procédures d'ablation [13]. En effet, le dépôt de chaleur réel et donc l'extension de la lésion dans les tissus sont difficiles à évaluer. En conséquence le taux de réussite des procédures uniques de la RFCA reste relativement faible (~60%) pour tous les types d'AF [14]. Une autre limite importante de la RFCA est la difficulté de créer des lésions transmurales ou à mi-paroi dans les ventricules. En conséquence une ablation additionnelle à l'épicarde [8, 15] est parfois nécessaire. Pour cette raison la RFCA n'est pas parfaitement adaptée pour l'ablation des VT et un taux de réussite limité de 35% est rapporté dans la littérature [15].

Le but de cette thèse est de proposer de nouvelles approches ultrasonores pour des traitements cardiaques minimalement invasifs guidés par échographie : une approche dual-mode de thérapie et imagerie intracardiaque et une deuxième, basée sur les Ultrasons Focalisés à Haute Intensité (HIFU) guidés par ultrasons, par voie transœsophagienne au travers d'une collaboration avec le laboratoire LabTau (INSERM U1032).

Pour cela nous avons d'abord validé la précision et la viabilité clinique de l'Élastographie par Ondes de Cisaillement (SWE) en tant que modalité d'imagerie quantitative et temps réel pour l'ablation thermique in vivo. Ensuite nous avons implémenté la SWE sur un transducteur intracardiaque et validé la faisabilité d'évaluer l'ablation thermique in vitro et in vivo sur cœur battant de gros animal. La possibilité d'imager la vascularisation cardiaque aussi été étudiée, grâce à l'imagerie Doppler ultrarapide. Puis nous avons développé un transducteur intracardiaque dual-mode pour effectuer l'ablation et l'imagerie ultrasonores avec les mêmes éléments, sur le même dispositif. Les lésions thermiques induites par HIFU et contrôlées par la SWE ont été réalisées avec succès in vivo dans les oreillettes et les ventricules chez le gros animal. Enfin la SWE a été implémentée sur un dispositif d'imagerie et thérapie ultrasonores transœsophagien et la faisabilité de cette approche a été démontrée in vitro et in vivo. Pour finir, la perspective d'une imagerie acoustoélectrique ultrarapide est aussi étudiée.

Chapitre 2 : Suivi temps-réel de l'ablation thermique par Élastographie par Ondes de Cisaillement

Introduction

L'intérêt pour l'ablation thermique est grandissant ces dernières années, en particulier dans le domaine du traitement des tumeurs [16, 17]. Les techniques d'ablation thermique minimalement invasives comme la radiofréquence ou l'ablation par HIFU [18], présentent de nombreux avantages par rapport à la chirurgie classique. Dans certains cas l'ablation thermique est devenue une alternative standard à la chirurgie[19–21].

Dans ce chapitre nous nous concentrons sur le cas spécifique du traitement par ablation thermique dans le foie. Dans cet organe la sécurité et l'efficacité des thérapies thermiques, en particulier la radiofréquence, ont été largement étudiées [22] et d'importants taux de récidive tumorales ont été signalées [23]. Parmi les causes les plus importantes de

l'inefficacité d'ablation se trouve l'incapacité à contrôler précisément l'extension de l'ablation [24].

Il existe un besoin considérable pour une technique d'imagerie de suivi pour l'ablation. Actuellement le gold-standard pour un suivi non-invasif à l'aide de l'imagerie de température est l'imagerie par résonance magnétique (MRI). Cependant le MRI est associé avec plusieurs obstacles techniques (compatibilité des matériaux, espace limité pour l'intervention) et est coûteux. De plus la résolution temporelle est limitée et des mouvements rapides détériorent fortement les images.

Les effets induits thermiquement peuvent être quantifies par les changements des propriétés élastiques des tissus. Il a été montré que la cartographie quantitative de l'élasticité est d'une importance majeure car la dureté des tissus pendant la coagulation est directement liée à la dose thermique [25]. L'Élastographie par Ondes de Cisaillement [26] permet de fournir une visualisation objective, opérateur indépendante, des lésions thermiques [27, 28] en donnant le module d'Young local des tissus. De plus, grâce à l'imagerie ultrarapide par ondes planes, elle est peu affectée par les mouvements naturels présents in-vivo. À notre connaissance c'est la seule imagerie temps-réel pouvant satisfaire ces conditions.

Afin d'évaluer la faisabilité et la précision d'un suivi quantitatif de l'élasticité pendant les thérapies thermiques et pour déterminer le seuil de dureté qui prédirait la formation d'une nécrose par coagulation, nous avons mené une étude préclinique in-vivo dans laquelle la SWE a été utilisée pour cartographier les nécroses par coagulation induites thermiquement produites dans les foies de proc avec les systèmes de RFA et de HIFU.

Matériel et Méthodes

Au total quarante (n=36; n= 26 par RFA and n= 10 par HIFU) lésions thermiques ont été effectuées dans les foies de huit (n=8; RFA: n=5 et HIFU: n=3) porcs en utilisant une approche par chirurgie ouverte. Deux systèmes fixes d'ablation ont été utilisés, avec l'imagerie avec la thérapie parfaitement alignées.

Pour la RFA, deux électrodes ont été insérées dans le foie sous guidage par ultrasons et la nécrose par coagulation était produite par un système bipolaire radiofréquence connecté à un générateur électrochirurgical. La lésion thermique était créée 1.5-2.5 cm sous la surface du foie en environ 5min.

La thérapie par HIFU était effectuée avec un mono-élément par une procédure point par point. Les ultrasons étaient appliqués 20s à chaque point à raison de 9 à 20 points espacés de 1 à 2mm selon un motif rectangulaire, 20-30mm sous la surface du foie du point de vue du plan d'imagerie.

Les images de SWE et B-mode étaient acquises avec un échographe ultrarapide (Aixplorer, SuperSonic Imagine, France) en utilisant deux sondes linéaires. Les images étaient prises avant, pendant et après la procédure d'ablation. Après la procédure le foie était excisé et une analyse macro de chaque lésion était effectuée en profondeur à la même position et orientation que celle des images.

Les images de lésions sur les photos macros étaient automatiquement segmentées en utilisant le changement de couleur du à la nécrose. Les cartes d'élasticité étaient segmentées en utilisant des seuils de module d'Young progressifs. La justesse des cartes d'élasticité de lésions RF était estimée en termes de vrai positif (TP), faux positif (FP) et faux négatif (FN) par superposition avec les photos macro. Les cartes de lésions par HIFU étaient estimées en comparant les surfaces trouvées avec les deux techniques.

Résultats

Les 26 régions des lésions thermiques induites par RFA et les 10 par HIFU ont eu une élasticité moyenne de 6.4 ± 0.3 kPa (RFA) et 7.5 ± 1.2 kPa (HIFU) avant la chauffe et une élasticité moyenne de 38.1 ± 2.5 kPa (RFA, $p<0.0001$) et 26.6 ± 4.7 kPa (HIFU, $p<0.0001$) après la procédure qui a induit la nécrose par coagulation.

Au-dessus de 30 kPa la valeur prédictive positive (PPV) était au-dessus de 0.93 mais était associée à une faible sensibilité (Se) de 0.5. 20 kPa donnent le meilleur compromis entre la Se et la PPV (0.8 and 0.83, respectivement).

Pour les lésions induites par HIFU, le meilleur seuil du module d'Young a été de 21kPa, ce qui est en accord avec la RFA. La surface d'ablation estimée sur les cartes d'élasticité était très proche des surfaces trouvées par macro (RFA: 0.022 ± 0.22 cm^2 pour biais ± déviation standard; HIFU : 0.086 ± 0.20 cm^2) avec un intervalle de confiance entre -0.413 cm^2 et +0.459 cm^2 (RFA) and -0.483 cm^2 and +0.310 cm^2 comparé avec la surface moyenne des lésions (RFA: 0.751 cm^2; HIFU : 0.382 cm^2).

Conclusion

Dans cette étude nous avons démontré que l'Élastographie par Ondes de Cisaillement quantitative est capable de suivre en temps-réel l'ablation thermique in-vivo avec un fort contraste et une cartographie précise. La dureté quantifiée par la SWE était 2 à 6-8 fois plus grande (dans le cœur de la lésion) que dans les tissus sains environnants. Un seuil de dureté déterminé avec précision pourrait aider à visualiser les bords des lésions thermiques créées. En effet, en utilisant un seuil de d'élasticité de 20 kPa (deux fois plus grand que l'élasticité de base), nous avons pu prédire la nécrose avec une valeur prédictive positive de 0.83 et une sensibilité de 0.8. Le seuil très proche trouvé pour le HIFU a pu confirmer la robustesse de ce résultat. Nous pensons que ce travail peut constituer une base solide pour pousser le suivi d'ablation thermique par SWE plus loin.

Chapitre 3: Imagerie intracardiaque ultrasonore ultrarapide pour l'évaluation de l'ablation thermique

Introduction

Dans ce chapitre nous avons développé une approche intracardiaque d'imagerie ultrarapide pour l'évaluation de la thérapie par ablation thermique. Ce développement répond à un besoin clinique spécifique : le manque de contrôle et de suivi par imagerie des thérapies thermiques dans le cœur et plus spécifiquement dans le contexte de la RFCA. Le principal défi de l'imagerie intracardiaque consiste en la miniaturisation d'un transducteur d'imagerie pour pouvoir l'insérer dans les chambres cardiaque à travers le système veineux. Cette approche est déjà largement répandue dans les centres d'électrophysiologie [12]. L'objectif précis de ce travail a été de développer des outils d'imagerie originaux pour l'évaluation du traitement par RFCA. Pour atteindre cet objectif deux nouvelles modalités d'imagerie ont été testées et implémentées sur un transducteur d'imagerie ultrasonore intracardiaque : l'Élastographie par Ondes de Cisaillement (SWE) et le Doppler ultrarapide. Ce chapitre présente la faisabilité in-vitro et in-vivo de l'évaluation par la SWE de la dureté du myocarde pendant la RFCA ainsi que, pour la première fois, de la variation temporelle de la dureté des oreillettes dans un modèle in-vivo normal. Enfin nous présentons des résultats préliminaires du Doppler ultrarapide intracardiaque pour cartographier la micro-vascularisation du myocarde.

SWE : Matériel et méthodes

Un échographe ultrarapide (Aixplorer®, SuperSonic Imagine, France) a été utilisé pour exécuter les séquences de SWE avec un cathéter ultrasonore intracardiaque (6 MHz, 50-% de bande passante, 64 éléments, 0.2-mm pitch, 9F, Vermon, France).

La SWE a été d'abord validée dans des échantillons de ventricules porcins ex-vivo (N = 5). L'imagerie B-mode et la SWE ont été effectuées sur les tissus cardiaques avant et après la RFCA. Les surfaces des lésions ont été déterminées avec les changements de couleur des tissus pendant une étude marco et confrontées aux cartes de dureté données par la SWE.

L'imagerie par SWE a été ensuite effectuée in-vivo dans trois moutons (N = 3) avec au total six ablations cartographiées (N = 6). L'accès au cœur a été fait par la veine fémorale sous fluoroscopie. D'abord la dureté des tissus auriculaires normaux a été évaluée quantitativement ainsi que sa variation pendant le cycle cardiaque. La SWE a été ensuite effectuée après la RFCA sur les mêmes tissus.

SWE : Résultats

Une forte augmentation de dureté a été observée dans les régions traitées ex-vivo (module de cisaillement moyen parmi les échantillons avant ablation : 22±5 kPa, vitesse de l'onde de cisaillement moyenne (ct): 4.5±0.4 m s^{-1} et dans les zones d'ablation après traitement: 99±17 kPa, ct moyenne: 9.0±0.5 m s−1 pour un ratio d'augmentation moyen de 4.5±0.9).

In-vivo l'extension de la lésion était clairement visible sur les cartes de dureté. Au centre des lésions la vitesse de l'onde de cisaillement moyenne parmi les échantillons a augmenté de 1.8±0.3 $m.s^{-1}$ (module de cisaillement moyen : 3.3±1.0 kPa) avant ablation à 3.1±0.3 $m.s^{-1}$ (module de cisaillement moyen : 10±2 kPa) après ablation. Un ratio d'augmentation moyenne de la c_t de 1.8±0.3 a été trouvé (ratio d'augmentation moyenne du module de cisaillement: 3.1±0.9).

Parmi les échantillons une vitesse de l'onde de cisaillement moyenne de 1.4±0.2 $m.s^{-1}$ (2.3±0.7 kPa) a été mesurée sur tout le cycle cardiaque. La vitesse moyenne minimale de 1.0±0.1 $m.s^{-1}$ (1.0±0.2 kPa) a été mesurée après la décontraction auriculaire, alors que la vitesse moyenne maximale de 1.9±0.4 $m.s^{-1}$ (4.1±1.8 kPa) a été atteinte pendant la contraction

auriculaire. Après l'ablation la vitesse de l'onde de cisaillement moyenne des régions ablatées a augmenté significativement, cependant un repère temporel dans le cycle cardiaque a été nécessaire pour comparer le changement de dureté avant et après ablation.

Doppler ultrarapide

Les acquisitions ont été effectuées pendant le même protocole, avant et après la RFCA. Le traitement des données était basé sur le filtrage par décomposition en valeurs singulières (SVD) [29], pour filtrer les sources de signal énergétiques comme le mouvement tissulaire et garder les sources moins énergétiques provenant de la vascularisation du cœur. Les données sont présentées sous forme de Doppler Puissance, dans les ventricules, et ont été acquises pendant la diastole quand le flux coronarien est le plus important.

Des coronaires perpendiculaires et parallèles au plan d'imagerie ont été détectées dans le septum interventriculaire. Des résultats préliminaires mais prometteurs sont montrés.

Conclusion

Par ses capacités quantitatives et temps-réel, la SWE intracardiaque est une technique d'imagerie intra opérative prometteuse pour l'évaluation de l'ablation thermique pendant la RFCA. L'utilisation d'une barrette d'imagerie à l'intérieur du cœur, avec un scanner ultrarapide, donne l'accès à des modalités d'imagerie nouvelles et très intéressantes.

Chapitre 4: Approche intracardiaque de thérapie et imagerie dual-mode

Introduction

Dans ce chapitre une approche intracardiaque originale est proposée pour les traitements d'ablation cardiaque, basée sur la combinaison de la thérapie et imagerie par ultrasons sur un même dispositif intracardiaque dual-mode. Ce travail a été motivé par plusieurs raisons. Premièrement, les résultats d'imagerie intracardiaque obtenus dans le chapitre 3 sont prometteurs pour cartographier les lésions induites par RFCA, cependant la séparation de la thérapie et de l'imagerie sur deux systèmes nécessite l'usage de multiples cathéters et de systèmes de navigation complexes. Deuxièmement la thérapie par HIFU présente de nombreux avantages potentiels par rapport à la RFCA, qui pourraient bénéficier à l'ablation cardiaque, surtout dans le contexte des tachycardies ventriculaires (VT).

Dans ce travail, d'abord, un nouveau transducteur intracardiaque dual-mode a été conçu en collaboration avec Vermon (Tours, France). Nous avons caractérisé l'intensité en émission en parallèle avec la chauffe interne de la sonde pour plusieurs paramètres d'émission. Ensuite nous avons validé in-vitro les séquences de HIFU optimales adaptées à notre système, avec des conditions mimant celles du cœur. Enfin nous avons effectué une étude de faisabilité in-vivo pour le cathéter dual-mode dans quatre moutons (N = 4), avec une installation intracardiaque classique, et nous avons réalisé des ablations guidées par imagerie dans les oreillettes droites, les ventricules droits et les septums interventriculaires (IVS).

Matériel et méthodes

Le transducteur dual-mode est basé sur un cathéter d'échocardiographie intracardiaque standard (voir Chapitre 3) et a été modifié par Vermon pour supporter les émissions HIFU. Il est commandé par une électronique prototype programmable, constituée d'un échographe ultrarapide (Aixplorer®, SuperSonic Imagine, France) pour l'imagerie et d'une alimentation de haute puissance.

Premièrement, les meilleurs paramètres d'émission ont été évalués en termes de d'efficacité thermique, définie comme l'intensité en émission (W/cm^2) divisée par la chauffe interne du cathéter (°C). Deuxièmement, les séquences HIFU optimales ont été testées pour accroître la chauffe des tissus, tout en refroidissant le cathéter seulement avec des conditions mimant celles du cœur (un flux d'eau de 50mL/s).

Enfin, le HIFU a été exécuté in-vivo, sous guidage B-mode temps-réel du cathéter, dans les oreillettes droites (n = 6), dans les ventricules droits (n = 5) et dans le septum interventriculaire (n = 5) dans quatre moutons (N = 4). Parmi ces échantillons, l'évaluation des lésions par SWE a été effectuée dans deux moutons (N = 2, oreillette n = 3, ventricule n = 3, septum n = 3). Le cathéter a été inséré par la veine fémorale sous fluoroscopie. Après la procédure les lésions ont été marquées au TTC (2,3,5-triphenyl tetrazolium chloride) et le cœur était excisé pour une étude macro.

Résultats

La meilleure fréquence en émission s'est avérée d'être autour de 5.5MHz avec un signal d'excitation des éléments qui contient le moins d'harmoniques possible. Des intensités

jusqu'à 21.5 W/cm^2 (correspondant à une puissance acoustique totale de 4.6W) ont pu être atteintes.

Cinq (n = 5) lésions ont pu être obtenues avec succès dans les oreillettes. Quatre étaient transmurales. Les lésions avaient une longueur moyenne en grand axe de 7.5mm (4 à 10mm). Dans les ventricules trois lésions (n = 3) ont été réalisées dans la paroi libre. Une lésion était transmurale, une sur l'endocarde et une sur l'épicarde, alors toutes les procédures ont été effectuées à partir des chambres cardiaques. Toutes ces lésions avaient une profondeur approximative de 4mm. Dans le septum quatre lésions (n = 4) ont été réalisées : deux du côté du ventricule droit et deux du côté gauche alors que le cathéter se trouvait dans le ventricule droit.

Au total trois lésions (n = 3) auriculaires ont été évaluées avec succès avec la SWE, deux dans le ventricule droit (n = 2) et une dans le septum (n = 1).

Conclusion

Dans cette étude nous avons développé un nouveau système intracardiaque tout-ultrason, capable faire de la thérapie et de l'imagerie avec la même barrette. Le dispositif est une adaptation directe d'un cathéter d'imagerie et le réseau multiélément qui en résulte permet d'effectuer une thérapie par HIFU flexible couplée avec une imagerie de haute qualité, qui sont parfaitement alignées. In-vivo de nombreux types de tissus cardiaques (oreillettes, ventricules) ont été ablatés avec succès tout en étant contrôlés avec la SWE et l'imagerie B-mode temps-réel.

Ce système theranostique présente de nombreux potentiels avantages par rapport à la RFCA pour la thérapie dans les oreillettes mais aussi dans les ventricules où la RFCA et d'autres modalités de thérapie par contact sont limitées. En implémentant de nouvelles modalités d'imagerie ce système pourrait devenir un puissant outil pour le traitement des arythmies cardiaques.

Chapitre 5 : Imagerie de suivi par l'Élastographie par Ondes de Cisaillement transœsophagienne

Introduction

Dans ce chapitre nous proposons une deuxième approche basée sur les ultrasons par voie transoesophagienne. Ce travail a été motivé par l'approche transoesophagienne développée au laboratoire LabTau (INSERM 1032). Elle consiste à utiliser un dispositif transoesophagien d'imagerie-thérapie développé par Constanciel et al. [30, 31]. Dans ce système un transducteur transoesophagien conventionnel a été intégré à l'intérieur d'une sonde HIFU.

Dans cette étude nous étudions la faisabilité d'une approche de thérapie et imagerie duale sur le même dispositif transoesophagien. Nous montrons in-vivo que la SWE cardiaque quantitative peut être effectuée avec le système et nous montrons sur des échantillons ex-vivo que la SWE transoesophagienne peut cartographier l'étendue des lésions HIFU.

Matériel et méthodes

Un endoscope d'imagerie-thérapie conçu pour le HIFU guidé par ultrasons par voie transoesophagienne a été utilisé dans cette étude (Vermon, Tours, France). La partie active de ce système est faite transducteur HIFU de 8 anneaux tirant à 3MHz et d'un réseau circulaire d'imagerie de 64 éléments à 5MHz pour l'échocardiographie transoesophagienne classique intégré en son centre. L'imagerie était effectuée avec un Aixplorer.

Premièrement, la SWE était validée avec l'endoscope transoesophagien dans un moton in-vivo. La dureté d'oreillettes normales et de ventricules a été évaluée pendant le cycle cardiaque (n=11) et cartographiée (n=7). Deuxièmement, l'ablation par HIFU a été réalisée avec le dispositif d'imagerie-thérapie transoesophagienne dans des échantillons ex-vivo de poitrine de poulet (n=3), puis d'oreillettes (n=2) et de ventricules (n=2) de cœur de porc. La SWE a fourni des images de dureté des tissus avant et après ablation. Les surfaces des lésions ont été obtenues avec le changement de couleur des tissus à l'étude macro et ont ensuite été comparées à celles obtenues avec la SWE. La SWE a été effectuée avec la nouvelle imagerie ultrarapide par ondes divergentes [32].

Résultats

Pendant le cycle cardiaque la dureté a varié entre 0.5±0.1kPa et 6.0±0.3kPa dans les oreillettes et de 1.3±0.3kPa à 13.5±9.1kPa dans les ventricules. Il était possible de mesurer la dureté des tissus à tout moment du cycle cardiaque.

Les lésions thermiques étaient visibles sur toutes les cartes de SWE effectuées après ablation. Le module de cisaillement des zones traitées a augmenté jusqu'à 16.3±5.5kPa (vs. 4.4±1.6kPa avant l'ablation) dans la poitrine de poulet, jusqu'à 30.3±10.3kPa (vs. 12.2±4.3kPa) dans les oreillettes et jusqu'à 73.8±13.9kPa (vs. 21.2±3.3kPa) dans les ventricules. A l'étude macro, la surface des lésions a varié entre 0.1 et 1.5cm^2 dans la région du plan d'imagerie. Les profondeurs et largeurs des lésions estimées par SWE a été différente en moyenne de 0.8±2.3mm et -0.2±3.4mm respectivement par rapport à l'étude macro.

Conclusion

Nous avons montré la faisabilité du suivi d'ablation thermique par HIFU en utilisant un dispositif transoesophagien dual de thérapie et imagerie. La combinaison du HIFU, de l'imagerie ultrasonore et de la SWE sur le même système transoesophagien pourrait mener à un nouveau dispositif clinique pour un traitement plus sûr et contrôlé d'une large variété d'arythmies cardiaques.

Chapitre 6 : Autres perspectives en imagerie et conclusion générale.

Autres perspectives : la tomographie acoustoélectrique ultrarapide

Dans le contexte de la RFCA pour les arythmies auriculaires et ventriculaires, l'imagerie des courants électriques et des potentiels d'action dans le cœur sont effectués avec des systèmes intracardiaques mono ou multi-électrodes [12]; de nouveaux systèmes non-invasifs sont aussi implémentés en clinique [33]. Malgré l'indéniable utilité et fonctionnalité de ces systèmes il n'est pas possible de cartographier la densité de courant électrique avec une résolution spatiale en-dessous de 5mm [34, 35], ce qui pourrait aider à d'identifier des régions conductrices non-ablatées ou d'autres sources de dépolarisation, qui participeraient ou donneraient origine aux arythmies.

Il a récemment été montré que l'effet acoustoélectrique [36, 37] peut fournir du contraste directement à partir des densités de courant en mesurant l'impédance électrique modulée par ultrasons [38]. La technique consiste à insonifier un tissu avec un faisceau d'ultrasons focalisés en mesurant simultanément les différences haute-fréquence des potentiels. Quand l'onde ultrasonore atteint une région dans laquelle le courant circule, une différence haute-fréquence du potentiel peut être détectée.

Dans ce travail, premièrement, une étude de preuve de concept expérimentale a été conduite dans une configuration simple, pour montrer l'interaction acoustoélectrique dans des solutions ioniques, en commençant par un transducteur focalisé, puis en focalisant les ultrasons avec une sonde d'imagerie. Cette parie souligne la faiblesse de l'imagerie acoustoélectrique focale, même si une solution pour augment le ratio signal-à-bruit (SNR) est proposée.

Deuxièmement, nous avons développé la Tomographie Acoustoélectrique Ultrarapide (UAT), basée sur les émissions d'ondes planes. Les stratégies de reconstruction basées sur la transformée de Radon ont été conçues pour augmenter la cadence d'imagerie et fournir de hautes résolutions uniformes en spatial et temporel, tout en respectant les standards de la FDA pour les applications humaines. La validation dans des fantômes a été effectuée, montrant la viabilité de l'approche avec une sonde d'imagerie standard.

En utilisant une approche intracardiaque, cette technique pourrait potentiellement fournir des images de courants électriques cardiaques avec une résolution submillimétrique inégalée, qui pourrait aider à trouver ou diagnostiquer des circuits électriques arythmogènes ou anormaux dans le cœur.

Conclusion générale

Cette thèse a été l'opportunité de prendre avantage des possibilités de plus en plus nombreuses que les ultrasons peuvent offrir dans le domaine de l'imagerie médicale et de la thérapie et de les appliquer à un besoin particulier : le traitement des arythmies cardiaques. En choisissant une approche tout-ultrason pour la thérapie et pour l'imagerie, nos collaborateurs et nous avons développé deux dispositifs interstitiels, un cathéter intracardiaque dual-mode et un endoscope transoesophagien de HIFU guidé par ultrasons, tous les deux adaptés à l'environnement cardiaque.

Tout d'abord, nous avons validé la précision de la SWE à suivre les thérapies thermiques, comme la RFA ou le HIFU, in-vivo dans le foie. Les résultats obtenus sont très prometteurs et donnent des hautes valeurs de sensibilité et de valeur prédictive positive pour la détection des tissus ablatés et confirment les résultats précédents sur le lien des tissus coagulés thermiquement et des images d'élasticité.

Deuxièmement, nous avons implémenté la SWE et d'autres modalités d'imagerie sur un transducteur intracardiaque et avons testé le système in-vivo. En particulier nous avons validé la faisabilité de la SWE à pouvoir évaluer la RFCA classique dans le cœur et nous avons montré le potentiel d'autres imageries diagnostiques (par exemple la détection des coronaires par le Doppler ultrarapide).

Troisièmement, nous avons implémenté la thérapie HIFU sur le même transducteur pour obtenir un système capable d'effectuer de la thérapie contrôlée par image avec le même réseau d'éléments. Un tel système dual-mode présente une flexibilité très intéressante pour les procédures d'ablation pour la fibrillation auriculaire ainsi que pour les tachycardies ventriculaires. Grâce aux nombreuses possibilités d'imagerie et de thérapie que ce système offre, ses applications pourraient être diverses dans le cœur comme dans d'autres organes.

Enfin, nous avons participé au développement d'un second système ultrasonore dédié au cœur, en implémentant et validant la SWE pour l'évaluation de l'ablation par HIFU. Pour cela nous avons testé la SWE basée sur l'imagerie ultrarapide par ondes divergentes, développée précédemment, avec une sonde transoesophagienne. Nous avons montré la faisabilité de cartographier la dureté des tissus avec ce système in-vivo dans un cœur battant normal et in-vitro sur des tissus cardiaques avec des lésions induites par HIFU avec la même sonde. Au-delà du contrôle de l'ablation thermique, la SWE par approche transoesophagienne pourrait être montrée comme une modalité d'élastographie prometteuse pour les diagnoses cardiaques.

Mots-clefs : Ultrasons, Imagerie médicale, Échographie, Thérapies non-invasives, Arythmies cardiaques, Élastographie par ondes de cisaillement, Ultrasons Focalisés à Haute Intensité, Suivi d'ablation thermique, Échocardiographie intracardiaque, Échocardiographie transœsophagienne, Imagerie de Doppler ultrarapide, Imagerie acoustoélectrique

Bibliographie

[1] M. Zoni-Berisso, F. Lercari, T. Carazza, and S. Domenicucci, "Epidemiology of atrial fibrillation: European perspective.," Clin. Epidemiol. **6**, 213–20 (2014).

[2] A.S. Go *et al.*, "Heart disease and stroke statistics--2014 update: a report from the American Heart Association.," Circulation **129**(3), e28–e292 (2014).

[3] T.J. Wang *et al.*, "Temporal relations of atrial fibrillation and congestive heart failure and their joint influence on mortality: the Framingham Heart Study.," Circulation **107**(23), 2920–5 (2003).

[4] a J. Camm *et al.*, "Guidelines for the management of atrial fibrillation: the Task Force for the Management of Atrial Fibrillation of the European Society of Cardiology (ESC).," Eur. Heart J. **31**(19), 2369–429 (2010).

[5] S. Stewart, C.L. Hart, D.J. Hole, and J.J.. McMurray, "A population-based study of the long-term risks associated with atrial fibrillation: 20-year follow-up of the Renfrew/Paisley study," Am. J. Med. **113**(5), 359–364 (2002).

[6] M. Haïssaguerre *et al.*, "Spontaneous initiation of atrial fibrillation by ectopic beats originating in the pulmonary veins," N. Engl. J. Med. **339**(10), 659–666 (1998).

[7] S. Nattel, "New ideas about atrial fibrillation 50 years on.," Nature **415**(6868), 219–26 (2002).

[8] E.M. Aliot *et al.*, "EHRA/HRS Expert Consensus on Catheter Ablation of Ventricular Arrhythmias: developed in a partnership with the European Heart Rhythm Association (EHRA), a Registered Branch of the European Society of Cardiology (ESC), and the Heart Rhythm Society (HRS); i," Europace **11**(6), 771–817 (2009).

[9] J. De Bakker *et al.*, "Reentry as a cause of ventricular tachycardia in patients with chronic ischemic heart disease: electrophysiologic and anatomic correlation.," Circulation **77**(3), 589–606 (1988).

[10] P. Jaïs, M. Haïssaguerre, D. Shah, S. Chouairi, L. Gencel, and J. Clémenty, "A focal source of atrial fibrillation treated by discrete radiofrequency ablation," Circulation **95**(3), 572–576 (1997).

[11] B.B. Lerman *et al.*, "Mechanism of Repetitive Monomorphic Ventricular Tachycardia," Circulation **92**(3), 421–429 (1995).

[12] H. Calkins *et al.*, "2012 HRS/EHRA/ECAS Expert Consensus Statement on Catheter and Surgical Ablation of Atrial Fibrillation: recommendations for patient selection, procedural techniques, patient management and follow-up, definitions, endpoints, and research trial design.," Europace **14**(4), 528–606 (2012).

[13] R. Kobza *et al.*, "Late recurrent arrhythmias after ablation of atrial fibrillation: Incidence, mechanisms, and treatment," Hear. Rhythm **1**(6), 676–683 (2004).

[14] H. Calkins *et al.*, "Treatment of atrial fibrillation with antiarrhythmic drugs or radiofrequency ablation: two systematic literature reviews and meta-analyses.," Circ. Arrhythm. Electrophysiol. **2**(4), 349–61 (2009).

[15] J. Mallidi, G.N. Nadkarni, R.D. Berger, H. Calkins, and S. Nazarian, "Meta-analysis of catheter ablation as an adjunct to medical therapy for treatment of ventricular tachycardia in patients with structural heart disease.," Heart Rhythm **8**(4), 503–10 (2011).

[16] K.F. Chu and D.E. Dupuy, "Thermal ablation of tumours: biological mechanisms and advances in therapy.," Nat. Rev. Cancer **14**(3), 199–208 (2014).

[17] S.N. Goldberg, G.S. Gazelle, and P.R. Mueller, "Thermal Ablation Therapy for Focal Malignancy : A Unified Approach to Underlying Principles, Techniques, and Diagnostic Imaging Guidance," Am. Roentgen Ray Soc. **174**(2), 323–331 (2000).

[18] G. ter Haar, "Therapeutic applications of ultrasound.," Prog. Biophys. Mol. Biol. **93**(1-3), 111–29 (2007).

[19] R. Lencioni and L. Crocetti, "Local-Regional Treatment of Hepatocellular Carcinoma," Radiology **262**(1), 43–58 (2012).

[20] L. Solbiati, M. Ahmed, L. Cova, T. Ierace, M. Brioschi, and S.N. Goldberg, "Small Liver Colorectal Metastases Treated with Percutaneous Radiofrequency Ablation: Local Response Rate and Long-term Survival with Up to 10-year Follow-up," Radiology (2012).

[21] A.A.J.M. Van Tilborg *et al.*, “Long-term results of radiofrequency ablation for unresectable colorectal liver metastases: a potentially curative intervention.,” Br. J. Radiol. **84**(1002), 556–65 (2011).

[22] T. Livraghi, L. Solbiati, M.F. Meloni, G.S. Gazelle, E.F. Halpern, and S.N. Goldberg, “Treatment of focal liver tumors with percutaneous radio-frequency ablation: complications encountered in a multicenter study.,” Radiology **226**(2), 441–51 (2003).

[23] N.P. Reuter, C.E. Woodall, C.R. Scoggins, K.M. McMasters, and R.C.G. Martin, “Radiofrequency ablation vs. resection for hepatic colorectal metastasis: therapeutically equivalent?,” J. Gastrointest. Surg. **13**(3), 486–91 (2009).

[24] S. Mulier, Y. Ni, J. Jamart, T. Ruers, G. Marchal, and L. Michel, “Local recurrence after hepatic radiofrequency coagulation: multivariate meta-analysis and review of contributing factors.,” Ann. Surg. **242**(2), 158–171 (2005).

[25] E. Sapin-de Brosses, M. Pernot, and M. Tanter, “The link between tissue elasticity and thermal dose in vivo.,” Phys. Med. Biol. **56**(24), 7755–65 (2011).

[26] J. Bercoff, M. Tanter, and M. Fink, “Supersonic shear imaging: a new technique for soft tissue elasticity mapping,” IEEE Trans. Ultrason. Ferroelectr. Freq. Control **51**(4), 396–409 (2004).

[27] J. Bercoff, M. Pernot, M. Tanter, and M. Fink, “Monitoring thermally-induced lesions with supersonic shear imaging,” Ultrason. Imaging **40**, 29–40 (2004).

[28] B. Arnal, M. Pernot, and M. Tanter, “Monitoring of thermal therapy based on shear modulus changes: II. Shear wave imaging of thermal lesions.,” IEEE Trans. Ultrason. Ferroelectr. Freq. Control **58**(8), 1603–11 (2011).

[29] C. Demene *et al.*, “Spatiotemporal clutter filtering of ultrafast ultrasound data highly increases Doppler and fUltrasound sensitivity,” IEEE Trans. Med. Imaging (2015).

[30] E. Constanciel *et al.*, “Design and Evaluation of a Transesophageal HIFU Probe for Ultrasound-Guided Cardiac Ablation : Simulation of a HIFU Mini-Maze Procedure and Preliminary Ex Vivo Trials,” IEEE Trans. Ultrason. Ferroelectr. Freq. Control **60**(9), 1868–1883 (2013).

[31] E. Constanciel *et al.*, “Ultrasound-guided transesophageal HIFU exposures for atrial fibrillation treatment: First animal experiment,” Irbm **34**(4-5), 315–318 (2013).

[32] C. Papadacci, M. Pernot, M. Couade, M. Fink, and M. Tanter, “High-contrast ultrafast imaging of the heart.,” IEEE Trans. Ultrason. Ferroelectr. Freq. Control **61**(2), 288–301 (2014).

[33] M. Haissaguerre *et al.*, “Driver domains in persistent atrial fibrillation.,” Circulation **130**(7), 530–8 (2014).

[34] M. Haissaguerre *et al.*, “Noninvasive panoramic mapping of human atrial fibrillation mechanisms: A feasibility report,” J. Cardiovasc. Electrophysiol. **24**(6), 711–717 (2013).

[35] H.U. Klemm *et al.*, “Catheter motion during atrial ablation due to the beating heart and respiration: impact on accuracy and spatial referencing in three-dimensional mapping.,” Heart Rhythm **4**(5), 587–92 (2007).

[36] F.E. Fox, K.F. Herzfeld, and G.D. Rock, *The Effect of Ultrasonic Waves on the Conductivity of Salt Solutions*, Phys. Rev. **70**(5 & 6), 329–341 (1946).

[37] J. Jossinet, B. Lavandier, and D. Cathignol, “The phenomenology of acousto-electric interaction signals in aqueous solutions of electrolytes,” Ultrasonics **36**(1-5), 607–613 (1998).

[38] R. Olafsson, S. Member, R.S. Witte, S. Huang, and M.O. Donnell, “Ultrasound Current Source Density Imaging,” IEEE Trans. Biomed. Eng. **55**(7), 1840–1848 (2008).

Summary

Chapter 1. Introduction

1 Clinical context: cardiac arrhythmias

1.1 Cardiac anatomy

The heart is the blood pump of the body. The function of this organ is vital; a partial dysfunction can immediately severely affect the whole body.

The heart is located at the center of the chest, most of the time (during the respiratory cycle) ahead of the lungs. It is composed of four chambers, left and right atria and left and right ventricles (Figure 1-1a). The atria, anterooms of the ventricles, help filling these during the cardiac cycle and the final pumping effort is performed by the ventricles. The right part of the heart receives deoxygenated blood from the body and sends it to the lungs. The left part receives oxygenated blood from the lungs and sends it to whole body, the left ventricle thus has to provide much more effort and encounters more resistance than the right. In consequence its volume and thickness is more important (Figure 1-1b).

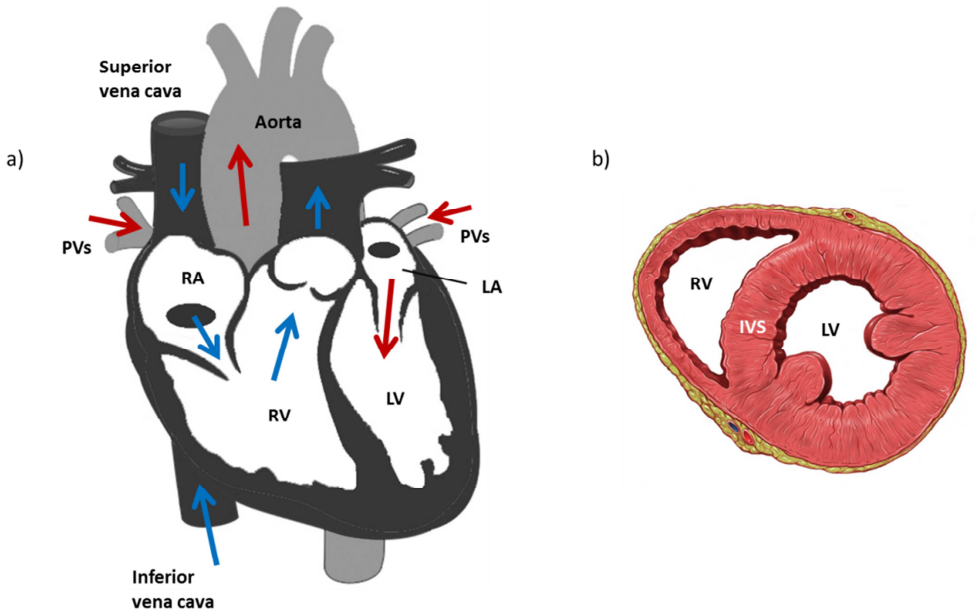

Figure 1-1 : Anatomical structure of the heart. (a) Global view showing, the four cardiac chambers and the schematic blood circulation (blue: deoxygenated blood; red: oxygenated).

(b) Cross section of the heart showing the muscular thickness and anatomy of the ventricles. RA: right atrium; LA: left atrium; RV: right ventricle; LV: left ventricle; IVS: interventricular septum; PVs: pulmonary veins. (CC for b: Patrick J. Lynch, medical illustrator; C. Carl Jaffe, MD, cardiologist).

The heart is a muscular, fibrous organ; the cardiac wall is composed of the inner endocardium, middle myocardium and the outer epicardium. The whole organ is surrounded by a sac called the pericardium. The cardiac cycle is composed a complete heart beat which covers the contraction (systole) and the relaxation (diastole). It begins on atrial systole (Figure 1-2): first, the atrio-ventricular (AV) valves open leading to a passive ventricular filling from the full of blood atria, second, atria contract and propel the remaining 20-30% volume of blood to the ventricles. Then AV valves close and ventricular systole begins leading to an isovolumic contraction. Pulmonary and aortic valve opening follows and the blood is ejected from the heart. Finally the valves close and isovolumic relaxation begins while the atria fill with blood.

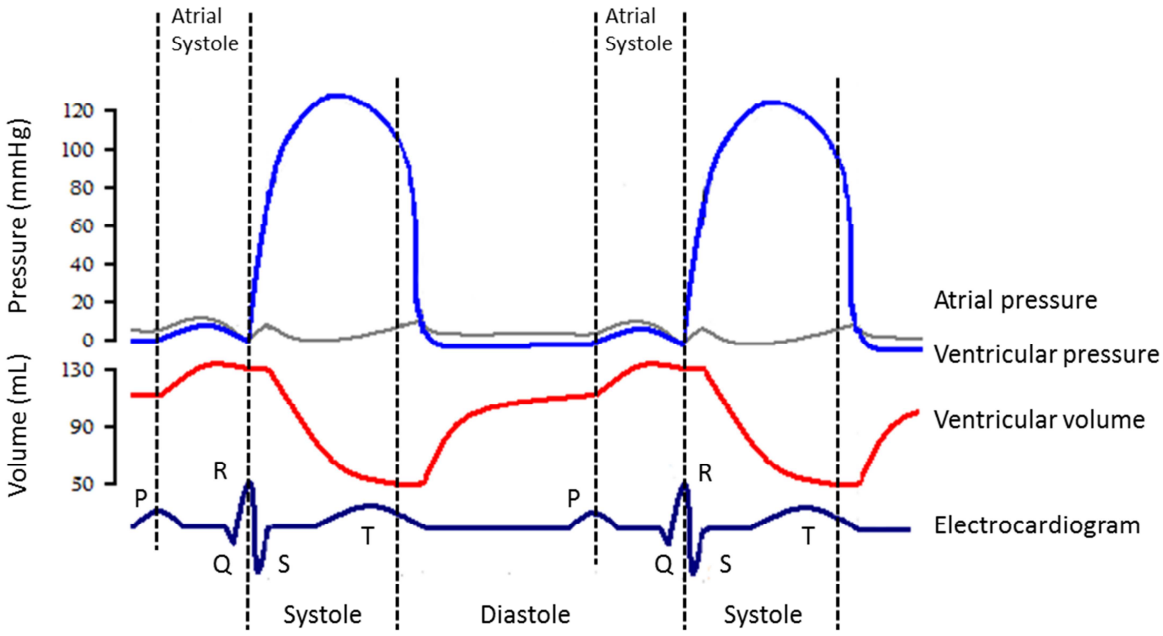

Figure 1-2 : Diagram of principal cardiac cycle events (contraction, relaxation), confronted to the electrocardiogram, ventricular volume, and ventricular and atrial pressures. (adapted from: http://en.wikipedia.org/wiki/Cardiac_cycle#/media/File:Wiggers_Diagram.png)

Heart rythmics are controlled with the sinoatrial node on the right atrium. This self-contracting node is connected in turn to the atrioventricular node, which constitutes the electrical junction between atria and ventricles. The electrical signal is propagated then to the ventricles by specialized tissue called the Purkinje fibres. Finally the whole organ contracts by

a successive chemical signal transmission from cardiac cell to cell. Both atria then both ventricles contract simultaneously. As a result variations of an electrical signal, the electrocardiogram (ECG), can be observed during the cardiac cycle which corresponds exactly to the different events of the cycle. The ECG is composed of a P-wave, which corresponds to the atrial contraction, followed by the QRS complex, the ventricular systole and ended by the T-wave, the ventricular diastole.

In average a human heart contracts 60 to 100 times per minute, with an output of 4 to 8 $L.min^{-1}$ (average 5.25 $L.min^{-1}$).

1.2 Cardiac arrhythmias

Heart rhythm disorders are associated with severe short and long term health risks. Atrial fibrillation (AF), the most frequent arrhythmia, which affects 2-3% of the European and North-American population [1], is associated with a 5 fold increased risk of stroke, with a 40% incidence of congestive heart failure[2, 3] and in general a doubled death rate[4, 5]. AF is caused by dysfunctional electrical activity that initially occurs in the pulmonary veins (PV) [6] or in the atria [7]. Ventricular tachycardias (VT) are related to an important risk of sudden cardiac death [2]. VTs can originate from electrical reentries within myocardial scar or early activation point sources in the ventricular muscle[8]. While VTs often require the implantation of an implantable cardioverter-defibrillator, both AF and VT can be treated with drug therapy, tissue ablation, or a combination of both.

Depending on the duration of arrhythmic episodes, AF is distinguished in few types. Paroxysmal AF is a self-terminating arrhythmia, usually under 48h. When AF lasts for more than 7 days or requires drug or electrical cardioversion for termination, it is called persistent. A long-standing persistent AF lasts for more than 1 year and requires a rhythm control strategy.

VT classification can be simplified to: premature ventricular complexes (less than 3 beats arising with a cycle length of < 600ms), non-sustained VT (duration of >3 beats and < 30s with a cycle length of < 600ms), sustained monomorphic VT (>30s duration or requiring earlier intervention due to hemodynamic instability; similar QRS configuration from beat to beat), sustained polymorphic VT (the same but with a continuously changing QRS).

1.3 Treatment of arrhythmia

1.3.1 Drug administration

A standard management strategy of AF is a first-line drug therapy[4, 9]. Depending on the symptoms, risks (thromboembolism) and structural heart diseases, drugs can be anticoagulative, rate controlling and antiarrhythmic. In parallel a drug or electrical cardioversion can be performed to acutely restore a sinus rhythm. Antiarrhythmic drugs (AAD) interfere with various types of ionic channels in cardiac tissues (sodium, potassium, calcium) or the sympathetic nervous system. However, the general success rate of AAD has been reported to be around 50% [10]. Moreover this kind of therapy is related to a variety of adverse effects encountered among approximately 30% of treated patients[10].

Depending on the nature of the VT and e.g. the presence of structural heart disease, priority management of this arrhythmia can be an implantation of an implantable cardiovereter-defibrillator or a pacemaker, AAD administration or ablation [8, 11].

1.3.2 Ablation

Cardiac ablation is settled as a second-line therapy for AF (i.e. when the AF is one or more drug refractory). It can be performed either by invasive surgery or by a minimally-invasive catheter ablation.

Surgical

Established by Cox et al. [12] surgical ablation strategy consists of the electrical isolation of all possible macro-reentrant circuits that may potentially develop in the atria. The isolation was performed with traditional surgical cut-and-sew incisions in the right and left atria, placed in a pattern letting most of the atrial myocardium to be still activated with the sinus node (Cox-Maze III procedure). Very high success rates were reported[13], however the complexity, technical difficulty and risks related to the procedure hampered a widespread application. The surgical incisions have then been replaced by linear ablation with Radio-Frequency (RF) energy, cryoablation and High-Intensity Focused Ultrasound (HIFU) (Cox-Maze IV). The largest study, reported on a success rate of 89% with or without AAD parallel administration and of 78% without AAD after 12months. Still, this procedure remains invasive and an incidence of major complications of 11% was reported (2% of deaths and approx. 2% of

stroke during operations). Today, the great majority of cardiac ablation is thus performed with catheter-based minimally-invasive procedures.

Minimally-invasive therapy

Minimally-invasive Radio-Frequency Catheter Ablation (RFCA) is a well-established alternative to surgery for the management of AF and a new therapeutic approach to treat VT occurrences. RFCA consists in the electrical isolation of common reentry sources [6, 14] or identified and localized foci [15, 16] through tissue thermal coagulation performed with an intracardiac RF catheter. For AF, the ablation pattern is frequently a simplified Cox-Maze procedure, called mini-Maze.

However, while RFCA is often monitored with electromapping[17–20], electrical impedance measurement [21], fluoroscopy [22], and intracardiac echocardiography [23], it suffers from a lack of precise ablation monitoring to assess the transmurality of the thermal lesion [8, 9], which is a crucial aspect for ensuring effective ablation procedures [24]. The actual heat deposition and thus the lesion extent in the tissues are indeed difficult to assess.

Another important limitation of RFCA is the difficulty of creating transmural or mid-wall lesions in the ventricles. As a consequence an additional epicardial ablation[8, 25] is sometimes needed. Therefore, RFCA is not perfectly adapted for VTs ablation, and a limited success rate of 35% is reported in the literature [25]. In parallel, the single-procedure success rate of RFCA remains relatively low (~ 60%) for all types of treated AF [10]. This rate is improved by repeating the procedures, with an average number of 1.3 procedures per patient a success rate of approx. 72% has been reported, increasing finally to 80% with additional AAD administration (refractory prior RFCA) [26]. Nonetheless the procedure remains time-consuming and still sometimes technically difficult: ablation lines are performed with a dot-by-dot strategy possibly leaving difficult to detect conducting gaps. New balloon-catheter-based systems with other energy sources than RF have been developed. Those include cryoenergy[27, 28], laser[29] or HIFU[30] (but was withdrawn from the market). Balloon-based systems are adapted for quick, single-to-several ablations, pulmonary vein isolation. Success rates approaching RFCA have been reported.

In summary, first, an imaging modality that could provide, in real-time, the spatial extent and the transmurality of ablated tissue could potentially reduce the procedure duration

and difficulty, and improve the effectiveness of existing ablation techniques. Second, a therapy modality that could overcome the local, contact-based energy deposition (RFCA, cryoablation and laser) and easily ablate large zones could also simplify the procedure and significantly improve VT ablation efficiency.

2 Ultrasound therapies

The possibility for ultrasound to produce lasting changes in biological systems has been revealed in 1927 by Wood and Loomis [31]. The therapies presented in this part, can be divided into three parts, thermal therapies, shockwave therapies and cavitation mediated therapies.

2.1 Therapy with ultrasound: history and concepts

2.1.1 HIFU: a thermal therapy

History and concept

Thermal therapies rely on the mechanism of absorption of the mechanical energy by the tissues and its conversion to heat. Two types of those therapies can be distinguished: hyperthermia and ablation. The principle of the first relies on raising the tissue temperature on a 43-50°C range for few minutes to an hour [32, 33]. While the procedure itself leads only to reversible damage [33, 34] it can be used as an adjuvant to radiation therapy [35] or to locally enhance drug- or chemotherapy [36–38].

Ablation relies on applying a local and intense beam in a tissue in order to reach temperatures above 50-55°C [33, 39] and create coagulation necrosis [34] usually within several seconds. The ultrasonic beam is usually highly focused [40] (HIFU, for: High Intensity Focused Ultrasound) leaving surrounding tissue unharmed, which constitutes one of the major advantages of this technique over radio-,curie- or proton therapy. Moreover it is a non-contact therapy, with the potential of being completely non-invasive (unlike RF-, cryo- or laser ablation). One of the actual limitations is that with most systems the ultrasonic beam is very localized and the ablation of large volumes necessitates long-treatment time. However, depending on the target it can also be an advantage. Thus, usually the lesion is first created within a small volume, then the beam is moved nearby and the process repeated. Formerly all

HIFU devices were composed of a single element and were mechanically moved [40]. To ablate larger volumes without movement the transducer's geometry can be altered [41] or the device's architecture can be a multielement transducer allowing for an electronic beam steering or a production of multiple simultaneous foci [42–44].

Lynn et al. [45] were the first to produce highly localized biological effects in tissues and were followed by the Fry brothers in the 1950s who treated over 100 patients for various neurological disorders [46, 47]. Early therapeutic systems were limited by a small choice of imaging techniques (Fry brothers were treating under X-ray imaging) and until the 1990s only one new noticeable system has been designed, for ophthalmological applications [48] (it was the first Food and Drugs Administration approved HIFU system, in 1988). Starting from the 1990s and the emergence of new sophisticated imaging techniques (good quality echography, MRI) HIFU experienced an important renewal of interest.

Today's HIFU patient treatments include (approximate number of treated patients up to 2012 [49]) prostate cancer[50] (45000), uterine fibroids[51] (20000), liver cancer (15000), bone metastases (1000), breast cancer (500) and brain, bone non-metastases, breast fibro-adenoma, kidney, thyroid, pancreas (approx. 500 in total). In total HIFU clinical trials or commercial treatments have been performed for more than 20 different applications, with an exponential growing since the 1990s [49]. Targeted tissues can be tumorous [33, 49, 52, 53], or not [33, 49, 53, 54].

HIFU dosimetry: the thermal dose

As for today no official thermal therapy dosimetry has been instituted. However a recent survey among physicists and engineers working in the field of ultrasound [55] indicated that the most popular and accepted dosimetry for ultrasound thermal therapies is the thermal dose. This in-situ quantification has been introduced by Sapareto and Dewey [56]. It relies on the principle of a thermally equivalent time exposition. The concept originates from the observation that there is an empirical relationship between exposure time and temperature for a biological tissue to exhibit cellular death. Given a time temperature profile T(i) the thermal dose (or CEM: cumulative equivalent minutes) is expressed as the equivalent cumulative time a tissue has been exposed to a 43°C temperature :

$$CEM_{43°C}(t) = \sum_{t_i<t} R^{43-T(i)}(t_i - t_{i-1})$$

With: $R = \begin{cases} 0.5\,, T(i) > 43°C \\ 0.25\,, T(i) \leq 43°C \end{cases}$ an empiric constant and $T(i) = \frac{T_i - T_{i-1}}{2}$ the mean temperature between time t_{i-1} and t_i. In other words this equation signifies that above 43°C a gain of 1°C on tissue temperature divides the needed exposure time by 2. The threshold of a $CEM_{43°C}$ to obtain a nearly 100% necrosis varies among different types of tissues and has been widely investigated. The typical $CEM_{43°C}$ threshold for muscular or myocardial tissue is 240min but only 30min for liver.

The concept of the thermal dose is directly used in MR or ultrasound thermometry to predict the extension of thermally induced lesions.

2.1.2 The other side: non-thermal therapies

Compared to HIFU, which reposes on long continuous emissions, shock-wave uses short but very high pressure pulses (for lithotripsy, typically a 1µs spike of approx. 50MPa followed by a 4µs -10MPa relaxation, with a pulse repetition frequency (PRF) of 1-2Hz at 150-300 kHz). Such a shock produces no-thermal effect but a high stress on the tissue at the focus, which disrupts the target. One of the most common usages of this modality is called lithotripsy, destined to dissolute kidney stones [57, 58]. Lithotripsy has been introduced in the 1980s and has since rapidly gained a very large acceptance to become the dominant treatment method. Shock-wave therapy is also widely used in physiotherapy [59] and with lower power for cardiac angiogenesis (see 2.2.2).

Histotripsy[60] is a second possible non-thermal modality. Similarly to shock-wave lithotripsy, this therapy relies on short but very energetic pulses. It is based on the local generation then mechanical excitation of a bubble cloud within the tissues. More specifically a burst of a few to 10-20 cycles at very high pressures (in order of +100 / -15 to -20 MPa) with frequencies in the range of 200kHz to 3MHz is sent and first few bubbles are generated in the tissue within the focal spot with the inertial cavitation mechanism. For a high probability to generate the bubbles, a peak negative pressure threshold, combined with other parameters has to be reached [61–63]. With a PRF high enough (between 20 Hz and 1kHz) a new

ultrasonic pulse arrives before the bubbles dissolves and a whole bubble cloud is generated. This cloud is then excited at every next pulse and the collapsing bubbles generate enough mechanical stress to disrupt and liquefy the tissue. The resulting fractionation can be used to create cavities, communications and mechanical ablation within the tissues with therapeutic purposes [64]. This mechanism has been applied in-vivo in the heart (see part 2.2.2), the kidney[65], the prostate [66], the liver [67]. Histotripsy has the advantage of being easily controllable with standard B-mode imaging as the bubble cloud appears as a very echogenic region and corresponds exactly to the treated area.

Very analogous to histotripsy, boiling histotripsy is a modality of tissue disruption mixing thermal and mechanical effects [64, 68]. Compared to histotripsy, longer shock-wave pulses are sent (millisecond range) which are strongly attenuated and absorbed by the tissue. The resulting heating generates rapidly a boiling bubble cloud, which in turn is mechanically excited by the ultrasonic pulses and disintegrates the tissue. An interesting possibility for this technique is to decellularize tissue, while the tissue is disrupted, the vascularization can be left behind [64].

Another usage of ultrasound for therapeutic purposes is ultrasound mediated drug delivery [38], by droplet vaporization, sonopration (increase of vascular permeability for drugs), sonophoresis (increase the permeability of the skin) or other. Sonothrombolysis is used to dissolute intravascular thrombuses [69], low-intensity pulsed ultrasound is recognized to enhance bone fracture healing [70] and finally ultrasound for cosmetics and adipose tissue removal [71].

2.2 Cardiac ultrasound therapy

Cardiac ultrasound therapy is challenging. The heart is deeply located behind the ribs at distances up to 15mm and is subject to rapid motion. Moreover possible fat layers in the vicinity of the rib cage can have a strongly aberrating and attenuating effect. A straightforward transthoracic approach is thus particularly demanding.

Despite those obstacles various ultrasound therapeutic systems have been developed in the last two decades [54, 72]. To overcome the ribs and distance issue a particular interest has been focused on endoscopic, interstitial and also surgical approaches. Yet, as the rib cage is an obstacle principally for thermal ablation, there is a gain of interest for other, non-thermal

ultrasound modalities, such as extracorporeal shock-wave therapy (ECWT) and histotripsy. To date only one surgical HIFU device (Epicor, St Jude Medical, Saint Paul, MN) is FDA approved and two ECWT systems (Storz Medical, Switzerland; Medispec, USA) are CE marked.

2.2.1 HIFU-based therapy

Open-chest and transthoracic studies

HIFU epicardial approaches were the first to be tested in the heart. Two studies from the same group[73, 74] reported first in-vivo cardiac ablation by using an open-chest surgery, with few additional trials with an intracardiac but invasive approach. With the same surgical method using additional B-mode guidance Strickberg et al. [75] reported on successful in-vivo atrioventricular junction ablation and another group performed lesions in the interventricular septum [76]. Finally by using a large aperture (22cm diameter) HIFU transducer, formerly dedicated for tumor ablation, Rong et al. [77] reported on first in-vivo transthoracic ablation in the interventricular septum in dogs. Yet the procedure required preparation (skin degassing, artificial hydrothorax) and the chosen cardiac zone was the less affected by motion.

The most advanced HIFU epicardial approach has been the Epicor Medical Cardiac Ablation System[78] (Saint Jude Medical, St. Paul, MN) performing linear lesions on the left atrium. The transducer was inserted through thoracoscopic approach and wrapped around the pulmonary veins along the epicardium. However, despite positive results [78, 79], the necessity of invasive surgery combined with similar results to the classical RFCA and the limitation, by its design, to the treatment of AF led Saint Jude Medical to stop the production of this system.

Many studies have been dedicated to overcome the rib barrier [80–84], principally for liver applications, by using large multi-element apertures. This obstacle can also be bypassed by performing ablation from inside of the body, with interstitial devices.

Interstitial devices

For cardiac ablation two approaches were investigated: transesophageal and intracardiac devices. The first report of an interstitial setup, without open-chest surgery has been reported by Ohkubo et al. [85], where an intracardiac HIFU catheter has been used with a classical femoral vein approach. The most promising intracardiac results were obtained with

balloon-based systems [30] dedicated for pulmonary vein isolation for atrial fibrillation ablation but the usage of those systems is definitively stopped. The reader is invited to consult Chapter4 part 1.2 for a more detailed historical on intracardiac systems.

Transesophageal approaches have also been proposed for cardiac HIFU ablation [86–89] and first animal in-vivo [90, 91] studies have been performed. In this original approach, less invasive than procedures involving catheter insertion into the heart, cardiac thermal lesions are performed through the esophagus with a HIFU endoscope.

Thermal ablation strategies have principally targeted atrial fibrillation and ventricular tachycardia disorders as well as the atrioventricular node ablation. Because of the different nature of the lesions or of effects they produce, non-thermal therapies have been dedicated to other cardiac pathologies.

2.2.2 Other, non-thermal therapies

Cardiac non-thermal therapies are divided into two modalities: ECWT and histotripsy.

Extra-corporeal shock-wave therapy

ECWT relies on sending the same individual shocked-pulses than for lithotripsy. For cardiac application the total power of energy is however ten-times smaller than for kidney stone lithotripsy. The first application for cardiac ECWT was the promotion of angiogenesis [92] to treat ischemic heart disease. Fukumoto et al. performed first successful trials on patients affected by artery coronary disease [93] and was followed by other larger studies [94]. Other groups used the same phenomenon to treat ischemic heart failure prior [95, 96] or not [97] to cardiac cell therapies . No complications were reported during those studies and no cardiac injuries have been reported in randomized trials [98]. ECWT has the advantage to be performed with a simple non-invasive transcostal approach.

Histotripsy

To our knowledge the first to report on in-vivo cardiac tissue disruption were Smith et al. [99]. The cardiac use of histotripsy has then been extensively studied by the University of Michigan group (Ann Arbor, Michigan). Atrial septal defects were achieved in vivo with an open chest approach [100] then in-vivo lesions were in fetal hearts in-utero [101] and in neonatal

pigs without surgery [102]. Finally a motion correction has been developed and successfully tested in-vivo on open-chest animals improving therapy targeting [103]. Another study performed cavitational microlesions by targeting contrast microbubbles in the heart[104] for tissue reduction with potential applications for hypertropic cardiomyopathy. No cardiac transcostal study on big adult animal has been reported however Kim et al. [67] successfully performed liver lesions with a straightforward transcostal approach. Compared to ECWT, histotripsy still has to overcome some technical obstacles and necessitates further safety studies before any first human studies.

2.3 Ultrasound-guided therapy

Every therapeutic modality has a substantial need for guidance, target imaging, therapy control and monitoring. Many ultrasound and non-ultrasound imaging techniques have been developed to address this demand. Chapter 2 part 1.1.2 describes in detail most of those modalities. In this thesis a particular focus is made on ultrasound imaging for therapy guidance and monitoring.

3 Introduction to echography

3.1 Conventional imaging

In conventional B-mode ultrasound imaging an image is acquired by a line-by-line successive beam focusing in front of the probe. For each focus, scatterers on the line reflect a part of the beam which is received and electronically adapted on reception (focusing in reception) to create an image, retrieve the scatterers' positions, on the line. The acquisition time is set by the go and return of the wave and the process is repeated a hundred times to create a whole image. Using linear arrays the beams are focused in front of the probe, using phased arrays (element pitch $\leq \lambda/2$) the beams can be steered outside of the frontal view. Typical frame rates can reach 50-100Hz with this technique.

3.2 Ultrafast imaging

To overcome the limited frame rate of focus-based imaging Tanter et al. [105] proposed to insonify the whole medium with one plane wave to create an image within a single emission-reception time. The beam was only focused on reception and thus the quality of the

image was lower. However the frame rate increased by a factor of a hundred, attaining up to 20000 images per second. This opened completely new perspectives in ultrasound imaging [106] by giving the possibility to observe transient effects which were too rapid before or by significantly increasing the sensitivity of already existing ultrasonic imaging modalities. Moreover Montaldo et al. [107] demonstrated that by sending tilted plane waves (several degrees) and coherently summing them in reception, it is possible to recreate synthetic focal spots within the medium and finally attain to the same quality of image with around 40 emissions than with focused imaging. Even though only few emissions are sufficient to improve the image significantly.

Recently Papadacci et al. [108] demonstrated, with the same rationale, that it is possible to recreate synthetic focuses by sending diverging waves with different virtual sources (virtual centre of the wide-beam diverging wave) with a phased array.

3.3 Shear-wave Elastography

The principle of SWE[109] relies on the synergetic combination of the acoustic radiation force [110] and ultrafast ultrasound imaging [106] leading to real time and quantitative imaging of stiffness. The acoustic radiation force obtained by focusing ultrasound using the imaging probe remotely generates push impulse, which results in the propagation of a shear-wave in the surrounding region that can be imaged with the same probe in real time using plane wave ultrafast imaging. It is possible then to derive visco-elastic properties of the tissue from the induced shear-wave propagation. When assuming the medium to be semi-infinite, the group velocity c_t of the shear-wave is proportional to the shear modulus μ of the examined tissue according to:

$$\mu = \rho c_t^2 \qquad (1.1)$$

where ρ is the local density.

To create a plane shear-wave rather than a cylindrical in deep tissues, it is possible to generate in a row 2-3 push impulses on a column pattern and create an elastic Cerenkov effect [111]. The advantage of this is that the whole depth of the image can be covered with a shear-wave and it is also much easier to calculate its speed. On the other side, it is profitable to

induce and acquire separately a few pushes in width to finally cover the whole image with shear-waves and average the acquisitions if the SNR is low [112].

To calculate the shear-wave speed locally a time-of-flight algorithm [109, 113] is used to track the shear-wave group velocity c_t and the shear modulus map is obtained from (1.1) for each acquisition. Corresponding quality maps are obtained from the algorithm's temporal 1-D cross-correlation. The final 'stiffness map' is obtained with a quality weighted average (least-squares mean) of the acquisitions.

4 Thesis overview

The goal of the thesis is to bring new solutions for cardiac therapy and imaging with minimally-invasive ultrasonic approaches. The privileged solutions are High-Intensity-Focused-Ultrasound (HIFU) for therapy and Shear-Wave Elastography for imaging and therapy evaluation.

In this purpose, first, we evaluated the accuracy and clinical viability of Shear-Wave Elastography (SWE) as a real-time quantitative imaging modality for thermal ablation monitoring in vivo.

Second we implemented SWE on an intracardiac transducer and validated the feasibility of evaluating thermal ablation in vitro and in vivo on beating hearts of a large animal model. Two novel imaging techniques were also developed and assessed on cardiac tissues: ultrafast Doppler imaging to detect small vessels and ultrafast acoustoelectric imaging to map acousto-electrical properties of cardiac tissues.

Third a dual mode intracardiac transducer was developed to perform both ultrasound therapy and imaging with the same elements, on the same device.

At last, SWE was implemented on a transesophageal ultrasound imaging and therapy device and the feasibility of transesophagial approach was demonstrated in vitro and in vivo.

Chapter 2. Real-time monitoring of thermal ablation using Shear-Wave Elastography

1 Introduction

This chapter introduces the concept of thermal ablation monitoring using Shear-Wave Elastography in vivo and will focus on its application in liver thermal therapy.

First the problematic of thermal ablation control is introduced and a state-of-the art among ultrasonic and other imaging modalities is provided, showing the unmet need of a real-time monitoring technique with good temporal and spatial resolution, flexible and objectively reliable.

Second, an in-vivo study is presented in porcine liver using Radio-Frequency Ablation (RFA) as well as High-Intensity Focused Ultrasound (HIFU). The results demonstrate that quantitative and real-time SWE stiffness mapping can be reliably linked to tissue coagulation and can precisely map the thermal ablation extension.

1.1 Control and monitoring of thermal ablation: overview

1.1.1 Thermal ablation

Recent years have witnessed a growing interest for thermal ablation, especially in the field of tumor treatment[34, 114]. Thermoablative minimally invasive techniques, such as radiofrequency[115], laser[116], microwave[117], cryoablation[118] and HIFU[33] ablation, present many advantages over classical surgery and resection. Tumors being treated are present in many organs including the liver[115], the breast[119], the lungs[120], the esophagus[121], the bones[122] and others. In some cases thermo-ablation has become a standard alternative to surgical resection [123–125]. All these minimally invasive therapies, except HIFU, consist in applying thermal energy to a probe inserted into the tumor mass to produce coagulation necrosis [126, 127].

In this chapter we will focus the attention to the specific case of thermal ablation treatment in the liver. In this organ the safety and effectiveness of thermal therapies,

especially radiofrequency, have been widely investigated[128], and high local tumor recurrence rates have been reported[129]. Among most important causes of ablative inefficiency pointed by meta-analysis studies is the inability to predict or control precisely the thermal ablation's extension[130]. This is induced by the fact that the ablative volume is predicted empirically without taking into account the actual anatomy and tissue properties, especially the effects of vascularization, in the direct vicinity and within the targeted area[130, 131]. Existing monitoring relies on target temperature and electrical properties measurement directly in contact with the ablation devices and has been proven of very limited efficiency.

Consequently a substantial need still exists for a precise monitoring technique of the ablation. Such monitoring technique would help, first, guiding the treatment and targeting the tissue, second, discriminating ablated from viable tissue, within and at the borders of the treated volume. Many imaging techniques have been developed in this direction but they have encountered several important limitations.

1.1.2 Ablation monitoring: state-of-the-art

Non-ultrasonic modalities

Current non-invasive monitoring gold standard for temperature mapping is magnetic resonance imaging (MRI). Temperature and by extension thermal dose deposition can be monitored with near real-time MRI sequences. This technique can accurately delineate the treated area and lower the risk of local recurrence[132–134]. In the research field, Magnetic Resonance Elastography (MRE)[135, 136] is another possibility to assess the extension of thermally ablated tissue.

However MR imaging is associated with several technical obstacles (MR compatible materials, limited space for intervention) and is expensive. The temporal and spatial resolutions are also limited and rapid motion affects strongly the imaging quality.

Computed-Tomography (CT) techniques for thermometry have also been investigated [137, 138]. This imaging modality has the potential to provide a good spatial resolution; on the other hand the obtained temperature-related contrast is limited. This technique also offers the possibility to map local vascularization and its absence or reduction due to thermal ablation[139]. Nonetheless the ionizing nature of this modality, with the related dangers and constraints for the physician, limits significantly the interest for its development.

Ultrasound imaging

Because of its low cost and wide availability for surgeons and interventional radiologists during laparotomy or laparoscopy, ultrasonography is one of the preferred modality for image guidance[119, 130, 140]. Moreover, thermal ablation effects are usually visible in real-time in ultrasound images. Indeed, the heating process during thermal ablation leads to the production of steam bubbles that are seen on the ultrasound images as a transient hyperechoic zone, and these artifacts are commonly used as a surrogate marker of target destruction[141–143]. Such clinical usage of ultrasound is however principally dedicated to tissue targeting and provides only qualitative and very incomplete information on target destruction. Furthermore, this hyperechoic zone disappears within several tens of minutes, and cannot be used afterwards to localize the treated zone. A robust and specific real-time imaging method to detect coagulation and precisely monitor the thermal ablation procedure is required.

Extensive work has been performed in the field of ultrasound to monitor various effects of thermal ablation on tissue. Several mechanisms are principally at stake: bubble formation, temperature dependence of the speed of sound, tissue thermal expansion and tissue coagulation. The first three points are transient effects dependent of temperature (speed of sound and thermal expansion) or of an empiric combination of acoustic power (for HIFU ablation) and temperature (bubbles), thereby they are suitable for ablation monitoring during the procedure. Final ablation size can be derived by accumulating such information e.g. by computing the thermal dose. On the other hand the final ablation effect is marked with tissue coagulation[34]. It can be observed during the treatment, but also after tissue's thermal relaxation, as the final physiological effect of the ablation.

Already observed on classical B-mode imaging, bubbles from boiling appear when the 100°C temperature threshold of tissue is reached. However another bubble formation mechanism, inertial cavitation[144], can occur below this temperature depending on ultrasound pressure. A passive detection of such created bubbles has been proposed by Mast et al.[145], where bubble detection is performed with a separated imaging array without any emission pulses. Based on this work, Coussios et al. proposed the Passive Acoustic Mapping (PAM) technique to map the formation of bubbles in real-time in ex-vivo tissue[146]. This type of mapping is very efficient in the detection of a HIFU beam in presence of cavitation, however it does not provide quantitative information on the necrosis and on the progression of the treatment. Moreover it is not capable of evaluating the thermal effect around the focal spot,

where tissue damage comes from non-cavitating thermal diffusion and thus not capable of predicting the whole area of ablation.

The speed of sound dependence in tissue and tissue thermal expansion has been widely investigated in order to map the local temperature[147–152]. Both effects generates an effective strain on ultrasound images that can be quantified precisely. The combination of these two effects is linear in the temperature range up to 50°C and temperature can be directly derived from the time shifts observed within the ultrasonic RF data or by B-mode speckle decorrelation. Above this threshold, the dependence becomes non-linear and temperature cannot be determined easily any more. At this point though tissue coagulation occurs rapidly and within certain conditions the strain generated by the change of tissue properties can be quantified with this technique[153]. One major limitation, however, of strain temperature imaging is its lack of robustness, as temperature is derived from time shifts occurring within successive frames and is thus very sensitive to motion[153]. In this field the most advanced developments are achieved by Ebbini et al. reporting real-time, up to 500Hz temperature monitoring [154, 155]. Such induced variations are also strongly tissue-dependent and sensitive to the fat content within the tissue [156]. This type of imaging, as well as bubble and cavitation detection, relies on transient effects that cannot provide information once the treatment is finished. Thus the final evaluation of the whole area or volume of treatment may be problematic.

Finally it has been also shown that thermal coagulation modulates tissue attenuation [152, 157–159] and the backscattered energy [160]. Yet such obtained contrast remains low, is also very tissue dependent and is based on relative changes, with all the limitations mentioned above.

Ultrasound elastography

Alternatively, thermally induced effects can be quantified by the changes in elastic properties of the tissues. Two phenomena are known and have been reported by many groups: the temperature dependence of tissue elasticity and the observed link between stiffening and thermal coagulation. This first effect has first been reported by Apter[161]. The link between structural collagen denaturation, its irreversibility above 60°C and stiffness changes was shown by [162–164]. Subsequently Wu et al.[135] completed an MR elastography study of thermally induced elasticity variations that highlighted inter alia a first reversible effect of elasticity

decrease between 20 and 60°C and a second of elasticity increase around 60°C and above. In the field of ultrasound, temperature dependence of soft tissue elasticity has been quantified only recently [165–167]. On the other hand tissue elasticity changes after coagulation have been measured using various US elastography techniques. These include static elastography[168–170] and acoustic radiation force based techniques[171–173].

Static elastography is a direct implementation of the Hooke's law. A static constraint is applied on the tissue, generally with the ultrasonic probe or a mechanical piece integrated within, that induces a deformation of the tissue which is measurable on standard B-mode images. This deformation is proportional to the tissue's Young modulus. However, in practice, it is very difficult to control and measure such applied force; thereby the technique provides only qualitative elastic information, which is consequently operator dependent. Moreover because of the time-consuming compression operation this technique is not easily implementable for a real-time in-vivo monitoring.

A similar issue is encountered with the acoustic radiation force based techniques which do not rely on shear-wave propagation. Acoustic Radiation Force Imaging[171, 174] (ARFI) and Harmonic Motion Imaging[172, 175] (HMI) remotely and locally induce a force that generates a vibration of the tissue. The amplitude of this vibration is again proportional to the elastic properties of the tissue, but it is not possible to measure such applied force and thus not possible to provide a quantitative assessment of the local stiffness.

Quantitative mapping of stiffness has been shown of major importance because tissue stiffness during tissue coagulation is directly linked to the thermal dose [176]. To our knowledge Shear-Wave Elastography [109] is the only real-time modality satisfying these conditions. This technique can provide an objective, operator independent, visualization of the thermal lesion boundaries[173, 177]. Moreover thanks to the Ultrafast plane wave imaging, it is relatively not affected by motion naturally present in-vivo.

To assess the feasibility and accuracy of quantitative elasticity monitoring during thermal therapy and to determine the elasticity threshold that predicts the formation of coagulation necrosis, we carried out an in vivo preclinical study in which SWE was used to map thermally induced coagulation necrosis areas produced in pig livers with an RFA and HIFU system.

2 In vivo experiences

In this study two types of thermal ablation systems were used: one composed of bipolar radiofrequency needles, the other using an ultrasonic HIFU transducer. As the two systems present many similarities, the evaluation of SWE to monitor ablation was analogous.

2.1 Materials and methods

All procedures were approved by the University Committee for animal research of the "Ecole de Chirurgie, Assistance Publique-Hôpitaux de Paris" and are in accordance with the guidelines issued by the National Institutes of Health for care of laboratory animals.

2.1.1 Animals and surgery

In total forty (n=40; n= 29 with RFA and n= 11 with HIFU) thermal lesions were carried out in the liver of eight (n=8; RFA: n=5 and HIFU: n=3) Landrace pigs (weight range: 30-35 kg) using an open surgery approach in a surgical suite dedicated to large animals. Anesthesia was induced by ear vein intubation with a mixture of morphine hydrochloride (0.5 mg/kg; Morphine Lavoisier, France) and propofol (4 mg/kg; Fresenius, France) and maintained with isoflurane (1.5%-2.5% for 1 L/min oxygen inhalation; Forene, Abbott, France). The anesthetized animal was in dorsal recumbency on a warming blanket to preserve the body temperature, and then the abdomen was shaved for laparotomy. Vital parameters were monitored throughout the surgery.

2.1.2 Thermal lesions

For both RFA and HIFU approaches a ventral midline laparotomy was performed for all the ablation and imaging protocol. Both systems were fixed on a mechanical arm, which remained immobile during the procedures.

RFA

Two electrodes were inserted in the liver under US guidance, and coagulation necrosis was produced with a bipolar radiofrequency system connected to an electrosurgical generator (Force FX-8C electrosurgical generator; Valleylab, Tyco Healthcare, Switzerland). The generator power was 4 W, the radiofrequency was 470 kHz, and the distance between the two

electrodes was always set to 7mm. To ensure a good imaging reproducibility, we created a self-maintained therapy-imaging device that kept the imaging probe fixed while a translational mechanism allowed the insertion of the electrodes at the focal plane of the probe (Figure 2-1a). A thermal “coagulation necrosis” lesion was created 1.5-2.5 cm beneath the liver surface in approximately 5 min without water vaporization or bubble formation.

HIFU

A similar setup was used for HIFU. A focused single element (2.25MHz, 38mm diameter, focused at 38mm, Imasonic, France) was fixed at the end of a confocal and motorized disposal (Figure 2-1b). The signal was generated with a function generator (AFG 3101, Tektronix, USA) and amplified (BT00100-AlphaS-CW, Tomco, Australia) to 35W of effective electric power, resulting in a pic positive pressure of 7.8±0.2MPa (measured in water) at the ultrasonic focus. The HIFU transducer was angled at 60° to the imaging plane of the imaging probe. The imaging probe remained fixed while the HIFU transducer was motorized with two translational stages (25mm travel range, PI, Germany) in directions parallel to the imaging plane. The dimensions of the HIFU focal spot at -6dB were 0.6mm in diameter and 4.3mm in depth, but as the transducer was angled, it resulted in an approximate ellipsoidal cross-section of 0.6mm by 1mm in the imaging (Figure 2-2).

During the HIFU procedure therapy was applied at one point for 20s then the transducer was moved parallel to the imaging plane: typically with steps of 1mm along its lateral axis and 2mm along depth totaling 9 to 20 positions in a rectangular pattern (Figure 2-2). Lesions were created 20-30mm deep in the liver from the imaging plane point of view.

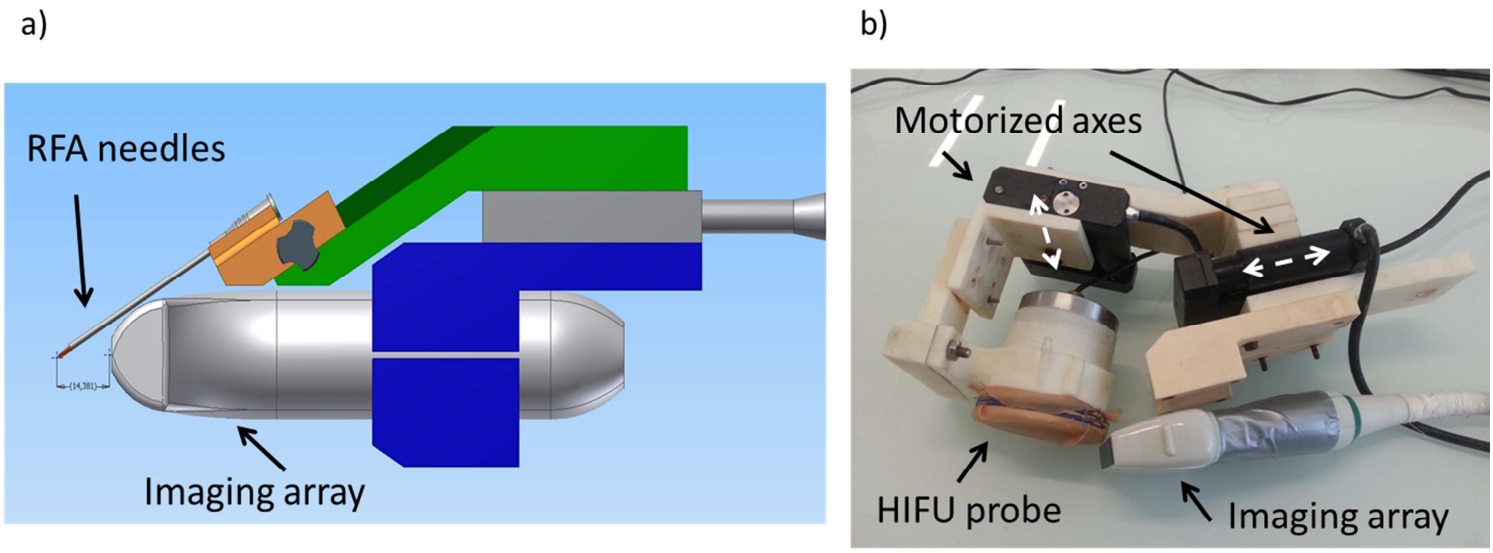

Figure 2-1 : Schematic and photograph of the RFA (a) and HIFU (b) imaging-therapy systems. Both imaging arrays are integral of the immobile mechanical arm (not represented). (a) The RFA system is composed of ablation needles that are inserted in tissue with the translation stage (green) that ensures a perfect alignment of the needles' tips with the imaging plane (15mm away from the transducer). (b) The HIFU probe is fixed on two motorized platines (black) and angles at 60° with the imaging plane. The possible translational range is 25*25mm^2 in parallel to the imaging plane.

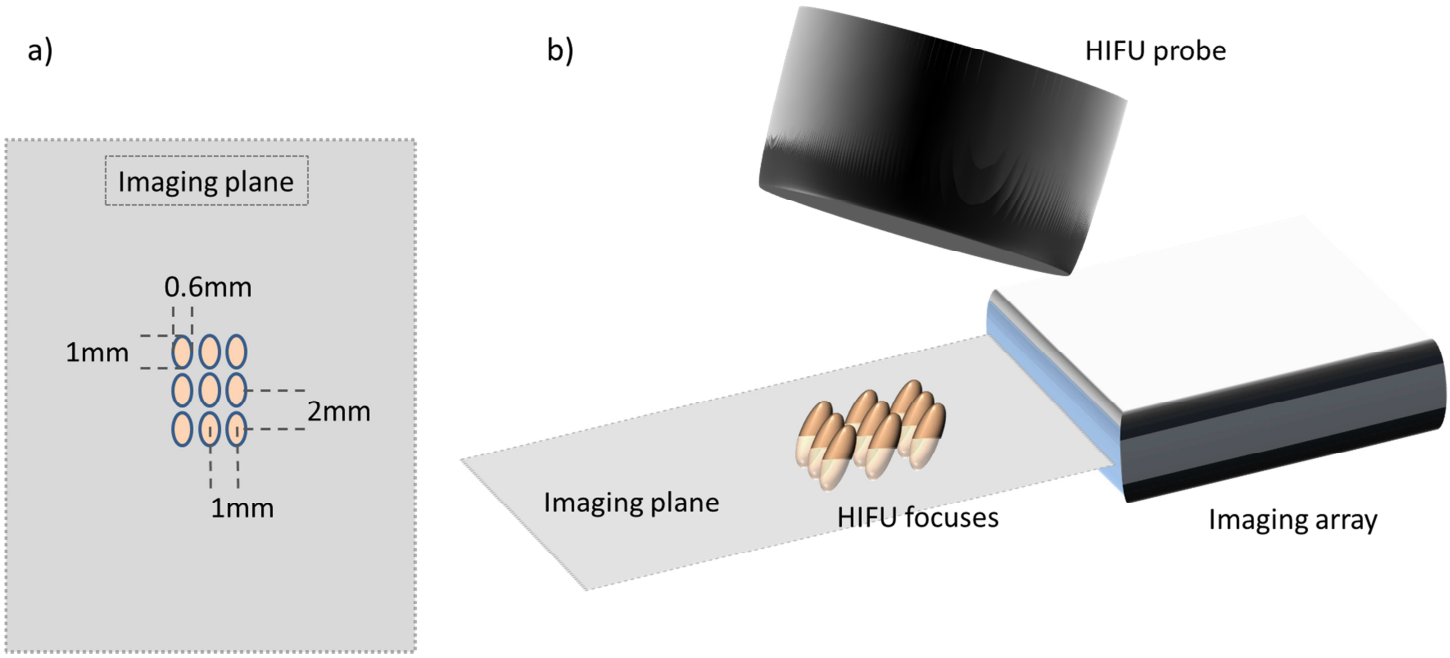

Figure 2-2 : Representations of the HIFU beam relative to the imaging plane. (a) Typical pattern of the performed therapy. HIFU focuses are seen as ellipsoidal cross-sections. (b) 3D representation of the imaging-therapy system.

2.1.3 Image collection

SWE and B-mode images were acquired with an ultrafast ultrasound scanner (Aixplorer, SuperSonic Imagine, France) using two linear probes (for RFA: 8MHz, 256

elements, 0.2mm pitch; for HIFU: 6MHz, 192elements, 0.2mm pitch, Vermon, France). Images were taken before the procedure for reference, every 30s during RFA thermal ablation and at the end of each HIFU focal position (i.e every 20s). At the end of the procedure an image was also taken every minute for 5 min. All images were taken in the focal plane. The imaging plane was used as the reference for sample dissection.

First, B-mode images were used for therapy guidance. Then, SWE images were recorded using the SonicSoftware tool (Supersonic Imagine, Aix-en-Provence, France), under the clinical mode of the scanner, as 2-D Young's modulus maps. Elastographic images and the corresponding B-mode images were acquired simultaneously and saved as static maps. To compare always the same area, images were acquired at the end of the expiratory phase of the respiratory cycle.

2.1.4 Exclusion criteria

An initial liver elasticity value >10 kPa was an exclusion criterion because such high value before any treatment revealed an artifact due to liver compression by the probe. When compression for technical reasons occurred, SWE measures cannot be considered reliable, and we chose to readjust probe and retake a reading. If not recognized during thermal procedure, we excluded lesion from the analysis.

2.1.5 Gross pathology

After in vivo US imaging, animals were euthanized by intravenous injection of 100 mg/kg sodium pentobarbital. The livers were resected and sliced in the focal plane. Gross examination of each lesion was performed in the same position and orientation in which it was previously imaged. Specimens were photographed beside a millimeter ruler. In accordance with previous reports[178, 179], typical macroscopic thermal lesions with a central "white zone" (Wz) of coagulation necrosis surrounded by a peripheral, hyperemic "red zone" (Rz) within the native liver tissue were found (Figure 2-3). A pathologist examined each region of interest to macroscopically differentiate the Wz and Rz areas. Specimens were then preserved in 10% formalin solution for microscopic analysis. Representative tissue samples were embedded in paraffin and stained with hematoxylin-eosin-safran.

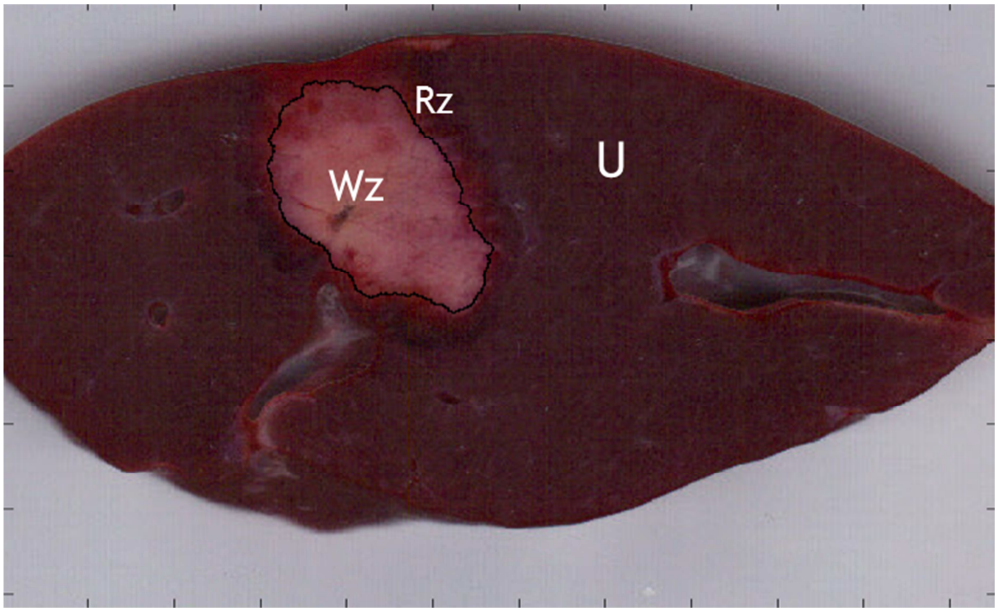

Figure 2-3 : pathological standard features of a thermal lesion in macro specimen, with segmented “white zone” (Wz) of necrosis coagulation, “red zone” (Rz) with red blood cells and untreated (U) healthy tissue.

2.1.6 Image analysis

For both RFA and HIFU, SWE and gross pathology images were analysed using a homemade software program written in Matlab (Mathworks, Natick, MA). For pathology photographs, the K-means[180] clustering was used to automatically segment the Wz only. The Rz contained a large amount of red blood cells and did not always correspond to complete coagulation necrosis. The same elastographic data as displayed on the scanner were used. A region of interest was manually positioned at the lesion location; then, the area corresponding to the lesion was automatically segmented, tissue stiffness was calculated before and after thermal ablation, and the mean elasticity values compared.

RFA specific data analysis

A new contour elastographic map (Figure 2-4) was built by dividing the pixels in zones corresponding to 5 kPa of elasticity, from 15 to 60 kPa. The contours of such created elasticity zones were considered as potential thresholds and tested in correlation with the in vivo findings. Indeed, after semiautomatic rigid registration of the elastographic and pathology image segmentation, the validity of the elastographic prediction was assessed by using a pixel-by-pixel analysis and by classifying the pixels in true positive (TP), false positive (FP) and false negative (FN), according to Figure 2-5. Areas that were classified as

stiff (i.e., above each threshold in kilopascals) and that overlapped with the coagulation necrosis were considered as true positive. Segmented coagulation areas that were not covered by the elastographic map were considered as false negative. Areas above each threshold in kilopascal without necrosis were considered as false positive. The positive predictive value (PPV) and sensitivity (Se) were calculated for each threshold.

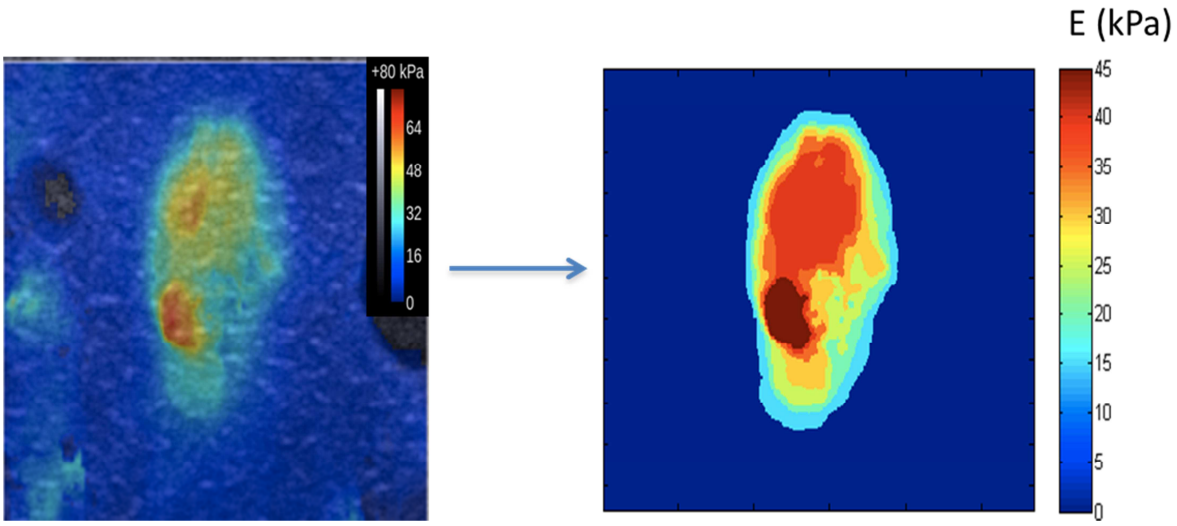

Figure 2-4 : Elastographic map of a thermal lesion obtained by Aixplorer[R] and pixel-by-pixel rebuilt contour map in Matlab (Young's modulus in kPa). The core of this lesion did not exceed 45 kPa.

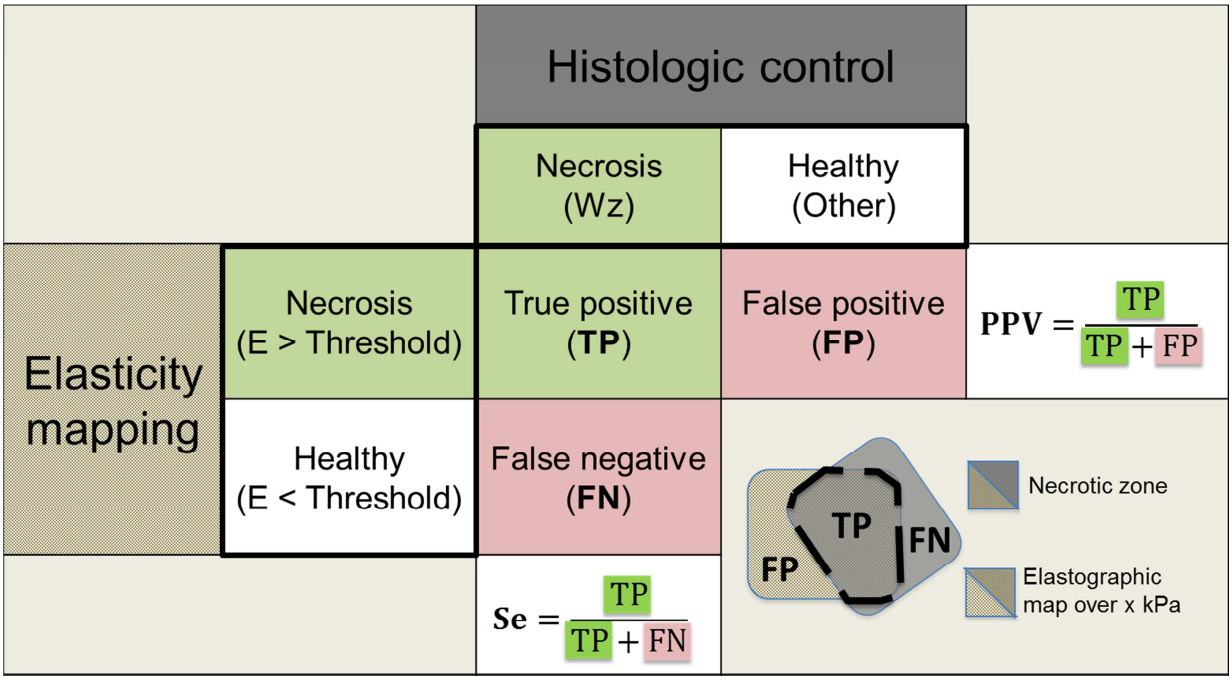

Figure 2-5 : Scheme of data analysis for Radio-Frequency Ablation data.

A radiologist with 20 y of experience interpreted blindly the B-mode images that corresponded to the studied SWE images and tried to outline the lesion boundaries, without knowledge of the elastographic maps. He knew a thermal ablative procedure had been performed following a protocol that avoided water vaporization and steam bubble formation. His mapping was estimated by using the NIH ImageJ software (National Institutes of Health) and compared with the surgical specimens.

This specific SWE data analysis was possible thanks to the physical markers left by the RFA needles. The needles were clearly seen on B-mode images during the procedure, as well as the inclusions they left in the tissue. By matching their position on the ultrasound images and on gross pathology, pixel-by-pixel comparisons were possible. This type of analysis was not possible with HIFU due to the absence of such markers.

HIFU specific data analysis

In the case of HIFU, segmentation of the elastographic maps was performed every 1kPa from 10kPa to 60kPa. As no viable markers were present on all ultrasonic and gross pathology images, no pixel-to-pixel comparison was possible. The best matching surface was the criterion to find the best threshold for SWE to delineate the boundaries of the lesions.

2.1.7 Statistical analysis

Statistical analyses were performed using Matlab. The mean elasticity values of the thermal lesion areas and their respective standard deviations were calculated. Elasticity values before and after ablation were compared with the two-sided Student t-test. The Bland-Altman graphical method was used to detect the presence of systematic bias and measurements outside of the 95% confidence interval. $P < 0.05$ was considered statistically significant.

2.2 Results

Three RFA and one HIFU lesions were excluded because of a pretreatment liver elasticity value >10 kPa. Figure 2-6 shows examples of SWE maps of thermal lesions performed (a) with the RFA setup, (b) with the HIFU setup. The remaining 26 areas of RFA and 10 HIFU thermal lesions had a mean elasticity value of 6.4 ± 0.3 kPa (RFA) and 7.5 ± 1.2 kPa (HIFU) before heating and a mean elasticity of 38.1 ± 2.5 kPa (RFA, $p<0.0001$) and 26.6

± 4.7 kPa (HIFU, p<0.0001) after the procedure that induced coagulation necrosis (Figure 2-7).

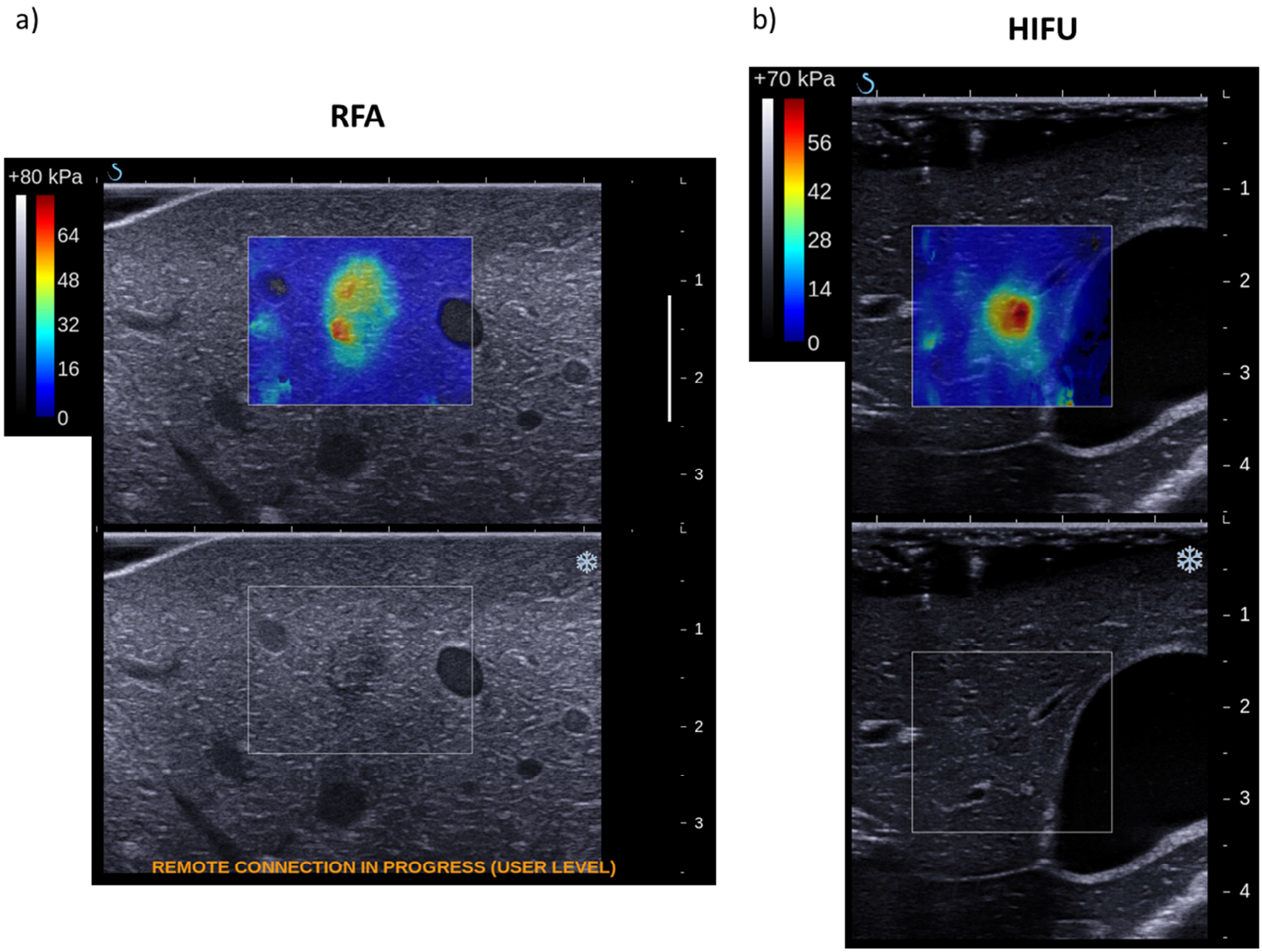

Figure 2-6 : Examples of (top) SWE maps of areas of liver ablated with (a) the RFA system, (b) the HIFU system and (bottom) the corresponding B-mode images. The boundaries of the lesions can be clearly delineated with SWE while they appear less contrasted and incomplete on B-mode.

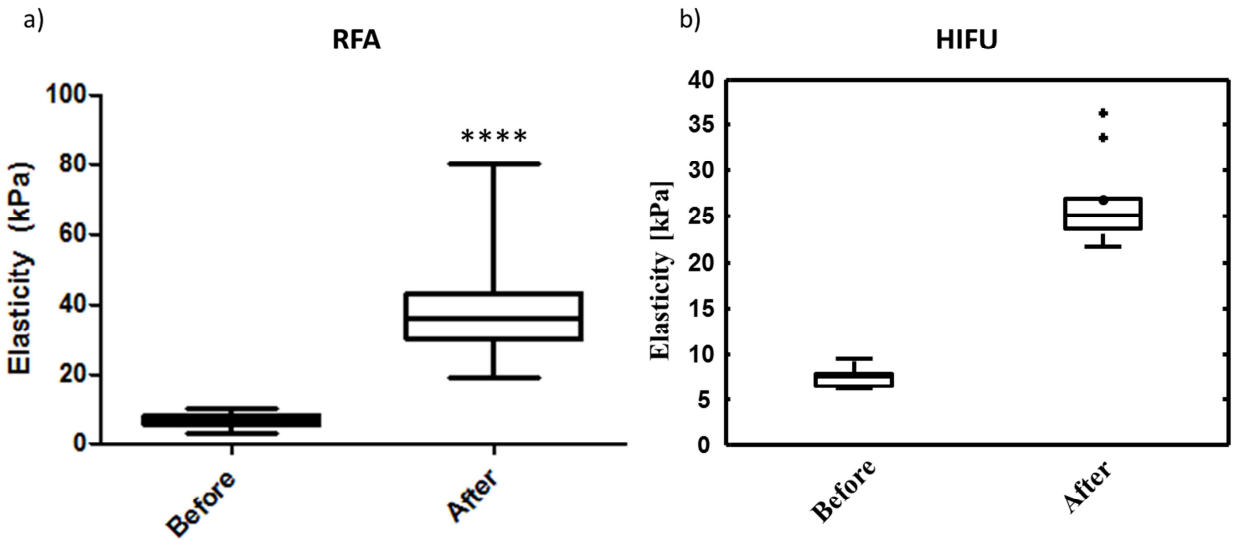

Figure 2-7 : Box plot representation of liver elasticity (Young's modulus [kPa]) calculated before and after ablation with RFA (a) and HIFU (b), in the areas identified as lesions. (a) The elasticity significantly increases ($p<0.0001$) from 6.4 ± 0.3 kPa to 38.1 ± 2.5 kPa. (b) The elasticity significantly increases ($p<0.0001$) from 7.5 ± 1.2 kPa to 26.6 ± 4.7 kPa.

2.2.1 Pathologic analysis

All thermal lesions showed the expected pathologic features, and the Wz and Rz could be clearly differentiated in all cases. For RFA lesions the Rz thickness was 0.8-1.5 mm and the mean measured Wz area was 75.1 ± 20 mm^2 (40.5 - 131.3 mm^2). For HIFU induced lesions the mean Wz area was 38.2 ± 11 mm^2 (18.2 - 55.8 mm^2).

2.2.2 Microscopic analysis

At low magnification (*5), the cell architecture of the Wz, Rz, and normal untreated tissue was clearly different (Figure 2-8). At higher magnification (*40), conventional hematoxylin-eosin-safran staining did not show prominent changes in the Wz other than a lighter staining of the tissue with faintly stained nuclei and distortion of the sinusoidal architecture[181]. The Rz appeared as congestive tissue with a large amount of red blood cells.

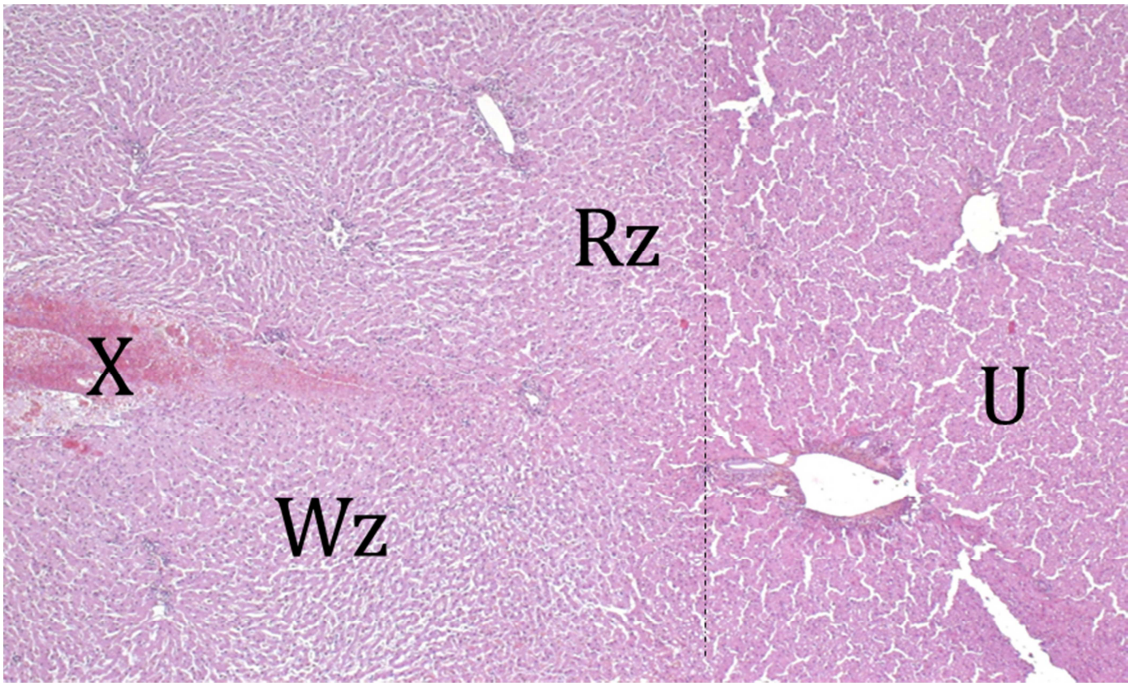

Figure 2-8 : Microscopic analysis of an RFA thermal lesion. Hematoxylin-eosin-safran staining, original magnification x5. Histopathological examination revealed a clear difference between the cellular architecture within the white zone (Wz), the right zone (Rz) and normal untreated tissue (U). X corresponds to a classical electrocautery lesion.

2.2.3 RFA lesions B-mode image analysis

The expert radiologist did not detect any lesion in three cases (11.5%), could determine only incompletely the lesion boundaries in 16 cases (61.5%) and completely outlined what he considered to be the lesions in seven cases (27%). The mean surface difference between the Wz in the gross specimens and the lesion area delimited by the radiologist in B-mode images was 42.5%.

2.2.4 Prediction of accurate visualization of coagulation necrosis

Se and PPV were calculated for different elasticity thresholds as described previously. Figure 2-9 shows the Se - PPV couples for the different studied elasticity thresholds of RFA lesions. Above 30 kPa, PPV was higher than 0.93 but was associated with Se values as low as 0.5. The curves showed that a 20 kPa threshold gave the best compromise between Se and PPV (0.8 and 0.83, respectively).

For HIFU induced lesions the best Young's modulus threshold was found to be 21kPa, which is in agreement with RFA. The Bland-Altman method (Figure 2-10) showed no bias on

RFA lesions estimation and a limited one for HIFU. The estimated ablation area size on elastographic maps was very close to the Wz size (RFA: 0.022 ± 0.22 cm^2 for bias ± standard deviation; HIFU : 0.086 ± 0.20 cm^2) with a confidence interval between -0.413 cm^2 and +0.459 cm^2 (RFA) and -0.483 cm^2 and +0.310 cm^2 compared with the mean size of the lesions (RFA: 0.751 cm^2; HIFU : 0.382 cm^2).

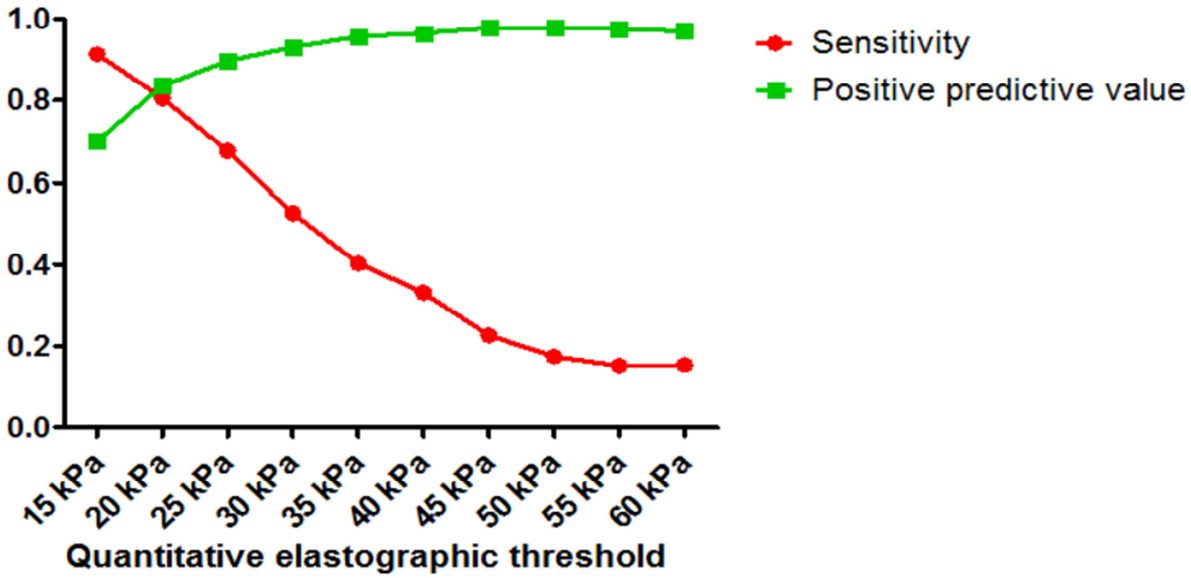

Figure 2-9 : RFA lesions: Sensitivity (Se) and positive predictive value (PPV) analysis of different quantitative elasticity thresholds. The 20kPa threshold is chosen as the best compromise between Se and PPV.

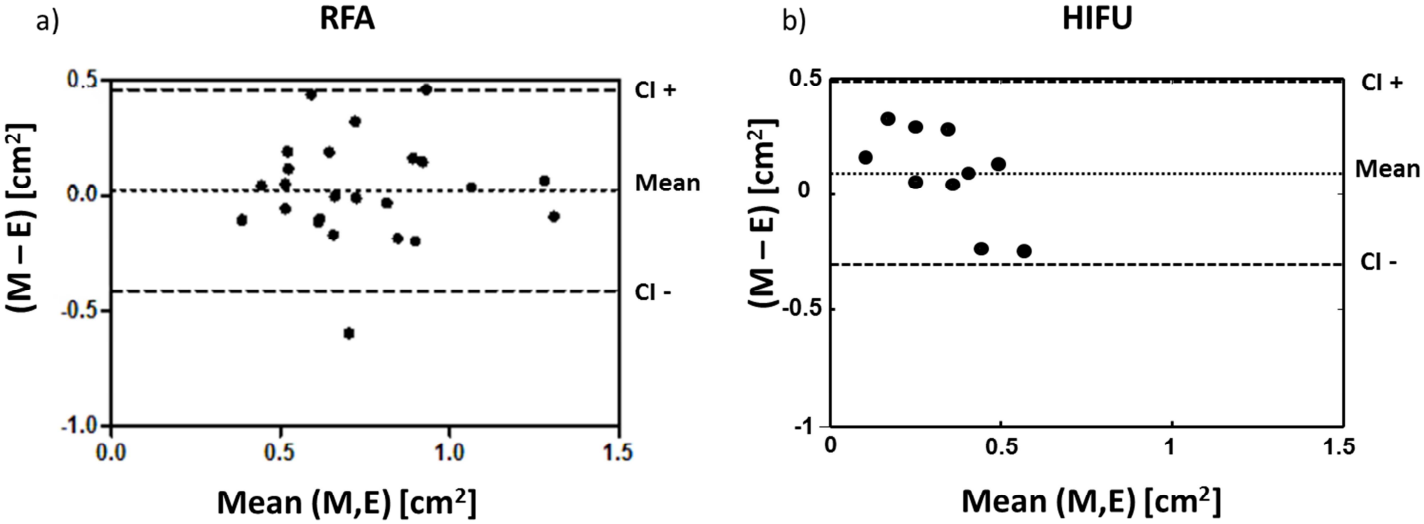

Figure 2-10 : Bland and Altman representation of the agreement between the surfaces of the SWE map (E) and the surfaces of macro specimen (M). Mean and limits of the confidence interval (CI) are represented by dot lines.

2.3 Discussion

In this study we have demonstrated that quantitative Shear-Wave Elastography is capable of a real-time monitoring of thermal ablation in-vivo with a high-contrast and good-accuracy mapping. The stiffness quantified by SWE was 2 to 6-8 times higher (in the core of the lesion) than in the surrounding healthy tissue, because of protein coagulation. An accurately determined elasticity threshold might help visualizing the boundaries of the created thermal lesion. Indeed, using an elasticity threshold of 20 kPa (two times higher than the native liver elasticity), we could predict cell necrosis with a Positive Predictive Value of 0.83 and Sensibility of 0.8. The very close threshold found for HIFU confirms the robustness of these results. The possibility of such an absolute threshold means that no preliminary acquisition would be needed before the ablation procedure and the determination of ablated tissue would be very straightforward.

In this study we mainly focalized on the precision and universality aspect of SWE to map, in-vivo, thermally coagulated tissue. As our reference was gross pathology investigation of excised tissue, it was not possible to confront it to the mapping acquired before the end of a procedure. Nevertheless, as mentioned in the Materials & Methods section, each procedure was also monitored during the ablation. Figure 2-11 shows an example of such monitoring of a HIFU ablation. In this case 20 successive spatially distributed (6*4mm^2 translation area) ablations were performed and the progressive appearance of the lesion is clearly visible, already after the second ablation (approximate ablated area: 2*2mm^2).

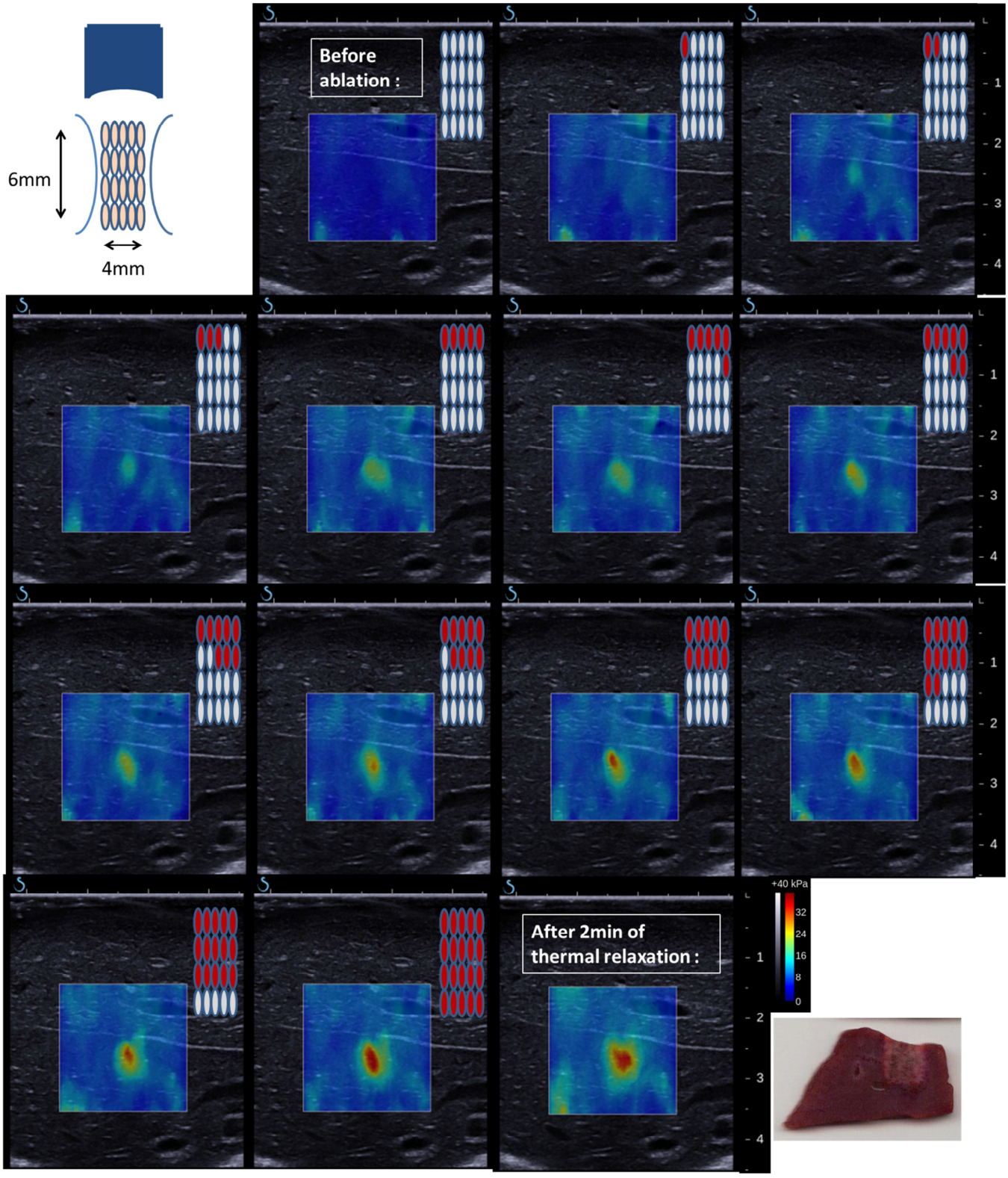

Figure 2-11 : Example of SWE monitoring of a HIFU ablation. Up right is represented the scheme of successive ablations performed in the tissue. In total HIFU was performed on 20 focal positions (15s per position), each separated of 1mm within a line and 2mm within a column. A selection of successive SWE maps with the scheme of the completed focal positions (in red) is represented from the up left to bottom right. A photograph of the excised tissue, cut along the imaging plane, is shown at bottom right (same spatial scale as for SWE).

Satisfactory clinical results using MR temperature mapping have also been reported [132, 133], but they are associated with the classical MR drawbacks in terms of costs and increased technical complexity. An ultrasonic technique is potentially less expensive and directly available in the operative room for surgeons or radiologists, as it is already the most used imaging modality for such procedures. Moreover, with MR temperature imaging, coagulation maps were estimated indirectly by computing the thermal dose. In contrast, tissue stiffness is an intrinsic property, which reflects the tissue organization at cellular and macroscopic level, and thus pathophysiological, potentially permanent, changes that occur during coagulation.

On the other hand a radiologist with experience in liver US imaging and liver radiofrequency procedures under B-mode guidance in humans could not clearly delineate thermal ablative lesions in 70% of the cases even in the absence of artifacts (gas bubble formation) that can alter US imaging and real-time estimation of the size of the thermal lesion. Although B-mode ultrasonography is the most commonly used guidance method for liver thermal ablative procedures, it is not precise enough for real-time monitoring of thermal ablation and prediction of the extent of coagulation necrosis[139].

Automatic segmentation of the liver specimens was used to avoid inter-individual differences. The pathologic findings showed a classical Wz of coagulation necrosis surrounded by a peripheral congestive Rz with a large amount of red blood cells. Like in previous reports [178, 179, 182], we defined as “coagulation necrosis” only areas with macroscopic features that were highly predictive of irreversible thermal cell damage. Histologic evidence of necrosis is commonly found in vivo 24-36 h after hepatocyte ischemic injury, and mitochondrial abnormalities are the earliest finding [183]. At the early stage analyzed in this study, only immunohistochemical vital dyes could clearly demonstrate loss of vitality immediately after thermal ablation [184–186].

This study has several limitations. First, because of the small sample size and the creation of standardized lesion, the findings should be cautiously interpreted. Nevertheless it demonstrates the capability of revealing millimetric lesions, which should be seen as an advantage. Second, healthy livers were treated because no pig liver cancer cell lines are currently available. Thus, the effectiveness and accuracy of elastography mapping remains to be evaluated using pseudotumor models[131] or cirrhotic liver. SWE might confirm MR Elastography findings that malignant tumors were stiffer than human healthy liver with

elasticity around 10 kPa [187] and 2 kPa [188], respectively. Thanks to this contrast, it could be possible to apprehend coagulation necrosis at the margin of the tumor [131]. Third, results were confronted to gross pathology macroscopic investigation, with possible small variations between the positions of the imaging plane and the excised tissue section. This variation was more important for HIFU induced lesions, because, no physical markers were present within the tissue. Fourth, this study was designed to monitor thermal procedures during open abdominal surgery; however, as SWE can assess and measure deep tissue stiffness, it might be also used for percutaneous radiofrequency ablation. Further studies need to be performed to test this specific assumption, but as suggested by Figure 2-12, that shows the map of a thermal ablation performed percutaneously (the ablation and the image), it is feasible.

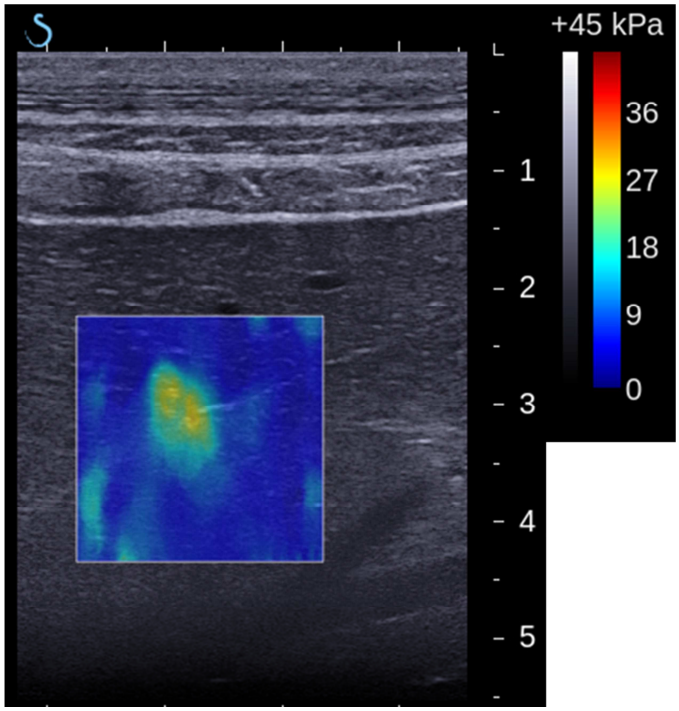

Figure 2-12 : SWE map performed in-vivo, percutaneously, of a RFA performed percutaneously as well. The different fat and muscular layers can be seen above the elastographic map.

Finally in this work we were limited to a two-dimensional (2D) monitoring of the thermal ablation. While such an imaging provides already a consequent amount of information, the treated volume can only be evaluated by a manual scanning of the tissue along the third dimension. This kind of operation could be a source of errors, of incorrect or insufficient volume evaluation and finally treatment. A simple way would be to motorize the two-dimensional probe and recreate a volume by successive scanning. Such a solution has been developed by Vermon (Tours, France) as the wobbling probes. These probes are

constituted of a 2D transducer, mounted on a rotating motor. By successive scans, within few seconds, a whole B-mode and SWE volume can be recreated on the Aixplorer scanner. Recently Athanasiou et al. [189] published very interesting results on the evaluation of breast tumor volumes with such obtained 3D SWE. We have performed acquisitions with the same system on RFA induced lesions from the study presented previously. Figure 2-13 represents examples of these acquisitions. By segmenting elasticity on all planes, the volume of ablation could be evaluated very easily. However the disadvantage of this system, in the case of thermal ablation monitoring, is the loss of the real-time aspect and also the big size of the probe. A perfectly suitable solution would be a 3D real-time SWE imaging with small probes. First promising results on the development of such novel systems have recently been published by Provost et al. [190]opening a new world for ultrasound imaging.

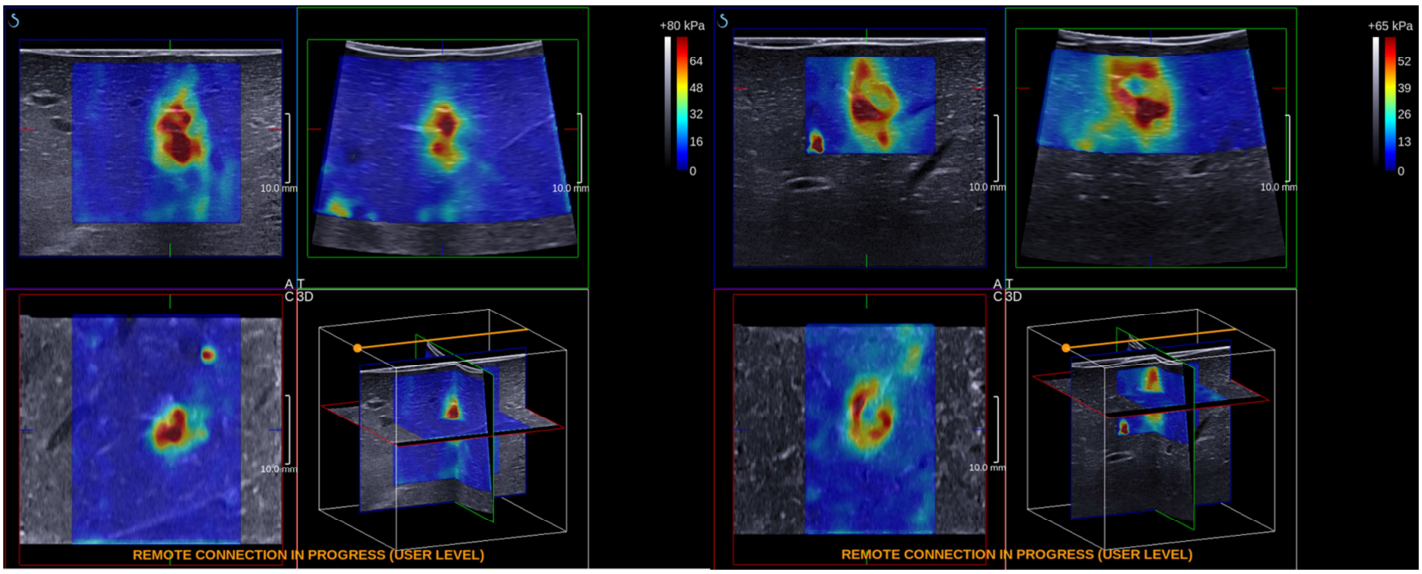

Figure 2-13 : Examples of a multi-plane representation of a 3D-SWE volume in in-vivo sheep liver that underwent RFA. Hard inclusions of thermal ablation are clearly visible.

3 Conclusions

The development of new imaging strategies to provide real-time assessment of the effectiveness of thermal procedures is an important issue for mini-invasive treatments, such as open or percutaneous ablative therapies. Completeness of a thermal ablation procedure is particularly difficult to determine in real time with the risk of leaving behind viable tumor cells. SWE is a new imaging modality that quantifies tissue stiffness and that is mostly used for diagnosis [191, 192]. Here, we confirm that areas of coagulation necrosis are significantly

stiffer than the surrounding tissue and we demonstrate that their boundaries can be predicted with effectiveness and reproducibility using SWE, preclinically. In previous studies [131, 193], US elastography has proven its interest and superiority compared with standard B-mode ultrasonography.

The major advantage of elastographic modalities to monitor and evaluate thermal ablation is that it quantifies both transient and non-transient tissue alterations. Changes linked to thermal coagulation appear during the ablation and remain within the tissue a long time after the procedure [168], it then possible to monitor them at the moment of the procedure and potentially perform a global evaluation at the end of a series of ablations.

As described in the introduction, SWE can be also used for local temperature monitoring, in the range of normal body temperature to 45°C. Thus when temperature in tissue is elevated, two effects interfere for elasticity estimation: stiffening due to thermal coagulation and softening due to temperature elevation[167]. As a consequence the area of ablated tissue may be underestimated during the ablation. However, as clinical thermal ablation is systematically over-performed to ensure a total elimination of targeted tissue [130], this might not be an issue. An intraoperative quantification of the combination of both contributions could be an interesting solution. In this study, as SWE thermometry was not in consideration, all final lesion surface quantification was performed after thermal relaxation to overcome a possible interference and simply to let the coagulation process end.

Finally we believe this work can constitute a solid basis to push SWE monitoring of thermal ablation forward. All data acquisition was performed with the clinical version of the Aixplorer Ultrafast scanner (SuperSonic Imagine, Aix-en-Provence, France), thus showing the maturity of the technique. As an important next step additional preclinical studies with pseudotumor models [194] are needed to validate this technique.

In this chapter we presented results, in the context of an existing clinical need, obtained for thermal ablation monitoring in the liver. This organ presents a homogeneous structure and is affected by motion, mostly respiratory, in a limited extent. In the following chapters SWE evaluation of thermal ablation will be presented in another part of the body: the heart. In this environment, motion, access and tissue structure imply a certain dose of adaptation.

Chapter 3. Intracardiac ultrafast ultrasound imaging for the evaluation of thermal ablation

1 Introduction

This chapter is the first of a series dealing about therapy and imaging of the heart. As presented in the introduction of this manuscript, cardiac ultrasound imaging and therapy are challenging to perform in a transthoracic approach because the heart is deeply located behind the ribs at distances up to 15 cm, and is subject to rapid motion.

In this chapter we develop an intracardiac ultrafast imaging approach for the assessment of thermal ablation therapy. This development addresses a specific clinical need: the lack of control and monitoring of thermal therapies in the heart and more specifically in the context of Radio-Frequency Catheter Ablation (RFCA) (see Chapter 1 part 1.3 for more details). The main challenge of intracardiac imaging approach consists in miniaturizing an imaging transducer to insert it in the cardiac chambers through the venous system. As it will be introduced in the following parts, this approach is already widespread in electrophysiology labs. The specific aim of this work is to develop novel imaging tools for the assessment of RFCA treatment. To achieve this objective, two novel imaging modalities have been investigated and implemented on an intracardiac ultrasound imaging transducer: Shear-Wave Elastography (SWE) and Ultrafast Doppler. This chapter will present the in-vitro and in-vivo feasibility of SWE evaluation of myocardial stiffness during RFCA and will present preliminary results of intracardiac Ultrafast Doppler to map the micro-vascularization of the myocardium.

2 Evaluation of atrial Radio-Frequency Ablation using intracardiac Shear-Wave Elastography

2.1 Introduction

2.1.1 RFCA ablation monitoring: state-of-the-art

Several techniques have been proposed for RFCA monitoring. Magnetic Resonance (MR) Temperature imaging [195] can provide the temperature elevation of the ablated region in quasi real time but is limited by its cost, complexity and the need of non-magnetic RF catheter. Intracardiac echocardiography (ICE) is being used routinely for the guidance of catheter ablation [196]. The placement of ICE and ablation catheters can be performed under fluoroscopy or with recent navigation systems that track in 3D the catheters using magnetic sensors placed on their tip [197]. Intracardiac ultrasound imaging can also provide qualitative information on the ablated zone by observing microbubble formation [196] or speckle variation [198] during ablation but those techniques cannot be used to assess the viability of the cardiac tissue. Intracardiac strain and strain rate imaging have been used to quantify myocardial deformation [199] but these techniques remained limited to the evaluation of myocardial function and cannot provide information on the atrial tissue viability after thermal ablation. Thermal strain imaging [200] quantifies also the strain induced by heat to provide temperature elevation during RFCA but does not provide information on the physical properties of tissues and thus is not capable of evaluating the lesions after thermal relaxation.

2.1.2 Intracardiac elastography

State-of-the-art

In order to visualize the thermal lesion with ultrasound, evaluation of tissue stiffness has recently been introduced as an effective means to map ablated regions[173, 177, 201, 202], providing stiffness contrasts between normal and ablated tissues of more than a factor of 2. As it has already been mentioned in the previous chapters, it was shown in vivo that the stiffening of a thermally ablated tissue is linked to the applied thermal dose [176], and thus, to its viability. Acoustic Radiation force imaging (ARFI), an ultrasound technique that provide images of relative tissue elasticity[202, 203], was recently shown capable to visualize intracardiac thermal lesions in canines in vivo [204] and in humans [205]. However, ARFI, as a relative stiffness imaging, requires the acquisition of a baseline, the tissue response before ablation, which is problematic during AF episodes.

In the field of cardiac imaging, Shear-Wave Elastography has already been successfully implemented to measure quantitatively the temporal variation of stiffness occurring in the myocardium in vivo during the cardiac cycle [206] and the fiber orientation of the different layers of the cardiac muscle [207]. An intracardiac ultrasound approach was proposed by Hollender *et al.*[208] in vivo to assess the stiffness the interventricular septum using a shear wave velocimetry technique and acoustic radiation force imaging (ARFI) for the characterization of infarcts in porcine heart in vivo [209].

New contribution

In this study, we have developed a novel, intracardiac, ultrasound-catheter-based SWE technique to image the extent of ablation lesions in vivo. First, we demonstrated the feasibility of SWE using an intracardiac ultrasound catheter by mapping the well-known increase in stiffness associated with radio-frequency ablation in ex vivo ventricular myocardial tissue. Second, we imaged, for the first time, the temporal variation of the stiffness of the atrial tissue in a normal, in vivo model, in order to determine the moment within the cardiac cycle at which the contrast between ablated and normal tissue is maximum. Finally, we demonstrate the feasibility of mapping the extent of radiofrequency ablation lesions in a beating heart, in vivo.

2.2 Materials and methods

2.2.1 Intracardiac Shear-Wave Elastography

In this study, an ultrafast ultrasound scanner (Aixplorer®, SuperSonic Imagine, France) was used to perform SWE sequences with an intracardiac ultrasound catheter (6 MHz, 50-% bandwidth, 64 elements, 0.2-mm pitch, 9F, Vermon, France), which consist in a radiation "push" ,i.e., the ultrasound focused emission used to generate a shear-wave defined by its duration and frequency (300 µs at 6 MHz in this study), followed by an ultrafast plane wave imaging sequence. The push parameters used in this study resulted in a peak positive pressure of 5MPa (measured in water) and a Mechanical Index of 1.0 at a 15-mm focus. The temperature elevation was below 1°C both in the focal region and at transducer face. Ultrafast imaging was performed using either one or three compounded (-1°, 0°, +1°) plane wave emissions at 7 MHz. The resulting imaging frame rate depended on the imaging depth – one compressional wave transmit and return time, and on the number of compounded plane

waves [107]. Up to 5 push and imaging sequences were used in order to increase the field of view and the signal-to-noise ratio of the shear modulus maps [112]. A time-of-flight algorithm [109, 113] was used to track the shear-wave group velocity c_t and the shear modulus map was obtained from (1) for each acquisition. Corresponding quality maps were obtained from the algorithm's temporal 1-D cross-correlation. The final 'stiffness map' was obtained with a quality weighted average (least-squares mean) of all five acquisitions.

The time-of-flight algorithm estimates the shear-wave group velocity locally. It is based on a sliding window estimator for each pixel within a lateral line. In our study all imaging acquisitions were laterally resolved at 100µm; the velocity was averaged on millimetric distances: 0.8mm for ex-vivo acquisitions, 1.1mm and 1.5mm for in-vivo compounded and non-compounded acquisitions respectively. Those values do not give but are related to the lateral resolution [210].

For in vivo acquisitions, additional post-processing was performed. More specifically, the curvature of the sample was manually delineated in post-processing and the shear wave velocity was measured along the direction parallel to the delineated boundary.

2.2.2 Ex-vivo experimental setup

Shear-Wave Elastography and Radio-Frequency Catheter Ablation were performed in freshly excised and degassed porcine heart samples. The five 10x30x30 mm^3 left ventricle samples obtained from two hearts (n = 5) were embedded in Agar gel (Figure 3-1). An acoustic absorber was fixed at the bottom of the plastic container containing the samples to avoid reflections. The container was placed in a tank filled with degassed and thermostatic (37°C) water. The ultrasound (US) transducer was positioned in water such that the imaging plane was perpendicular to the surface of the samples. The catheter was positioned using a 3-D motorized motion system. During ablation, the US catheter was moved away using the motors and the Radio-Frequency Ablation (RFA) catheter (Saint Jude and EPTechnology, EPT-1000XP) was positioned on the center of the zone previously imaged by the US transducer. A ground plate fixed at the bottom of the container collected the current delivered by RFCA.

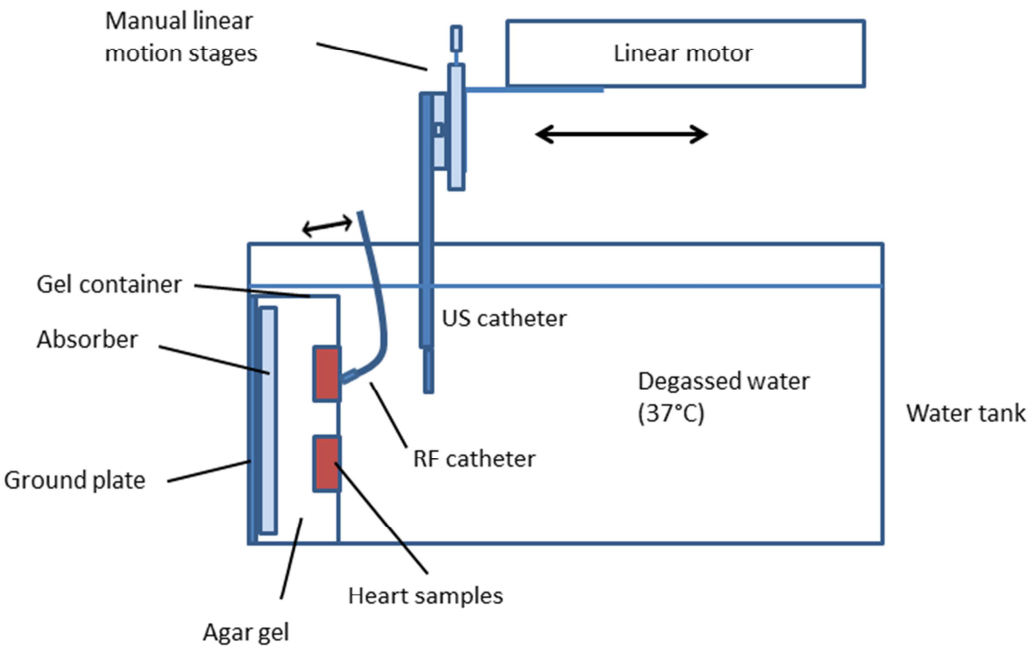

Figure 3-1 : Ex-vivo experiments setup. Heart samples were fixed in Agar gel and immersed in degassed water. The US imaging catheter was placed mechanically on the transverse plane and distance to the samples was controlled with a motor. The US catheter was precisely put away and back to perform SWE before and after RFA. The RFA catheter was mechanically positioned in the center of the US image to perform ablation and then driven away.

2.2.3 Ex-vivo sequences

The US catheter was placed approximately 4 mm away from the sample's surface. A B-mode image was acquired and then SWE was performed – pushes were generated at a depth of 6 mm. Imaging depth was fixed at 12 mm which resulted in a PRF of 27.8 kHz and a final frame rate of 9300 images/s after compounding. The total sequence duration was 18 ms. The catheter underwent motion resulting from a kick-back in response to the generated radiation force, which appeared in the images as a global motion undergone by the entire image (i.e. with a low spatial frequency) and was corrected by applying a spatial high-pass filter (fc = $60m^{-1}$) onto the tissue velocity maps. A Butterworth temporal low-pass filter (cut-off frequency: 1400Hz) was also applied to each pixel to remove high frequency noise.

The RFA catheter was positioned in the center of the imaged zone to perform the ablation and the ultrasound catheter was then driven away. A heating of 2*2min with 8 Watts of electrical power was performed. After ablation the RFA catheter was removed and the imaging catheter was precisely driven to its initial position.

SWE was performed again and a new stiffness map was obtained. SWE was performed several minutes after ablation in order to insure that the tissue temperature was back to 37 degrees, hence avoiding any potential false positives caused by the variation of the shear modulus with temperature when the necrosis threshold is not reached [166].

A gross pathology study was performed at the end of the study. More specifically, the heart samples were cut along the imaging plane of the ultrasound transducer, under control of the B-mode imaging, removed from the gel and photographed. Depth and size of the lesion were estimated by identifying the boundary of the variation in tissue color using a k-means clustering algorithm [180], by discriminating viable tissue (red) from ablated (white). According to the results obtained by Sapin-de Brosses *et al.*[176] and Mariani *et al.*[201] (Chapter2), a shear modulus increase ratio of 2 to 3 between normal and ablated tissue can be used to discriminate ablated from non-ablated tissue. In this study, a 60-kPa threshold was used to determine lesions' boundaries.

2.2.4 In-vivo experimental setup

The study was approved by the University of Bordeaux guidelines on the use and care of animals. Three 40 to 50 kg sheep were studied. The animals were pre-anesthetized by injecting 10–20 mg/kg of ketamine hydrochloride, and general anesthesia was maintained with an infusion of sodium pentobarbital (2.5 mg/kg/hour) and ketamine hydrochloride (2 mg/kg/hour). The sheep were ventilated with 25% humidified oxygen via a tracheostomy. After the *in-vivo* procedure the animals were euthanized. Treated hearts were collected and placed in a formaldehyde solution. Gross pathology was performed to assess the presence of a lesion, although co-registration with SWE was not performed.

An incision was performed in the thigh of the animal to access the femoral vein. The RFA catheter and the ultrasound imaging transducer were inserted into steerable sheaths (12F) and introduced via the femoral vein into the right atrium, under fluoroscopy (Figure 3-2a). The alignment of the ablation and monitoring devices was performed using the ultrasound catheter B-mode imaging. Figure 3-2b shows such an alignment as seen under fluoroscopy. Automated R-wave detection was used to precisely start acquisitions at a specific cardiac event on the ECG. Note however that all acquisitions were performed in a single cardiac cycle.

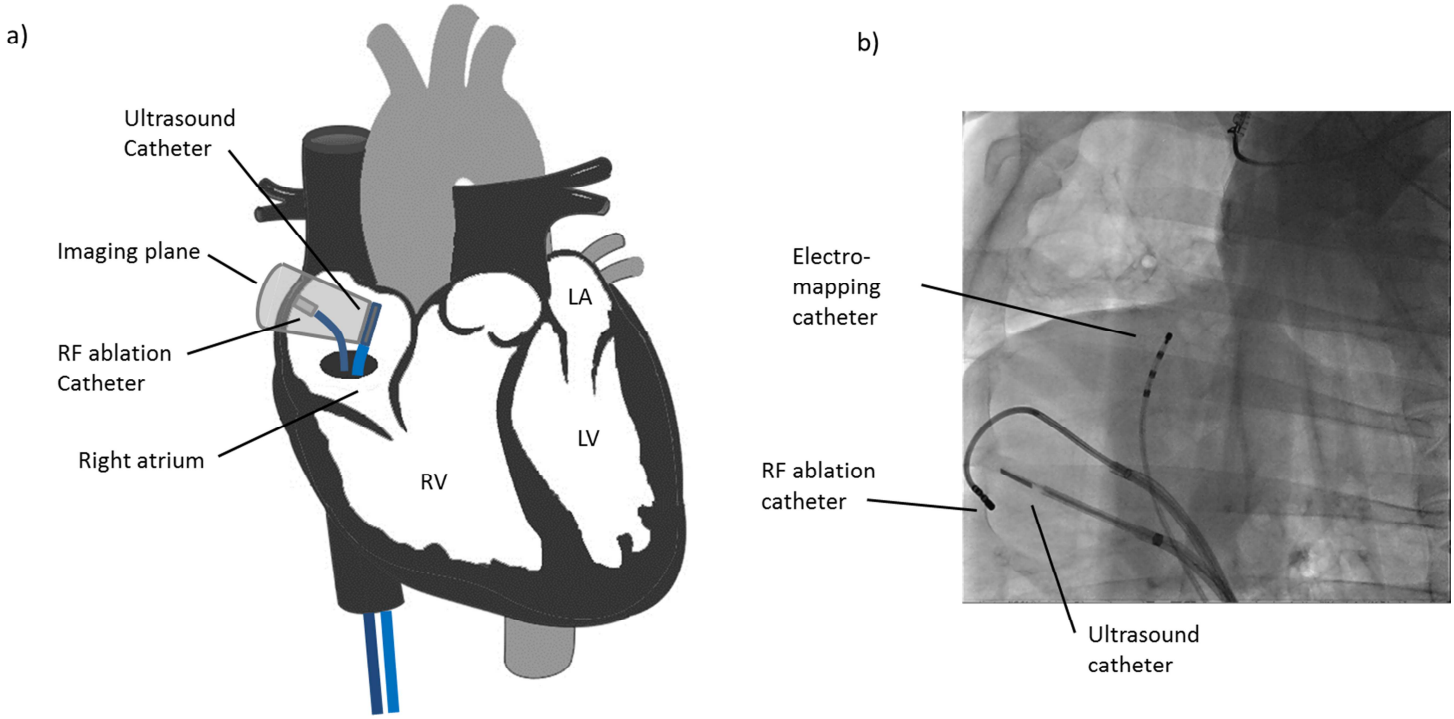

Figure 3-2 : (a) Example of US and RFA catheters placement in the right atrium. The catheters are inserted through the jugular vein. (b) Example of US and RFA catheters alignment monitored under fluoroscopy.

2.2.5 In-vivo sequences

Two types of acquisitions were performed in vivo: the time variation of stiffness during the cardiac cycle was measured quantitatively and stiffness maps were performed before and after RFCA. Because of potential guided-waves effect occurring *in vivo* in the atria which consist of a thin layer of several mm, shear-wave speed is provided instead of shear modulus as the principal quantification result.

In vivo stiffness maps of ablated atrium

The ablation and imaging catheters were first aimed at a normal region of the right atrium under fluoroscopy. The tip of the ablation device was put in contact with the tissue using electrical impedance monitoring. The ultrasound transducer was positioned at a distance of approximately 8 mm from the tissue under B-mode imaging guidance while insuring that the RFA catheter was located at the center of the ultrasound imaging plane.

The ablation catheter tip was then removed from the image by manually steering the sheath and a stiffness mapping was performed on the normal tissue. The acquisitions were

triggered at the R-wave of the ECG, which corresponds to the beginning of atrial diastole. Depending on the acquisition, the push focal distance was set at a depth varying between 6 and 12 mm while the imaging depth was fixed at 20 mm for an imaging PRF of 18.9 kHz. Either 30 compounded images at a 6.3-kHz frame rate or 100 images at the 18.9-kHz frame rate were obtained, for a total acquisition time of 28ms. A temporal Butterworth band-pass filter (cutoff frequencies for compounded images: 100-600Hz; cutoff frequencies for non-compounded images: 100-1000Hz) was used to isolate the shear-wave. For each frame the spatial mean tissue velocity, resulting from the catheter-tissue relative movement, was also removed. Total automated time of beamforming and processing data for the final map was typically 7.5s using a laptop computer, with manual delineation requiring 3 supplementary seconds.

The RF catheter was then positioned back onto the tissue in the center of the imaging plane and ablation was performed. Temperature and electrical impedance of the tip of the catheter were monitored to control tissue heating and avoid boiling.

After ablation, the RFA catheter was removed and a stiffness mapping was performed again with the same parameters.

Time variation of stiffness driven by cardiac contraction

To investigate the temporal pattern of atrial stiffening in normal tissue (N = 5, sheep N = 3), we performed ten 4-ms-long single-push SWE acquisitions during a single cardiac cycle (sinus rhythm) at a rate of one every 60 ms, with the first acquisition triggered on the R-wave peak of the ECG. The entire single cycle was sampled by 10 SWE acquisitions. Spatiotemporal representations of the shear wave were obtained by averaging the tissue velocity along the thickness (i.e., axially) of the tissue. The slope of a linear least-squares fit of the lateral position of the maxima of the waveform as a function of time provided the mean shear-wave group velocity estimates.

The same acquisition was performed at the same position in the tissue (N = 4, sheep = 3) after ablation.

Statistical analysis

All results are given with their standard deviation (SD) within or across samples. Changes in myocardial stiffness were analyzed using a paired two-tailed *t*-test to evaluate the significance of difference between individual values before and after ablation. Statistical significance was inferred for $p<0.05$.

2.3 Results

2.3.1 Ex vivo study

Figure 3-3 shows the variation of the shear modulus in an ex vivo sample before and after ablation. Before ablation (Figure 3-3a), the shear modulus is homogeneous throughout the sample and is approximately 21±9kPa (corresponding shear wave velocity: c_t = 4.4±0.9m.s^{-1}) within the sample, with a small number of artifacts, most likely attributable to remaining air bubbles in the sample. Figure 3-3b shows the resulting stiffness map in the same sample after RFCA. The mean shear modulus increased from 21±9kPa (c_t = 4.4±0.9m.s^{-1}) to 109±82kPa (c_t = 9.7±2.9m.s^{-1}) in the lesion.

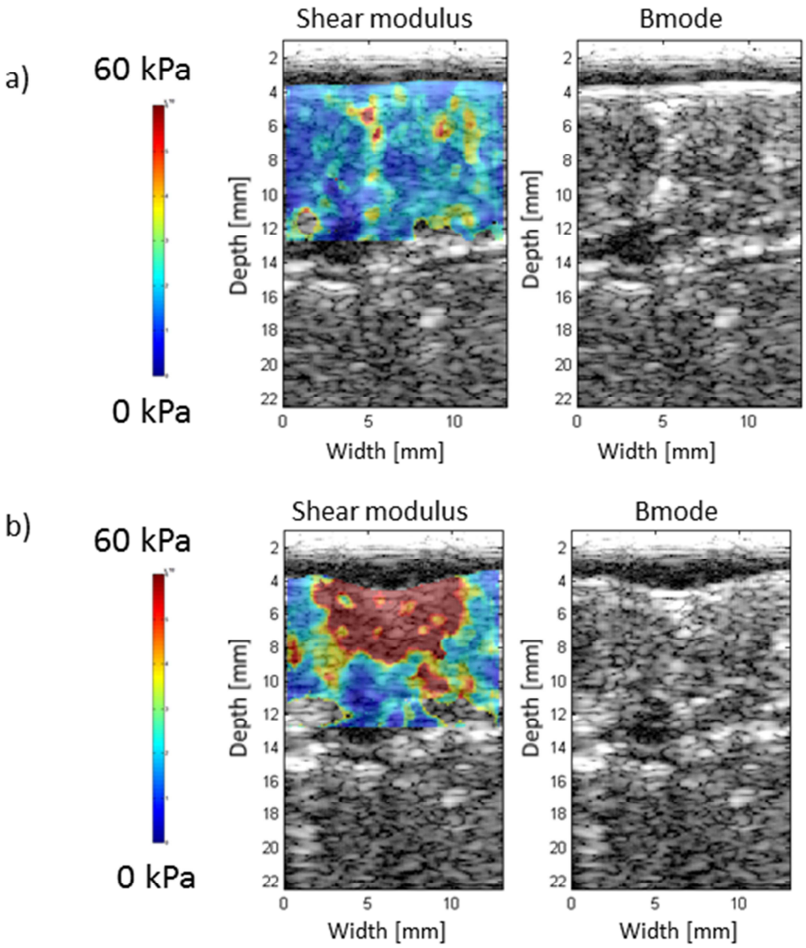

Figure 3-3 : Shear modulus maps (a) before and (b) after ablation in a left ventricular ex vivo sample. The mean shear modulus before ablation was 21±9 kPa. After a 2*2min 8W heating with the RFA catheter and a 5 min thermal relaxation, the mean shear modulus increased to 109±82kPa in the region identified as the lesion (shear modulus threshold of 60 kPa), corresponding to an increase factor of 5.2.

Mean lesion depths were measured with gross pathology and with SWE at the center line of the lesion and were found to be in good agreement with an approximate depth of 3 mm (Figure 3-4). The average shear modulus across samples obtained in the ablated zones was 99±17kPa (average c_t: 9.0±0.5 $m.s^{-1}$) for a mean shear modulus across samples before ablation of 22±5kPa (average c_t: 4.5±0.4 $m.s^{-1}$, $p < 0.005$) (Figure 3-5). A mean shear modulus increase ratio across samples of 4.5±0.9 was found (mean c_t increase ratio: 2.0±0.3), which shows the very high contrast that can be obtained with this technique. In contrast, we did not observe any significant qualitative changes on the B-mode images.

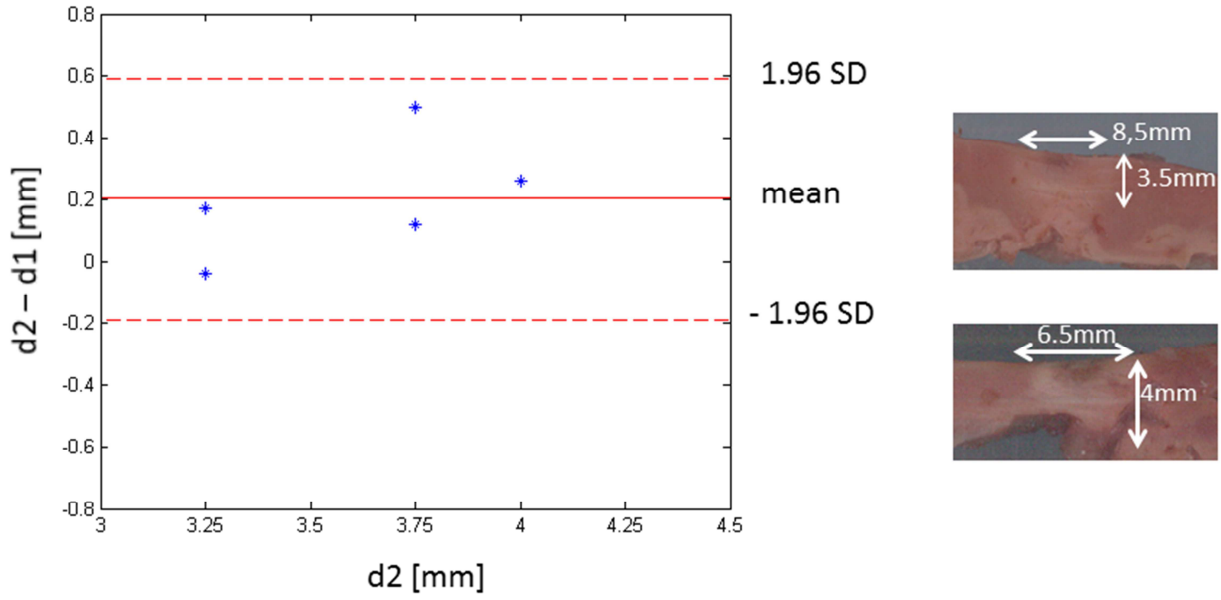

Figure 3-4 : Lesions' depths determined with SWE with a shear modulus threshold of 60 kPa (d1), compared against gross pathology (d2) plotted within 95% limits of agreement (± 1.96 standard deviation (SD) of the difference). A mean lesion depth of 3mm was found with gross pathology and the average absolute difference found with SWE was 0.20mm. Two examples of lesion tissue color change are shown.

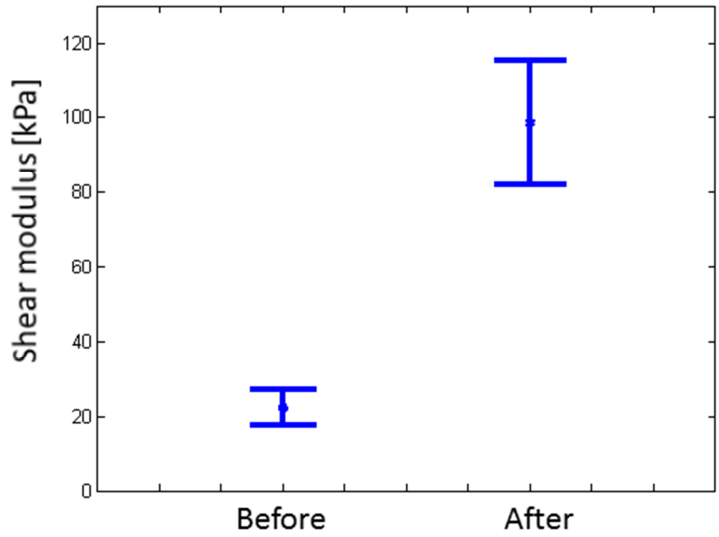

Figure 3-5 : Average shear modulus across ex-vivo samples (n=5) before and after ablation. The mean value increased from 22±5kPa to 99±17kPa, i.e. a ratio of 4.5±0.9 in the lesions' boundaries.

2.3.2 In vivo study

Time variation of normal atrial stiffness

Intracardiac SWE was first performed in normal atrial tissue. Normal atrial stiffness and its variation during the cardiac cycle were measured at a total of five atrial locations in the three animals. Figure 3-6a shows an example of shear wave speed measured in normal atrium (lateral wall) and its variation with stress (pressure and atrial contraction) during the cardiac cycle. The shear wave speed was found to vary from 1.0 $m.s^{-1}$ to 1.5 $m.s^{-1}$ (corresponding shear modulus: 1.0kPa to 2.4kPa) during the cardiac cycle. The shear-wave speed curve presented four main phases depicting the atrial cycle: *1) Atrial filling*: from 60ms after the R-wave to 50 ms after the T-wave, the shear-wave speed increased from 1.0 $m.s^{-1}$ to 1.5 $m.s^{-1}$ (1.0kPa to 2.4kPa); *2) Ventricular filling* : from 50 ms after the T wave to the P-wave the shear-wave speed decreased from 1.5 $m.s^{-1}$ to 1.0 $m.s^{-1}$ (2.4kPa to 1.2kPa); *3) Atrial contraction*: from the P-wave to 60 ms before the R-wave the shear-wave speed increased to 1.4 $m.s^{-1}$ (2.2kPa); and *4) Atrial relaxation*: from 60 ms before the R-wave to 60ms after the R-wave the shear-wave speed dropped to 1.0 $m.s^{-1}$ (1.1 kPa).

Similar time variation was found at the five locations in the three animals. Over the samples a mean atrial shear-wave velocity of 1.4±0.2 $m.s^{-1}$ (2.3±0.7 kPa) was measured over the cardiac cycle. The mean minimal velocity of 1.0±0.1 $m.s^{-1}$ (1.0±0.2 kPa) was measured after atrial relaxation, whereas the mean maximal velocity of 1.9±0.4 $m.s^{-1}$ (4.1±1.8 kPa) was reached during atrial contraction.

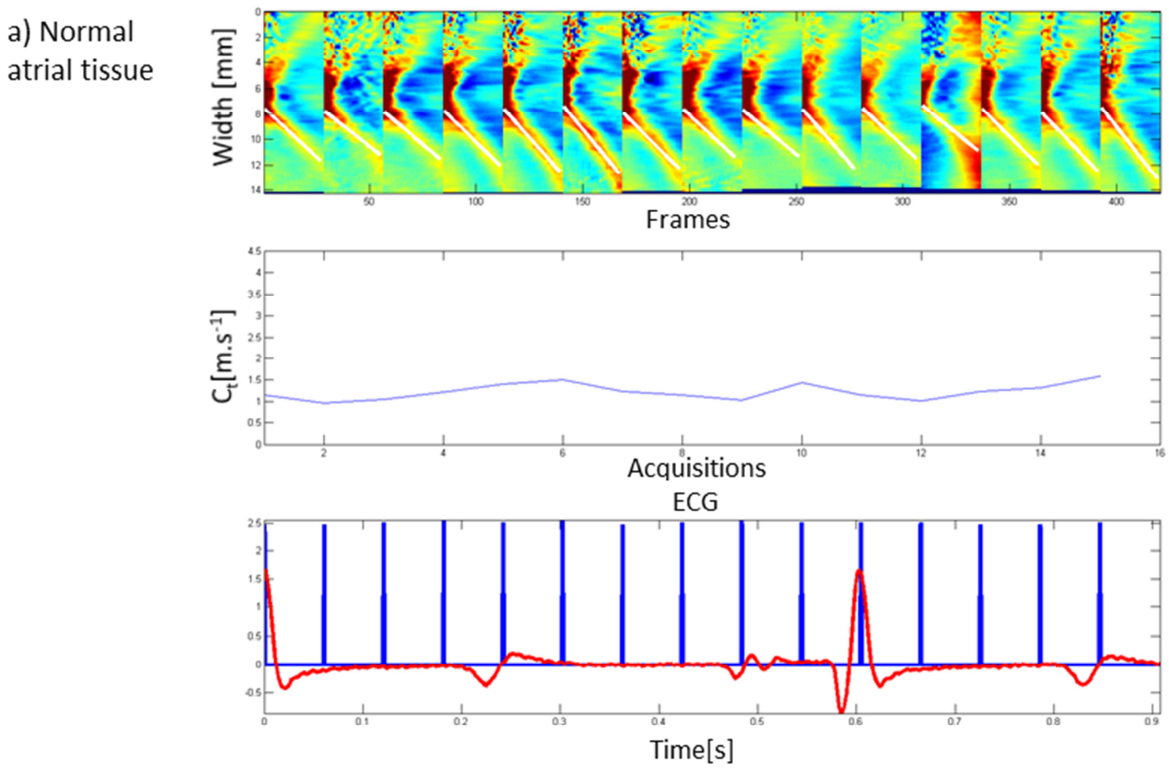

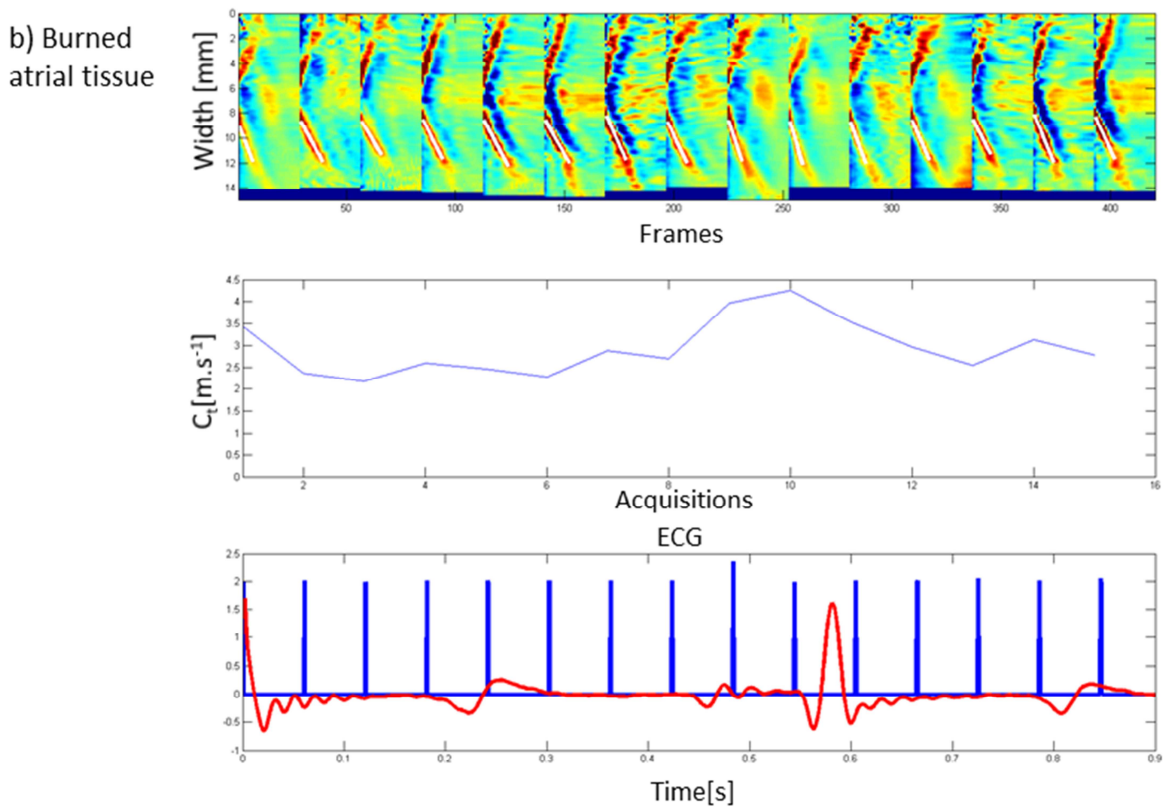

Figure 3-6 : Time variation of stiffness in a right atrium zone (lateral wall) (a) before and (b) after ablation. For each sample a total of 15 acquisitions were performed, at a rate of one every 60ms, corresponding to 10 acquisitions per heart cycle. Every shear-wave acquisition is represented spatiotemporally with a linear fit (white line) on the successive shear-wave maxima. The resulting shear-wave speeds are given below with corresponding ECG timings. (a) The shear-wave speed of normal atrial tissue varied from 1.0 m.s-1 to 1.5 m.s-1 with a mean value of 1.2±0.2 m.s-1. Two peaks are present: one at the end of atrial blood filling, one at atrial systole. (b) The shear-wave speed of ablated atrial tissue varied from 2.3 m.s-1 to 4.3 m.s-1 with a mean value of 2.9±0.7 m.s-1. A very strong peak is visible on atrial systole and a relatively low on the blood filling.

Time variation of ablated atrial stiffness

The atrial stiffness was then measured after ablation. Figure 3-6b shows the increase of shear wave speed for the same location as in Figure 3-6a. Within the cardiac cycle the temporal average of the shear wave speed increased to 2.9±0.7 m.s^{-1} (9.5 ±5.0 kPa) and larger temporal variations can be observed. The temporal shape differed slightly from the normal tissue, but the atrial contraction and relaxation phases are still visible: a large increase appeared (from 2.3 to 4.3 m.s^{-1}; from 5.5 kPa to 19.2 kPa) at the beginning of the atrial systole followed by a relaxation. In contrast, the atrial shear-wave speed increased moderately during the passive filling (from 2.2 to 2.6 m.s^{-1}; from 5.0 kPa to 7.1 kPa).

Figure 3-7 summarizes the average stiffness variations over all the different locations in normal and ablated tissues. The minimal, mean and maximal stiffness values within one cardiac cycle are shown. All these values were found to increase significantly in ablated tissues. The mean shear-wave speed of ablated atrium was found to increase significantly to 2.4±0.4 $m.s^{-1}$ (6.3±2.0 kPa, $p<0.002$), the mean minimal velocity increased to 1.7±0.4 $m.s^{-1}$ (3.1±1.6 kPa, $p<0.05$) and the mean maximal value to 3.5±0.5 $m.s^{-1}$ (13±4kPa, $p<.001$).

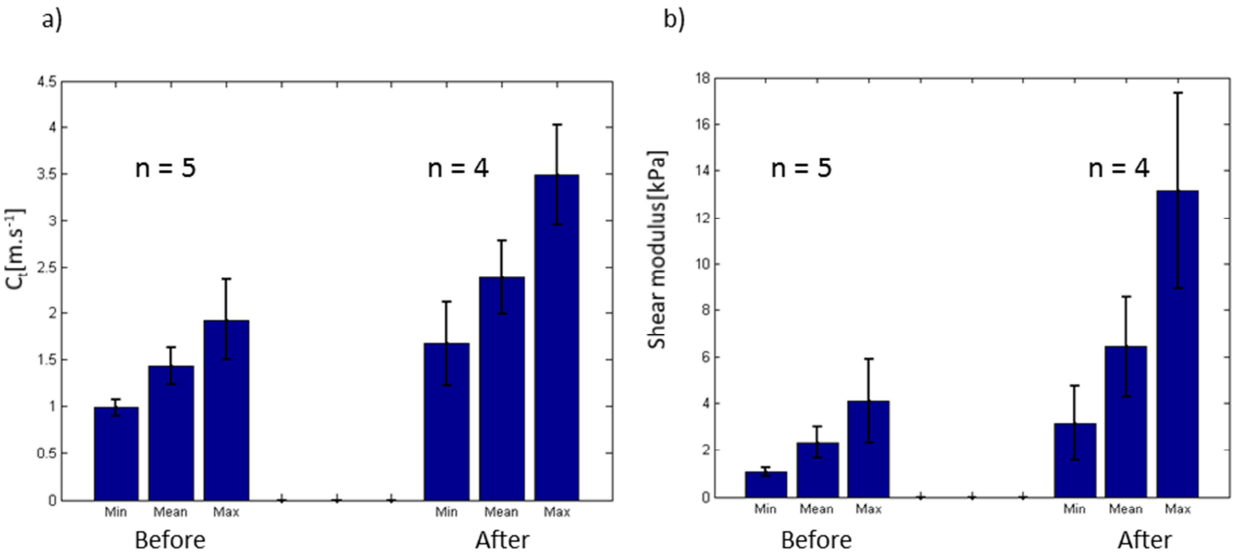

Figure 3-7 : Minimal/Mean/Maximal shear-wave speed (a) and shear modulus (b) measured in the right atrium, within one cardiac cycle, before (averaged across n=5 samples) and after ablation (n=4). Shear-wave speed in normal tissue varied across samples from 1.0±0.1 m.s-1 to 1.9±0.4 m.s-1 (corresponding shear modulus: 1.0±0.2kPa to 4.1±1.8kPa) with an average of 1.4±0.2 m.s-1 (2.3±0.7kPa) and from 1.7±0.4 m.s-1 to 3.5±0.5 m.s-1 (3.1±1.6kPa to 13±4kPa) with an average of 2.4±0.4 m.s-1 (6.3±2.0kPa) in ablated tissue.

Stiffness mapping of ablated atrium

The R-wave was chosen as a time reference point for stiffness mapping of normal and ablated tissues. Figure 3-8 shows several examples of stiffness maps obtained before and after ablation at different locations of the right atrium. In Figure 3-8a, the lesion is visible as a region of high shear wave speed. The mean shear-wave speed increased from 1.6±0.3 $m.s^{-1}$ to 3.3±0.4 $m.s^{-1}$ (2.9±1.0 kPa to 12±3 kPa) in the central region of the lesion. The border of the lesion seems to be visible on the left side of the lesion. At this location the stiffness remained unchanged compared to the normal stiffness. The lesion observed on gross pathology showed a good agreement in dimensions (approximate diameter of 5mm) and transmurality of the same ablation area found with SWE. Figure 3-8b and Figure 3-8c show other examples of

RFCA lesions with variations respectively of 1.8±0.2 $m.s^{-1}$ to 3.4±0.4 $m.s^{-1}$ (3.3±0.7 kPa to 12±3 kPa) and from 1.4±0.2 $m.s^{-1}$ to 2.6±0.2 $m.s^{-1}$ (2.3±0.7 kPa to 7.3±1.3 kPa).

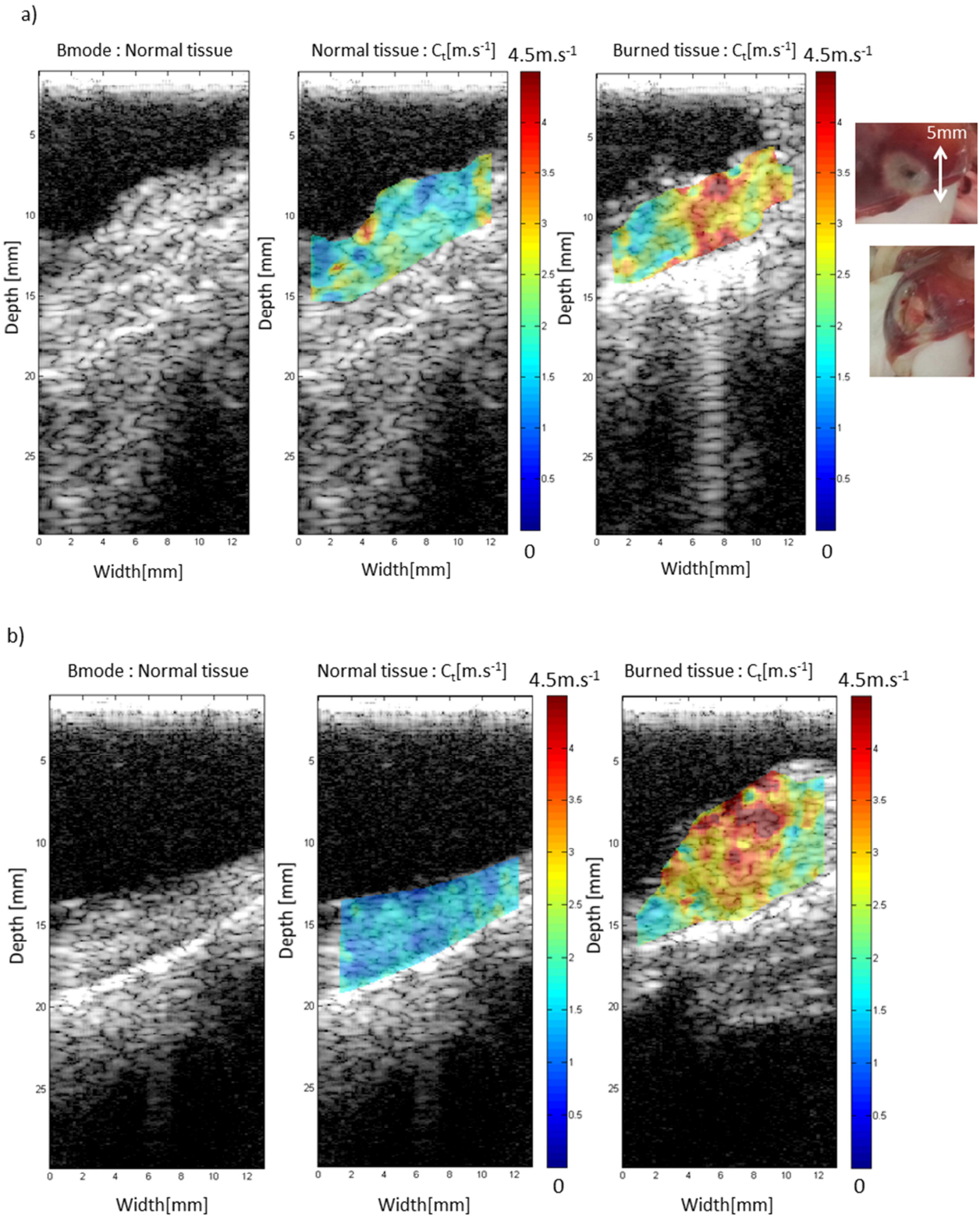

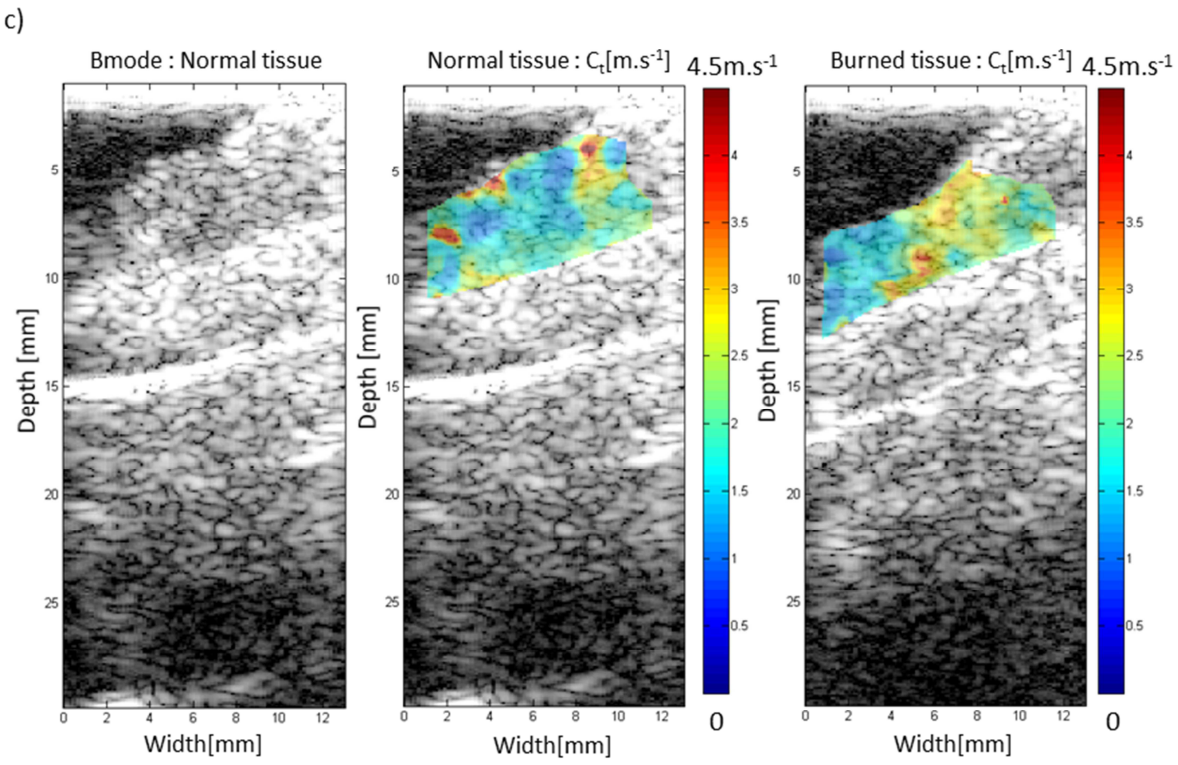

Figure 3-8 : Shear-wave speed maps in normal (middle), ablated (right) right atrial tissue, with Bmode images taken before ablation (left). The mean shear-wave speed value varied in the central region of the sample from 1.6±0.3 m.s-1 in normal tissue to 3.3±0.4 m.s-1 in the ablated zone (a), from 1.8±0.2 m.s-1 to 3.4±0.4 m.s-1 (b), from 1.4±0.2 m.s-1 to 2.6±0.2 m.s-1 (c). Maps acquired after ablation clearly reveal the presence of lesions. Validation against gross pathology (a) shows a good agreement between width and depth (transmurality) found with SWE of the presented lesion.

A total of 6 ablation locations were mapped with SWE in the three animals. A significant increase of atrial stiffness was found for 5 lesions. One lesion exhibited no significant change, but this lesion was not found after the heart was explanted. For each of the 5 lesions with stiffness increase, the mean stiffness was calculated in a 3mm-diameter area in the center of the lesion (average shear-wave speed across samples: 3.1±0.3 $m.s^{-1}$, average shear modulus: 10±2 kPa) and compared against the mean stiffness before ablation in the same 3mm-diameter area (average c_t across samples: 1.8±0.3 $m.s^{-1}$, average shear modulus: 3.3±1.0 kPa) (Figure 3-9). A mean c_t increase ratio of 1.8±0.3 was found (mean shear modulus increase ratio: 3.1±0.9).

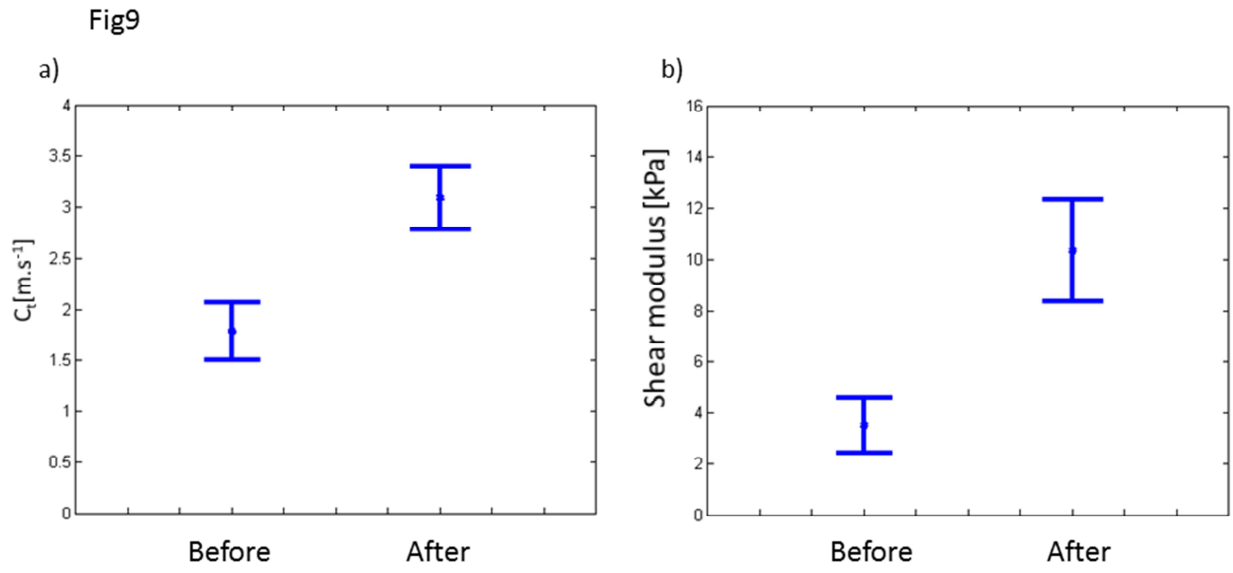

Figure 3-9 : Average shear-wave speed (a) and shear modulus (b) across in-vivo samples (n=5) before and after ablation. The mean shear-wave speed increased from 1.8±0.3 m.s-1 (mean shear modulus: 3.3±1.0 kPa) to 3.1±0.3 m.s-1(mean shear modulus: 10±2 kPa), i.e. a ratio of 1.8±0.3 (mean shear modulus increase ratio: 3.1±0.9) in the considered 3mm-diameter lesion's centers.

2.4 Discussion

In this study, Shear-Wave Elastography was implemented on a standard intracardiac imaging transducer to map the thermal lesions induced with RFCA in cardiac tissue ex vivo and in vivo. Intracardiac SWE was first investigated in ex-vivo heart samples (N = 5). Lesions were induced with a clinical RFA catheter and stiffness mapping was performed before and after ablation in the same plane. A large shear modulus ratio was obtained (2 to 5 folds) between healthy and ablated tissue and provided a reliable quantity to determine lesions' boundaries, as validated against gross pathology.

The feasibility of intracardiac SWE was then demonstrated in vivo in sheep (N = 3). At first, as atrial tissue – as well as ventricles – is active during the cardiac cycle, we investigated its normal stiffness' temporal profile during the entire cardiac cycle. Little attention has been given previously to the time variation of atrial stiffness, and there is currently no data in our knowledge that could be used to determine at what time of the cardiac cycle the stiffness mapping should be performed. By measuring the variation of normal atrial stiffness within one cardiac cycle, we found that this variation was approximately 50% during the whole cardiac cycle, which is lower than the variation observed in the ventricles [206, 208, 211, 212]. More important variations of atrial stiffness were found after ablation. Therefore, a time

point was required to compare stiffness before and after. The R-wave was found as a good reference time point: the R-wave is easy to detect and the atrial stiffness of ablated and normal tissues is relatively low at this time point which is better to provide shear velocity estimates [210]. The time variation profile of those variations was found consistent with passive and active cardiac events of the right atrium. The shear-wave speed curve presents a first increase of 50% during the passive filling of the atrium. The opening of the tricuspid valve then leads to the passive emptying of the chamber, which is associated with a decrease in the shear-wave speed. The P-wave corresponds to the atrial systole – an increase of pressure and also active stiffening (40% increase of the shear-wave-speed). Finally, before the R-wave – i.e., the onset ventricular contraction – the atrium has a smaller volume, is relaxed and has a low stiffness.

Based on these measurements, the R-wave was chosen as a reference time point for mapping the atrial tissue. Indeed, any time point of the cardiac cycle could have been chosen because the stiffness in normal tissue does not vary strongly during the cardiac cycle. Nevertheless, in order to compare the different acquisitions, it is important to compare the stiffness at the same time point, and the R-wave presented a practical reference time point.

N=6 RFCA lesions were mapped with SWE in the right atrium. The stiffness in the lesion increased significantly in 5 lesions. Based on the in vitro results, a 2 fold increase of the shear wave speed was determined as a threshold for the lesion detection. If this threshold is applied on the in vivo results, the boundary of the lesion can be determined on the SWE maps. However, further work is necessary to confirm that this threshold can discriminate ablated tissue from viable tissues.

Atrial stiffness measured in vivo by SWE was in good agreement with values reported in the literature on mechanical testing measurements of excised atrial tissues. Bellini et al. [213] reported a shear modulus between 1.56 and 8.84 kPa in 9 excised human right atrial samples. In right atrial in vivo sheep tissues, we found a shear modulus between 1.0 and 4.1 kPa. In contrast, because of myocardium contracture and rigor mortis stiffening several hours after excision, ex-vivo ventricular samples exhibited much higher values of shear modulus.

An advantage of SWE is its real time capability due to ultrafast imaging that permits the acquisition a stiffness map within a single heartbeat. Thanks to this use of plane wave imaging, SWE satisfies the ALARA principle ("As low as reasonably acceptable"). Stiffness

maps were acquired within 20ms for a single cardiac cycle and could be processed in quasi-real time.

Motion artifacts due to cardiac contraction remain very limited and do not affect the tracking of the shear wave within cardiac tissues. Indeed since the heart wall motion has a lower frequency content [214, 215] than the shear wave tissue velocity (temporal frequency content from 100 to 400Hz) it can be removed using spatial and temporal filters [206, 212].

These results suggest that SWE could be used in a clinical setting for the monitoring of atrial stiffness in patients even during arrhythmia and is the subject of on-going studies in our group.

The time-of-flight algorithm used for shear-wave velocity mapping was originally designed and optimized for shear waves propagating in a direction parallel to the probe. As our results indicated that shear waves generated using a 6-MHz probe were guided and as such propagated following the geometry of the atrial tissue, the algorithm was adapted to take into account the varying direction of propagation. While this modification currently requires user input, tissue's curvature was entered manually by selecting several points of its surface on B-mode images, the process could be automated in a relatively straightforward manner and allow for real-time processing.

Another advantage of SWE is its capability to provide quantitative values of the shear modulus. In vivo, the absolute value of the shear-wave speed increased strongly after ablation (the maximal shear modulus reached 13 kPa). As suggested by the results obtained during the cardiac cycle (Figure 3-7) one has to be careful when choosing the absolute value of stiffness to determine the presence of a lesion in vivo. Systolic (typically maximal) stiffness before ablation can be superior to the diastolic (typically minimal) in a lesion. However, when considering a specific instant of the cardiac cycle, the post-ablation shear-wave speed was always much higher than the pre-ablation shear-wave speed. If a stiffness threshold of ablated tissue can be determined experimentally and confirmed in more experiments and in different parts of the atria, the post ablation mapping could be sufficient to determine the ablation zone without the need for pre-ablation mapping. This is of particular importance for the identification of ablated zones in patients with recurring AF.

However, current limitations to SWE include the fact that the shear modulus relation to shear-wave group velocity as described in Chapter1 was verified under purely elastic and semi-infinite assumptions, which may not be correct for atrial tissues as the atrial wall is thin and viscoelastic. However, in future work, these effects could be taken into account in the shear modulus calculation with appropriate models including visco-elastic [216] and guided wave propagation models [212, 217]. Guided wave effects need to be carefully addressed in order to establish a quantitative threshold of ablated tissue. While including such corrections in acquisition sequences using an intracardiac catheter is the object of on-going work, the approach used in this study is a simple, first-order approximation to the mapping of the stiffness.

Ex-vivo characterization of shear modulus mapping with SWE was based on gross pathology tissue investigation. This technique intrinsically implies variations in the measurement of lesions' boundaries: indeed, after ablation, the tissue was manually cut following the US imaging plane with a possible deviation that we estimate to be, based on observation, of approximately ±0.5 mm inducing imprecise lesions' boundaries determination with the optical images.

Another limitation of this study is the small number of animals investigated. The small size of the study makes it difficult to draw definite conclusions about the reproducibility of the technique.

Finally, another major limitation we encountered during the in vivo study was the lack of navigation system which made very challenging the alignment of the ultrasound and RFA catheters. Fluoroscopy was used to identify the position of both devices in the heart and their relative approximate position, the alignment of the catheters was made under US B-mode, but it was very difficult to precisely ensure that the imaging plane was located at the center of the lesion. Additionally the catheters were moving during the procedure, this could explain the difference of the tissue's shape before and after ablation on Figure 3-8b. A precise navigation system could be of assistance to locate both catheters, and the accuracy of the alignment will be evaluated in a future study.

Even better, the capability of ultrasound to both image and thermally ablate tissues present a great potential for dual mode approaches [218] with intracardiac probes. A single catheter system could be developed, capable of both ablation and monitoring with the same

transducer elements. Such intracardiac dual mode transducer would provide an intracardiac treatment of atrial fibrillation with controlled monitoring of necrosis. The work presented in this article corresponds to a first step towards these full ultrasound-based atrial fibrillation treatments.

3 Intracardiac Ultrafast Doppler imaging

3.1 State-of-the-art and concepts

Another important effect of thermal ablation, in addition to the change of elastic properties of ablated tissues, evaluated with SWE, is the modification of the micro-vascularization. This effect can be imaged with CT[139] (as mentioned in the previous chapter), contrast-enhanced MRI [219], contrast-enhanced ultrasound B-mode imaging [220] or more generally with ultrasound Doppler imaging [219].

Cardiac vascular flow imaging is an important tool for the diagnosis of various cardiovascular diseases e.g. myocardial infarction or coronary artery stenosis. Gold standard techniques are CT [221] and MRI [222] that provide angiographic images with high sensitivity but necessitate the injection of contrast agents, suffer from low frame rates and are not real-time. On the other hand currently existing ultrasound contrast enhanced real-time imaging [223] suffers from poor sensitivity resulting in the detection of only main arteries.

In past several years a new ultrasound imaging technique, Ultrafast Doppler[224], has been developed. It is based on Ultrafast imaging presented in the first chapter. It has the advantage of providing a full blood flow characterization with a high sensitivity and in real-time. It provides access to completely new imaging modalities such as functional ultrasound (fUS) in the brain [225, 226] or high sensitivity cerebral blood flow imaging in the neonates [227] and has recently been used for cardiac imaging providing the left ventricular hemodynamic function with a transthoracic approach [228] as well as the feasibility of coronary flow imaging after thoracotomy [229].

In this work we implemented Ultrafast Doppler imaging on the intracardiac transducer in order to investigate the feasibility of coronary mapping with the intracardiac approach to assess the possibility of detection of the variation of vasculature after RFCA. We tested the technique in-vivo on two sheep (N = 2).

3.2 Methods

3.2.1 Experimental setup

The acquisitions were performed in sheep (n = 2) during the same protocol described in part 2.2.4 of this chapter for RFCA evaluation with intracardiac SWE. Ultrafast Doppler was thus performed on the same tissues that were imaged with SWE. Acquisitions were taken before ablation in the ventricles to assess the presence of coronaries. Since cardiac perfusion occurs during relaxation, the acquisitions were triggered on ventricular diastole.

3.2.2 Ultrafast Doppler imaging

Sequences

In this study two sets of parameters were tested for ultrafast Doppler sequences. In the first case a series of 11 tilted plane waves (-5:0:5°) at 6.5MHz were sent with a PRF of 19.6 kHz for an imaging depth of 16mm. After compounding in total 1400 images were obtained for a final frame rate of 1.8 kHz and a total acquisition time of 786ms. In the second case a series of 3 plane waves (-2 0 2°) at 5MHz was sent with a PRF of 16.1 kHz for an imaging depth of 30mm. After compounding 1200 images were obtained with a final frame rate of 5.4 kHz and an acquisition time of 223ms.

Data processing

The data processing in based on Singular Value Decomposition (SVD) filtering, a technique very recently introduced in the field of Ultrafast Doppler imaging [230]. Briefly, it is based on the hypothesis of a high spatiotemporal coherence of the tissue signal, compared to the blood flow. It means that it is possible to separate both sources of signal by carefully choosing a rejection threshold of n first singular vectors of the SVD from the total raw signal (a rejection of the most energetic sources).

In this work we performed SVD by choosing sliding temporal windows within the final compounded frames. For the first sequence signal was processed within 30 frames (corresponding to 17ms of acquisition) every 20 frames (11ms) and first 20 eigenvectors were rejected. For the second sequence, signal was processed within 200 frames (37ms of acquisition) every 50 frames (9ms) and first 140 eigenvectors were rejected. Finally power

Doppler images were calculated by integrating over time the resulting signal on the considered temporal window.

3.3 Results

Figure 3-10 shows an example of acquisition in an interventricular septum, performed with the first set of parameters. SVD filtering revealed localized energetic spots corresponding very probably to coronary flow (perpendicular to the imaging plane).

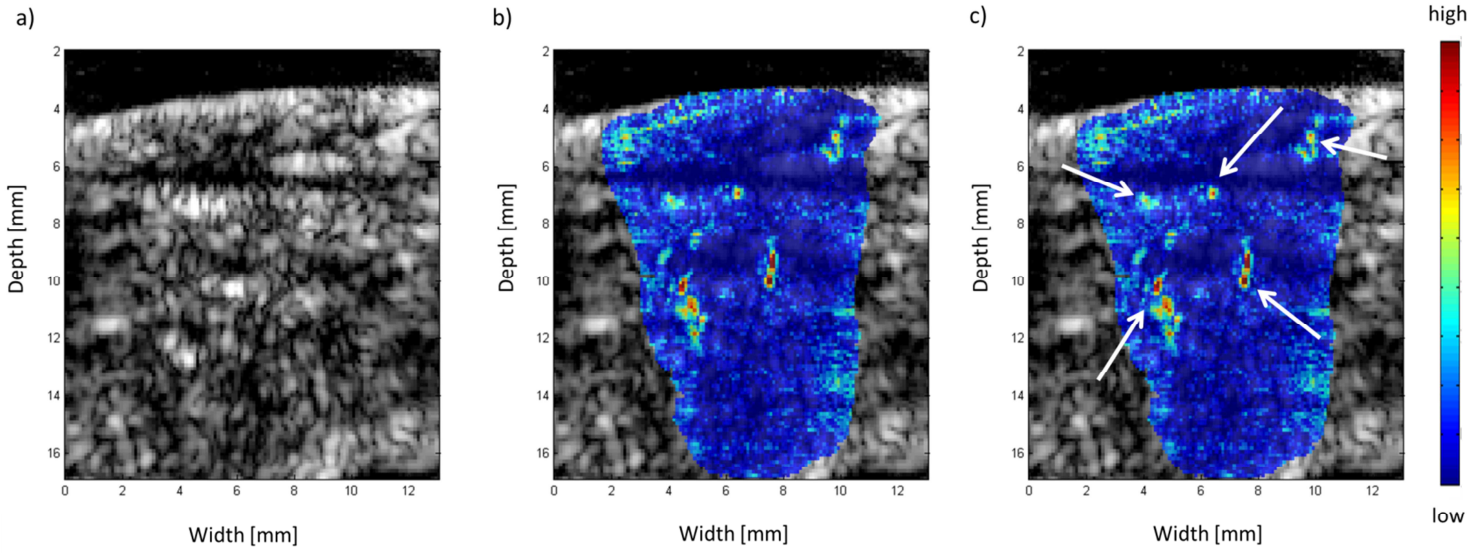

Figure 3-10 : Ultrafast Doppler acquisition in an interventricular septum. (a) Sum of the 30 Bmode images used for processing. (b) Power Doppler image after SCD filtering revealing energetic signals within the tissue. (c) The indicated spots presumably correspond to coronary flow.

Figure 3-11 shows an example of a second acquisition in the interventricular septum, with the other set of parameters. After the SVD filtering very thin (few hundreds of microns) structures appear within the tissue.

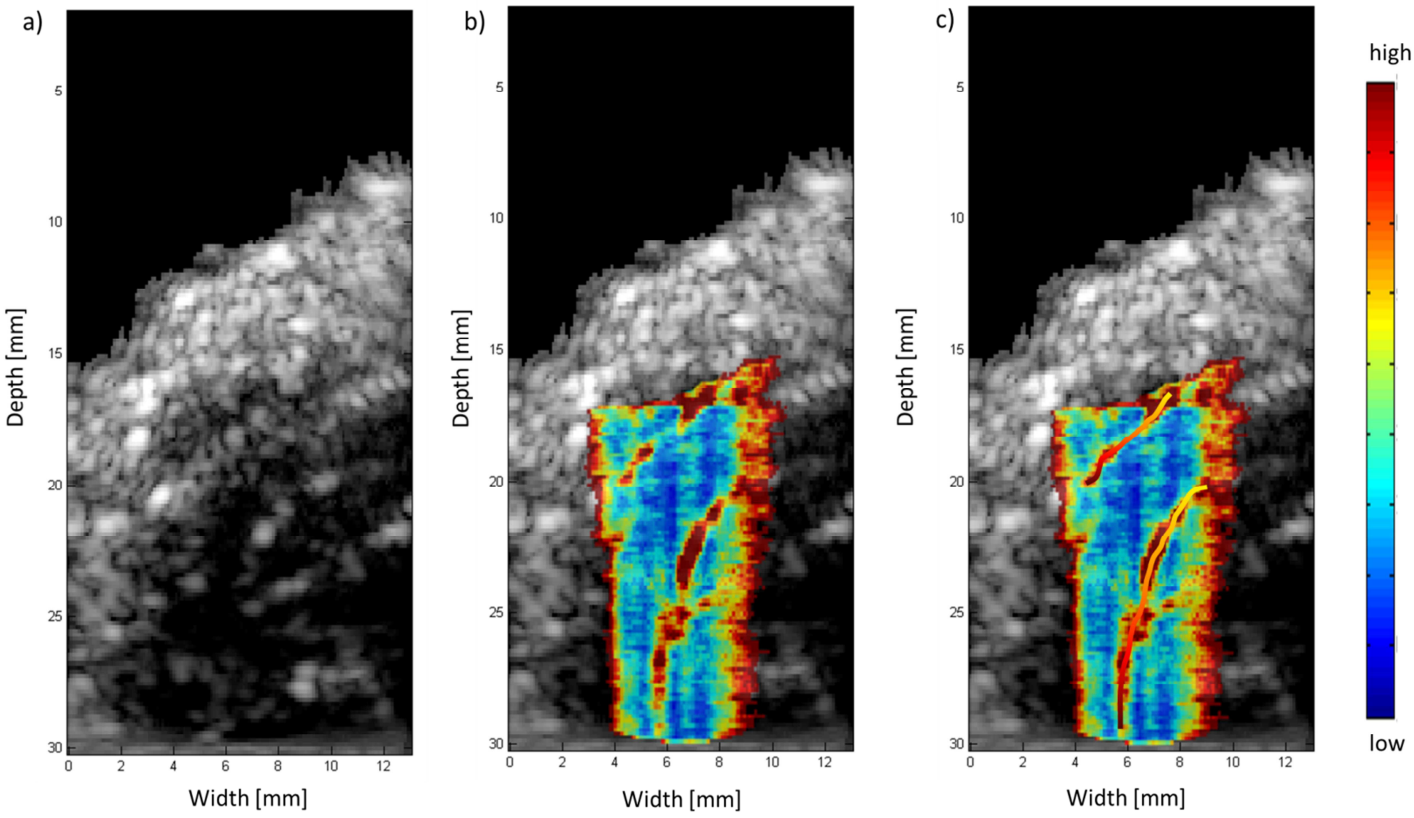

Figure 3-11 : Power Doppler acquisition with SVD filtering revealing coronary-like structures. (a) B-mode image of the cardiac wall. (b) Power Doppler acquisition within a 37ms window (200 frames). Two coronaries may be visible. (c) Most probable positions of the coronaries.

3.4 Discussion

While the examples shown in the results section are promising, consequent work needs to be done to confirm the possibilities of the intracardiac Ultrafast Doppler imaging. The processing of the coronary mapping necessitates improvement to increase the sensibility of the technique in order to make a study on the vascular effect of thermal ablation possible. Nevertheless even a simple introduction of the SVD filtering shows new potentials for intracardiac Ultrafast Doppler.

4 Conclusion

In this chapter we have shown the capability of Shear-Wave Elastography to map Radio-Frequency Ablation lesions in ex-vivo myocardial tissues with high contrast (mean shear modulus increase ratio of 4.5±0.9) using an intracardiac catheter. In vivo feasibility has been demonstrated for lesion evaluation as well as for the estimation of the shear-wave speed

and shear modulus time profile of atria. This technique reveals very promising for the evaluation of Radio-Frequency Catheter Ablation and more generally intracardiac thermal ablations.

We have also shown other possibilities of imaging with an intracardiac transducer, with possible applications for thermal ablation evaluation (Ultrafast Doppler Imaging of lesions) but also for other diagnostic imaging (Ultrafast Doppler revealing coronaries). Those new approaches are at the stadium of a promise but could become in the near future real new imaging modalities for the intracardiac approach.

Beyond current state of the art, the work presented in this chapter, in particular intracardiac SWE, was a first step towards a theranostic intracardiac ultrasound system combining monitoring and ablation capabilities on the same probe. Indeed, as discussed previously, we think the usage of two independent catheters, one for therapy, one for imaging, could be related to an important risk of errors for thermal lesions mapping. In the next chapter we present a novel intracardiac system presenting a dual-mode therapy-imaging approach all performed with the same elements of the same device.

Chapter 4. Intracardiac dual-mode therapy and imaging approach

1 Introduction

1.1 Motivation

In this chapter, a novel intracardiac approach is proposed for cardiac ablation treatments based on the combination of ultrasound therapy and imaging on the same intracardiac dual mode transducer. This work was motivated by several reasons. First, the results of intracardiac imaging obtained in Chapter 3 are promising for mapping RFCA lesions, however, the separation of therapy and imaging on two separate systems, requires the use of multiple catheters and complex navigation systems. Second, as discussed previously (Chapter 1), HIFU therapy presents many potential advantages over RFCA that could be beneficial for cardiac ablation especially in the context of ventricular tachycardia (VT). The idea of catheter-based cardiac HIFU is not new and several systems have already been developed and tested even pre-clinically.

1.2 Intracardiac HIFU: state-of-the-art

A general overview of cardiac HIFU has been presented previously (Chapter 1). Here we will draw attention on catheter-based approaches. Various catheter-based systems and designs, dedicated for minimally-invasive cardiac HIFU ablation, have been studied in the last two decades.

In a similar approach than the intraoperative Epicor system, some designs are dedicated for an epicardial approach without, however, the need for extensive surgery. Such approach is already performed with RFCA to create lesions in the ventricles for VT treatement[231], trying to overcome the low energy penetration of this technique[8]. Hynynen et al. [74, 232] were first to perform in-vivo epicardial HIFU-induced lesions with catheter-based designs obtaining lesions depths up to 8.5mm. More recently Koruth et al.[233] tested another design capable of creating lesions in the myocardium up to 15mm deep leaving vital coronary structures intact. To note, an original system, based on non-thermal shock-wave tissue

disruption has also been proposed recently[234], but lesion formation was limited only to 3mm. Although designed for minimally-invasive usage, all these systems were tested with surgical sternotomy. Still, if not performed with surgery, the epicardial approach may be more limited for maneuverability and finally the flexibility of the ablation.

Intracardiac HIFU approaches have also been investigated. A first in-vivo proof of concept has been performed by He et al. [73], but with a catheter insertion via the cardiac chambers. Ohkubo et al. [85] designed and realized first in-vivo HIFU ablation using a high power transducer by the classical femoral vein approach and obtained maximal lesions' depths up to 8-10mm. However, motivated by new anatomical findings in the field of atrial fibrillation [6], new balloon-based systems have been designed for an efficient pulmonary vein (PV) isolation. As other balloon-based systems, those transducers were capable of creating circumferential lesions around PVs with single-up-to-several sonications. A first system, conceived by Atrionix (Sunnyvale, CA, USA), underwent pre-clinical tests[235, 236] but was limited by an architecture unsuitable for a variable PV anatomy. A second system (ProRhythm, Ronkonkoma, NY), presenting a more adapted design to perform PV isolation, has also been investigated in humans [30, 237]. Despite promising performances and safety algorithms the system led unfortunately to two patient deaths and its clinical usage has been stopped[238, 239]. By the nature of the probe design, the circumferential focus was fixed and probably too deep, leading to atrio-esophageal fistulas even after focus reduction and with esophageal temperature monitoring.

All those systems presented interesting ablation performances but were not accompanied with imaging modalities to control the effective lesion formation. This issue has been extensively presented in Chapter 3 and the balloon example may have shown once again the importance for such control.

Only few experimental image-guided HIFU systems, designed for intracardiac usage, have been reported. Gentry et al. designed a cylindrical forward looking catheter [240, 241] composed of a HIFU ablation ring, with in its center a custom 2-D imaging array. The group reported first in-vitro ablations and preliminary imaging. Another possibility for image guidance is MRI, Carias et al. [242] published recently first achievements on MRI compatible intracardiac HIFU catheters with successful in-vitro ablation. On the other side of the wall, to complete the therapy-imaging devices list, new systems based on RF ablation, but with integrated ultrasound imaging have been successfully tested in-vivo [198–200].

This lack of performant ultrasound-based therapy-imaging devices is caused by the challenges of the intracardiac environment, principally the combination of miniaturization accompanied with the need of sufficient HIFU performances and manoeuvrability, which leave very little space for imaging. Therefore a possible solution, satisfying all those requirements, is to design a hybrid transducer, combining therapy and imaging on the same elements. Such ultrasonic systems are called dual-mode transducers and have already been used for other applications.

1.3 Dual-mode intracardiac catheter

1.3.1 State-of-the-art

The concept of dual-mode arrays has been introduced by Ebbini et al. [243, 244] and is based on usage of the same elements for imaging and ablation. The first advantage underlined for this type of probe was the quick feedback it can provide to control therapy. This feature was applied for transcostal therapy in the liver or kidney to avoid an excessive exposure at the rib locations [81] and to finally provide a real-time feedback during therapy to enhance ablation control [245]. However in our concern the main advantage dual-mode arrays offer, is the miniaturization of the image-controlled therapy device.

Few interstitial dual-mode systems have been proposed for liver or biliary applications. Two designs are based on single [246] or five-element [247] high-power transducers performing sector-imaging by a mechanical rotation of the probe. A third one was composed of a 32-element array and has been successfully tested in-vivo on rabbit tumorous liver models[248], providing high emission intensities (110W/cm^2) and good quality B-mode imaging.

1.3.2 Dual-mode intracardiac catheter

In our case the system relies on a standard intracardiac imaging transducer which underwent only few modifications to provide high intensities and thermally support HIFU sequences for ablation. The goal is to benefit from all the imaging modalities presented in Chapter 3 and in parallel be capable of creating lesions using the same aperture. The alignment and devices size issues could be thus easily solved. Moreover thanks to the multi-element architecture, therapy with this device could be very flexible: with only the electronic

steering, large zones of tissue could be ablated without moving the transducer. Even more, whereas in atria the transmural aspect of the lesion is desired, in the case of ablation for ventricular tachycardia, only certain layers of the cardiac wall need sometimes to be targeted.

In this work, first, a new dual mode intracardiac transducer was designed in collaboration with Vermon (Tours, France). We have characterized the output intensity with an acoustic balance setup in parallel with the internal heating of the probe for several emission parameters. Second, we validated in vitro optimal HIFU sequences adapted to our device with heart-mimicking conditions. Finally we performed an in-vivo feasibility study for the dual-mode catheter in four sheep (n = 4) with a standard intracardiac setup and performed image guided ablations in right atria, right ventricles and interventricular septa (IVS).

2 In vitro HIFU performance characterization

2.1 Materials

2.1.1 Dual-mode intracardiac transducer

The dual-mode transducer (Figure 4-1a) was based on a regular intracardiac echocardiography (ICE) catheter[249] (6 MHz, 50-% bandwidth, 64 elements, 0.2-mm pitch, 9F, Vermon, France) and has been customized by Vermon to support HIFU emissions. It was driven by fully programmable prototype electronics (256 emission, 128 reception channels, SuperSonic Imagine, France) consisting of an ultrafast ultrasound scanner (Aixplorer®, SuperSonic Imagine, France) for imaging, combined with a high power supply (up to 10W per channel) for therapy. A thermistance set at the basis of the catheter's tip, before the active surface, was monitoring the internal heating of the transducer.

2.2 Output and thermal characterization

2.2.1 Methods

An acoustic balance setup (Sartorius CPA423S) was used to characterize the transducer's output intensity against the internal heating of the catheter in water at ambient temperature (22°C) for 2s emissions (Figure 4-1b). The power electronics elements' excitation signal was square-shaped with adjustable central frequency and duty cycle of the

active state (percentage of time the signal is ‘on’ during one period) (Figure 4-2). First, measures were performed to find the best emission configuration for those two parameters: (1) the central emission frequency (range: 4MHz to 7MHz); (2) the duty cycle of the square signal (range: 5% to 100%). Results were presented in terms of thermal efficiency defined here as the output intensity (W/cm^2) divided by the internal heating of the catheter (°C). Second, the transducer’s output against internal heating was measured for the best configuration that was found.

a)

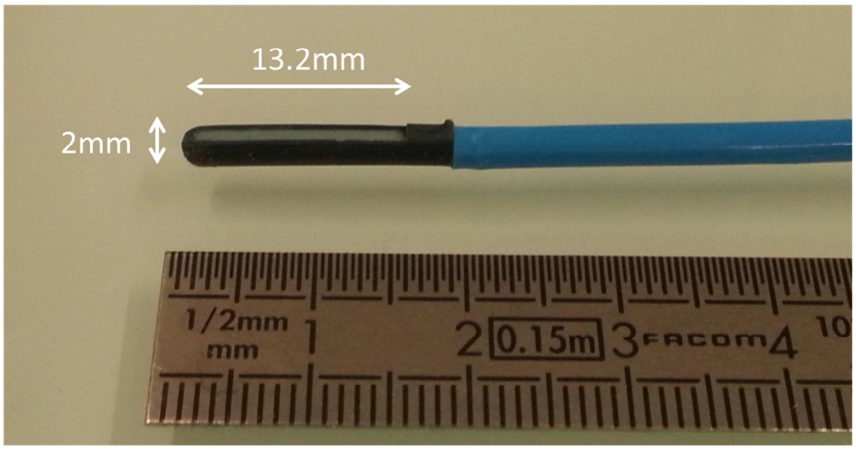

b)

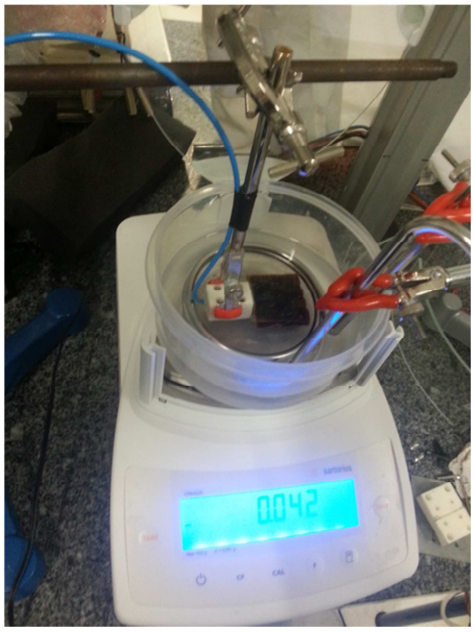

Figure 4-1 : (a) The intracardiac dual-mode transducer (dark gray) with the dimensions of the active surface (light gray). (b) Acoustic balance setup. The catheter (blue wire) was emitting plane waves on an acoustic absorber (brown resin) for 2 seconds. The radiation force created within the absorber is directly proportional to the output power and can be measured with a high precision balance.

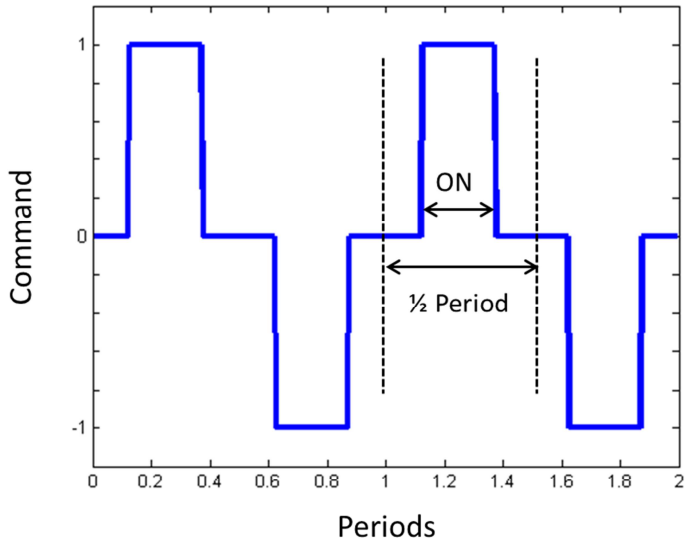

Figure 4-2 : schematic of the command signal applied on the transducer. The duty cycle represents the percentage a signal is 'ON' (-1 or 1) over the period time.

2.2.2 Results

Figure 4-3a shows the thermal efficiency of the transducer versus the central frequency of the emission. Whereas the maximum sensitivity of the transducer was around 7.1MHz and the central frequency 6.4MHz, the best efficiency measured by the ratio of output intensity and internal temperature was found around 5.75MHz.

The thermally most efficient duty cycle of the command signal was found to be 0.75 (Figure 4-3b). This is due to the harmonic contents of the square waveform transmitted by the electronics. Such waveform contains a large amount of third harmonics which depends on the duty cycle. In theory, the lowest content of harmonics is found for a duty cycle of 0.8 which is very close to the result found here. This suggests that even if the harmonics are outside of the bandwidth of the transducer, they may participate to the heating of the probe.

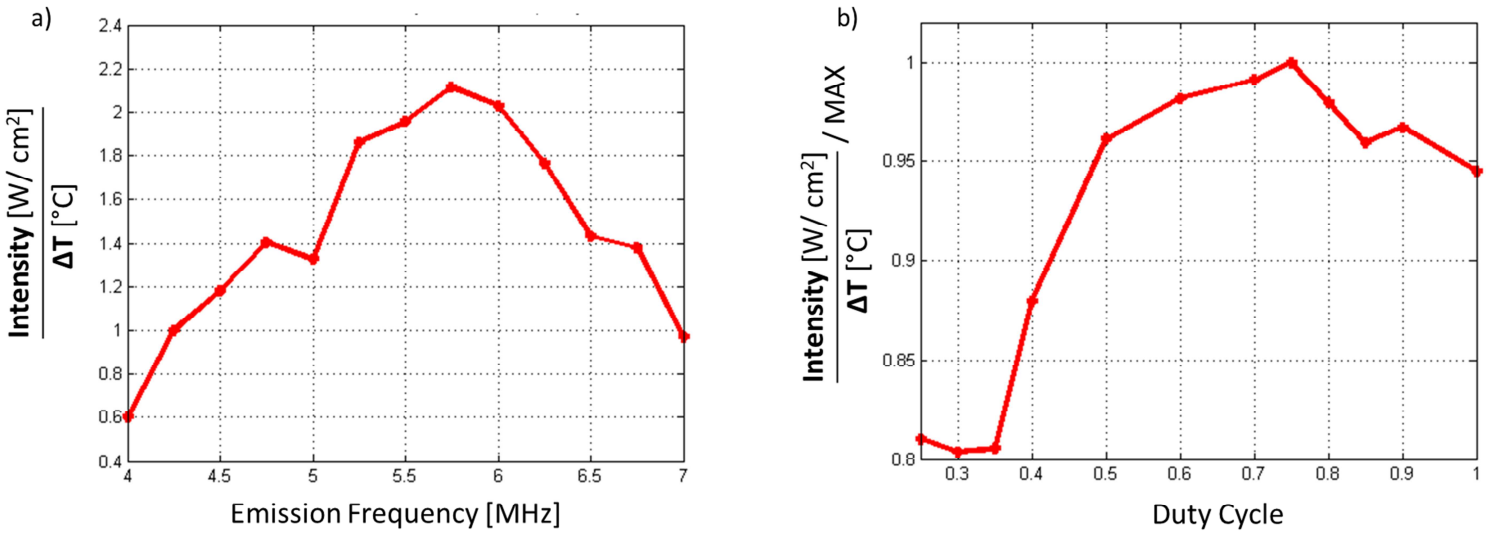

Figure 4-3 : Thermal characterization of the transducer in terms of (a) emission central frequency, (b) command signal duty cycle. (a) The thermally most efficient emission was found around 5.75MHz. (b) The best excitation duty cycle was found around 0.75.

Figure 4-4 represents the transducer's output intensity measured with emissions found most efficient in terms of internal heating of the transducer (5.5MHz and duty cycle of 0.75). Intensities up to 21.5 W/cm^2 (corresponding to a total acoustic power of 4.6W) have been reached for a maximal temperature increase inside the catheter of 9.0°C during the 2s emissions. The temperature increase was found to be linearly dependent with the output intensities.

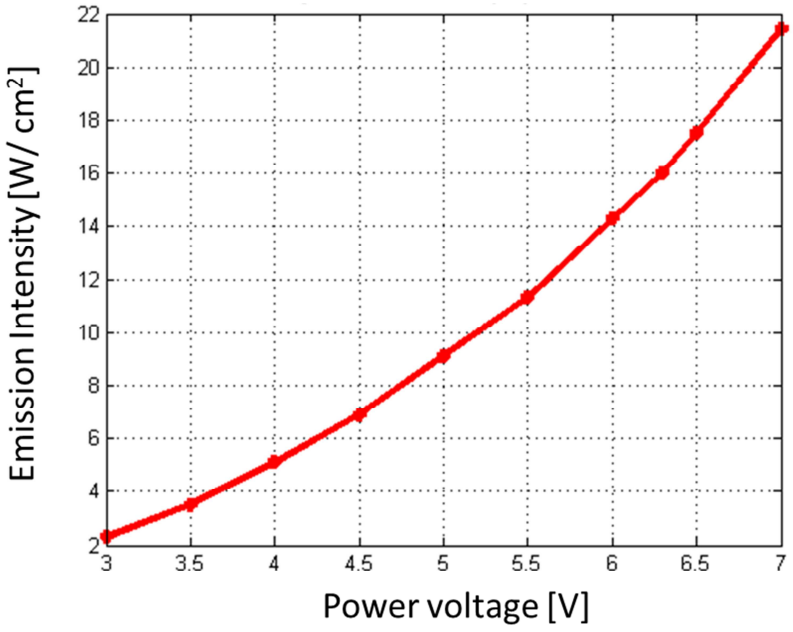

Figure 4-4 : Intracardiac transducer's output intensity (W/cm2) against power supply voltage for 2s constant emissions. A maximal intensity of 21.5W/cm2 has been characterized.

2.2.3 Discussion

These first measurements were promising, suggesting that the catheter may support important emission intensities (nearly 18W/cm^2) that could be sufficient to thermally induce lesions. Continuous emissions were performed 10s with 11W/cm2 with a good stability of the transducer. By emitting during 10s at 11W/cm^2 at 10mm, we could observe the formation of impacts on a Plexiglas plate (Figure 4-5a), as well as we managed to create in-vitro, a first lesion in chicken breast (in a 37°C bath) (Figure 4-5b). The continuous emission strategy is the most effective to create thermal lesions but it was not possible exceed those intensities and emission time. Thus we had to adapt the HIFU sequences to enhance the cooling of the catheter and avoid its destruction and study the cooling effect itself by imitating the intracardiac blood flow characteristics.

a)

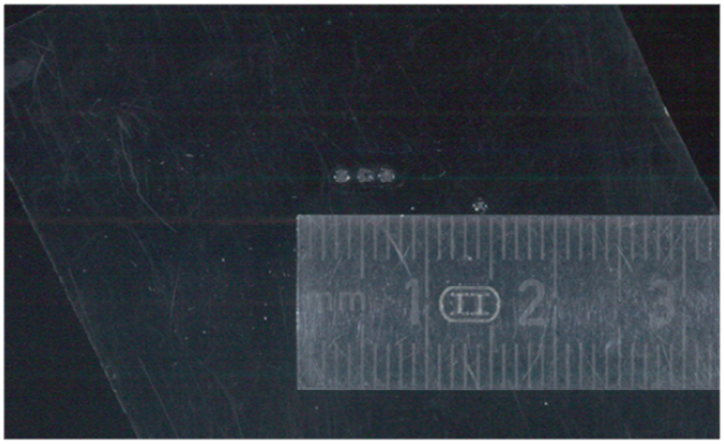

b)

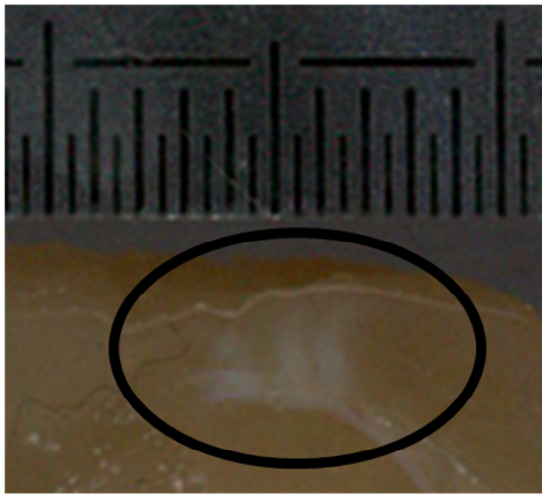

Figure 4-5 : First thermal effects obtained with 10s continuous emissions at 11W/cm^2 with the catheter. (a) Three impacts created in a Plexiglas plate, obtained with the electronic steering of the array, without movement. (b) Three lesions created in a chicken breast (approx. 1.5*2.5mm^2 total surface) obtained in the same manner.

2.3 In-vitro thermal tests

2.3.1 Methods

An excised 30*30*10mm^3 bovine skeletal muscle was placed on an acoustic absorber, in a degassed water tank at 22°C. A thermocouple was inserted inside the tissue, 4mm below the surface. The ultrasound transducer was placed 5mm above surface of the tissue and

parallel to it (Figure 4-6). The water in tank underwent a constant flow of approximately 50mL/s to imitate cardiac intracavitary blood dynamics.

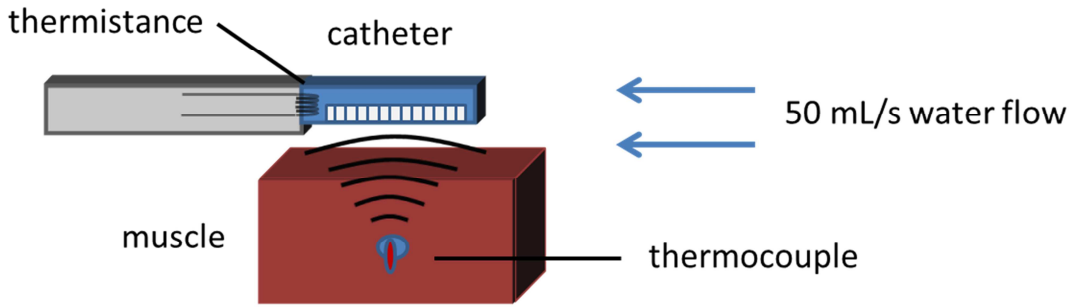

Figure 4-6 : Schematics of the in-vitro setup. The HIFU beam is focalized near a thermocouple inserted in the bovine muscle. A constant water flow is induced to imitate intracardiac pumping conditions.

Transducer's HIFU emissions were tested by focusing ultrasound 1mm under the tip of the thermocouple. The sequences (5.5MHz, output intensity 16.5W/cm^2, 0.75 Duty Cycle) were composed of 500ms emissions followed by 500ms pauses to enhance the transducer's cooling by the flow. Total sequence durations were increased progressively from 10 to 120s. Temperatures in the catheter and in the tissue were monitored simultaneously.

2.3.2 Results

Figure 4-7b shows an example of the bovine tissue temperature when focusing with the transducer next to the thermocouple. While a strong flow was induced in the bath, temperature measured in the tissue was growing during the 2 minutes of ultrasound focusing for a maximal ΔT of 8.4°C. In contrast temperature in the catheter was stabilized after 20s of emission (Figure 4-7a) for a maximal increase of +16.5°C (39.5°C).

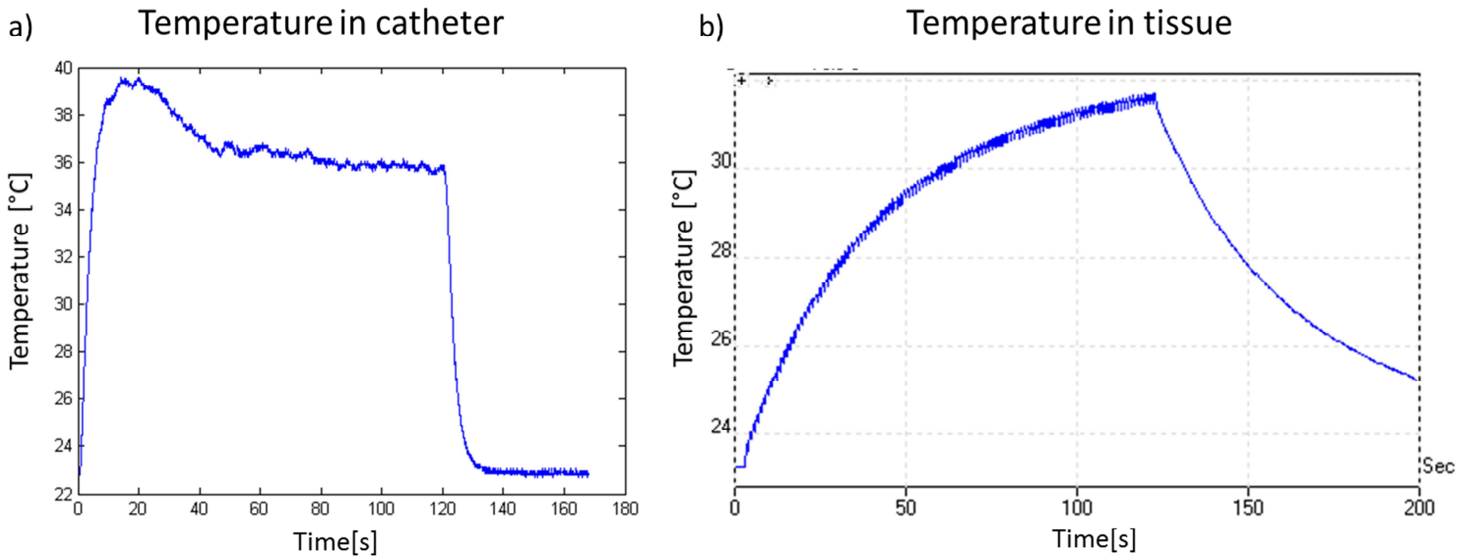

Figure 4-7 : Temperatures measured in (a) the catheter, (b) a bovine muscle, during a 2min HIFU sequence. A water flow was induced in the environment which stabilized the catheter's internal heating (maximal ΔT of 16.5°C at 20s), while the temperature in the muscle (4mm below the surface) was increasing during the whole sequence.

2.4 Discussion

In this part we have characterized the transducer's output within a non-destructive and repeatable range. An emission frequency of 5.5MHz has been chosen as it was very close to the thermally most efficient frequency for this model of transducer and as emissions at this frequency were very stable in time. It is also a good compromise between tissue penetration and absorption as both wide (ventricles: up to 2cm - 2.5cm) and thin (some parts of atria are under 1mm wide) tissues were targeted in the study.

The sequence construction of 500ms emission followed by 500ms of pause was found as the best compromise to rapidly heat the targeted tissue and take advantage of the natural blood cavitary flow in the heart to cool the transducer down. Thanks to the little dimensions of the transducer (9F i.e. 3mm of diameter) temperature in the device can be easily controlled, while temperature in tissue decreases with much longer constants. Taking advantage of this no supplementary cooling was needed even for sequences up to 2 minutes.

Taking benefit of the results presented in this part as well as in Chapter3 we proceeded to the in-vivo feasibility validation of this therapy-imaging system.

3 In vivo experiments

3.1 Materials and methods

3.1.1 In-vivo experimental setup

The study was approved by the University of Bordeaux guidelines on the use and care of animals. Two 40 to 50 kg sheep were studied. The animals were pre-anesthetized by injecting 10–20 mg/kg of ketamine hydrochloride, and general anesthesia was maintained with an infusion of sodium pentobarbital (2.5 mg/kg/hour) and ketamine hydrochloride (2 mg/kg/hour). The sheep were ventilated with 25% humidified oxygen via a tracheostomy.

An incision was performed in the thigh of the animal to access the femoral vein. The ultrasound catheter was inserted into a steerable sheath (12F) and introduced via the femoral vein into the right atrium, under fluoroscopy. The positioning of the device was made under its real-time B-mode imaging. Automated R-wave detection was used to precisely start SWE imaging acquisitions at a specific cardiac event on the ECG. In the right ventricular free wall or the IVS SWE mapping was triggered between the T-wave and the QRS complex on the ECG, which corresponds to the ventricular diastole. In the atria SWE sequences were triggered at the QRS complex which is the beginning of the atrial diastole. All SWE acquisitions were performed within a single cardiac cycle. As the duration of the HIFU sequences was much longer than one cardiac cycle (1-4min against ~650ms respectively) they were not ECG-triggered.

HIFU has been performed, under the catheter's real-time B-mode guidance, in right atria (n = 6) in right ventricles (n = 5) and in the interventricular septum (n = 5) in four sheep (N = 4). Among these SWE lesions' evaluation has been performed in two sheep (N = 2; atrium n = 3, ventricle n = 3, septum n = 3).

At the end of the in-vivo procedure, a sternotomy was made to access the heart. In order to mark the ablated tissue the aorta was clamped and a solution of 2,3,5-triphenyl tetrazolium chloride (TTC) at 1% was directly injected into this artery to force a diffusion in the right coronary arteries and finally in the right atrium and ventricle (the TTC solution marks the living tissue in red and leaves the dead as is). The animals were then euthanized.

Treated hearts were collected, lesions identified, photographed and finally frozen for further gross pathology evaluation.

3.1.2 In-vivo HIFU-SWE sequences

The catheter was inserted in the right atrium and ventricle under fluoroscopy. It was then positioned at a distance between 5 and 15mm from tissue under its B-mode imaging. A SWE mapping acquisition was performed on normal tissue before HIFU ablation and then after the whole therapy sequence. The catheter was not moved during the whole imaging-therapy procedure, meaning that all final lesions were obtained with only one position of the transducer.

HIFU therapy sequences

In this study we performed in-vivo ablation with intensities at the transducer's output ranging from 14.5W/cm^2 to around 20W/cm^2, at a frequency of 5.5MHz (with a Duty Cycle of 0.75). Each HIFU sequence was composed of 500ms emission followed by 500ms of pause, repeated for a total time of 2 to 4min for one focus. Depending on the sample, the focus was electronically moved several times axially and/or laterally for a few millimeters and the sequence was repeated (in total: average 4 focuses (2 to 7, mean total time: 8min30s) in the atria and 8 focuses (3 to 12, mean time: 20min30s) in the ventricles and IVS). HIFU was performed in the range of 5-20mm in depth and centered from element 12 to 52 (-4mm to +4mm from the center).

In general the whole transducer's surface was active for all sequences. However when the cardiac wall was in contact with some elements of the catheter's tip during contraction these elements (5 to 10) were turned off for the whole HIFU sequence to avoid potential damage (caused by an insufficient blood-flow-driven cooling). Additionally during each sequence, to avoid damaging the probe, the catheter's temperature was monitored – an elevation temperature of 12°C was fixed as a threshold that was stopping the sequence. No additional transducer's cooling was used but the natural cardiac blood flow.

SWE imaging sequences

In this study, SWE sequences were performed in the same manner that was described in Chapter 3 (part 2.2.1) with some parameters adjusted. In all tissues 5 shear-wave

generations (push time of 300µs at 5.5MHz each) and imaging sequences (two compounded plane waves (-2°, +2°) at 7MHz) were performed. In the atria the shear-wave generation was consisting of one push, performed in average 2mm below the surface (between 5mm and 15mm). In the ventricles, to cover a larger depth within the tissue and generate a shear plane wave, two pushes (150µs each) were generated one after the other (separated of 3mm in depth, with the first 2mm below the surface), as explained by Bercoff et al[111]. Imaging depth was fixed at 20mm resulting in a PRF of 18.9 kHz and an imaging frame after compounding of 9.4 kHz. Up to 75 final images were obtained for a total acquisition time of 41ms in maximum.

A temporal Butterworth high-pass filter (cutoff frequency: 1000Hz) was applied to each pixel to isolate the shear-wave. For each frame the spatial mean tissue velocity, resulting from catheter-tissue relative movement, was also removed. Finally a directional filter [250] was used to remove regressive shear-waves and improve the SNR. The same time-of-flight algorithm as in Chapter 3 was applied to track the shear-waves. All imaging acquisitions were laterally resolved at 100µm; the velocity was estimated on a mean 1.2 mm kernel. As already mentioned those values do not give but are related to the lateral resolution. Total automated time of beamforming and processing data for the final map was typically 7.5s using a laptop computer with a 3s manual segmentation of the atrial walls (Chapter 3).

The same SWE mapping was performed before and after HIFU ablation by carefully choosing the same trigger within the cardiac cycle.

3.2 Results

3.2.1 HIFU therapy

Atria

Five (n = 5) lesions have been successfully achieved in the atria. Four were transmural, for a mean wall thickness of 2mm, the last was 8mm deep but for a wall thickness (including fat layers) of 12mm. The lesions had a mean long-axis length of 7.5mm (4 to 10mm). Figure 4-8 shows an example of ablation strategy and result in a right atrial tissue (posterior septum). In this case five different positions were targeted, for two minutes each (a) and the final lesion exhibited a volume of 10*5*2mm^3 (transmural) on gross pathology (b).

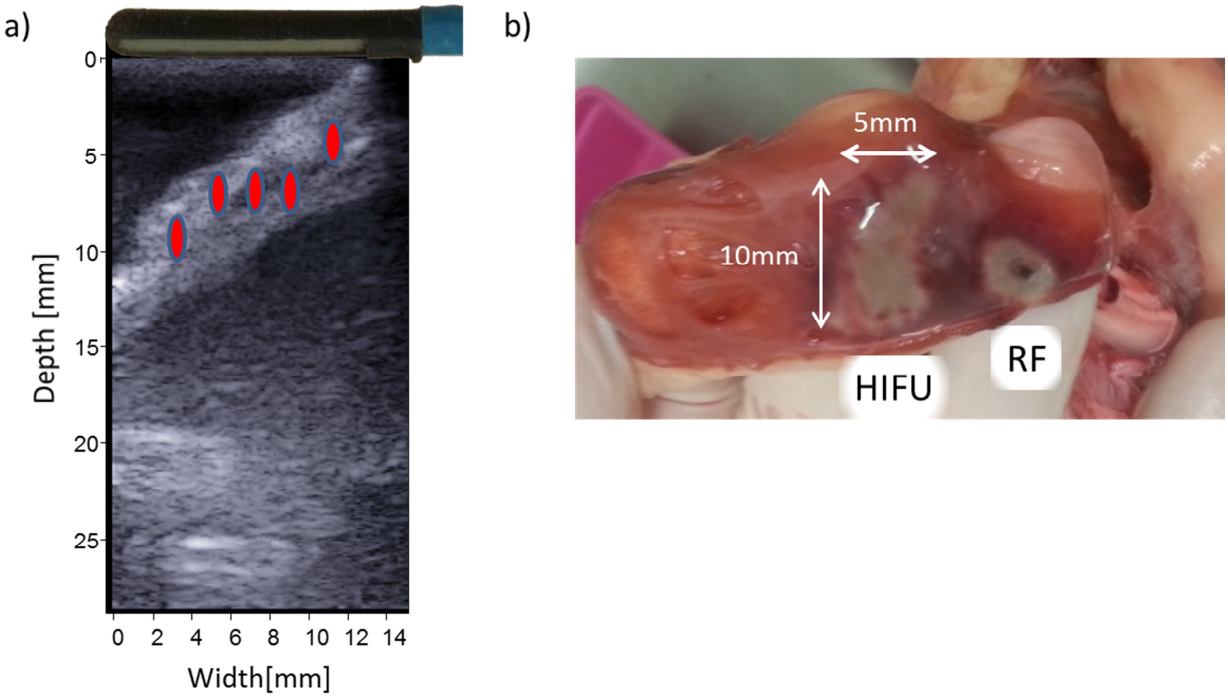

Figure 4-8 : Example of ablation performed in the right atrium. (a) The successive HIFU focal positions are represented on a B-mode image obtained with the catheter. The focal spots were fixed while the tissue was moving (the image is acquired at a mean position during the cardiac cycle). (b) The final linear lesion had a volume of 10*5*2mm3 and was transmural. Next to the HIFU lesion was performed a classical RF catheter ablation for comparison.

Ventricles and IVS

In the ventricles three lesions (n = 3) have been successively performed in the free wall. One was transmural, one on the endocardium and one on the epicardium, while all the procedures were performed from the cardiac chambers. All those lesions were approximately 4mm deep. Figure 4-9 shows the photographs of the transmural (a) and epicardial (b) lesion. The transmural lesion had a volume of 10*6*4mm^3 and was achieved with three four-minute ablations.

In the IVS four lesions (n = 4) have been realized: two on the right ventricular side and two on the left ventricular side, while targeting from the right ventricles. A mean depth of 3mm has been obtained (2 to 4mm) with a mean width of 4mm.

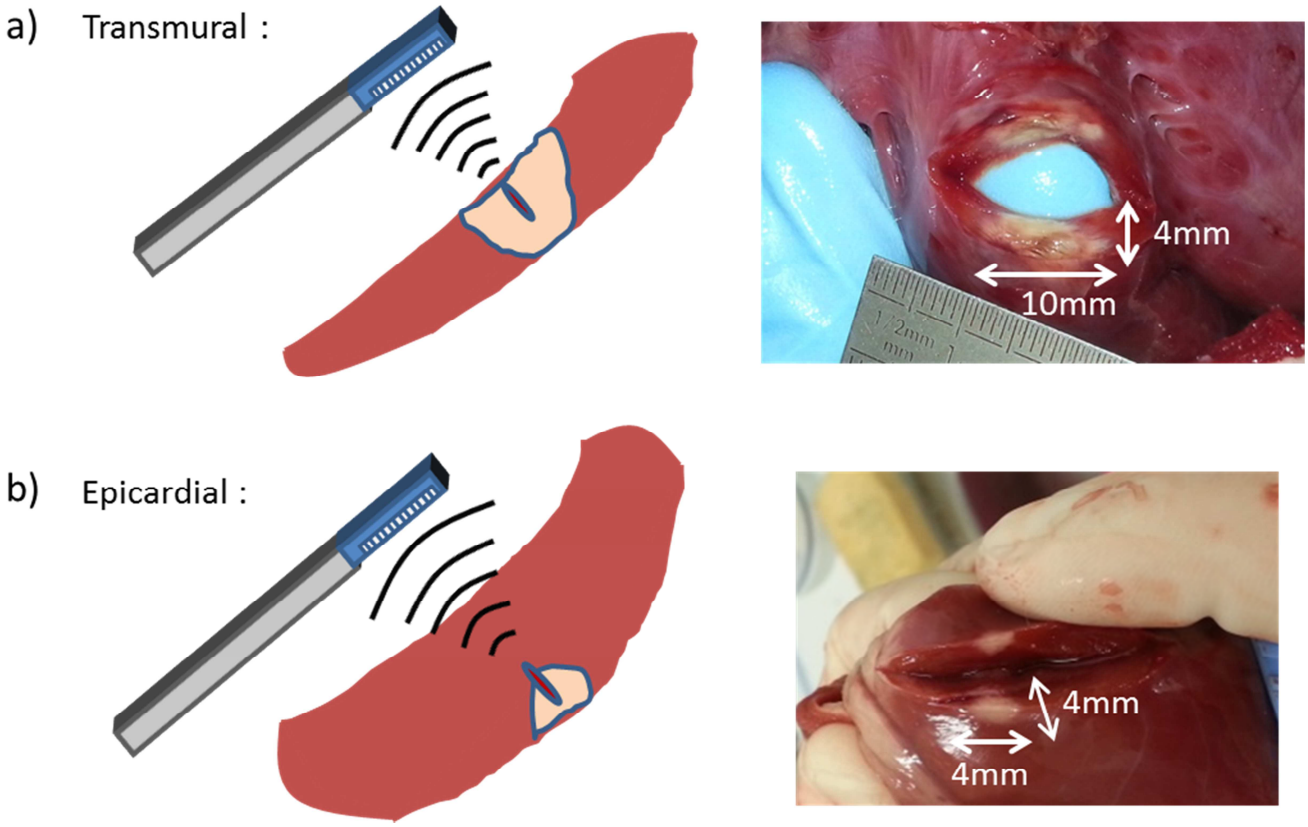

Figure 4-9 : Examples of lesions achieved in the right ventricular free wall, with their schematically represented positions. (a) A 10*6*4mm3 transmural lesion realized with 3 focal positions of 4min each. (b) An epicardial lesion (4*3*4mm3) achieved while focusing from the interior of the heart.

Table 4-1 summarizes all the lesions achieved during the procedures. It separates the different cardiac walls and the types of ablated layers.

Table 4-1 : Summary of all the intracardiac HIFU attempts and results. (RV: right ventricle; IVS: interventricular septum)

Intracardiac HIFU	Atrium	RV free wall	IVS
Attempts : Total	6	5	5
Gross confirmed	5	3	4
Transmural - Endocardial - Epicardial	4 - 1 - 0	1 - 1 - 1	0 - 2 - 2

3.2.2 SWE imaging

Among all the 12 lesions achieved in this study only one was slightly visible on the real-time B-mode imaging (Figure 4-10). The corresponding lesion found on gross pathology was not completely coagulated. This result exhibited the low sensitivity of B-mode imaging for lesion imaging and confronted us on the need of other imaging modality.

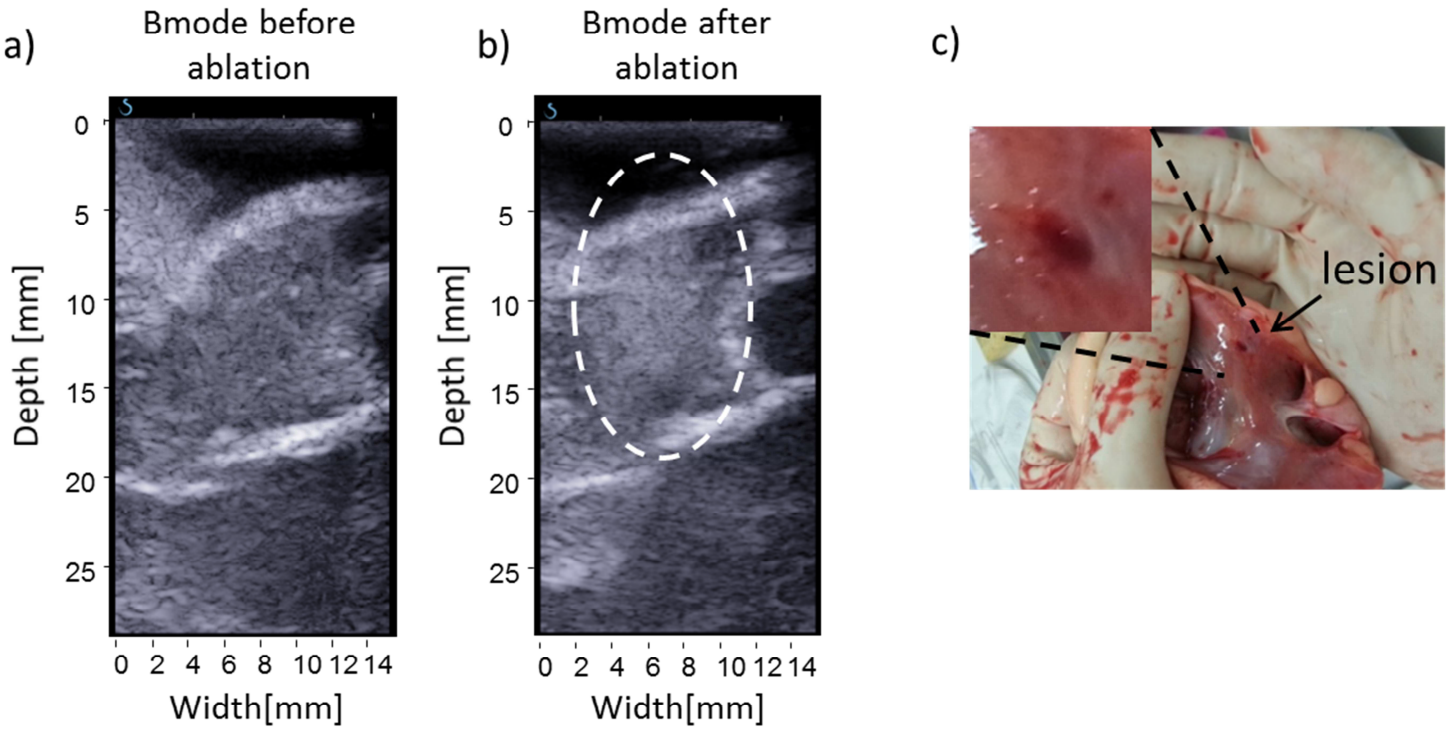

Figure 4-10 : The only lesion detected on the real-time B-mode imaging of the catheter. (a) B-mode image before ablation. (b) B-mode image after ablation. (c) Photograph of the lesion on gross pathology study. The lesion was not completely coagulated.

Figure 4-11 displays an example of a HIFU ablation evaluation with SWE in a right atrium. The thin wall was targeted with two focal spots in the center (Figure 4-11a). In this region the shear modulus increased from 4.5±1.2kPa (before ablation Figure 4-11b) to 19.0±5.2kPa (after ablation Figure 4-11c). On gross pathology study (Figure 4-11d) the presence of the lesion was confirmed and presented dimensions in agreement with those suggested by the SWE map.

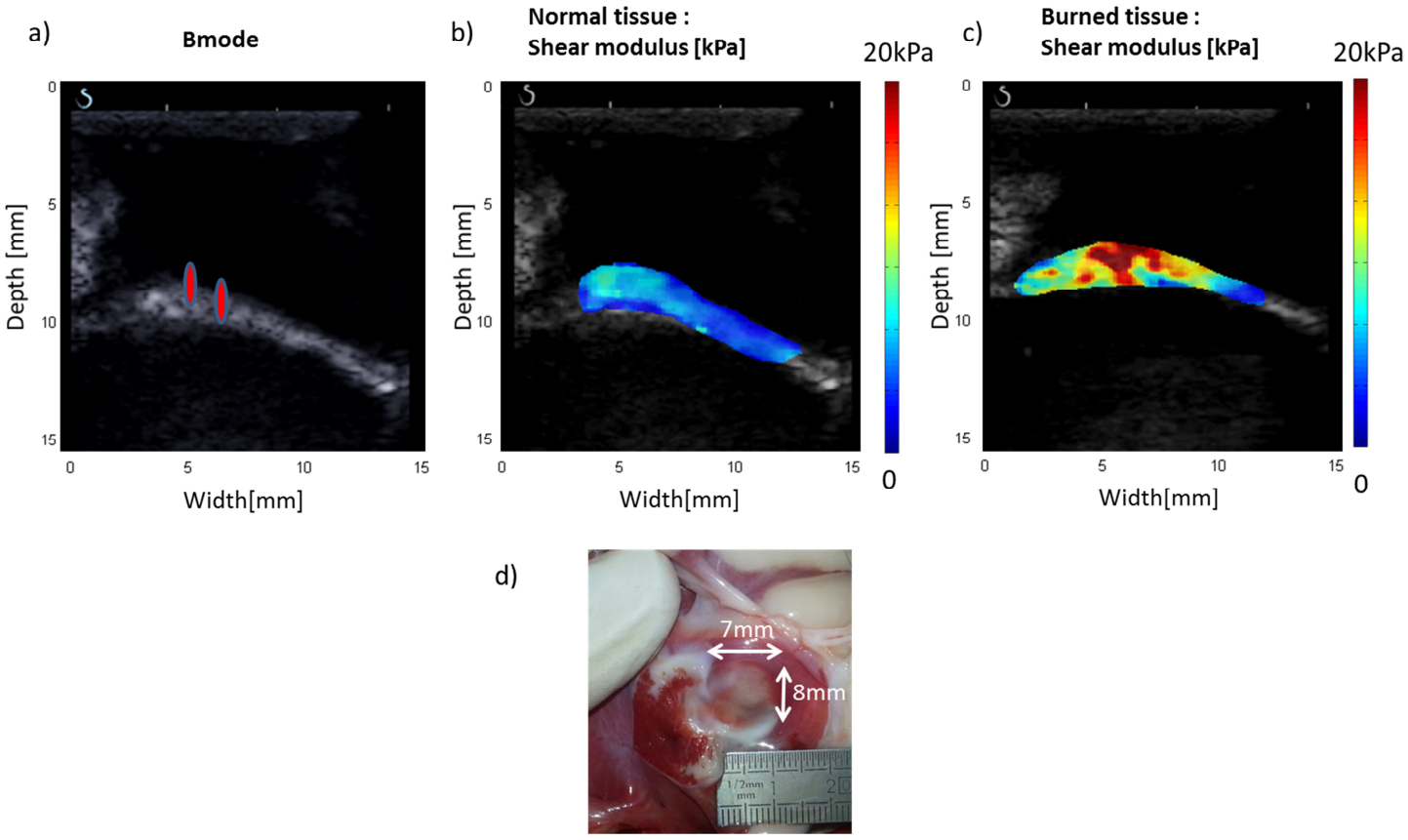

Figure 4-11 : Example of SWE mapping, before and after HIFU ablation in the right atrium, all with the dual-mode catheter. (a) The tissue was targeted with two focal spots for 2min each (represented on a B-mode image before ablation). (b) The mean shear modulus was 4.5±1.2kPa before ablation and (c) 19.0±5.2kPa after ablation. (d) The approximate dimensions of the lesion exhibited on gross pathology (d) were in agreement with the SWE map.

Figure 4-12 shows an example of identified ablation in the IVS. A little lesion has been obtained (Figure 4-12c) but the dimensions seen on SWE map agree well. The shear modulus increased from 2.2±0.3kPa (before ablation Figure 4-12a) to 5.7±1.2kPa (after ablation Figure 4-12b).

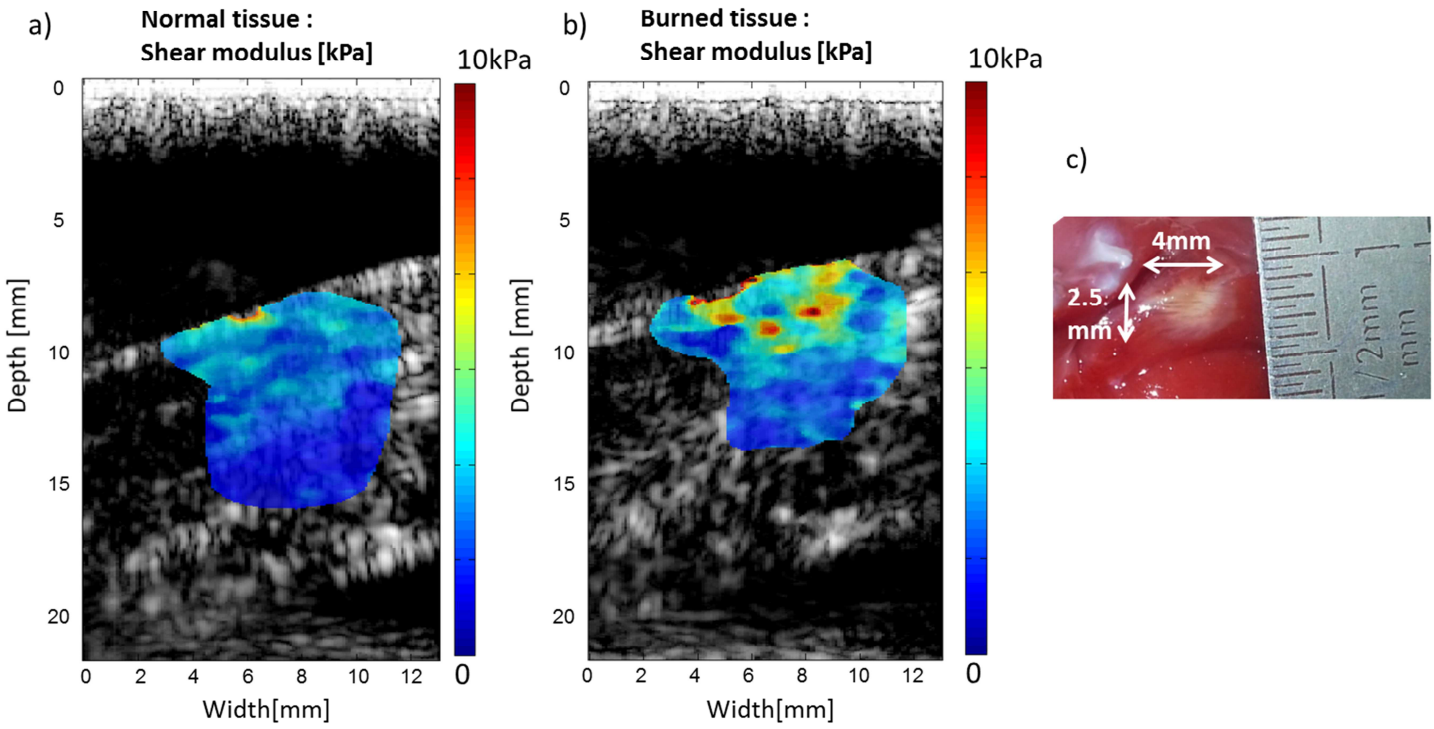

Figure 4-12 : Example of a SWE HIFU evaluation in the interventricular septum. The shear modulus increased from 2.2±0.3kPa before ablation (a) to 5.7±1.2kPa after ablation, in the center of the lesion (b). The dimensions of the lesion on gross pathology photograph (c) were in good agreement with the stiffness map.

Figure 4-13 represents an example of ablation evaluation obtained in the RV free wall. HIFU therapy has been targeted following a column shape in the center of the image (Figure 4-13a). A same stiffening shape can be observed on the SWE after ablation, with a shear modulus increase from 2.9±0.8kPa to 8.5±1.7kPa.

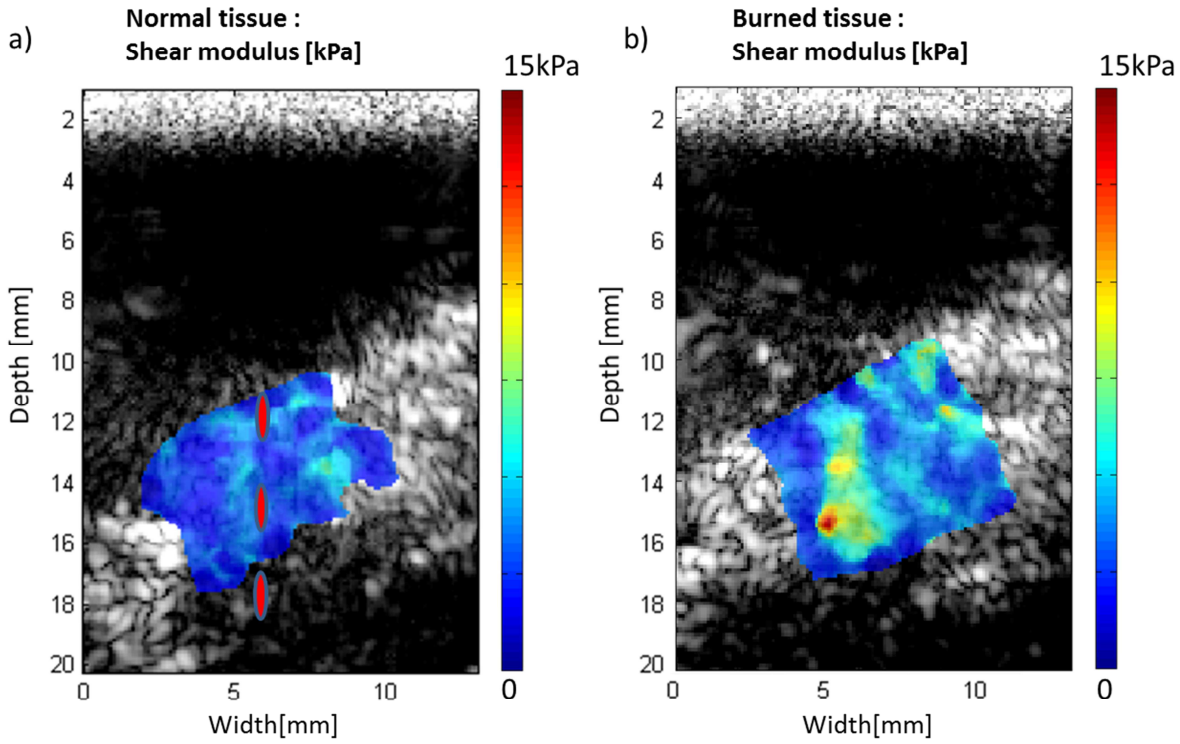

Figure 4-13 : Example of a SWE stiffness mapping in the right ventricle before and after HIFU ablation. (a) The tissue was targeted following a column pattern. The mean shear modulus before ablation was 2.9±0.8kPa in the central zone. (b) After ablation the map exhibited a stiff region of the same pattern as the ablation, with a mean shear modulus of 8.5±1.7kPa in its center.

In total three atrial lesions (n = 3) have been evaluated with SWE, two in the right ventricle (n = 2) and one in the IVS (n = 1). The mean shear modulus within atrial tissue increased from 4.3±0.4kPa before ablation to 14.0±4.4kPa after ablation and within ventricular tissues (RV and IVS) from 2.6±0.4kPa to 8.1±2.2kPa, for final mean stiffness (shear modulus) ratios before-after ablation of 3.3±0.8 in the atria and of 3.1±0.7 in the ventricles.

4 Discussion

In this second part of the validation of a dual-mode intracardiac transducer, we tested and successfully validated the in-vivo feasibility of performing both HIFU therapy and its evaluation with real-time Bmode and Shear-Wave Elastography (SWE). In total twelve (n = 12) successful ablations have been performed in the right atria (n = 5), in the right ventricular (RV) free wall (n = 3) and the interventricular septum (IVS) (n = 4), in four (N = 4) sheep.

Among them three (n = 3) atrial, two (n = 2) RV and one (n = 1) IVS were evaluated with SWE by using the same catheter.

Such a dual-mode intracardiac device presents many advantages. Motivated first by a need for intracardiac thermal ablation control and evaluation, second by a lack of performant therapy devices for ventricular ablation, this system has the potential to address both issues. The problem of therapy and imaging alignment, raised in the previous chapter, is completely resolved, as the same transducer is used for both. The advantages of SWE over B-mode imaging have already been discussed in the 2nd and 3rd Chapters and were confirmed once again in this study: while all ablations were monitored with real-time B-mode, only 1 lesion has been identified with this technique. In contrast all atrial lesions monitored with SWE have been clearly distinguished.

HIFU therapy, as well, presents majors advantages over RFCA. It is a non-contact therapy meaning that the exact position and distance relative to the tissue are not critical, whereas it is an important issue for RF based ablation [251]. Moreover, thanks to the multi-element architecture of the device, HIFU therapy can be very flexible and large zones can be targeted without moving the transducer: in this study lesions up to 10mm wide and 4mm deep have been created, without intervention, in the atria and the ventricles. Preliminary results have shown that it could be possible to target separate layers in the cardiac tissues (endocardium, myocardium, epicardium), as epicardium-only lesions have already been achieved. This is an important requirement for ventricular ablation where scared tissues can artificially create electrical reentry loops and where the ablation need is very local[8]. Finally the novelties of this device are its therapeutic and imaging modalities; while this system is directly adapted from a clinically used imaging array and such ultrasonic transducers are routinely used during atrial fibrillation ablation[9, 23]. This suggests that the implementation of this apparatus could, in fine, be straightforward as the methodologies would remain similar. As the imaging and therapeutic possibilities of this dual-mode catheter are potentially multiple, the device could be either used as an only imaging or therapy system or as an all-in support for RFCA for example in atrial ablation.

However, several limitations of this study have to be addressed. Lesions' depths obtained with the device (4mm in maximum) were not bigger than the best performances that are reported for RFCA: because of its little aperture (13.2*2mm^2 of active surface) the device is still limited in power. Maximal emission intensities applied in study were approaching

21W/cm^2 corresponding to an acoustical power of 5.5W at the transducer's surface. This was sufficient for atrial ablation, but for ventricles a gain could be necessary. Moreover treatment times were also longer than for RFCA. Typically a circular 5mm*5mm transmural atrial lesion can be created within 1min with RFCA, whereas in this study we performed atrial HIFU ablation in average with four 2min-focuses (for final transmural lesions of 7.5mm*5mm in average). Still, there is much space to improve those performances. First, the cardiac wall movement was not addressed during ablation: HIFU focuses remained fixed during the 2 and 4min sequences of ablation. At first glance, as the focal spot is small (an ellipse of approx. 0.2*1mm in the focal plane when focusing at 10mm), in the atria this wall movement may enhance a larger heating and finally ablation, because the movement amplitude and also the tissue perfusion are not important. In contrast, in most ventricular walls the perfusion and wall movement may be too important to make this phenomenon beneficial, thus a tracking of the wall could be profitable. Second, the therapy sequence composed of 500ms of emission, followed by 500ms may not be optimal in-vivo. During the procedures, we could observe that differences on the cooling of the catheter, with the blood flow, were important depending the location of the catheter. A threshold of +12°C on catheter's the temperature rise was fixed as an emergency stop during ablation and the intensity was adjusted at each location to maximize the output without exceeding this temperature. Nevertheless we did not study whether it would be more profitable to lower the output and lower the pause or increase the power and the pause. Finally the advantage of our system is that it was using only natural blood flow to cool down, but it could be possible, to bring additional cooling e.g. by the guiding sheath (it was successfully tested in vitro).

In this study we performed SWE only before and after ablation, yet the pauses within the therapy sequences could be used to perform imaging and finally achieve a real-time monitoring of the therapy. The imaging itself is limited: only linear and no sector-based imaging is possible with this array. This directivity of the elements, however, is beneficial for therapy as it allows to maximize the energy, locally, in front of the transducer.

Finally we did not investigate any possible injuries outside the heart, after excision. As it was introduced in this chapter, atrio-esophageal fistulas were the reason of failure of a very promising previous HIFU system, however here the ablation could be in fine very well controlled. The focal spots are thinner, they can be flexibly positioned and, above all, all the therapy is controlled with imaging.

An important perspective for this work is to directly investigate the electrical effects of the ablation on the cardiac tissue and to validate a local electrical isolation. This is the next step of the study, still, we know that the tissues identified as lesions on gross pathology were viably dead as a well-recognized tissue marker was used. The HIFU ablation itself is thermally induced, in the same way as RFCA. During our procedures no navigation system was used, it would be important in the future to implement necessary markers to be able to locate precisely our system in the heart.

5 Conclusion

In this study we developed a novel intracardiac all-ultrasound system capable to perform both therapy and imaging by using the same aperture. The device is a direct adaptation of an imaging catheter and the resulting multi-element array allows a flexible HIFU therapy coupled with a high-quality imaging which are perfectly aligned. In-vivo many types of cardiac tissues (atrial, ventricular) have been successfully ablated and controlled with SWE and real-time B-mode imaging.

This theranostic system presents many potential advantages over RFCA for therapy in atria but also in the ventricles where RFCA and other contact-based therapeutic modalities are limited. By implementing novel ultrasound imaging modalities it could become a powerful tool for cardiac arrhythmias treatment. Finally, as the same type of instruments is already in clinical routine usage, the implementation and acceptance of this device could be done without consequent efforts.

In the next chapter an alternative approach for all-ultrasound cardiac arrhythmias treatment is proposed: a transesophageal ultrasound-guided HIFU probe. This next system is based on the same observation that a viable lesion control coupled with flexible therapy is needed for the heart.

Chapter 5. Transesophageal shear-wave elastography monitoring

1 Introduction

1.1 Transesophageal ultrasound-guided-HIFU device

In this chapter we propose a second approach based on transesophageal ultrasound. This work was motivated by the therapeutic transesophageal approach developed at LabTau Inserm U1032 by Cyril Lafon, Jean-Yves Chapelon, Elodie Constanciel, and William Apoutou N'djin in collaboration with cardiologists from Lyon Hospital. It consists of a single transesophageal imaging-therapy device recently developed by Constanciel et al. [89, 91]. In this device, a conventional transesophageal imaging transducer was embedded inside a HIFU transducer. The position of the HIFU beam can be electronically adjusted, and anatomical guidance is done under real-time transesophageal echocardiography (TEE).

As in systems presented in the previous chapters, the therapeutic procedure requires an accurate guidance system of the HIFU beam as well as an imaging modality to control the creation of thermal lesion at the targeted tissue. In the context of transesophageal therapy Magnetic Resonance Imaging (MRI) has been proposed [90] but is costly, requires specific MR compatible ultrasound transducers for per procedural analysis, and suffers from a low imaging frame rate which is an important issue in this precise cardiac application.

Ultrasound imaging has also been proposed for providing treatment guidance and lesion monitoring in real time. Indeed TEE is widely used in clinical practice and can be integrated relatively easily in the same probe. TEE is commonly used before RFCA procedures or cardioversion to detect endocardial thrombi [9, 252]. It is sometimes used for catheter ablation guidance[253, 254] or more generally for guiding interventional cardiac procedures [252, 255]. However, the monitoring and assessment of HIFU treatment remains limited with TEE, because thermal lesions do not appear with sufficiently high contrast on conventional B-mode images.

1.2 Transesophageal Shear-Wave Elastography

In this study, we propose the use of TEE shear-wave elastography (SWE) to assess quantitatively the HIFU ablation procedure. The evaluation of tissue stiffness with this technique in cardiac and non-cardiac organs has already been widely discussed in the previous chapters including skeletal muscle [177], liver[201] (see Chapter 2) or the myocardium[249] (see Chapter 3 & 4). Despite a large interest of imaging cardiac elasticity, SWE has not been implemented yet in the context of transesophagial echocardiography. This implementation is not straightforward as TEE probes are characterized by small apertures while requiring a large field of view (FOV). Moreover, SWE assessment of ablated cardiac tissues has not been reported in the literature to our knowledge using HIFU treatment. The objectives of this study are twofold: first to show in vivo that cardiac SWE can be performed with a TEE probe in order to provide a map of myocardial stiffness in a beating heart. Second, to show the feasibility of TEE-SWE to map HIFU-induced lesions in vitro with the ultrasound-guided HIFU (USgHIFU) probe[89, 91]. These two steps are required before this technique can be used in vivo to generate and image thermal lesions using a single imaging-therapy transesophageal ultrasound endoscope.

2 In-vitro and in-vivo SWE

2.1 Materials and methods

2.1.1 Transesophageal ultrasound-guided HIFU probe

An imaging-therapy endoscope designed for transesophageal USgHIFU ablation has been used in this study (Vermon, Tours, France). The active part of the system was made of a 3-MHz HIFU transducer with a 5-MHz TEE imaging transducer embedded at its center. The HIFU transducer is geometrically focused at 40mm and is composed of 8 isosurface concentric rings, which allow the focal depth to be varied between 15 to 55 mm by dynamic focusing. The active surface (Figure 5-1a) is a portion of a sphere, 30 mm in diameter, truncated at 14 mm along the axis of endoscope (18 mm in diameter) and has a total active area of 3cm2. It presents a circular opening (12mm diameter) in its center for the TEE imaging probe. The prototype was mounted on a flexible and steerable medical endoscope and capable of delivering 10W/cm2 for 15s or 15W/cm2 for 3s.

The HIFU transducer was driven by a multi-channel amplifier (Image Guided Therapy, Pessac, France), which could generate up to 20 W per channel.

The TEE imaging probe at first independent, then embedded in the USgHIFU endoscope, is a circular 1D phased array composed of 64 elements (PA5.0/64, 5MHz, 0.15mm pitch, Vermon, Tours, France). It is designed for conventional TEE echocardiography but for that purpose, the transducer is usually mounted on a rotary motor.

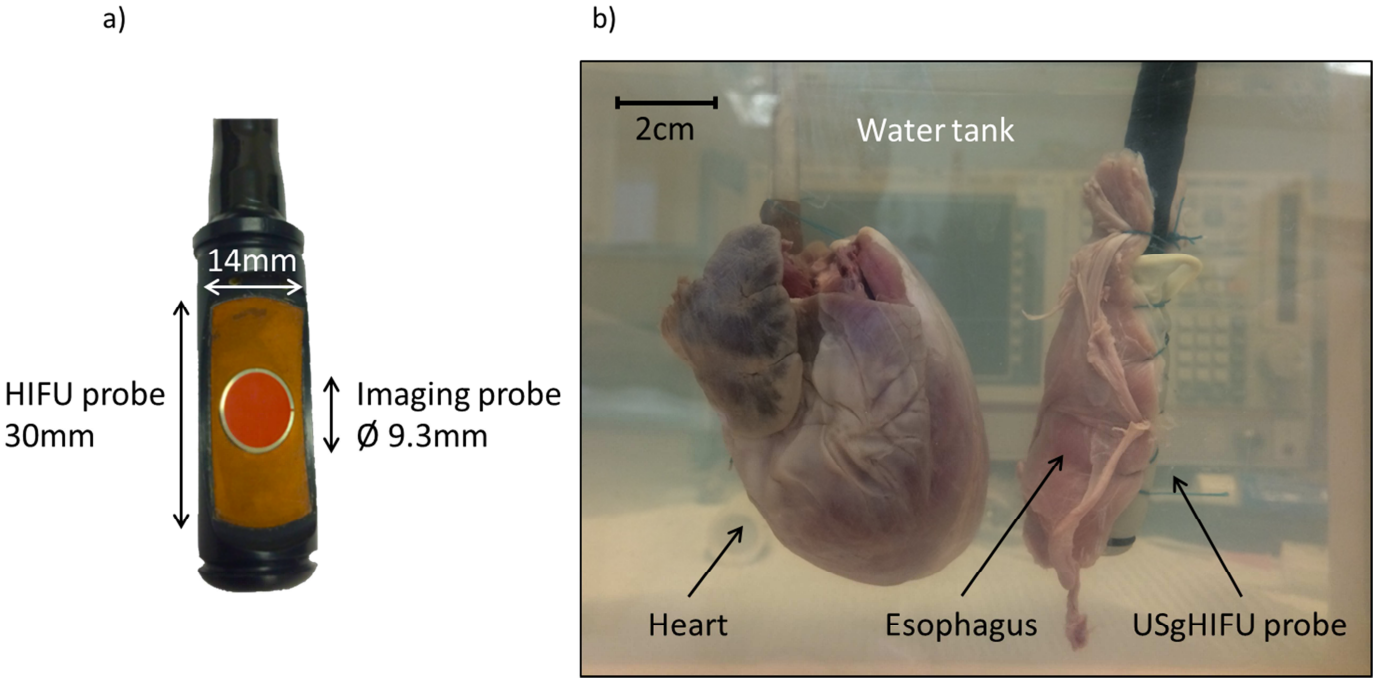

Figure 5-1: (a) Physical configuration of the transesophageal USgHIFU device. The imaging probe (red) is inserted at the center of the truncated hemispherical HIFU transducer (orange). The whole system is mounted on a steerable endoscope. (b) In vitro experimental setup. A balloon, containing circulating cooling water, covers the device. An esophagus is attached around the balloon. The device aims a porcine heart positioned at distance of 2 to 3cm from it. The setup is immobile and put in a thermostatic 37°C saline tank.

2.1.2 Diverging-waves Shear-Wave Elastography

In this study, an ultrafast ultrasound scanner (Aixplorer®, SuperSonic Imagine, France) was used to perform SWE sequences with the TEE imaging probe, mounted in the center of the HIFU transducer. The sequences consisted in a radiation "push" ,i.e., the ultrasound focused emission used to generate a shear-wave defined by its duration and frequency (400 µs at 4MHz), followed by an ultrafast divergent waves [108] imaging sequence. The push parameters resulted in a peak positive pressure of 6.3MPa (measured in water) and peak negative of -4MPa which corresponds to a derated pressure of -1.6MPa with a

Mechanical Index of 0.8. Ultrafast imaging was performed using either two divergent waves emissions (represented by virtual sources placed at [-1.2;1.2] mm laterally and 8mm axially) or three divergent waves emissions (represented by virtual sources placed at [-0.725; 0; 0.725] mm laterally and 3.9mm axially) at 5 MHz. Coherent compounding of the diverging waves emissions was applied as explained in [108] , in order to restore a synthetic focus in transmit. In receive a conventional dynamic beamforming algorithm implemented on GPU (cuda, nvidia geforce K5000) was used to compute the stack of ultrafast imaging acquisition. 35 compounded images were obtained. A Butterworth temporal low-pass filter (cut-off frequency: 800Hz) was applied to each pixel to remove high frequency noise and a directional filter [250] was used to remove regressive shear-waves and improve the Signal-to-Noise Ratio (SNR). For each frame the spatial mean tissue velocity was also removed. The resulting imaging frame rate depended on the imaging depth – one compressional wave transmit and return time, and on the number of compounded divergent waves [108]. From 5 to 7 push and imaging sequences were used in order to increase the field of view and the SNR of the shear modulus maps [112], for a maximal total acquisition duration of 43ms. A time-of-flight algorithm [113] was used to track the shear-wave group velocity c_t and the shear modulus map was obtained from (1.1) for each acquisition. Corresponding quality maps were obtained from the algorithm's temporal 1-D cross-correlation. The final 'stiffness map' was obtained with a quality weighted average (least-squares mean) of all 5 to 7 acquisitions. A spatial median filter (in vivo: $1*1mm^2$; in vitro: $2.5*2.5mm^2$) was applied on the final maps.

The time-of-flight algorithm estimates the shear-wave group velocity locally. It is based on a sliding window estimator for each pixel within a lateral line. In our study all imaging acquisitions were laterally resolved at 120µm; the velocity was averaged on 2mm of distance. Those values do not give but are related to the lateral resolution [210].

2.1.3 In-vivo experimental setup

This study was conducted with the approval of the Animal Care and Use Committee of the Hopital Européen Georges Pompidou (PARCC) according to the European Commission guiding principles (2010/63/EU). One sheep of 45kg was anesthetized with thiopentothal (0.5 ml/kg), intubated and ventilated at 15 ml/kg with 2% isofluorane and oxygen. A sternotomy was performed and the thorax was filled with saline water. The TEE probe was placed in the thorax in front of the heart walls including the left and right ventricular free walls, and the left

and right atrial walls at a distance of 10 to 30 mm using the real-time Bmode guidance. After the procedure the animal was euthanized.

In order to investigate the feasibility of in vivo cardiac SWE with a TEE probe, two types of sequences have been performed.

First, the time variation of stiffness during the cardiac cycle was measured in the left atrium and in the right and left ventricles. Ten single-push 10-ms-long SWE sequences were performed in the myocardium at a rate of every 50ms, covering a whole cardiac cycle. Each push was centered laterally. The tissue velocity of each acquisition was averaged along 5mm in tissue's depth providing two-dimensional spatiotemporal representations of the shear-wave propagation[206, 249]. The positions of the maxima of the waveform were fitted (least-squares linear regression) as a function of time to eventually obtain one shear-wave speed and shear modulus value per push.

Second, stiffness maps were performed in the atrium, in the ventricular free walls and in the septum at end-diastole. Pushes were generated at a fixed depth between 20 and 30mm depending on the wall. The ventricular septum was imaged across the right or left ventricular wall with pushes generated up to 45mm in depth. Ultrafast imaging depth was fixed at 50mm in average, which resulted in a PRF of 9.8 kHz and a final frame rate of 4900 images/s after compounding (2 virtual sources).

All acquisitions were performed within a single cardiac cycle.

2.1.4 Ex-vivo experimental setup

Shear-Wave Elastography and HIFU were performed *in-vitro* on chicken breast samples (n=3) and on two (n=2) entire ex-vivo porcine hearts for a total of seven (n=7) thermal lesions. The samples were fixed on a plastic stem and immerged in a degassed and thermostatic (37°C) water tank. In chicken breast large lesions were created by rotating the probe, in heart samples by varying the focusing depth of the HIFU beam such as the probe was immobile during the whole procedure. The whole HIFU/imaging prototype was cooled with 15°C water that was circulating inside a latex transducer cover fixed at the two extremities of the transducer.

For the heart samples, several tissues were targeted including the right ventricle, the left atrium, and the left auricle. Finally, an ex vivo esophagus was inserted around the transducers and a lesion was performed in the left ventricle with ablation and imaging performed through the esophagus (Figure 5-1b).

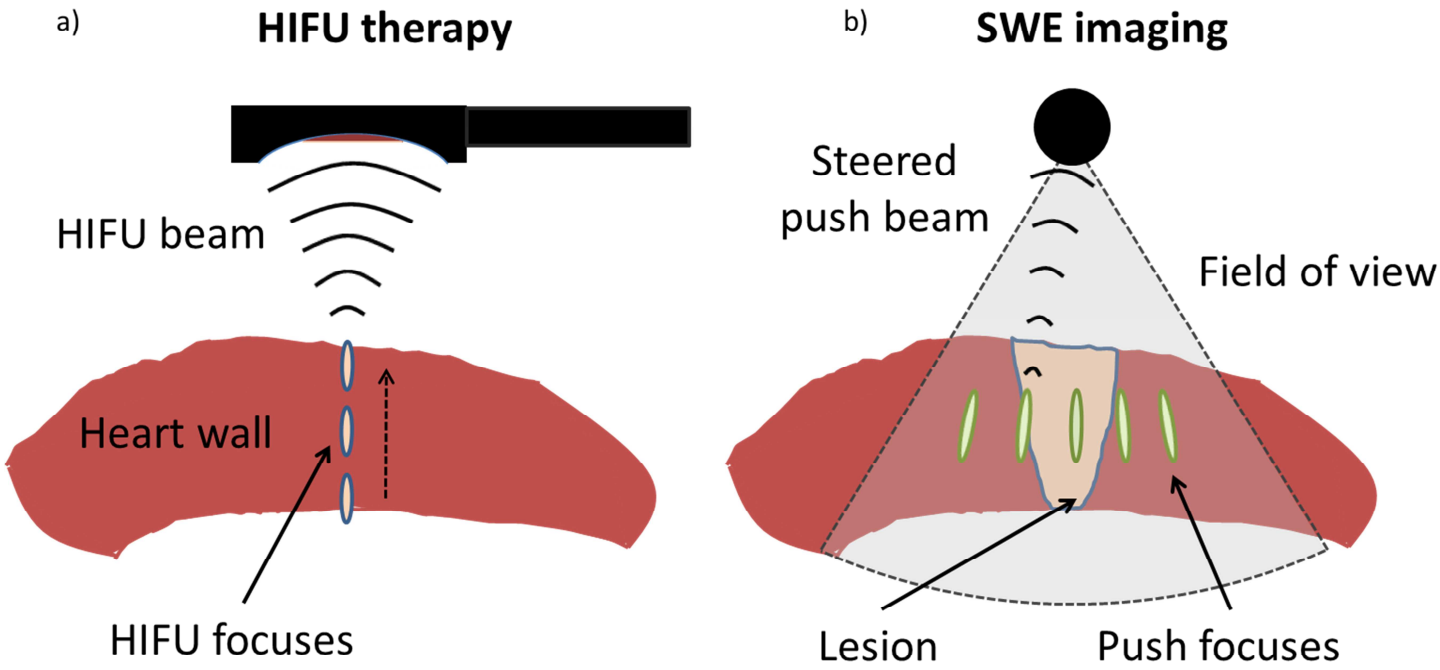

Figure 5-2 : Schematic representation of the in-vitro therapy-imaging configuration. For the heart samples the probe was not moved during the whole procedure. (a) HIFU therapy is performed through the entire wall depth using the electronic steering along the central axis of the probe. (b) SWE imaging is realized before and after ablation. Five to seven laterally steered pushes (focusing using the imaging probe) are performed to cover the whole field of view of the probe with shear-waves, of which propagation is acquired with diverging-waves ultrafast imaging.

Imaging

Figure 5-2 represents a schematic view of the therapy-imaging sequences performed in-vitro. The HIFU prototype was placed approximately 25 mm away from the sample's surface (Figure 5-2a). A B-mode image was acquired and then SWE was performed – pushes were generated at an average depth of 30 mm (Figure 5-2b). In chicken breast, imaging depth was fixed at 50 mm which resulted in a PRF of 9.8 kHz and a final frame rate of 3300 images/s after compounding (3 virtual sources). In the heart, imaging depth was fixed at 40 mm which resulted in a PRF of 12.3 kHz and a final frame rate of 6200 images/s after compounding (2 virtual sources). The total processing time, including image beamforming and tissue velocity estimation was less than 1 minute.

Therapy

In chicken breast HIFU ablation was performed using the prototype's geometric focusing (40mm). One HIFU sequence consisted of 25 single exposures (4s on /6s off), with an emission acoustic intensity of 9W/cm^2. Two to three sequences were performed per sample, for each of which, the probe was rotated by -2° or 2° relatively to the initial position and parallel to the imaging plane.

In the heart HIFU ablation was performed without moving the prototype. Several HIFU sequences were performed, each at different depth by electronically moving the focal spot – typically from 35 to 25 mm with steps of 2mm. One HIFU sequence consisted of 2 single exposures (15s on /10s off), with an emission acoustic intensity of 11W/cm^2.

Final B-mode images were taken and the same SWE mapping was performed after HIFU ablation.

Gross pathology

At the end of the experiments a gross pathology study was performed. More precisely, the samples were cut along the imaging plane of the ultrasound transducer, under control of the B-mode imaging, removed from water and photographed.

Segmentation

The dimension of SWE lesions were compared to the gross pathology. More specifically, depth and width of the lesions were compared between lesion-segmented images obtained for both techniques. Lesion's boundaries were discriminated on the gross pathology photographs by identifying the variation in tissue color using a k-means clustering algorithm [180], by discriminating viable tissue (red) from ablated (white).

Because the initial stiffness varies significantly across the different tissues and samples, we chose to set arbitrarily a threshold of relative stiffness increase to discriminate the ablated and normal tissue. A ratio of 1.7 was set based on previous results obtained by Sapin-de Brosses *et al.*[176] and Mariani *et al.*[201] which showed that the mean shear modulus increase was approximately twofold. The biggest and central discriminated region was identified as the lesion. Then the images underwent morphological opening by a 1mm-

diameter disk, to smooth the obtained boundaries. Depth and width of the lesions were finally calculated with the extreme longitudinal and lateral boundaries of the remaining zone.

2.2 Results

2.2.1 In-vivo

Myocardial stiffness and its temporal variation over one cardiac cycle were obtained in the atrial and the ventricular walls. In the right atrium stiffness was found to vary from 0.5±0.1kPa to 6.0±0.3kPa during the cardiac cycle. Right ventricular stiffness ranged from 1.3±0.3kPa in diastole to 13.5±9.1kPa in systole, whereas left ventricular stiffness varied between 1.3±0.2kPa and 12.5±5.1kPa. Figure 5-3 represents two examples of variations of the shear modulus, (a) in the right atrium, (b) in a left ventricle. The shape of the atrial stiffness' variation (a) is in accordance with the one already observed by our group [249] : the shear modulus increases at the atrial systole (P-wave) and during the atrial blood filling (from the end of the QRS complex to the T-wave till the opening of the tricuspid valve). In contrast, ventricular stiffness' variation is shown in Figure 5-3b. A strong increase of stiffness is found in systole (from the QRS complex to the T-wave) followed by a softening in diastole (from the T-wave to the QRS complex).

Secondly, myocardial stiffness was mapped at end-diastole in atrial and ventricular walls. Figure 5-4 presents examples of shear modulus map acquired in (a) the right atrium, (b) right ventricle and (c) interventricular septum (acquired through the right ventricular wall). In the right atrium (a) the mean shear modulus within the sample is 1.3±0.3kPa; in the right ventricle (b) 1.7±0.5kPa; in the interventricular septum (c) 1.9±0.6kPa. Over the ventricular stiffness' maps, performed between the P-wave and the beginning of the QRS complex, the average shear modulus was: 1.8±0.2kPa (right ventricle), 2.3±0.4kPa (left ventricle), 1.8±0.2kPa (interventricular septum).

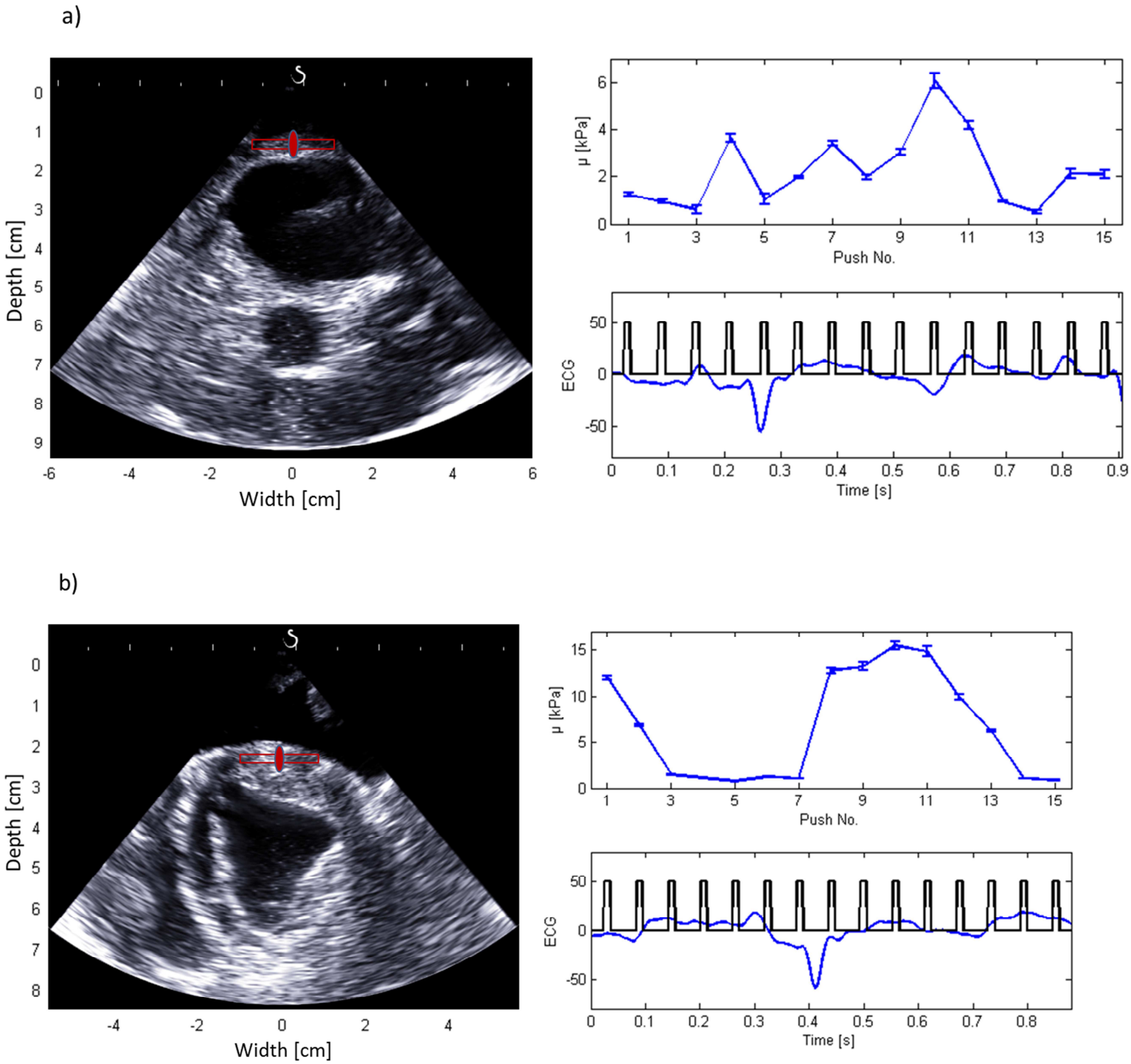

Figure 5-3 : Time variation of stiffness in a (a) right atrium and (b) left ventricle free wall. On each tissue 15 acquisitions were performed, at a rate of every 50ms, corresponding to ten acquisitions per heart cycle. Positions of pushes are represented on corresponding Bmode images (left) with the areas where the shear-wave propagation was considered. The obtained shear modulus values (right up) are represented for each acquisition with the corresponding ECG signal (right down). Error bars correspond to the standard error obtained for each shear modulus value, when operating the linear regression on the shear-wave's slope position. (a) The shear modulus varied in the right atrium from 0.5±0.1kPa to 6.0±0.3kPa with a mean value of 2.5±1.7kPa. The peak at push no.4 corresponds to the atrial systole, at push no.10 to the end of atrial blood filling followed by the opening of the tricuspid valve and atrial emptying. (b) In the left ventricle the shear modulus varied from 0.8±0.1kPa to 15.5±0.4kPa

for a mean value of 7.4±6.3kPa. The important increase in stiffness corresponds to the ventricular systole.

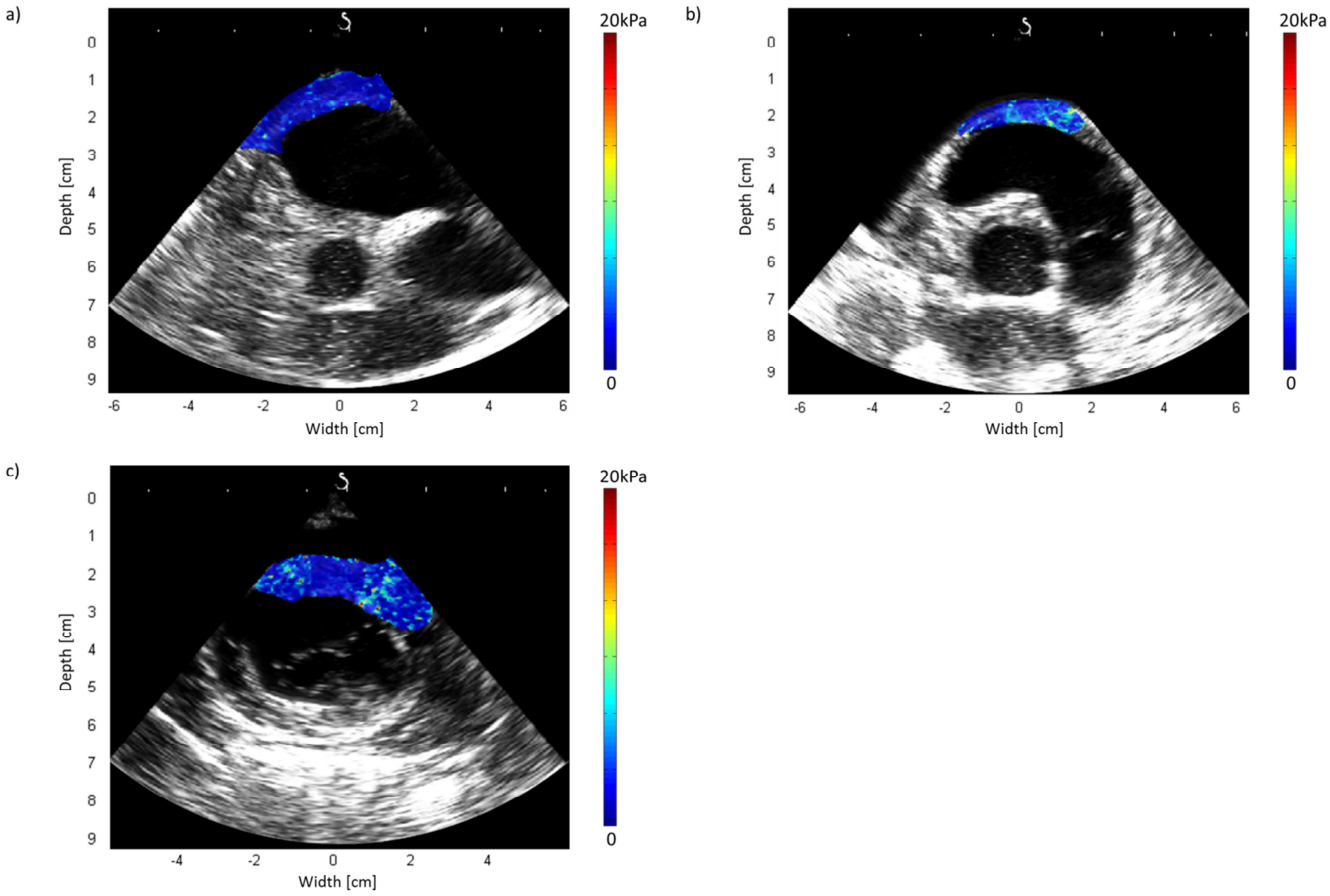

Figure 5-4 : Shear modulus maps of a (a) right atrium, (b) right ventricle free wall and (c) the interventricular septum, superimposed on Bmode images. The mean shear modulus within: (a) the atrial wall, acquired 50ms before the P-wave (atrial systole), is 1.3±0.3kPa; (b) the right ventricle, acquired between the P-wave and the beginning of the QRS complex (ventricular diastole), is 1.7±0.5kPa; (c) the interventricular septum, acquired between the P-wave and QRS complex (ventricular diastole), is 1.9±0.6kPa.

2.2.2 Stiffness mapping of ablated tissues

Figure 5-5 shows the maps of the shear modulus in three different tissues (respectively chicken breast, left ventricle and left atrium before and after HIFU ablation, as well as the corresponding gross pathology pictures. On Figure 5-5a stiffness appears to be relatively homogeneous over the sample, with a mean shear modulus μ of 4.8±1.1 kPa in the central zone, before ablation. In contrast, a stiff region associated to the ablated tissue, is visible after treatment, with an average μ of 20.5±10.0 kPa (corresponding to a ratio of the shear modulus before/after ablation of 5.0±3.2) in the same central zone. Figure 5-5b shows the stiffening of a left ventricular wall when both ablation and SWE were performed through the wall of an

esophagus. The ablated zone appears as a hyperechogenic region at an approximate depth of 1cm in the tissue. No imaging parameters were changed for this acquisition. The mean stiffness increased from 21.2±3.3kPa to 73.8±13.9kPa in the central region of the tissue (ratio of 3.7±1.2). In contrast, on B-mode images, no clear echogenic borders were visible after ablation. The little left atrial lesion on Figure 5-5c appears as highly contrasted; it increases from a mean value of 12.2±4.3 kPa to 30.3±10.3 in the center of the lesion (ratio of 3.2±2.0).

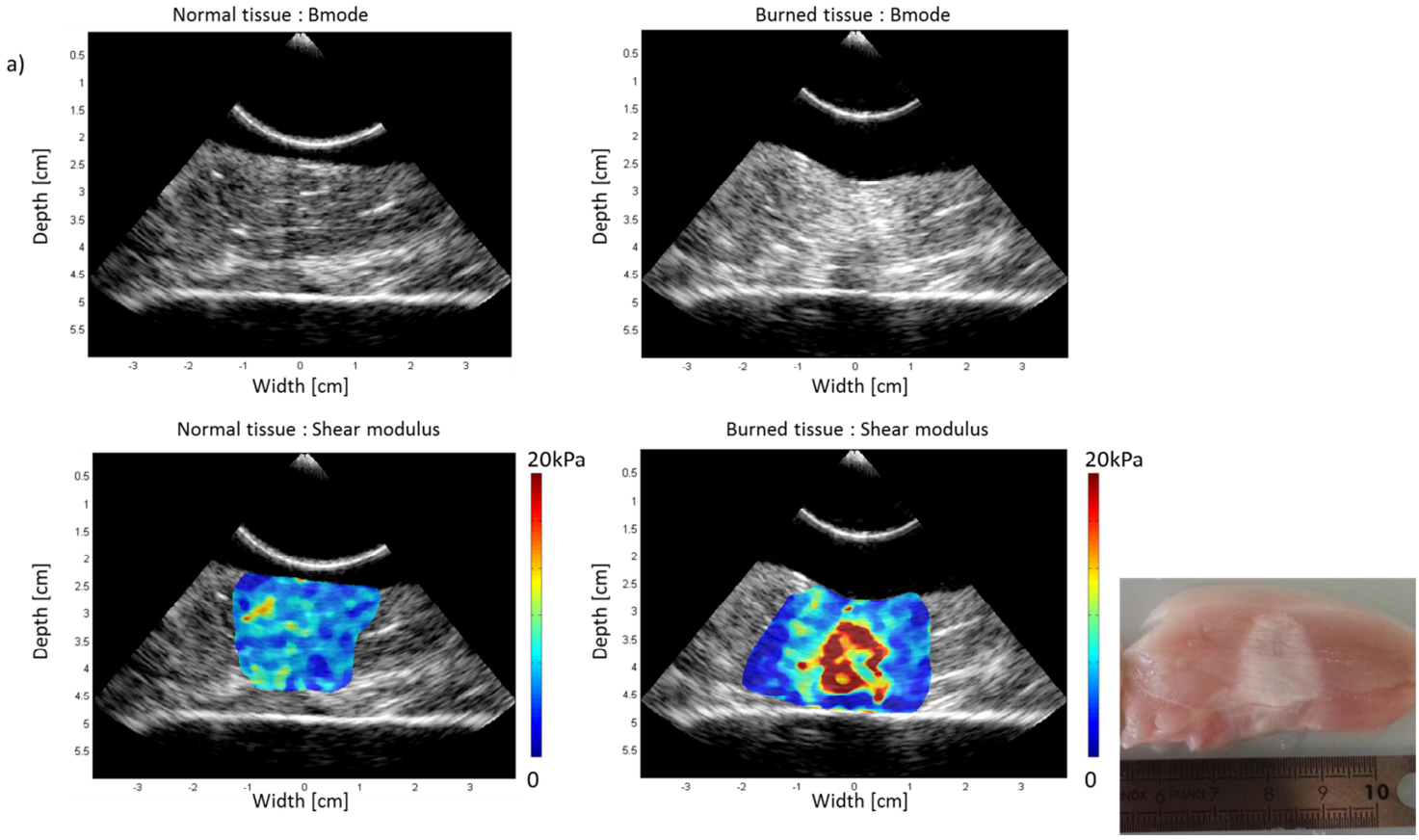

b)

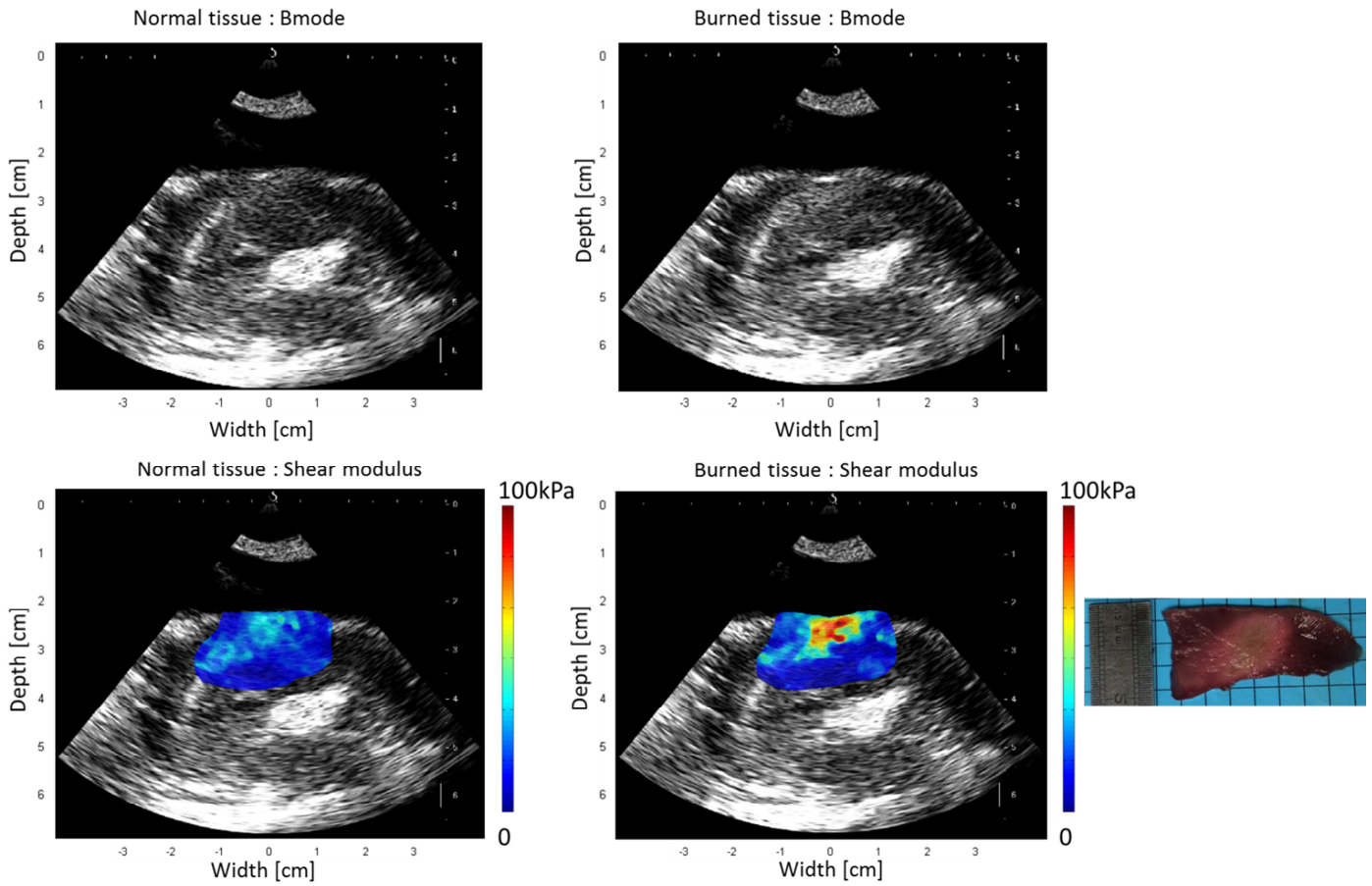
Normal tissue : Bmode
Burned tissue : Bmode
Depth [cm]
Width [cm]
Normal tissue : Shear modulus
Burned tissue : Shear modulus
100kPa
0

c)

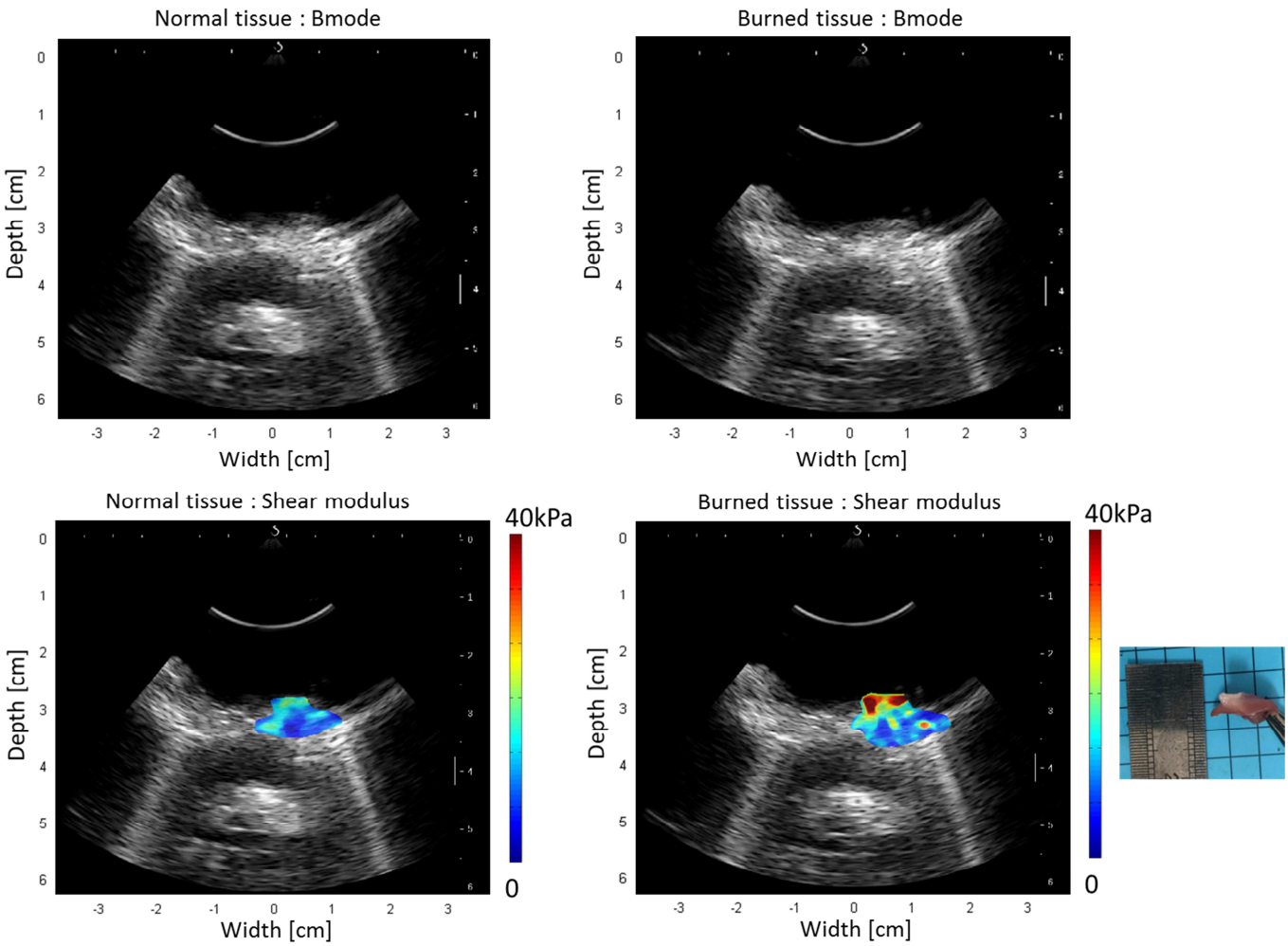

Figure 5-5 : Shear modulus maps in normal (down left), ablated (down middle) in vitro tissues, with corresponding Bmode images before and after ablation (respectively up left and up right) and a photography of the gross pathology section (down right). The mean shear modulus increased from 4.8±1.1 kPa before ablation to 20.5±10.0 kPa in the central-8mm-diamater zone of the chicken breast tissue (a), from 21.2±3.3kPa to 73.8±13.9kPa in the central-8mm-diameter zone of the left ventricle with SWE and HIFU performed through an esophagus (b), from 12.2±4.3 kPa to 30.3±10.3 in the central-5mm-diameter zone of the right atrium (c).

In total 7 HIFU ablations were performed and mapped with SWE. The presence of a lesion was clearly seen on all stiffness maps. Table 5-1 summarizes the treatment procedures and the mean shear moduli found for all samples before and after ablation. The mean stiffness ratios pre and post treatment calculated in an 8mm-diameter area in chicken breast and ventricles and in a 5mm-diameter in atria were respectively approximately 3.8, 3.0 and 2.2.

Table 5-1: Summary of all SWE and HIFU procedures

	Therapy					SWE				Gross pathology	
Samples	Emission Intensity [W/cm²]	Depth [mm] (Max:step:min)	Probe rotation (°) (Min:step:Max)	Duration [s] per position	Esophagus ?	μ Before [kPa]	μ After (kPa)	Depth [cm]	Width [cm]	Depth [cm]	Width [cm]
Chicken 1	9	40	-2:2:2	25*4	no	4.8±1.1	20.5±10.0	1.45	1.74	1.72	1.57
Chicken 2	9	40	-2:2:2	25*4	no	5.7±1.3	18.4±7.3	1.29	1.17	1.52	1.53
Chicken 3	9	40	0:2:2	25*4	no	2.6±0.7	10.0±5.2	1.54	1.50	1.56	1.76
Ventricle 1	11	37:2:25	No	2*15	no	12.8±5.4	32.8±7.6	0.88	1.20	0.64	0.64
Ventricle 2	11	40:2:25	No	4*15	yes	21.2±3.3	73.8±13.9	0.91	1.23	1.30	1.51
Atrium 1	11	37:2:27	No	2*15	no	12.2±4.3	30.3±10.3	0.46	0.66	0.36	0.36
Atrium 2	11	37:2:27	No	2*15	no	10.8±4.1	19.8±3.9	0.38	0.35	0.34	0.37

2.2.3 SWE agreement with gross pathology

Figure 5-6 shows (a) the segmentations performed on the gross pathology samples presented on Figure 5-5 and (b) an example of segmentation performed on a SWE stiffness map with the measurement of the lesion's dimensions.

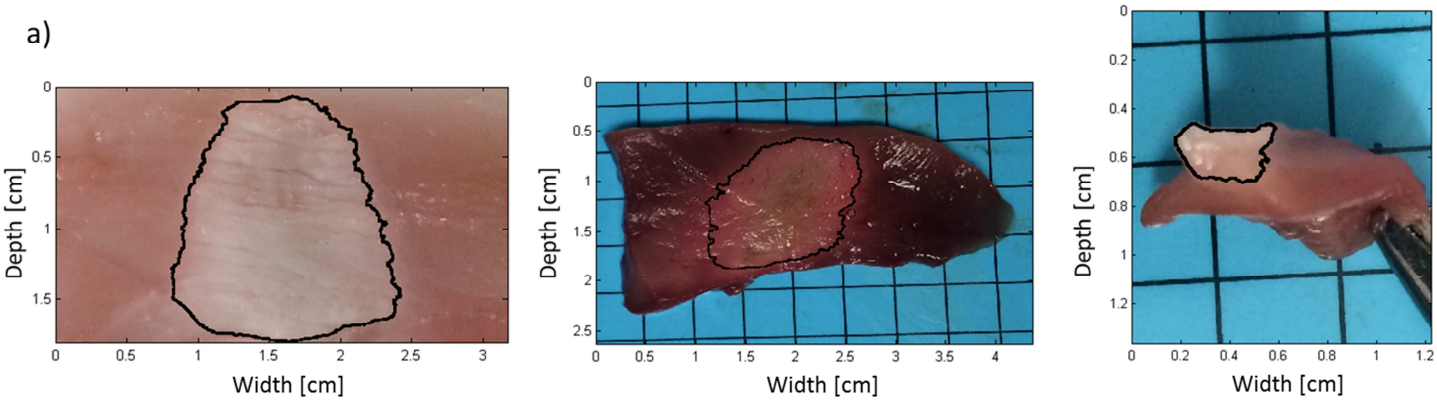

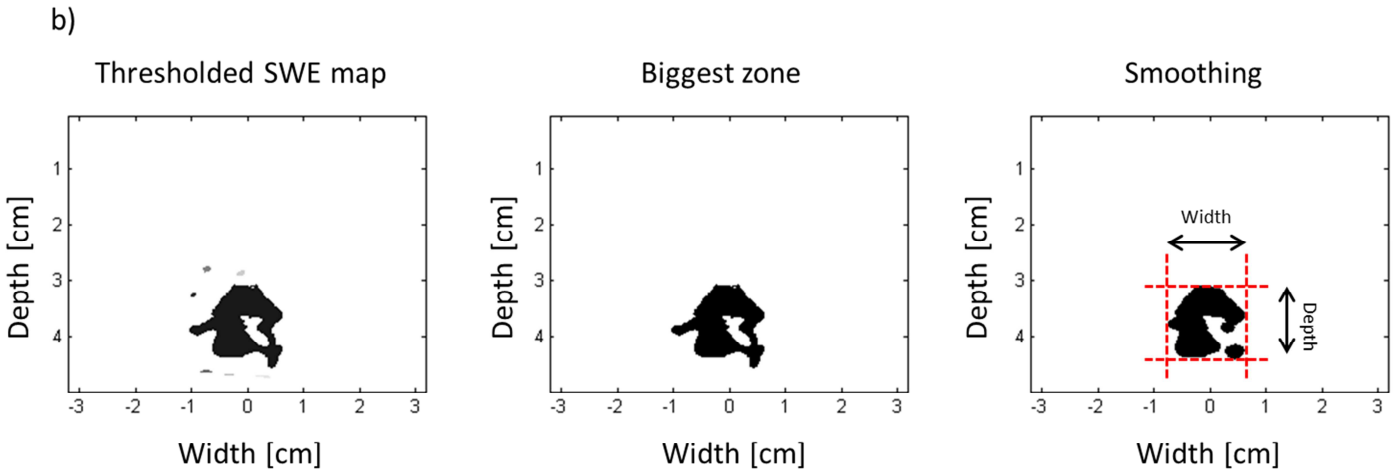

Figure 5-6 : (a) Examples of automatic segmentation on images of gross pathology sections of ablated tissues (respectively from left to right: chicken breast, porcine left ventricle, porcine right atrium). (b) Example of the automated treatment of a segmented chicken breast stiffness map after ablation. A threshold is first applied on the shear modulus map (left), the biggest surface is kept (middle), then a morphological (1mm diameter disk) opening is applied to smooth the boundaries, finally such obtained lateral and axial extremities are considered as lesion's width and depth (right).

The agreement of lesions' depths and widths determined with gross pathology and SWE is represented on Figure 5-7. The median difference between both techniques found in depth was 0.2mm, with first and third quartiles ranging from -0.8 to 2.6mm. In width a median difference of 0.2mm was found with first and third quartiles ranging from -2.7 to 2.7mm for a mean depth of 10.6±6.0mm and width of 11.1±6.2mm found with gross pathology.

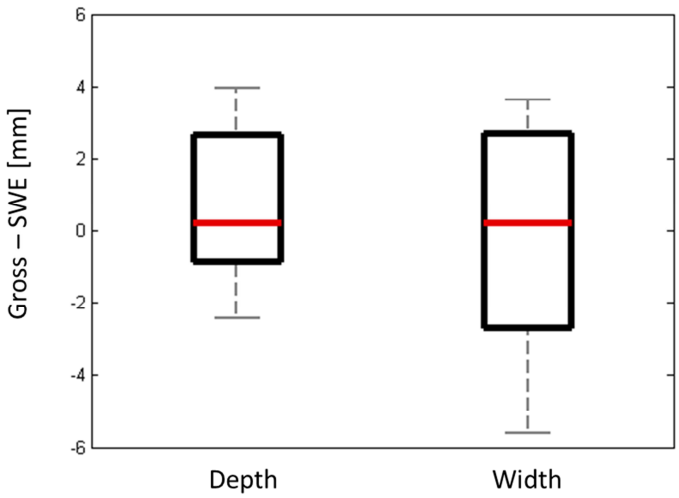

Figure 5-7 : Difference of lesions' depth and width determined with gross pathology against SWE, represented on boxplots. In depth a median difference of 0.2mm was found with first

and third quartiles ranging from -0.8 to 2.6mm. In width a median difference of 0.2mm was found with first and third quartiles ranging from -2.7 to 2.7mm.

2.3 Discussion

In this study we have investigated the feasibility of using shear wave elastography for the evaluation of HIFU induced thermal lesions in a transesophageal setup. We verified, first, the feasibility of performing cardiac SWE with a conventional imaging TEE probe in vivo, in an open chest setup. We successfully performed SWE mapping in the atrium and in the ventricles at the ventricular end-diastole. Additionally we investigated the time variation of stiffness in the atrium and in the ventricles. The measured stiffness values are in accordance with previous in vivo studies on a beating heart in open chest [206, 212], transthoracic [256] or intracardiac setup [208, 249].

Second, we combined, in a single transesophageal device, an imaging and a therapeutic transducer to perform ultrasound-guided HIFU on ex vivo cardiac and muscular tissues. We have demonstrated that shear wave elastography can map the thermal lesions with a high contrast. Whereas TEE B-mode imaging was unable to observe the thermal lesions, it appeared clearly on post-treatment shear modulus maps. Moreover, the dimensions of the lesions measured on the maps agreed well with the dimensions of the lesions observed on gross pathology. This agreement was particularly good along depth of the TEE image, in the transmural direction of the ablated wall which is a crucial aspect of an effective ablation procedure.

Despite the small dimension of the TEE imaging transducer, shear waves were generated and imaged successively at a depth up to 50 mm. Ultrafast imaging was performed over a large field of view using the emission of diverging waves at very high frame rates. To increase the imaging quality, coherent compounding of 2 to 3 diverging waves was used. Beyond the evaluation of HIFU lesions, our results suggest that TEE may be an interesting way to provide myocardial stiffness which is challenging in transthoracic imaging on some patients. To our knowledge, this study reports the first implementation of shear wave elastography on a transesophageal transducer. The absence of other studies may be justified by the difficulty to implement TEE on animal models. Indeed, quadrupeds, the most common subjects, present anatomical differences in the vicinity of the heart and esophagus with bipeds. The area between those organs is occupied by bronchi and lungs which degrade

significantly the quality of cardiac TEE imaging and compromise potential transesophageal HIFU. Thus the following step of our study would be the use of the USgHIFU transesophageal device on biped non-human subjects. It is important to note that the presence of other tissues between the probe and the studied samples was not precluding for obtaining shear modulus maps of a good quality: SWE has been successfully performed in the interventricular septum through a left or right ventricular wall in-vivo and in the left ventricle through an esophagus and the cooling balloon in-vitro.

One limitation in this study is the fact that there was no absolute threshold of stiffness for ablated tissues, within their different types (breast, atrial, ventricular muscle). This comes from the various conservation conditions of the tissues which resulted in very different initial stiffness. Moreover, in some of the samples, the measured shear velocity may not be directly linked to the shear modulus in thin tissues such as the atrial wall. In such small layers, shear waves are guided which results in dispersive propagation. As the assumption of infinite medium is not true anymore it limits the validity of the quantitative stiffness measurement. However, we showed here that the stiffness contrast on the post treatment map was high enough to delineate the lesion. Moreover, previous work indicated that the elasticity contrast changes (ie. Ratio between shear modulus during the treatment and the initial shear modulus before treatment) is a very sensitive marker for thermal necrosis independently from the initial tissue stiffness value [176]. Furthermore the precision of SWE on HIFU lesions with the TEE probe has to be further investigated, a limited number of samples are presented here, yet their variety demonstrate the flexibility of the technique. SWE determined lesions were compared to measurements operated on gross pathology sections. Those sections were realized approximately within 1mm of the ultrasonic imaging plane implying an error on the effective lesions' sizes.

Another limitation is the need to improve processing time to obtain shear modulus maps. The beamforming and stiffness map calculations were performed respectively on the scanner and a laptop using Matlab® and were performed within one minute. Nevertheless all acquisitions were performed within a single heartbeat thus SWE based on diverging waves ultrafast imaging can potentially be real-time, as it is already clinically with plane wave imaging. However this technical optimization was not the goal of the study.

As a final point, the combination of transesophageal SWE and HIFU on a same device could present some advantages over intracardiac Radio-Frequency Catheter Ablation. The

system is potentially capable of creating transmural lesions in the atria and in the ventricles [91] or possibly, by extension, select the ventricular layer (epicardium, myocardium, endocardium) to ablate. This need is encountered during ablation procedures for ventricular tachycardia and, to our knowledge, no minimally invasive technique is capable to do so [8]. The system presents an imaging transducer, perfectly aligned with the therapy probe. The lesion can be precisely imaged at its center, which is particularly important to evaluate the transmurality of the ablation. Thanks to the wide TEE beam, guidance within the heart is also facilitated and potentially no fluoroscopy would be needed for the procedure. The HIFU technique requires no contact with the targeted tissue while this is problematic with RFCA [251]. Finally as the probe is not in the vascular and particularly cardiac system, the thrombogenic risk could be significantly reduced.

On the other hand the use of a transesophageal access implies some other risks. TEE-associated morbidity is reported to be uncommon: from 0.2% to 0.5% in non-operatory and from 0.2% to 1.2% in operatory settings[257]. The anatomy of the USgHIFU device is different from a classical TEE probe thus the injury risks will have to be carefully evaluated. During therapy the HIFU probe heats (up to 65°C at its surface) but the temperature of the external balloon, containing the cooling liquid, did not exceed 37°C even with the presence of an esophagus. Finally preoperative TEE is already routinely performed before RFCA procedures (50% of a systematic usage is reported for VT RFCA [8]). To perform intraoperative TEE with transesophageal HIFU a general anesthesia would be needed, however general anesthesia is already frequently performed during RFCA (approximately 50% of the procedures [8]).

3 Conclusion

In this study we have shown the feasibility of shear-wave elastography with a transesophageal ultrasound-guided HIFU probe to map cardiac stiffness in vivo and to map thermal HIFU-induced lesions in cardiac tissues in vitro. Transesophageal SWE is a promising technique to improve the ablation control and predict thermal lesions extent. This endoscopic HIFU-SWE combination in-vivo would be the upcoming step of the study. Furthermore, beyond the main scope of this study, transesophageal SWE could be proven as a promising elastographic modality for cardiac diagnostics.

The transesophageal approach presents as a very interesting alternative to the intracardiac dual-mode system. While those systems are at an early stadium of development and some technical uncertainties have to be resolved, the main advantage of the intracardiac system may be its proximity with the tissue, resulting in fine in better imaging resolution and potentially a more localized ablation. On the other hand the transesophageal approach benefits from a large field of view and potentially a better capacity to ablate larger cardiac zones. As the intracardiac dual-mode system has already been validated in-vivo and similar therapeutic approaches have already existed in clinics, the implementation of this approach may seem more straightforward than the transesophageal one. Nevertheless more studies will have to determine whether one of these approaches could have a better clinical viability or, in contrary, whether they could become complementary.

Chapter 6. Other imaging perspectives and general conclusion

1 Other imaging perspectives: Ultrafast acoustoelectric tomography

1.1 Introduction

1.1.1 State-of-the-art and concepts

Imaging the electrical activity of the body is central to the diagnosis of and treatment planning for some of our most pressing healthcare challenges, including heart and brain diseases. However, there exists no clinical imaging modality yet in which the contrast originates directly from voltage or current. Indeed, technologies aimed at mapping the brain activity such as, e.g., functional magnetic resonance imaging [258, 259], diffuse optical imaging [260], and functional ultrasound [225] rely on slow physiological correlates such as the blood-oxygen-level dependent (BOLD) effect, blood oxygenation, or blood flow. While action potentials travel at speeds on the order of meters per second, the hemodynamic response acts as a filter that blurs electrical phenomena above the Hz range and therefore greatly limits the non-invasive study of brain activity. Physiological correlates have also been used in the heart, such as the transient mechanical response to electrical activation, i.e., the Electromechanical Wave, and recent studies suggest they can reflect in a one-to-one fashion the electrical activity[261, 262]. However, as with all physiological correlates, uncertainty arises regarding the strength of that correlation in diseased tissues [263].

In the context of RFCA for atrial and ventricular arrhythmias electrical current and action potentials imaging in the heart are performed with mono or multi electrode intracardiac systems [9]; new non-invasive systems were also implemented in clinics [20]. Despite the undeniable utility and functionality of these systems, it is not possible to map the electrical current density with spatial resolution under 5mm [264, 265], which could help to identify unablated, conducting regions or other depolarization sources participating or originating the arrhythmia.

The acoustoelectric effect [266, 267] has recently been shown to provide contrast directly from current densities by measuring ultrasound-modulated electrical impedance [268]. Multiple studies have been conducted and demonstrated the potency of the approach, e.g., by mapping the electrical activity in nerves ex vivo [269] and in the heart ex vivo [270]. More specifically, the technique consists in insonifying a tissue with a focused ultrasound beam while simultaneously measuring high-frequency differences of potentials. When the ultrasound wave reaches a region in which an electrical current flows, a high-frequency difference of potential can be detected. Proper synchronization and knowledge of the speed of sound in tissue can then be used to form image lines with lateral resolution and signal-to-noise ratios that vary with depth. Many such lines can then be obtained by moving the focal region laterally and in turn concatenated to form an image. The main limitation of such an approach is the limited signal-to-noise ratio (SNR) of the detected differences of potential. Indeed, averaging over multiple acquisitions is usually necessary. To palliate this issue, the length of the ultrasound pulse can be increased, but such an approach lowers both the axial and lateral resolutions. Finally, to achieve sufficient frame rates to track the electrical activation, low line densities are required.

1.1.2 New potential for intracardiac imaging

In this work, first, an experimental proof of concept study has been conducted in a simple setup to demonstrate the acoustoelectric interaction in ionic solutions, beginning with a single-element focalized transducer, then by focalizing ultrasound with an imaging probe. This part underlines the weaknesses of focal acoustoelectric imaging, even though a solution for signal SNR increasing is proposed.

Second, we developed Ultrafast Acoustoelectric Tomography (UAT), based on plane wave emissions. Reconstruction strategies based on the Radon transform were devised to increase the frame rate and provide uniformly high spatial and temporal resolutions while respecting FDA standards for human use. Validation in phantoms was conducted, showing the viability of the approach with a standard imaging probe.

1.2 Focused acoustoelectric imaging

In this first part the acoustoelectric (AE) effect was studied in ionic (saline) solutions, by using focalized ultrasound. The current was generated externally and injected into the

environment. Ultrasound was send through an acoustic window and the AE effect was measured with electrodes within the environment.

1.2.1 Single-element transducer

Methods

The experimental setup was composed of four parts (Figure 6-1a):

- The study environment (Figure 6-1b), composed of an 18.5*4.5*2mm^3 saline solution (0.9% NaCl) in an open silicon cavity. The alternative current was uniformly injected at the extremities of the cavity with cylindrical steel electrodes. The environment was set in a box with an acoustic window at its bottom.
- The current injection electronics. A 500Hz sinusoidal current was amplified, low pass filtered (2nd order RC filter, 10.6kHz cutoff frequency) and injected to the saline environment through a transformer (Z218A6C, OEP, UK) in order to create a floating mass injection. The current within the saline solution, in order of dozens of mA, was measured at the extremities of a 10Ω resistance between the transformer and the solution.
- The reception electronics. Measurement was performed with the injection electrodes, to filter the current out, the signal was high-pas filtered (2nd order RC filters, 30kHz cutoff frequency), amplified with a differential amplifier (Lecroy, Chestnut Ridge, NY), averaged 512 times and sampled with an oscilloscope (Tektronix, Beaverton, OR) and registered on a laptop.
- The ultrasound transducer. In this part it was a single-element transducer (2.5MHz, 25mm geometrical focus, F/D 1, Imasonic, France) fixed on a 2D motorized setup to scan the entire saline environment.

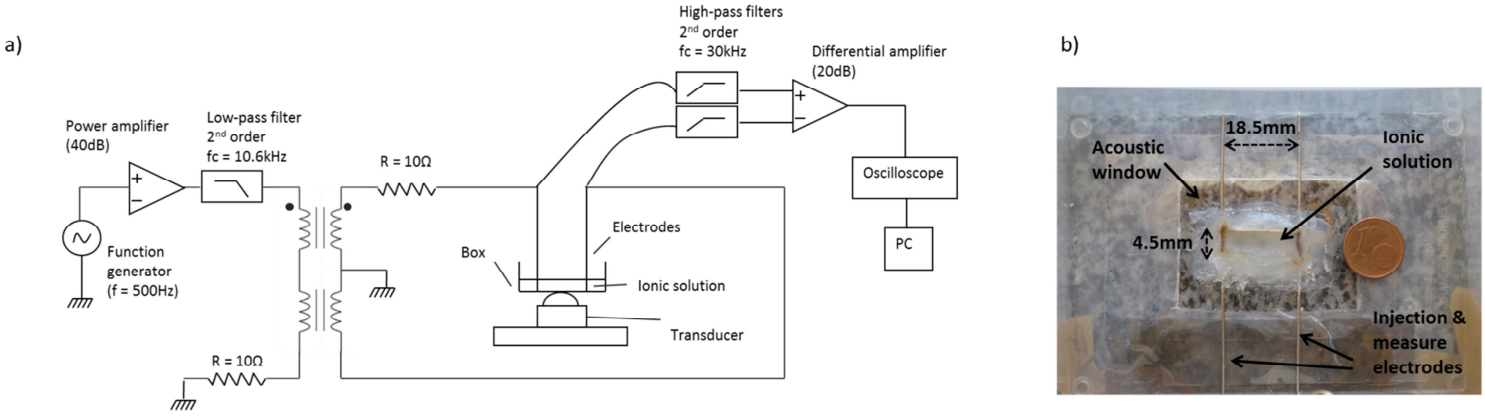

Figure 6-1 : Acoustoelectric setup with a single-element transducer. (a) Schematics of the whole setup, showing (left) the current injection electronics, (middle) the transducer and the saline environment (box), (right) the measure and registering electronics. (b) Photograph of the ionic environment seen from above. The saline solution lies within a rectangular cavity made with silicon. The current injecting and measure electrodes are on both sides of the cavity. An acoustic window let pass the ultrasound.

In this setup the ultrasonic beam (2 cycles, 2.5MHz, 5MPa peak positive pressure, -4.5MPa peak negative) was focalized within the saline solution (injected current: 13.5mA) on the negative peaks of the current. and the whole environment was scanned by a motorized displacement of the transducer (500µm steps).

Results

Figure 6-2a shows an example of an impedance modulation (AE effect) on a temporal signal acquired in the middle of the cavity. The 512-times averaged signal has an amplitude of 90µV. Figure 6-2b the amplitude of the effect in the whole cavity, the effect presents a higher amplitude near the electrodes (left and right) and is uniform between.

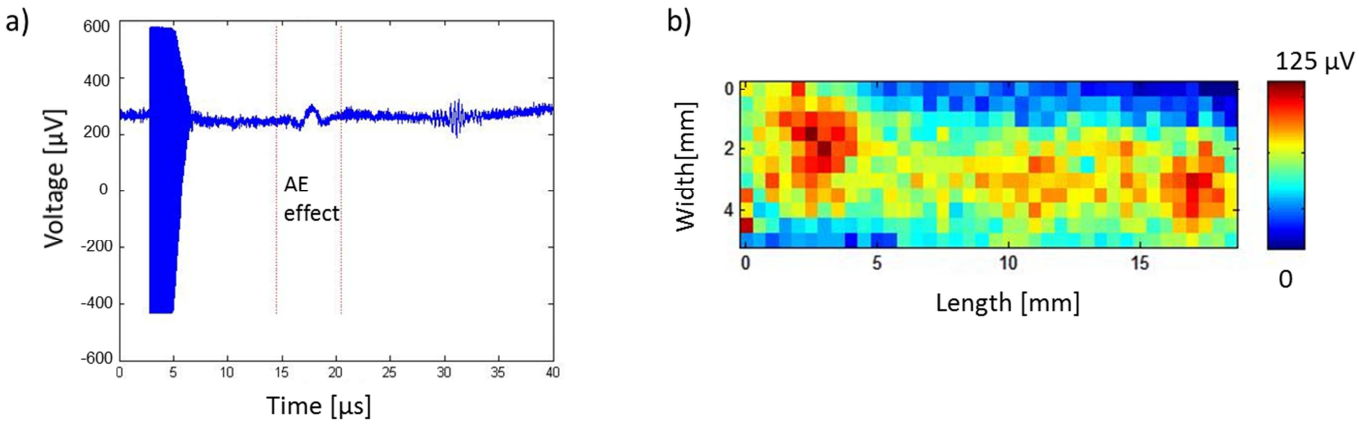

Figure 6-2 : Examples of the AE effect in the saline solution (after suppression of the amplification). (a) Temporal signal acquired in the middle of the cavity (averaged 512 times). Before 5µs the ultrasonic emission can be seen as a very high amplitude perturbation. Between 15µs and 20µs the low-frequency (approx. 300kHz) AE effect appears (90µV peak-to-peak amplitude). Between 30µs and 35µs a new perturbation appears, corresponding to the come and return of the ultrasonic wave which re-excites the transducer. (b) 2D scan of the saline cavity, showing the amplitude of the AE effect as on (a). The signal is stronger near the electrodes (left and right) and is more uniform between.

Discussion

With this setup the AE effect could be clearly demonstrated. However it presented several limitations. First, the signal had to be averaged 512 times because of a very weak SNR caused by the limited efficiency of the reception electronics and the low amplitude of the effect itself. Second, a mechanical scan had to be performed to obtain a 2D map of the saline environment. With approx. 4s of measurement (with averaging and registering) per spatial point, the whole scan duration was of approx. 25min. Finally because of the low SNR, the pressures induced in the solution were high (-4.5MPa of peak negative pressure), resulting in a MI of 2.8 which is above the accepted limit of 1.9.

To increase the SNR, we have improved the reception electronics, which gave us the possibility to decrease the pressure needed to measure the AE effect and perform a study by using a linear imaging array.

1.2.2 Imaging array

Modified setup

In the second setup the reception electronics have been improved. A 40dB amplifier has been added on the output of the differential one (Figure 6-3) and a low-pass filter (1st order RC, 1MHz cutoff frequency). As a consequence the SNR was significantly improved and the single-element transducer was replaced with a linear imaging array (4MHz center frequency, 128 elements, 0.33mm pitch, Vermon, France). The AE effect was measured by focusing with the array at 37mm through a coupling gel (polyvinyl alcohol).

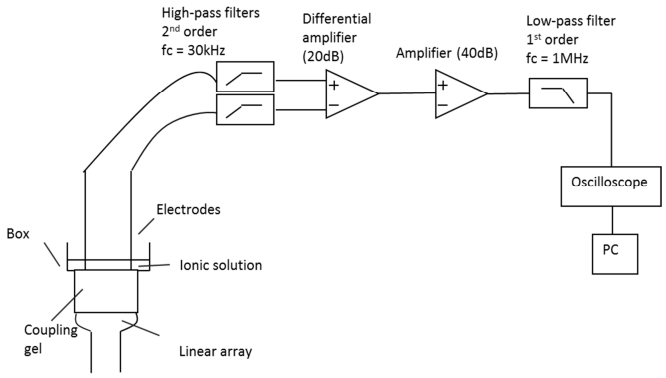

Figure 6-3 : Modifed part of the setup. Ultrasonic modulation of impedance in the saline solution was induced with an imaging linear array through a coupling gel. An amplifier and a low-pass filter have been added to increase the SNR of the AE effect.

Multiple focusing

Thanks to these modifications the SNR was significantly improved and AE effects down to 15µV could be detected. However, the linear probe had a large aperture (42.2mm) and focusing at 37mm with all the elements to create one focal spot was not profitable because of the directivity of the elements.

Taking this to account and for the constant sake to improve the SNR as well as the amplitude of the AE effect a compromise has been chosen. The elements of the probe were divided in four parts to create up to four focal spots simultaneously with a spatial distance of 3.3mm (1cm in total) between each. More specifically an emission pattern based on the Hadamard matrix has been chosen:

Given the Hadamard matrix $H_{AE} = \begin{bmatrix} 1 & 1 & 1 & 1 \\ 1 & -1 & 1 & -1 \\ 1 & 1 & -1 & -1 \\ 1 & -1 & -1 & 1 \end{bmatrix}$

An emission pattern has been chosen as: $H = (H_{AE} + 1)/2 = \begin{bmatrix} 1 & 1 & 1 & 1 \\ 1 & 0 & 1 & 0 \\ 1 & 1 & 0 & 0 \\ 1 & 0 & 0 & 1 \end{bmatrix}$

If $F = \begin{bmatrix} a \\ b \\ c \\ d \end{bmatrix}$ are the different focal spots,

The final received signal is: $S = H * F = \begin{bmatrix} a+b+c+d \\ a+c \\ a+b \\ a+d \end{bmatrix}$

And the signal corresponding to each focal spot can be retrieved with: $F = H^{-1} * S$

An acquisition was made using this technique, i.e. four emissions were performed corresponding to each line of H. The retrieved AE effect corresponding to each focal spot was confronted to a supplementary measure, were each focal spot was generated independently using the corresponding part of the array.

Results

Figure 6-4 shows the results obtained in the saline solution when performing the Hadamard emission pattern and the retrieved AE effect corresponding to each focal spot. When focusing with 4 simultaneous focal spots the AE effect had an amplitude of 180µV, down to 64µV with two extreme spots, whereas when focalizing with one spot it had 28-48µV at the extremities and 80µV in the center. This latter difference is due to the fact that the extreme foci were performed with a high steering and the pressure pattern was not uniform between the foci. The global amplitudes and thus the SNR were improved with multiple foci.

Finally the confrontation between the signals retrieved by matrix inversion or by independent measurement was very promising. The amplitude pattern was respected (high amplitude in the center and low at the extremities) with differences on the range of 5-35%.

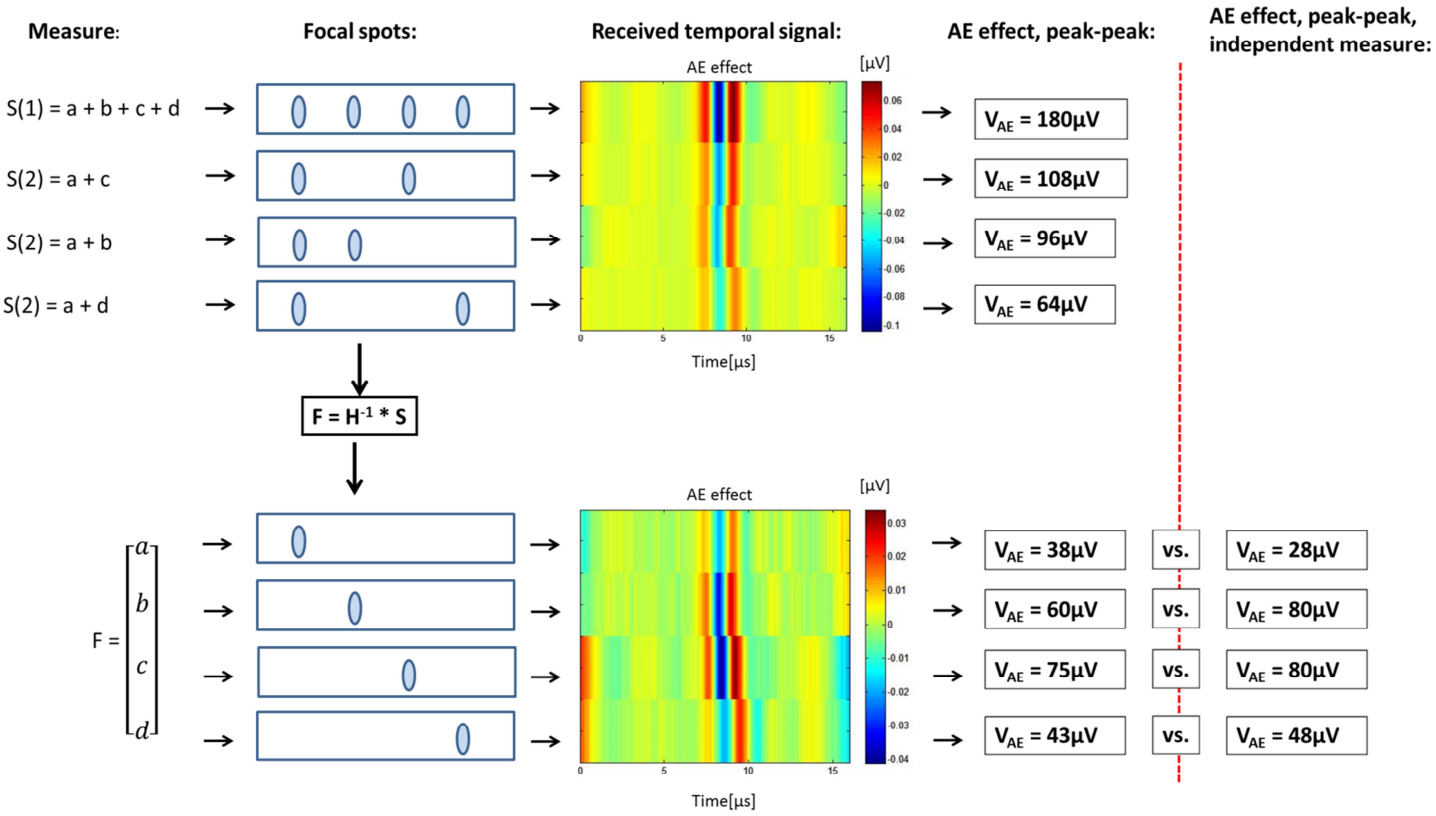

Figure 6-4 : Resume of the Hadamard technique with the obtained results. 1st column: matrix representation of the reception signal (up) and the retrieved signal (down). 2nd column: schematic representation of the induced (up) and corresponding retrieved (down) focal spots. 3rd column: received temporal signal centered on the AE effect (up), retrieved AE temporal signal (down). 4th column: peak-to-peak amplitude of the measured AE effect (up) and the retrieved AE effect (down). 5th column: comparison to the AE effect measure with the corresponding single focus.

Discussion

While the results shown with Hadamard matrix were interesting and show a potential way to improve the quality of the AE effect measures with an imaging array, an important limitation was not addressed. Regarding a cardiac application, imaging based on focalized beams present an insufficient temporal resolution to observe and image many transient events that occur in the heart. In this study an important temporal averaging was needed to observe the signal. However there was a very important way for improvement by designing dedicated, low-noise electronics. Still, 128 single emissions would be necessary to create a whole image with a good resolution. In order to answer to this limitation a completely new setup has been designed with novel Ultrafast plane-wave imaging of the current density.

1.3 Ultrafast Acoustoelectric Tomography

1.3.1 Methods

1.3.1.1 Image Formation

Forward problem

Figure 6-5 shows a typical acoustoelectric imaging setup. An ultrasound transducer and a pair of electrodes are placed onto the object to image. The emission of an ultrasound wave triggers the recording of highly amplified, high-frequency biopotentials. The biopotentials V detected by the pair of electrodes can be modelled as follows:

$$V' = \int_{Volume} K\rho J(\boldsymbol{x})\,\Delta P(\boldsymbol{x})d\boldsymbol{x} \qquad (3.1)$$

Where K is a constant of interaction of approximately 10^{-9} Pa^{-1} in a 0.9% NaCl solution [267], ρ is the resistivity of the medium, ΔP is the pressure variation, and $J(\boldsymbol{x})$ is the detected current density distribution, i.e., the scalar product of the current density in the medium and the sensitivity vector of the electrodes. When the variation in pressure is caused by a transducer array emitting a plane wave, $\Delta P(x,y,z,t)$ can be parametrized as a function of the emission angle θ and time t. Ignoring the elevational direction z, we have: $\Delta P(x,y) = \Delta P(q\sin\theta + ct\cos\theta, q\cos\theta + ct\sin\theta)$, where q and ct indicate the direction parallel and perpendicular to the wavefront, respectively (Figure 6-6).

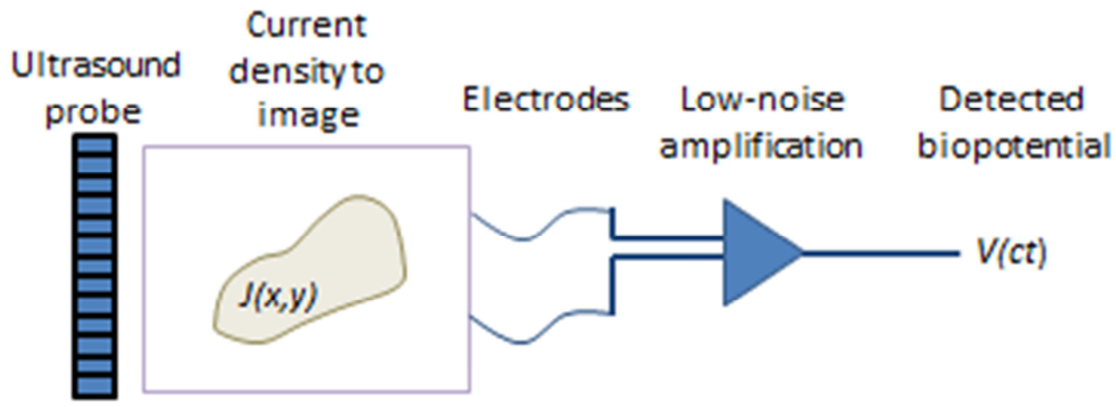

Figure 6-5 : Typical Acoustoelectric Imaging experimental setup. An ultrasound probe is used to create a pressure variation in a medium undergoing a current density. Electrodes are used to detect this variation and the amplified biopotentials can be used to reconstruct images, given a known sound velocity c.

Consider the ideal case of a Dirac delta distribution emission, i.e., that the ultrasound transducer can emit an infinitely short pulse (i.e., with infinite bandwidth); the acoustoelectric signal then becomes:

$$V(\theta,t) = \int_{-\infty}^{+\infty} J(q\sin\theta + ct\cos\theta, q\cos\theta + ct\sin\theta)dq \; \mathrm{V}(\theta,\mathrm{t}) = \int_{-\infty}^{+\infty} \mathrm{J}(\mathrm{q}\sin\theta + \mathrm{ct}\cos\theta, \mathrm{q}\cos\theta + \mathrm{ct}\sin\theta)\mathrm{dq} \; \mathrm{V}(\theta,\mathrm{t}) = \int_{-\infty}^{+\infty} \mathrm{J}(\mathrm{q}\sin\theta + \mathrm{ct}\cos\theta, \mathrm{q}\cos\theta + \mathrm{ct}\sin\theta)\mathrm{dq},$$

or, equivalenty,

$$\begin{aligned} V(\theta,t) &= R[J](\theta,ct) \\ &= \int_{-\infty}^{+\infty}\int_{-\infty}^{+\infty} J(x,y)\delta(x\sin\theta + \mathrm{y}\cos\theta - ct)dxdy \end{aligned}$$

where V = V'/Kρ and R[J] denotes the Radon transform. In practice, however, a finite bandwidth will be emitted by the ultrasound array, resulting in the convolution in the ct variable of the Radon Transform:

$$V(\theta,t) = W(ct) * R[J](\theta,ct),$$

where W(ct) is the emitted waveform. For example, a standard pulse excitation results in the following convolution kernel:

$$W(ct) = e^{\frac{-(ct)^2}{-(n\lambda)^2}} \sin\frac{ct}{m\lambda} \;,$$

where n and m can be tuned within the bandwidth of the ultrasound transducer. Note that this convolution kernel is equivalent to a ridgelets transform [271] of the current density distribution. Indeed, in the previous example, setting m = n and ignoring the z dimension, this kernel consists of a ridgelets decomposition with parameters a = nλ, b = ct and θ. The ridgelets decomposition benefits from a number of mathematical properties, such as a Parseval-Plancherel relationship, a reconstruction formula, sparse representation of objects that are smooth away from line discontinuities, and can be expressed as a composition of a wavelets transform and a Radon transform. More specifically, denoting the wavelet and ridgelet transforms by *WT[.]*, and *RT[.]* respectively, it can be shown that

$$V = RT[J] = WT[R[J]],$$

Inverse problem

Both the wavelets and Radon transform have well known inversions, and, therefore, we have,

$$J = R^{-1}[WT^{-1}[V]].$$

In practice, however, both the emission angles and the bandwidth available will be limited. Typically, emission angles will be constrained within ±20° and the bandwidth to 50% of the central emission frequency. These limitations transform a fully sampled k-space into a limited-angle annulus, resulting in an axial resolution proportional to the pulse width and a lateral resolution approximately 3 times bigger, i.e., worse, since sin(20°) = 0.342.

The inversion process is two-fold: first invert the wavelets transform, and then invert the Radon transform. Numerous strategies exist to invert the angle-limited Radon transform. The most common is probably filtered back-projection, which consists in applying a ramp filter to the Radon projection prior to back-projection, which itself is equivalent to beamforming.

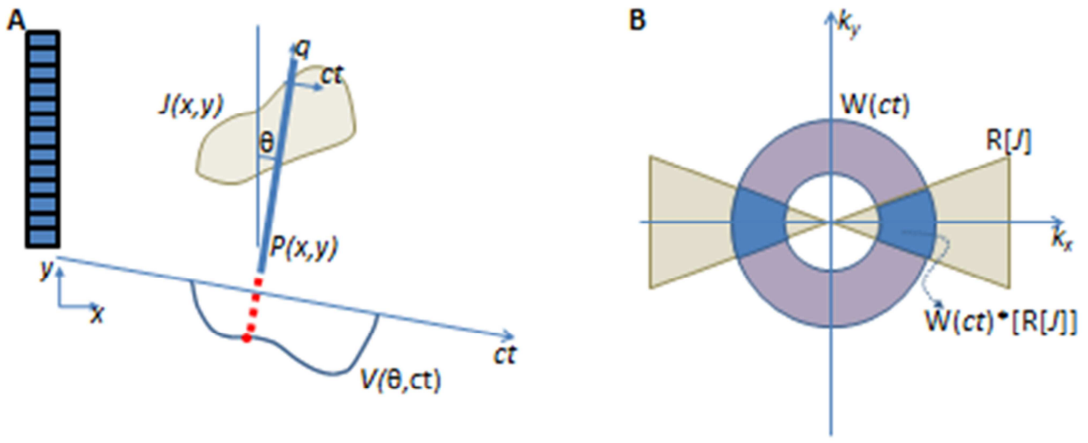

Figure 6-6 : Ultrafast acoustoelectric imaging direct problem. (A) In the ideal case of a Dirac pulse emission, the biopotentials measured correspond to the integration of the detected current density over an infinitely narroy wavefront, which is defined as a Radon transform when performed over 180°. (B) In reality, the wavefront will be constrained to a limited bandwidth in k-space due to the limited bandwidth of the ultrasound probe and to the limited emission angles that can be produced with a linear array. The different regions sampled by the angle-limited Radon transform R[J] and the emitted waveform W(ct) are indicated in different colors, along with their intersections.

Ideally, we would like to maximize the signal-to-noise ratio (SNR), which is notably low due to the weakness of the acoustoelectric effect. SNR can be improved by limiting the level of noise. Given that the ridgelet transform is a sparsifying basis that will represent the current density distribution with a small number of very large coefficients and a large number of small coefficients, denoising can be performed by thresholding the biopotential values [272, 273]. This thresholding can be carried out by simply removing 'small' values, but we can also include a priori knowledge to perform that task. More specifically, it is beneficial to emit twice at the same angle but with an inverted waveform since by subtracting the resulting signals V^+ and V^-, any systemic artifact is rejected. Additionally, since we know that both V^+ and V^- are sparse, i.e., they contain a few large values but mostly values below the noise level that can be eliminated without altering significantly the resulting reconstruction, we conducted a normalized cross-correlation between corresponding windows in V^+ and V^-. This results in a value close to zero in noisy regions and -1 in presence of signal, indicating which regions to threshold. This approach was carried out to limit the level of noise in all the results shown herein.

1.3.1.2 Experimental Setup

Plane waves between -20 and 20 degrees were emitted using an Aixplorer system (Supersonic Imagine, France) with a 6-MHz linear array probe (MI < 1.9). For images of Figure 6-7, electrodes potentials were high-passed filtered before entering a 1-MHz bandwidth differential preamplifier (Lecroy, Chestnut Ridge, NY), an amplifier (Olympus NDT, Waltham, MA), and then averaged up to 512 times and sampled on an oscilloscope (Tektronix, Beaverton, OR). Currents were applied and imaged in two phantoms containing a 0.9% NaCl solution: 1) a Tygon tube with an inner diameter of 0.87 mm, and 2) a triangular-prism-shaped container with a base of 2 mm and a height of 5 mm. Results of Figure 6-8 were obtained using customized active electrodes based on an ultralow noise biopotential amplifier (G = 2000, AD8428, Analog instruments) with very high common-mode rejection ratio (140 dB) and a 3.5-MHz bandwidth. Currents were generated using a 9V battery. No averaging was necessary. The phantom used consisted in a 2-mm wide box containing a 0.9%-NaCl solution.

1.3.2 Results

Figure 6-7 A and B show the reconstructions using 51 projections from -20 to 20° at 1-MHz bandwidth, of phantom 1 and 2, respectively. Phantom 1 reveals the typical resolution that can be achieved using UAT, i.e., approximately 1 mm. The signal originates solely from the region undergoing the current. The oscillating signal obtained in that region is also consistent with theory and corresponds approximately to the impulse function of the system. Phantom 2 shows that UAT can be used to reconstruct quantitatively complicated structures. Indeed, one can observe that the reconstructed current density increases linearly from the base of the triangle to its apex, as the cross-sectional area decreases, as expected in theory. Moreover, because of the band-limited nature of the image, the signal is stronger near variations in the image. For example, near the upper boundary of the container, the current transitions from a region not undergoing any current density to a region undergoing negative current density, which is reflected by the blue color on the image. Symmetrically, when the current density transitions from a negative value to a null value in the lower region of the container, the signal obtained is positive.

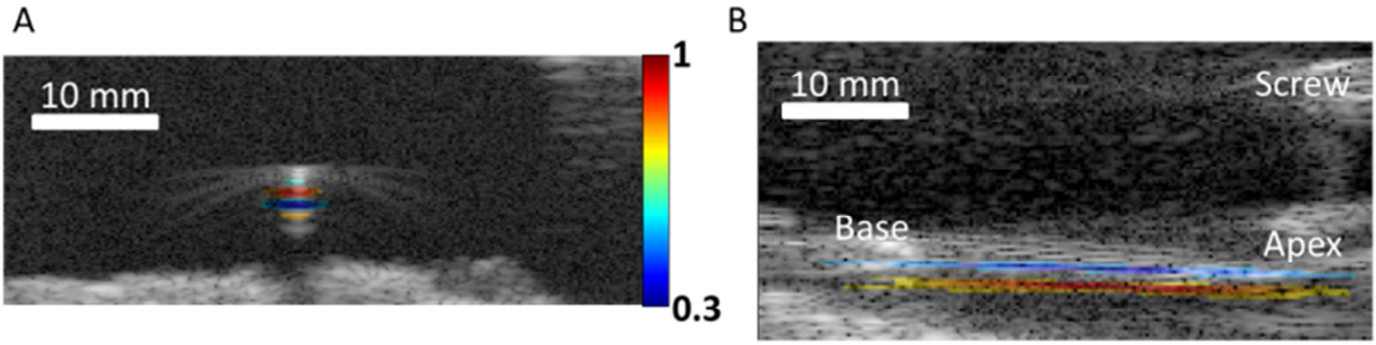

Figure 6-7 : Ultrafast Acoustoelectric Imaging in 0.9% NaCl phantoms. (A) Reconstruction of the current density inside a tygon tube. (B) Triangular-prism-shaped container. The intensity of the reconstructed current density increases near the apex, as expected due to the reduction in the conductor cross-section.

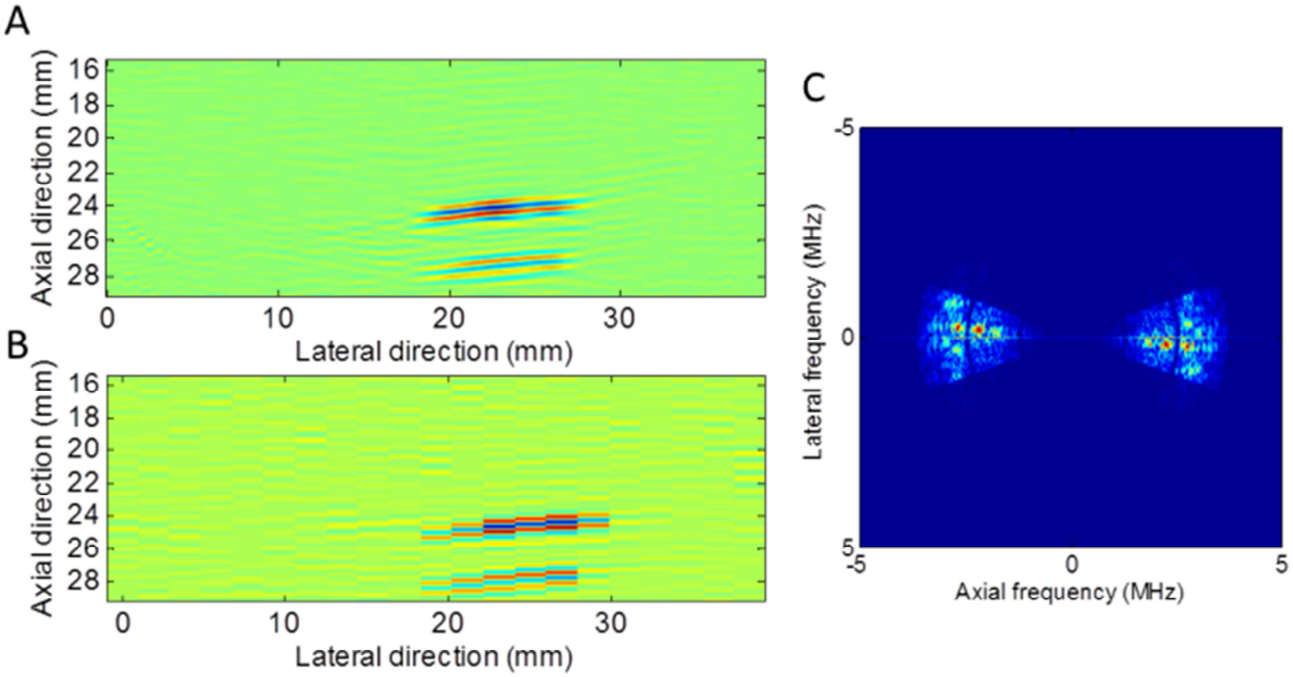

Figure 6-8 : Acoustoelectric Imaging of a 2-mm wide box filled with a 0.9%-NaCl solution. (A) Plane wave reconstruction using 21 plane-waves between -10 and 10 degrees. (B) 21-focused emissions image. (C) K-space of the reconstruction in A.

Figure 6-8 shows a comparison of acoustoelectric images obtained using plane waves (Figure 6-8A) and focused emissions (Figure 6-8B). In both cases, 21 emissions were used. One can observe that the image obtained using plane wave is of better quality and less pixelated, indicating that a better image quality can be obtained for a given number of emission, or, inversely, that the frame rate can be increased (as the frame rate is dictated by the number of emissions necessary to generate an image). Figure 6-8C shows the k-space of the reconstruction of Figure 6-8A, and clearly showing the cropped-annulus shape predicted by our reconstruction model.

1.3.3 Discussion

The objective of this study was to determine the feasibility of performing high frame rate current density imaging while preserving high spatial resolution. We have shown that by using plane wave emissions, the inverse problem becomes easily tractable as it can be decomposed into well-known inverse problems and provides high frame rates and uniformly high axial and lateral resolution. Examples provided in phantoms demonstrated the feasibility of the method.

Achieving high frame rates in acoustoelectric imaging is crucial for future applications as action potentials are propagating rapidly. For example, the heart can depolarize completely in less than 60 ms. To track this activation sequence, it is necessary to achieve frame rates on the order of hundreds of hertz. A typical approach consisting of imaging a 20-cm deep heart with 64 emissions leads to a frame rate of 120 Hz, or, only 7 images during the activation sequence, assuming no averaging is necessary. Plane wave approaches could significantly reduce the number of emissions needed for a given image quality, as has been shown in ultrasound imaging [107], therefore expanding possible applications of acoustoelectric imaging.

Similarly to approaches based on focused emissions, UAT suffers from small signal to noise ratios. This issue can be addressed via improved instrumentation, as we have demonstrated in this study using active electrodes. Moreover, improved sequences and signal processing strategies could be used to limit the influence of noise. One approach would consist in performing pulse compression [274] by emitting a chirp that covers the entire available ultrasound bandwidth. In that case, we replace the truncated wavelets transform by a convolution with a chirp, which can be inverted using a matched filter. This strategy should, in theory, maximize the SNR without altering the imaging frame rate. In the case of the inversion of the Radon transform, strategies such as compressed sensing could also be considered [275–277].

Potential clinical applications of UAT are numerous as the simplicity of the required instrumentation makes this approach highly translational. Indeed, low frequency electrocardiograms (ECG) are already recorded with virtually every echocardiographic exam. By simply replacing the current ECG acquisition systems by high frequency amplification, one could detect the acoustoelectric potentials and perform UAT without modifying currently existing clinical protocols and with most commercially-available ultrasound scanners.

By using an intracardiac approach, this technique could potentially provide images of cardiac electrical currents with an unachieved sub-millimetric resolution, which would help to find or diagnose arrhythmogenic or unwanted electrical pathways.

2 General Conclusion

This thesis was an opportunity to take benefit from the more and more various possibilities ultrasound can offer in the field of medical imaging and therapy and apply them to a particular need: the treatment of cardiac arrhythmias. By choosing an all-ultrasound approach for both therapy and imaging, our collaborators and us, have developed two interstitial devices, an intracardiac dual-mode catheter and an ultrasound-guided-HIFU transesophageal endoscope, both adapted for the cardiac environment.

More specifically during this work we have adapted and validated on the two systems many ultrasound imaging modalities (Ultrafast imaging, Shear-Wave Elastography, Ultrafast Doppler and Acousto-Electric Imaging) which have been developed at the Institut Langevin during recent years, in order to guide and control therapy, as well as provide new diagnostic possibilities. We have also participated in the development and validated the intracardiac device for HIFU thermal therapy to obtain finally a miniaturized all-ultrasound theranostic system.

In order to achieve these goals, first, we validated the accuracy of SWE to monitor thermal therapies, RFA and HIFU, in-vivo in the liver, an organ that is an easier environment than the heart: more homogeneous and less affected by motion. The obtained results were very promising, giving high sensitivity and positive predictive values for ablated tissue detection, and confirmed the previous results on the link of thermally coagulated tissue and elastographic images. While this study could have impacts in cancer ablation in the liver, to us it showed also the robustness of the SWE technique and confirmed the pertinence to apply it for thermal ablation monitoring in the heart.

Second, we implemented SWE and other imaging modalities on the intracardiac transducer and tested the system in-vivo. In particular we validated the feasibility of SWE to evaluate classical RFCA in the heart and showed the potential for other diagnostic imaging (e.g. the coronary detection with Ultrafast Doppler).

Third, we implemented HIFU therapy on the same transducer to obtain a device capable to perform image-controlled therapy with the same aperture. Such a dual-mode system presents a very interesting flexibility for the procedures of ablation for atrial fibrillation as well as for ventricular tachycardia. Thanks to the numerous imaging and

therapeutic possibilities it offers its applications could be various in the heart as well as in other organs.

Finally we participated to the development of the second heart dedicated ultrasonic system by implementing and validating SWE for the evaluation of HIFU ablation. For this, we have tested the previously developed SWE based on diverging-waves ultrafast imaging, with a transesophageal probe. We showed the feasibility of stiffness mapping with the system in-vivo on a normal beating heart and in vitro on cardiac tissues with HIFU induced lesions by the same probe. Beyond the scope of thermal ablation control the SWE transesophageal approach could be proven as a promising elastographic modality for cardiac diagnostics.

By its applicative nature, the main tasks of this thesis were based on system development and the adaptation of already existing ultrasonic modalities and techniques on miniaturized devices, for the demanding cardiac environment. Thanks to the scientific knowledge, experience, enthusiasm and very rich environment within the Institut Langevin as well as among all the other partners the project resulted in two new and very promising devices to address one of the most prevalent cardiac disorder. The so far very promising results show a product of a very positive collaboration among several partners. By providing a concrete therapeutic and potentially diagnostic solution this work could help ultrasound to propagate and gain recognition in the medical field for cardiac but also non-cardiac applications. From my point of view, ultrasound is the most promising medical imaging and therapy modality and has still the biggest room for improvement. It was very exciting to work and participate to the world of these translational physics and to be a part of a chain connecting public research with industry and the hospital world.

Publications related to the thesis

Peer-reviewed Journals:

1. **W. Kwiecinski**, J. Provost, R. Dubois, F. Sacher, M. Haïssaguerre, M. Legros, A. Nguyen-Dinh, R. Dufait, M. Tanter, and M. Pernot. "Quantitative evaluation of atrial radio frequency ablation using intracardiac shear-wave elastography." *Medical physics* 41, no. 11 (2014): 112901. (Chapter 3)
2. A. Mariani, **W. Kwiecinski**, M. Pernot, D. Balvay, M. Tanter, O. Clement, C. A. Cuenod, and F. Zinzindohoue. "Real time shear waves elastography monitoring of thermal ablation: in vivo evaluation in pig livers." *Journal of Surgical Research* 188, no. 1 (2014): 37-43. (Chapter 2)
3. **W. Kwiecinski**; F. Bessière; E. Constanciel Colas; W.A. N'Djin; M. Tanter; C. Lafon, and M. Pernot. "Cardiac shear-wave elastography using a transesophageal transducer: Application to the mapping of thermal lesions in ultrasound transesophageal cardiac ablation" *Physics in Medicine and Biology,*Submitted (Chapter 5)
4. O. Villemain; **W. Kwiecinski**; A. Bel; J. Robin; P. Bruneval; B. Arnal; M. Tanter; M. Pernot and E. Messas. “Non-invasive ultrasonic chordal cutting” *Journal of the American College of Cardiology: Cardiovascular Interventions,*Submitted (Chapter 1)
5. **W. Kwiecinski** ; F. Sacher ; J. Provost ; M. Legros ; A. Nguyen-Dinh ; R. Dufait ; R. Dubois; M. Tanter and M. Pernot. “In-vivo HIFU atrial and ventricular ablation and monitoring using a customized dual-mode intracardiac echocardiography catheter”, To be submitted (Chapter 4)
6. J. Provost, **W. Kwiecinski**, M. Fink, M. Tanter, M. Pernot. “Ultrafast acoustoelectric imaging”, In preparation (Chapter 6)

Peer-reviewed conference proceedings:

1. **W. Kwiecinski**; J. Provost; R. Dubois; F. Sacher; M. Haïssaguerre; M. Legros; A. Nguyen-Dinh; R. Dufait ; M. Tanter ; M. Pernot. “Validation of an intracardiac ultrasonic therapy–imaging dual mode transducer”, *IRBM*, in press (Chapter 4)

Other conference proceedings:

1. J. Provost, **W. Kwiecinski**, M. Fink, M. Tanter, M. Pernot. "Ultrafast acoustoelectric imaging." Biomedical Imaging (ISBI), 2014 IEEE 11th International Symposium on, pp. 702-705. IEEE, 2014. (Chapter 6)

Abstracts, international conferences:

1. **W. Kwiecinski**; M. Pernot; M. Fink; M. Tanter. “Feasibility of radio-frequency cardiac ablation monitoring using shear-wave imaging in intracardiac echocardiography”, IEEE International Ultrasonics Symposium, Dresden, Germany, 2012
2. **W. Kwiecinski**, J. Provost, M. Legros, A. Nguyen-Dinh, R. Dufait, M. Tanter, and M. Pernot. “Feasibility of HIFU cardiac therapy and monitoring using shear-wave imaging with dual mode intracardiac catheter”, ISTU 13th International Symposium of Therapeutic Ultrasound, Shanghai, China, 2013
3. **W. Kwiecinski**, A. Mariani, M. Pernot, D. Balvay, C. A. Cuenod, M.Fink, M. Tanter, F. Zinzindohoue. “Real time shear wave imaging of HIFU thermal ablation: in vivo evaluation in pig livers”, ISTU 13th International Symposium of Therapeutic Ultrasound, Shanghai, China, 2013
4. **W. Kwiecinski**, J. Provost, M. Legros, A. Nguyen-Dinh, R. Dufait, M. Tanter, and M. Pernot. “Feasibility of HIFU cardiac therapy and monitoring using shear-wave imaging with dual mode intracardiac catheter”, IEEE International Ultrasonics Symposium, Prague, Czech Republic, 2013
5. **W. Kwiecinski**, J. Provost, M. Legros, A. Nguyen-Dinh, R. Dufait, F. Sacher, R. Dubois, M. Haïssaguerre, M. Tanter, and M. Pernot “In-vivo HIFU atrial and ventricular ablation and monitoring using a dual-mode high-frequency intracardiac catheter”, IEEE International Ultrasonics Symposium, Chicago, USA, 2014
6. **W. Kwiecinski** ; F. Sacher ; J. Provost ; M. Legros ; A. Nguyen-Dinh ; R. Dufait ; R. Dubois; M. Tanter and M. Pernot. “In-vivo HIFU atrial and ventricular ablation and monitoring using a customized dual-mode intracardiac echocardiography catheter”, ISTU 15th International Symposium of Therapeutic Ultrasound, Utrecht, Netherlands, 2015
7. **W. Kwiecinski**; F. Bessière; E. Constanciel Colas; W.A. N'Djin; M. Tanter; C. Lafon, and M. Pernot. “Feasibility of Shear-Wave Elastography for evaluation of

cardiac transesophageal HIFU ablation" , ISTU 15th International Symposium of Therapeutic Ultrasound, Utrecht, Netherlands, 2015

Abstracts, national conferences:

1. **W. Kwiecinski**; J. Provost; R. Dubois; F. Sacher; M. Haïssaguerre; M. Legros; A. Nguyen-Dinh; R. Dufait ; M. Tanter ; M. Pernot. "Dual-mode intracardiac ultrasonic transducer for thermal ablation therapy and real-time quantitative assessment of the treatment", RITS colloquium Recherche en Imagerie et Technologies pour la Santé, Dourdan, France, 2015

Prices:

1. « Young Researcher Price » for best oral presentation, RITS colloquium Recherche en Imagerie et Technologies pour la Santé, Dourdan, France, 2015

Bibliography

[1] M. Zoni-Berisso, F. Lercari, T. Carazza, and S. Domenicucci, “Epidemiology of atrial fibrillation: European perspective.,” Clin. Epidemiol. **6**, 213–20 (2014).

[2] A.S. Go *et al.*, “Heart disease and stroke statistics--2014 update: a report from the American Heart Association.,” Circulation **129**(3), e28–e292 (2014).

[3] T.J. Wang *et al.*, “Temporal relations of atrial fibrillation and congestive heart failure and their joint influence on mortality: the Framingham Heart Study.,” Circulation **107**(23), 2920–5 (2003).

[4] a J. Camm *et al.*, “Guidelines for the management of atrial fibrillation: the Task Force for the Management of Atrial Fibrillation of the European Society of Cardiology (ESC).,” Eur. Heart J. **31**(19), 2369–429 (2010).

[5] S. Stewart, C.L. Hart, D.J. Hole, and J.J.. McMurray, “A population-based study of the long-term risks associated with atrial fibrillation: 20-year follow-up of the Renfrew/Paisley study,” Am. J. Med. **113**(5), 359–364 (2002).

[6] M. Haïssaguerre *et al.*, “Spontaneous initiation of atrial fibrillation by ectopic beats originating in the pulmonary veins,” N. Engl. J. Med. **339**(10), 659–666 (1998).

[7] S. Nattel, “New ideas about atrial fibrillation 50 years on.,” Nature **415**(6868), 219–26 (2002).

[8] E.M. Aliot *et al.*, “EHRA/HRS Expert Consensus on Catheter Ablation of Ventricular Arrhythmias: developed in a partnership with the European Heart Rhythm Association (EHRA), a Registered Branch of the European Society of Cardiology (ESC), and the Heart Rhythm Society (HRS); i,” Europace **11**(6), 771–817 (2009).

[9] H. Calkins *et al.*, “2012 HRS/EHRA/ECAS Expert Consensus Statement on Catheter and Surgical Ablation of Atrial Fibrillation: recommendations for patient selection, procedural techniques, patient management and follow-up, definitions, endpoints, and research trial design.,” Europace **14**(4), 528–606 (2012).

[10] H. Calkins *et al.*, “Treatment of atrial fibrillation with antiarrhythmic drugs or radiofrequency ablation: two systematic literature reviews and meta-analyses.,” Circ. Arrhythm. Electrophysiol. **2**(4), 349–61 (2009).

[11] C.T. Pedersen *et al.*, “EHRA/HRS/APHRS expert consensus on ventricular arrhythmias.,” Europace **16**(9), 1257–83 (2014).

[12] J.L. Cox *et al.*, “The surgical treatment of atrial fibrillation. III. Development of a definitive surgical procedure.,” J. Thorac. Cardiovasc. Surg. **101**(4), 569–83 (1991).

[13] S.M. Prasad *et al.*, “The Cox maze III procedure for atrial fibrillation: long-term efficacy in patients undergoing lone versus concomitant procedures,” J. Thorac. Cardiovasc. Surg. **126**(6), 1822–1827 (2003).

[14] J. De Bakker *et al.*, “Reentry as a cause of ventricular tachycardia in patients with chronic ischemic heart disease: electrophysiologic and anatomic correlation.,” Circulation **77**(3), 589–606 (1988).

[15] P. Jaïs, M. Haïssaguerre, D. Shah, S. Chouairi, L. Gencel, and J. Clémenty, “A focal source of atrial fibrillation treated by discrete radiofrequency ablation,” Circulation **95**(3), 572–576 (1997).

[16] B.B. Lerman *et al.*, “Mechanism of Repetitive Monomorphic Ventricular Tachycardia,” Circulation **92**(3), 421–429 (1995).

[17] J.J. Langberg, M. Harvey, H. Calkins, R. el-Atassi, S.J. Kalbfleisch, and F. Morady, “Titration of power output during radiofrequency catheter ablation of atrioventricular nodal reentrant tachycardia.,” Pacing Clin. Electrophysiol. **16**(3 Pt 1), 465–70 (1993).

[18] H.L. Estner *et al.*, "Electrical isolation of pulmonary veins in patients with atrial fibrillation: reduction of fluoroscopy exposure and procedure duration by the use of a non-fluoroscopic navigation system (NavX).," Europace **8**(8), 583–7 (2006).

[19] M. Scaglione *et al.*, "Visualization of multiple catheters with electroanatomical mapping reduces X-ray exposure during atrial fibrillation ablation.," Europace **13**(7), 955–62 (2011).

[20] M. Haissaguerre *et al.*, "Driver domains in persistent atrial fibrillation.," Circulation **130**(7), 530–8 (2014).

[21] M. Vaseghi *et al.*, "Impedance monitoring during catheter ablation of atrial fibrillation.," Heart Rhythm **2**(9), 914–20 (2005).

[22] S. Sporton, M. Earley, A. Nathan, and R. Schilling, "Electroanatomic versus fluoroscopic mapping for catheter ablation procedures," J. Cardiovasc. Electrophysiol. **15**(July 2003), 310–315 (2004).

[23] Z.M. Hijazi, K. Shivkumar, and D.J. Sahn, "Intracardiac echocardiography during interventional and electrophysiological cardiac catheterization.," Circulation **119**(4), 587–96 (2009).

[24] R. Kobza *et al.*, "Late recurrent arrhythmias after ablation of atrial fibrillation: Incidence, mechanisms, and treatment," Hear. Rhythm **1**(6), 676–683 (2004).

[25] J. Mallidi, G.N. Nadkarni, R.D. Berger, H. Calkins, and S. Nazarian, "Meta-analysis of catheter ablation as an adjunct to medical therapy for treatment of ventricular tachycardia in patients with structural heart disease.," Heart Rhythm **8**(4), 503–10 (2011).

[26] R. Cappato *et al.*, "Updated worldwide survey on the methods, efficacy, and safety of catheter ablation for human atrial fibrillation.," Circ. Arrhythm. Electrophysiol. **3**(1), 32–8 (2010).

[27] J.G. Andrade *et al.*, "Efficacy and safety of cryoballoon ablation for atrial fibrillation: a systematic review of published studies.," Heart Rhythm **8**(9), 1444–51 (2011).

[28] D.L. Packer *et al.*, "Cryoballoon ablation of pulmonary veins for paroxysmal atrial fibrillation: first results of the North American Arctic Front (STOP AF) pivotal trial.," J. Am. Coll. Cardiol. **61**(16), 1713–23 (2013).

[29] S.R. Dukkipati *et al.*, "Pulmonary vein isolation using a visually guided laser balloon catheter: the first 200-patient multicenter clinical experience.," Circ. Arrhythm. Electrophysiol. **6**(3), 467–72 (2013).

[30] B. Schmidt *et al.*, "Pulmonary vein isolation by high-intensity focused ultrasound: first-in-man study with a steerable balloon catheter.," Heart Rhythm **4**(5), 575–84 (2007).

[31] R.W. Wood and A.L. Loomis, "XXXVIII. The physical and biological effects of high-frequency sound-waves of great intensity," London, Edinburgh, Dublin Philos. Mag. J. Sci. **4**(2), 417–436 (1927).

[32] T. V. Samulski *et al.*, "Clinical experience with a multi-element ultrasonic hyperthermia system: Analysis of treatment temperatures," Int. J. Hyperth. **6**(5), 909–922 (1990).

[33] G. ter Haar, "Therapeutic applications of ultrasound.," Prog. Biophys. Mol. Biol. **93**(1-3), 111–29 (2007).

[34] K.F. Chu and D.E. Dupuy, "Thermal ablation of tumours: biological mechanisms and advances in therapy.," Nat. Rev. Cancer **14**(3), 199–208 (2014).

[35] a. N. Guthkelch *et al.*, "Treatment of malignant brain tumors with focused ultrasound hyperthermia and radiation: results of a phase I trial," J. Neurooncol. **10**(3), 271–284 (1991).

[36] J.R. Tacker and R.U. Anderson, "Delivery of antitumor drug to bladder cancer by use of phase transition liposomes and hyperthermia.," J. Urol. **127**(6), 1211–4 (1982).

[37] R. Staruch, R. Chopra, and K. Hynynen, “Localised drug release using MRI-controlled focused ultrasound hyperthermia.,” Int. J. Hyperthermia **27**(2), 156–71 (2011).
[38] O. Couture, J. Foley, N.F. Kassell, B. Larrat, and J. Aubry, “Review of ultrasound mediated drug delivery for cancer treatment : updates from pre-clinical studies,” Transl. Cancer Res. **3**(5), 494–511 (2014).
[39] M.R. Bailey, V. a. Khokhlova, O. a. Sapozhnikov, S.G. Kargl, and L. a. Crum, “Physical mechanisms of the therapeutic effect of ultrasound (a review),” Acoust. Phys. **49**(4), 369–388 (2003).
[40] G. ter Haar and C. Coussios, “High intensity focused ultrasound: physical principles and devices,” Int. J. Hyperth. **23**(2), 89–104 (2007).
[41] D. Melodelima, W.A. N’Djin, H. Parmentier, S. Chesnais, M. Rivoire, and J.-Y. Chapelon, “Thermal ablation by high-intensity-focused ultrasound using a toroid transducer increases the coagulated volume. Results of animal experiments.,” Ultrasound Med. Biol. **35**(3), 425–35 (2009).
[42] D.R. Daum and K. Hynynen, “A 256-element ultrasonic phased array system for the treatment of large volumes of deep seated tissue.,” IEEE Trans. Ultrason. Ferroelectr. Freq. Control **46**(5), 1254–68 (1999).
[43] M. Pernot, J.-F. Aubry, M. Tanter, J.-L. Thomas, and M. Fink, “High power transcranial beam steering for ultrasonic brain therapy,” Phys. Med. Biol. **48**(16), 2577–2589 (2003).
[44] E.S. Ebbini and C.A. Cain, “Multiple-focus ultrasound phased-array pattern synthesis: optimal driving-signal distributions for hyperthermia.,” IEEE Trans. Ultrason. Ferroelectr. Freq. Control **36**(5), 540–8 (1989).
[45] J.G. Lynn, R.L. Zwemer, a J. Chick, and a E. Miller, “a New Method for the Generation and Use of Focused Ultrasound in Experimental Biology.,” J. Gen. Physiol. **26**(2), 179–193 (1942).
[46] W.J. Fry, F.J. Fry, J.W. Barnard, R.F. Krumins, and J.F. Brennan, “Ultrasonic Lesions in Mammalian Central Nervous System,” Science (80-.). **122**(3179), 1091–1091 (1955).
[47] W.J. Fry and F.J. Fry, “Fundamental neurological research and human neurosurgery using intense ultrasound.,” IRE Trans. Med. Electron. **ME-7**, 166–181 (1960).
[48] D.J. Coleman *et al.*, “Therapeutic Ultrasound in the Treatment of Glaucoma,” Ophthalmology **92**(3), 347–353 (1985).
[49] D. Tyshlek *et al.*, “Focused ultrasound development and clinical adoption: 2013 update on the growth of the field,” J. Ther. Ultrasound **2**(1), 2 (2014).
[50] L. Poissonnier *et al.*, “Control of Prostate Cancer by Transrectal HIFU in 227 Patients,” Eur. Urol. **51**(2), 381–387 (2007).
[51] E.A. Stewart *et al.*, “Clinical outcomes of focused ultrasound surgery for the treatment of uterine fibroids.,” Fertil. Steril. **85**(1), 22–9 (2006).
[52] O. Al-Bataineh, J. Jenne, and P. Huber, “Clinical and future applications of high intensity focused ultrasound in cancer,” Cancer Treat. Rev. **38**(5), 346–353 (2012).
[53] D.L. Miller, N.B. Smith, M.R. Bailey, G.J. Czarnota, K. Hynynen, and I.R.S. Makin, “Overview of therapeutic ultrasound applications and safety considerations.,” J. Ultrasound Med. **31**(4), 623–34 (2012).
[54] M. a. O’Reilly and K. Hynynen, “Emerging non-cancer applications of therapeutic ultrasound,” Int. J. Hyperth. **00**(00), 1–9 (2015).
[55] A. Shaw, G. ter Haar, J. Haller, and V. Wilkens, “Towards a dosimetric framework for therapeutic ultrasound,” Int. J. Hyperth. **00**(00), 1–11 (2015).
[56] S. Sapareto and W. Dewey, “Thermal dose determination in cancer therapy,” Int. J. Radiat. Oncol. Biol. Phys. **10**(6), 787–800 (1984).

[57] A.Z. Weizer, P. Zhong, and G.M. Preminger, “New concepts in shock wave lithotripsy.,” Urol. Clin. North Am. **34**(3), 375–82 (2007).
[58] N. Bhojani and J.E. Lingeman, “Shockwave lithotripsy-new concepts and optimizing treatment parameters.,” Urol. Clin. North Am. **40**(1), 59–66 (2013).
[59] G. Haupt, “Use of extracorporeal shock waves in the treatment of pseudarthrosis, tendinopathy and other orthopedic diseases.,” J. Urol. **158**(1), 4–11 (1997).
[60] Z. Xu *et al.*, “Controlled ultrasound tissue erosion.,” IEEE Trans. Ultrason. Ferroelectr. Freq. Control **51**(6), 726–736 (2004).
[61] E. Vlaisavljevich, A. Maxwell, M. Warnez, E. Johnsen, C. a. Cain, and Z. Xu, “Histotripsy-induced cavitation cloud initiation thresholds in tissues of different mechanical properties.,” IEEE Trans. Ultrason. Ferroelectr. Freq. Control **61**(2), (2014).
[62] E. Vlaisavljevich *et al.*, “Effects of tissue stiffness, ultrasound frequency, and pressure on histotripsy-induced cavitation bubble behavior,” Phys. Med. Biol. **60**, 1–17 (2015).
[63] A.D. Maxwell, C. a Cain, T.L. Hall, J.B. Fowlkes, and Z. Xu, “Probability of cavitation for single ultrasound pulses applied to tissues and tissue-mimicking materials.,” Ultrasound Med. Biol. **39**(3), 449–65 (2013).
[64] V. a. Khokhlova *et al.*, “Histotripsy methods in mechanical disintegration of tissue: Towards clinical applications,” Int. J. Hyperth. **00**(00), 1–18 (2015).
[65] Y. Kim *et al.*, “Developmental impact and lesion maturation of histotripsy-mediated non-invasive tissue ablation in a fetal sheep model.,” Ultrasound Med. Biol. **39**(6), 1047–55 (2013).
[66] W.W. Roberts, D. Teofilovic, R.C. Jahnke, J. Patri, J.M. Risdahl, and J. a Bertolina, “Histotripsy of the Prostate Using a Commercial System in a Canine Model.,” J. Urol. **191**(3), 860–865 (2013).
[67] Y. Kim, E. Vlaisavljevich, G.E. Owens, S.P. Allen, C. a Cain, and Z. Xu, “In vivo transcostal histotripsy therapy without aberration correction.,” Phys. Med. Biol. **59**(11), 2553–68 (2014).
[68] T.D. Khokhlova, M.S. Canney, V. a. Khokhlova, O. a. Sapozhnikov, L. a. Crum, and M.R. Bailey, “Controlled tissue emulsification produced by high intensity focused ultrasound shock waves and millisecond boiling,” J. Acoust. Soc. Am. **130**(5), 3498 (2011).
[69] S. Parikh *et al.*, “Ultrasound-accelerated thrombolysis for the treatment of deep vein thrombosis: initial clinical experience.,” J. Vasc. Interv. Radiol. **19**(4), 521–8 (2008).
[70] D. Gebauer, E. Mayr, E. Orthner, and J.P. Ryaby, “Low-intensity pulsed ultrasound: effects on nonunions.,” Ultrasound Med. Biol. **31**(10), 1391–402 (2005).
[71] M.W. Mann, M.D. Palm, and R.D. Sengelmann, “New Advances in Liposuction Technology,” Semin. Cutan. Med. Surg. **27**(1), 72–82 (2008).
[72] B. Nazer, E.P. Gerstenfeld, A. Hata, L. a Crum, and T.J. Matula, “Cardiovascular applications of therapeutic ultrasound.,” J. Interv. Card. Electrophysiol. (2013).
[73] D.S. He *et al.*, “Application of ultrasound energy for intracardiac ablation of arrhythmias.,” Eur. Heart J. **16**(7), 961–966 (1995).
[74] J.E. Zimmer, K. Hynynen, D.S. He, and F. Marcus, “The feasibility of using ultrasound for cardiac ablation.,” IEEE Trans. Biomed. Eng. **42**(9), 891–7 (1995).
[75] S. a Strickberger, T. Tokano, J.U. Kluiwstra, F. Morady, and C. Cain, “Extracardiac ablation of the canine atrioventricular junction by use of high-intensity focused ultrasound.,” Circulation **100**(2), 203–208 (1999).
[76] R. Otsuka *et al.*, “Extracardiac ablation of the left ventricular septum in beating canine hearts using high-intensity focused ultrasound.,” J. Am. Soc. Echocardiogr. **20**(12), 1400–6 (2007).

[77] S. Rong *et al.*, “Septal ablation induced by transthoracic high-intensity focused ultrasound in canines.,” J. Am. Soc. Echocardiogr. **26**(10), 1228–34 (2013).
[78] J. Ninet *et al.*, “Surgical ablation of atrial fibrillation with off-pump, epicardial, high-intensity focused ultrasound: results of a multicenter trial.,” J. Thorac. Cardiovasc. Surg. **130**(3), 803–9 (2005).
[79] T.J. Klinkenberg *et al.*, “Feasibility and outcome of epicardial pulmonary vein isolation for lone atrial fibrillation using minimal invasive surgery and high intensity focused ultrasound.,” Europace **11**(12), 1624–31 (2009).
[80] J. Kluiwstra, Y. Zhang, P. VanBaren, S.A. Strickberger, E.S. Ebbini, and C.A. Cain, “Ultrasound phased arrays for noninvasive myocardial ablation: initial studies,” in *Ultrason. Symp.*(1995), pp. 1605–1608.
[81] J.R. Ballard, A.J. Casper, Y. Wan, and E.S. Ebbini, “Adaptive transthoracic refocusing of dual-mode ultrasound arrays.,” IEEE Trans. Biomed. Eng. **57**(1), 93–102 (2010).
[82] J.-F. Aubry, M. Pernot, F. Marquet, M. Tanter, and M. Fink, “Transcostal high-intensity-focused ultrasound: ex vivo adaptive focusing feasibility study.,” Phys. Med. Biol. **53**(11), 2937–2951 (2008).
[83] B. Quesson *et al.*, “A method for MRI guidance of intercostal high intensity focused ultrasound ablation in the liver.,” Med. Phys. **37**(6), 2533–2540 (2010).
[84] F. Marquet, J.F. Aubry, M. Pernot, M. Fink, and M. Tanter, “Optimal transcostal high-intensity focused ultrasound with combined real-time 3D movement tracking and correction.,” Phys. Med. Biol. **56**(22), 7061–80 (2011).
[85] T. Ohkubo, K. Okishige, Y. Goseki, T. Matsubara, K. Hiejima, and C. Ibukiyama, “Experimental study of catheter ablation using ultrasound energy in canine and porcine hearts.,” Jpn. Heart J. **39**(3), 399–409 (1998).
[86] X. Yin, L. Epstein, and K. Hynynen, “Noninvasive transesophageal cardiac thermal ablation using a 2-D focused, ultrasound phased array: a simulation study,” Ultrason. Ferroelectr. … **53**(6), 1138–1149 (2006).
[87] S. Pichardo and K. Hynynen, “Circumferential lesion formation around the pulmonary veins in the left atrium with focused ultrasound using a 2D-array endoesophageal device: a numerical study.,” Phys. Med. Biol. **52**(16), 4923–42 (2007).
[88] S. Pichardo and K. Hynynen, “New design for an endoesophageal sector- based array for the treatment of atrial fibrillation: a parametric simulation study.,” IEEE Trans. Ultrason. Ferroelectr. Freq. Control **56**(3), 600–12 (2009).
[89] E. Constanciel *et al.*, “Design and Evaluation of a Transesophageal HIFU Probe for Ultrasound-Guided Cardiac Ablation : Simulation of a HIFU Mini-Maze Procedure and Preliminary Ex Vivo Trials,” IEEE Trans. Ultrason. Ferroelectr. Freq. Control **60**(9), 1868–1883 (2013).
[90] J. Werner, E.-J. Park, H. Lee, D. Francischelli, and N.B. Smith, “Feasibility of in vivo transesophageal cardiac ablation using a phased ultrasound array.,” Ultrasound Med. Biol. **36**(5), 752–60 (2010).
[91] E. Constanciel *et al.*, “Ultrasound-guided transesophageal HIFU exposures for atrial fibrillation treatment: First animal experiment,” Irbm **34**(4-5), 315–318 (2013).
[92] T. Nishida *et al.*, “Extracorporeal cardiac shock wave therapy markedly ameliorates ischemia-induced myocardial dysfunction in pigs in vivo,” Circulation **110**(19), 3055–3061 (2004).
[93] Y. Fukumoto *et al.*, “Extracorporeal cardiac shock wave therapy ameliorates myocardial ischemia in patients with severe coronary artery disease,” Coron. Artery Dis. **17**(1), 63–70 (2006).
[94] Y. Wang *et al.*, “A modified regimen of extracorporeal cardiac shock wave therapy for treatment of coronary artery disease,” Cardiovasc. Ultrasound **10**(1), 35 (2012).

[95] B. Assmus *et al.*, “Effect of shock wave-facilitated intracoronary cell therapy on LVEF in patients with chronic heart failure: the CELLWAVE randomized clinical trial.,” JAMA **309**(15), 1622–31 (2013).

[96] A. Aicher, C. Heeschen, K.I. Sasaki, C. Urbich, A.M. Zeiher, and S. Dimmeler, “Low-energy shock wave for enhancing recruitment of endothelial progenitor cells: A new modality to increase efficacy of cell therapy in chronic hind limb ischemia,” Circulation **114**(25), 2823–2830 (2006).

[97] Y. a. Vasyuk *et al.*, “Initial clinical experience with extracorporeal shock wave therapy in treatment of ischemic heart failure,” Congest. Hear. Fail. **16**(october), 226–230 (2010).

[98] P. Yang *et al.*, “Randomized and double-blind controlled clinical trial of extracorporeal cardiac shock wave therapy for coronary heart disease,” Heart Vessels (295), 284–291 (2012).

[99] N.B. Smith and K. Hynynen, “The feasibility of Using Focused Ultrasound for transmyocardial revascularization,” Ultrasound Med. Biol. **24**(7), 1045–1054 (1998).

[100] Z. Xu, G. Owens, D. Gordon, C. Cain, and A. Ludomirsky, “Noninvasive creation of an atrial septal defect by histotripsy in a canine model.,” Circulation **121**(6), 742–9 (2010).

[101] Y. Kim *et al.*, “Non-invasive pulsed cavitational ultrasound for fetal tissue ablation: Feasibility study in a fetal sheep model,” Ultrasound Obstet. Gynecol. **37**(4), 450–457 (2011).

[102] G.E. Owens *et al.*, “Therapeutic ultrasound to noninvasively create intracardiac communications in an intact animal model.,” Catheter. Cardiovasc. Interv. **77**(4), 580–8 (2011).

[103] R.M. Miller, Y. Kim, K.-W. Lin, C. a Cain, G.E. Owens, and Z. Xu, “Histotripsy cardiac therapy system integrated with real-time motion correction.,” Ultrasound Med. Biol. **39**(12), 2362–73 (2013).

[104] D.L. Miller, C. Dou, G.E. Owens, and O.D. Kripfgans, “Optimization of Ultrasound Parameters of Myocardial Cavitation Microlesions for Therapeutic Application,” Ultrasound Med. Biol. **40**(6), 1228–1236 (2014).

[105] M. Tanter, J. Bercoff, L. Sandrin, and M. Fink, “Ultrafast compound imaging for 2-D motion vector estimation: application to transient elastography.,” IEEE Trans. Ultrason. Ferroelectr. Freq. Control **49**(10), 1363–74 (2002).

[106] M. Tanter and M. Fink, “Ultrafast imaging in biomedical ultrasound,” IEEE Trans. Ultrason. Ferroelectr. Freq. Control **61**(1), 102–119 (2014).

[107] G. Montaldo, M. Tanter, J. Bercoff, N. Benech, and M. Fink, “Coherent plane-wave compounding for very high frame rate ultrasonography and transient elastography.,” IEEE Trans. Ultrason. Ferroelectr. Freq. Control **56**(3), 489–506 (2009).

[108] C. Papadacci, M. Pernot, M. Couade, M. Fink, and M. Tanter, “High-contrast ultrafast imaging of the heart.,” IEEE Trans. Ultrason. Ferroelectr. Freq. Control **61**(2), 288–301 (2014).

[109] J. Bercoff, M. Tanter, and M. Fink, “Supersonic shear imaging: a new technique for soft tissue elasticity mapping,” IEEE Trans. Ultrason. Ferroelectr. Freq. Control **51**(4), 396–409 (2004).

[110] A.P. Sarvazyan, O. V Rudenko, S.D. Swanson, J.B. Fowlkes, and S.Y. Emelianov, “Shear wave elasticity imaging: a new ultrasonic technology of medical diagnostics.,” Ultrasound Med. Biol. **24**(9), 1419–35 (1998).

[111] J. Bercoff, M. Tanter, and M. Fink, “Sonic boom in soft materials: The elastic Cerenkov effect,” Appl. Phys. Lett. **84**(12), 2202–2204 (2004).

[112] M. Tanter *et al.*, “Quantitative assessment of breast lesion viscoelasticity: initial clinical results using supersonic shear imaging.,” Ultrasound Med. Biol. **34**(9), 1373–86 (2008).
[113] J. McLaughlin and D. Renzi, “Using level set based inversion of arrival times to recover shear wave speed in transient elastography and supersonic imaging,” Inverse Probl. **22**(2), 707–725 (2006).
[114] S.N. Goldberg, G.S. Gazelle, and P.R. Mueller, “Thermal Ablation Therapy for Focal Malignancy : A Unified Approach to Underlying Principles, Techniques, and Diagnostic Imaging Guidance,” Am. Roentgen Ray Soc. **174**(2), 323–331 (2000).
[115] S.A. Curley *et al.*, “Radiofrequency ablation of unresectable primary and metastatic hepatic malignancies: results in 123 patients.,” Ann. Surg. **230**(1), 1–8 (1999).
[116] A.J. Welch, M. Motamedi, S. Rastegar, G.L. LeCarpentier, and D. Jansen, “Laser thermal ablation,” Photochem. Photobiol. **53**(6), 815–823 (1991).
[117] G. Carrafiello *et al.*, “Microwave tumors ablation: Principles, clinical applications and review of preliminary experiences,” Int. J. Surg. **6**(SUPPL. 1), 65–69 (2008).
[118] M. Shafir, R. Shapiro, M. Sung, R. Warner, A. Sicular, and A. Klipfei, “Cryoablation of unresectable malignant liver tumors,” Am. J. Surg. **171**(1), 27–31 (1996).
[119] Z. Zhao and F. Wu, “Minimally-invasive thermal ablation of early-stage breast cancer: A systemic review,” Eur. J. Surg. Oncol. **36**(12), 1149–1155 (2010).
[120] C.J. Simon *et al.*, “Pulmonary Radiofrequency Ablation: Long-term Safety and Efficacy in 153 Patients,” Radiology **243**(1), 268–275 (2007).
[121] N.J. Shaheen *et al.*, “Radiofrequency ablation in Barrett’s esophagus with dysplasia.,” N. Engl. J. Med. **360**(22), 2277–2288 (2009).
[122] C.J. Simon and D.E. Dupuy, “Percutaneous minimally invasive therapies in the treatment of bone tumors: thermal ablation.,” Semin. Musculoskelet. Radiol. **10**(2), 137–44 (2006).
[123] R. Lencioni and L. Crocetti, “Local-Regional Treatment of Hepatocellular Carcinoma,” Radiology **262**(1), 43–58 (2012).
[124] L. Solbiati, M. Ahmed, L. Cova, T. Ierace, M. Brioschi, and S.N. Goldberg, “Small Liver Colorectal Metastases Treated with Percutaneous Radiofrequency Ablation: Local Response Rate and Long-term Survival with Up to 10-year Follow-up,” Radiology (2012).
[125] A.A.J.M. Van Tilborg *et al.*, “Long-term results of radiofrequency ablation for unresectable colorectal liver metastases: a potentially curative intervention.,” Br. J. Radiol. **84**(1002), 556–65 (2011).
[126] B. Decadt and A.K. Siriwardena, “Radiofrequency ablation of liver tumours: systematic review.,” Lancet. Oncol. **5**(9), 550–60 (2004).
[127] D. Li, J. Kang, B.J. Golas, V.W. Yeung, and D.C. Madoff, *Minimally invasive local therapies for liver cancer*, Cancer Biol. Med. **11**(4), 217–236 (2014).
[128] T. Livraghi, L. Solbiati, M.F. Meloni, G.S. Gazelle, E.F. Halpern, and S.N. Goldberg, “Treatment of focal liver tumors with percutaneous radio-frequency ablation: complications encountered in a multicenter study.,” Radiology **226**(2), 441–51 (2003).
[129] N.P. Reuter, C.E. Woodall, C.R. Scoggins, K.M. McMasters, and R.C.G. Martin, “Radiofrequency ablation vs. resection for hepatic colorectal metastasis: therapeutically equivalent?,” J. Gastrointest. Surg. **13**(3), 486–91 (2009).
[130] S. Mulier, Y. Ni, J. Jamart, T. Ruers, G. Marchal, and L. Michel, “Local recurrence after hepatic radiofrequency coagulation: multivariate meta-analysis and review of contributing factors.,” Ann. Surg. **242**(2), 158–171 (2005).
[131] M.G. Van Vledder *et al.*, “Intra-operative ultrasound elasticity imaging for monitoring of hepatic tumour thermal ablation.,” HPB (Oxford). **12**(10), 717–23 (2010).

[132] H. Rempp *et al.*, “Threshold-based prediction of the coagulation zone in sequential temperature mapping in MR-guided radiofrequency ablation of liver tumours,” Eur. Radiol. **22**(5), 1091–1100 (2012).
[133] M. Lepetit-Coiffé *et al.*, “Real-time monitoring of radiofrequency ablation of liver tumors using thermal-dose calculation by MR temperature imaging: Initial results in nine patients, including follow-up,” Eur. Radiol. **20**(1), 193–201 (2010).
[134] B. Quesson, J. a. De Zwart, and C.T.W. Moonen, “Magnetic resonance temperature imaging for guidance of thermotherapy,” J. Magn. Reson. Imaging **12**(4), 525–533 (2000).
[135] T. Wu, J.P. Felmlee, J.F. Greenleaf, S.J. Riederer, and R.L. Ehman, “Assessment of thermal tissue ablation with MR elastography.,” Magn. Reson. Med. **45**(1), 80–87 (2001).
[136] N. Corbin *et al.*, “Interventional MR elastography for MRI-guided percutaneous procedures,” Magn. Reson. Med. **00**, n/a–n/a (2015).
[137] P. Bruners *et al.*, “CT-based temperature monitoring during hepatic RF ablation: feasibility in an animal model.,” Int. J. Hyperthermia **28**(1), 55–61 (2012).
[138] P. Saccomandi, E. Schena, and S. Silvestri, “Techniques for temperature monitoring during laser-induced thermotherapy: an overview.,” Int. J. Hyperthermia **29**(7), 609–19 (2013).
[139] C.H. Cha *et al.*, “CT Versus Monitoring Ablation Sonography for Radiofrequency in a Porcine Liver,” Imaging **175**(3), 705–711 (2000).
[140] S.A. Curley, F. Izzo, L.M. Ellis, J. Nicolas Vauthey, and P. Vallone, “Radiofrequency ablation of hepatocellular cancer in 110 patients with cirrhosis.,” Ann. Surg. **232**(3), 381–91 (2000).
[141] S. Goldberg *et al.*, “Image-guided Tumor Ablation: Standardization of Terminology and Reporting Criteria,” J. Vasc. Interv. Radiol. **16**(6), 765–778 (2005).
[142] E.S. Ebbini and G. Ter Haar, “Ultrasound-guided therapeutic focused ultrasound: Current status and future directions,” Int. J. Hyperth. **00**(00), 1–13 (2015).
[143] M. a. Lewis, R.M. Staruch, and R. Chopra, “Thermometry and ablation monitoring with ultrasound,” Int. J. Hyperth. **31**(2), 163–181 (2015).
[144] B. a. Rabkin, V. Zderic, and S. Vaezy, “Hyperecho in ultrasound images of HIFU therapy: Involvement of cavitation,” Ultrasound Med. Biol. **31**(7), 947–956 (2005).
[145] T.D. Mast, V.A. Salgaonkar, C. Karunakaran, J.A. Besse, S. Datta, and C.K. Holland, “Acoustic emissions during 3.1 MHz ultrasound bulk ablation in vitro.,” Ultrasound Med. Biol. **34**(9), 1434–48 (2008).
[146] C. Jensen, R. Ritchie, M. Gyöngy, J. Collin, T. Leslie, and C. Coussios, “Spatiotemporal monitoring of high-intensity focused ultrasound therapy with passive acoustic mapping,” Radiology **262**(1), 252–261 (2012).
[147] T. Varghese *et al.*, “Ultrasound monitoring of temperature change during radiofrequency ablation: preliminary in-vivo results,” Ultrasound Med. … **28**(3), 321–329 (2002).
[148] M. Pernot and M. Tanter, “Temperature estimation using ultrasonic spatial compound imaging,” Ultrason. … **51**(5), 606–615 (2004).
[149] N.R. Miller, J.C. Bamber, and G.R. ter Haar, “Imaging of temperature-induced echo strain: preliminary in vitro study to assess feasibility for guiding focused ultrasound surgery.,” Ultrasound Med. Biol. **30**(3), 345–56 (2004).
[150] R. Seip and E.S. Ebbini, “Noninvasive estimation of tissue temperature response to heating fields using diagnostic ultrasound,” IEEE Trans. Biomed. Eng. **42**(8), 828–839 (1995).

[151] R. Souchon *et al.*, “Monitoring the formation of thermal lesions with heat-induced echo-strain imaging: A feasibility study,” Ultrasound Med. Biol. **31**(2), 251–259 (2005).
[152] J.C. Bamber and C.R. Hill, “Ultrasonic attenuation and propagation speed in mammalian tissues as a function of temperature.,” Ultrasound Med. Biol. **5**(2), 149–157 (1979).
[153] C.H. Seo, Y. Shi, S.-W. Huang, K. Kim, and M. O’Donnell, “Thermal strain imaging: a review.,” Interface Focus **1**(4), 649–64 (2011).
[154] D. Liu and E. Ebbini, “Real-time 2-D temperature imaging using ultrasound,” Biomed. Eng. IEEE Trans. … **57**(1), 12–16 (2010).
[155] A. Casper, D. Liu, and E.S. Ebbini, “Realtime control of multiple-focus phased array heating patterns based on noninvasive ultrasound thermography,” IEEE Trans. Biomed. Eng. **59**(1), 95–105 (2012).
[156] N.R. Miller, J.C. Bamber, and P.M. Meaney, “Fundamental limitations of noninvasive temperature imaging by means of ultrasound echo strain estimation,” Ultrasound Med. Biol. **28**(10), 1319–1333 (2002).
[157] A. Anand and P.J. Kaczkowski, “Monitoring formation of high intensity focused ultrasound (HIFU) induced lesions using backscattered ultrasound,” Acoust. Res. Lett. Online **5**(3), 88 (2004).
[158] C.A. Damianou, “Dependence of ultrasonic attenuation and absorption in dog soft tissues on temperature and thermal dose,” J. Acoust. Soc. Am. **102**(1), 628 (1997).
[159] H. Zhong, M.-X. Wan, Y.-F. Jiang, and S.-P. Wang, “Monitoring imaging of lesions induced by high intensity focused ultrasound based on differential ultrasonic attenuation and integrated backscatter estimation.,” Ultrasound Med. Biol. **33**(1), 82–94 (2007).
[160] R.M. Arthur, W.L. Straube, J.D. Starman, and E.G. Moros, “Noninvasive temperature estimation based on the energy of backscattered ultrasound,” Med. Phys. **30**(6), 1021 (2003).
[161] J.T. Apter, “Influence of composition on thermal properties of tissues,” in *Biomech. its Found. Object.*, edited by Y. Fung, N. Perrone and M. Anliker (Prentice-Hall, London, 1972), pp. 217–235.
[162] J. Lepetit, A. Grajales, and R. Favier, “Modelling the effect of sarcomere length on collagen thermal shortening in cooked meat: consequence on meat toughness,” Meat Sci. **54**(3), 239–250 (2000).
[163] N.T. Wright and J.D. Humphrey, “Denaturation of collagen via heating: an irreversible rate process.,” Annu. Rev. Biomed. Eng. **4**, 109–28 (2002).
[164] M.S. Wall, X.-H. Deng, P.A. Torzilli, S.B. Doty, S.J. O’Brien, and R.F. Warren, “Thermal modification of collagen,” J. Shoulder Elb. Surg. **8**(4), 339–344 (1999).
[165] N. Benech and C. a Negreira, “Monitoring heat-induced changes in soft tissues with 1D transient elastography.,” Phys. Med. Biol. **55**(6), 1753–65 (2010).
[166] E. Sapin-de Brosses, J.-L. Gennisson, M. Pernot, M. Fink, and M. Tanter, “Temperature dependence of the shear modulus of soft tissues assessed by ultrasound.,” Phys. Med. Biol. **55**(6), 1701–18 (2010).
[167] B. Arnal, M. Pernot, and M. Tanter, “Monitoring of thermal therapy based on shear modulus changes: I. shear wave thermometry.,” IEEE Trans. Ultrason. Ferroelectr. Freq. Control **58**(2), 369–78 (2011).
[168] F. Kallel, R. Stafford, R. Price, R. Righetti, J. Ophir, and J. Hazle, “The feasibility of elastographic visualization of HIFU-induced thermal lesions in soft tissues,” Ultrasound Med. Biol. **25**(4), 641–647 (1999).

[169] R. Souchon *et al.*, “Visualisation of HIFU lesions using elastography of the human prostate in vivo: Preliminary results,” Ultrasound Med. Biol. **29**(7), 1007–1015 (2003).
[170] T. Varghese, J. Zagzebski, and F.L. Jr, “Elastographic imaging of thermal lesions in the liver in vivo following radiofrequency ablation: preliminary results,” Ultrasound Med. Biol. **28**(02), 1467–1473 (2002).
[171] B.J. Fahey, K.R. Nightingale, D.L. Stutz, and G.E. Trahey, “Acoustic radiation force impulse imaging of thermally- and chemically-induced lesions in soft tissues: Preliminary ex vivo results,” Ultrasound Med. Biol. **30**(3), 321–328 (2004).
[172] C. Maleke and E.E. Konofagou, “Harmonic motion imaging for focused ultrasound (HMIFU): a fully integrated technique for sonication and monitoring of thermal ablation in tissues.,” Phys. Med. Biol. **53**(6), 1773–1793 (2008).
[173] J. Bercoff, M. Pernot, M. Tanter, and M. Fink, “Monitoring thermally-induced lesions with supersonic shear imaging,” Ultrason. Imaging **40**, 29–40 (2004).
[174] K.R. Nightingale, M.L. Palmeri, R.W. Nightingale, and G.E. Trahey, “On the feasibility of remote palpation using acoustic radiation force,” J. Acoust. Soc. Am. **110**(1), 625 (2001).
[175] J. Vappou, G.Y. Hou, F. Marquet, D. Shahmirzadi, J. Grondin, and E.E. Konofagou, “Non-contact, ultrasound-based indentation method for measuring elastic properties of biological tissues using Harmonic Motion Imaging (HMI),” Phys. Med. Biol. **60**, 2853–2868 (2015).
[176] E. Sapin-de Brosses, M. Pernot, and M. Tanter, “The link between tissue elasticity and thermal dose in vivo.,” Phys. Med. Biol. **56**(24), 7755–65 (2011).
[177] B. Arnal, M. Pernot, and M. Tanter, “Monitoring of thermal therapy based on shear modulus changes: II. Shear wave imaging of thermal lesions.,” IEEE Trans. Ultrason. Ferroelectr. Freq. Control **58**(8), 1603–11 (2011).
[178] N. Goldberg, G.S. Gazelle, C.C. Compton, P.R. Mueller, and K.K. Tanabe, “Treatment of Intrahepatic Malignancy with Radiofrequency Ablation,” Cancer **88**(11), 2452–2463 (2000).
[179] P.L. Pereira *et al.*, “Radiofrequency ablation: in vivo comparison of four commercially available devices in pig livers.,” Radiology **232**(2), 482–490 (2004).
[180] J. Hartigan and M. Wong, “Algorithm AS 136: A k-means clustering algorithm,” Appl. Stat. **28**(1), 100–108 (1979).
[181] J.P. McGahan, P.D. Browning, J.M. Brock, and H. Tesluk, “Hepatic ablation using radiofrequency electrocautery.,” Invest. Radiol. **25**(3), 267–270 (1990).
[182] Y. Kim, H. Rhim, H.K. Lim, D. Choi, M.W. Lee, and M.J. Park, “Coagulation necrosis induced by radiofrequency ablation in the liver: histopathologic and radiologic review of usual to extremely rare changes.,” Radiographics **31**(2), 377–90 (2011).
[183] B.G. Rosser and G.J. Gores, “Liver cell necrosis: Cellular mechanisms and clinical implications,” Gastroenterology **108**(1), 252–275 (1995).
[184] M.T. Gettman *et al.*, “Radiofrequency coagulation of renal parenchyma: comparison of effects of energy generators on treatment efficacy.,” J. Endourol. **16**(2), 83–8 (2002).
[185] Y.N. Kim *et al.*, “The effect of radiofrequency ablation on different organs: ex vivo and in vivo comparative studies.,” Eur. J. Radiol. **80**(2), 526–32 (2011).
[186] A.E. Wennerberg, M.A. Nalesnik, and W.B. Coleman, “Hepatocyte paraffin 1: A monoclonal antibody that reacts with hepatocytes and can be used for differential diagnosis of hepatic tumors,” Am. J. Pathol. **143**(4), 1050–1054 (1993).
[187] S.K. Venkatesh *et al.*, “MR elastography of liver tumors: Preliminary results,” Am. J. Roentgenol. **190**(6), 1534–1540 (2008).

[188] D.H. Lee, J.M. Lee, J.K. Han, and B.I. Choi, “MR elastography of healthy liver parenchyma: Normal value and reliability of the liver stiffness value measurement.,” J. Magn. Reson. Imaging **38**(5), 1215–23 (2013).

[189] A. Athanasiou, H. Latorre-Ossa, A. Criton, A. Tardivon, J.L. Gennisson, and M. Tanter, “Feasibility of Imaging and Treatment Monitoring of Breast Lesions with Three-Dimensional Shear Wave Elastography.,” Ultraschall Med. (2015).

[190] J. Provost *et al.*, “3D ultrafast ultrasound imaging in vivo.,” Phys. Med. Biol. **59**(19), L1–L13 (2014).

[191] A. Athanasiou, A. Tardivon, and M. Tanter, “Breast lesions: quantitative elastography with supersonic shear imaging—preliminary results 1,” Radiology **256**(1), 297–303 (2010).

[192] A. Evans *et al.*, “Quantitative shear wave ultrasound elastography: initial experience in solid breast masses.,” Breast Cancer Res. **12**(6), R104 (2010).

[193] M. Zhang *et al.*, “Real-time sonoelastography of hepatic thermal lesions in a swine model,” Med. Phys. **35**(9), 4132 (2008).

[194] D. Eun *et al.*, “A Novel Technique for Creating Solid Renal Pseudotumors and Renal Vein-Inferior Vena Caval Pseudothrombus in a Porcine and Cadaveric Model,” J. Urol. **180**(4), 1510–1514 (2008).

[195] B.D. de Senneville, S. Roujol, P. Jaïs, C.T.W. Moonen, G. Herigault, and B. Quesson, “Feasibility of fast MR-thermometry during cardiac radiofrequency ablation,” NMR Biomed. **25**(4), 556–562 (2012).

[196] N.F. Marrouche *et al.*, “Phased-array intracardiac echocardiography monitoring during pulmonary vein isolation in patients with atrial fibrillation: impact on outcome and complications.,” Circulation **107**(21), 2710–6 (2003).

[197] D. Schwartzman and H. Zhong, “On the use of CartoSound for left atrial navigation.,” J. Cardiovasc. Electrophysiol. **21**(6), 656–64 (2010).

[198] M. Wright *et al.*, “Real-time lesion assessment using a novel combined ultrasound and radiofrequency ablation catheter.,” Hear. Rhythm **8**(2), 304–12 (2011).

[199] D. Stephens *et al.*, “Experimental studies with a 9F forward-looking intracardiac imaging and ablation catheter,” J. ultrasound Med. **28**(2), 207–215 (2009).

[200] C.H. Seo *et al.*, “The feasibility of using thermal strain imaging to regulate energy delivery during intracardiac radio-frequency ablation,” IEEE Trans. Ultrason. Ferroelectr. Freq. Control **58**(7), 1406–1417 (2011).

[201] A. Mariani *et al.*, “Real time shear waves elastography monitoring of thermal ablation: in vivo evaluation in pig livers.,” J. Surg. Res. **188**(1), 37–43 (2014).

[202] S.A. Eyerly, S.J. Hsu, S.H. Agashe, G.E. Trahey, Y. Li, and P.D. Wolf, “An in vitro assessment of acoustic radiation force impulse imaging for visualizing cardiac radiofrequency ablation lesions.,” J. Cardiovasc. Electrophysiol. **21**(5), 557–63 (2010).

[203] S.J. Hsu, B.J. Fahey, D.M. Dumont, P.D. Wolf, and G.E. Trahey, “Challenges and implementation of radiation-force imaging with an intracardiac ultrasound transducer.,” IEEE Trans. Ultrason. Ferroelectr. Freq. Control **54**(5), 996–1009 (2007).

[204] S. a Eyerly *et al.*, “Intracardiac acoustic radiation force impulse imaging: a novel imaging method for intraprocedural evaluation of radiofrequency ablation lesions.,” Hear. Rhythm **9**(11), 1855–62 (2012).

[205] T.D. Bahnson *et al.*, “Feasibility of Near Real-Time Lesion Assessment during Radiofrequency Catheter Ablation in Humans using Acoustic Radiation Force Impulse Imaging.,” J. Cardiovasc. Electrophysiol. **25**(12), 1275–1283 (2014).

[206] M. Couade *et al.*, “In vivo quantitative mapping of myocardial stiffening and transmural anisotropy during the cardiac cycle.,” IEEE Trans. Med. Imaging **30**(2), 295–305 (2011).

[207] W.-N. Lee *et al.*, “Mapping myocardial fiber orientation using echocardiography-based shear wave imaging.,” IEEE Trans. Med. Imaging **31**(3), 554–62 (2012).
[208] P.J. Hollender, P.D. Wolf, R. Goswami, and G.E. Trahey, “Intracardiac echocardiography measurement of dynamic myocardial stiffness with shear wave velocimetry.,” Ultrasound Med. Biol. **38**(7), 1271–83 (2012).
[209] P. Hollender, D. Bradway, P. Wolf, R. Goswami, and G. Trahey, “Intracardiac acoustic radiation force impulse (ARFI) and shear wave imaging in pigs with focal infarctions,” IEEE Trans. Ultrason. Ferroelectr. Freq. Control **60**(8), 1669–82 (2013).
[210] T. Deffieux, J.-L. Gennisson, B. Larrat, M. Fink, and M. Tanter, “The variance of quantitative estimates in shear wave imaging: theory and experiments.,” IEEE Trans. Ultrason. Ferroelectr. Freq. Control **59**(11), 2390–410 (2012).
[211] R.R. Bouchard, S.J. Hsu, M.L. Palmeri, N.C. Rouze, K.R. Nightingale, and G.E. Trahey, “Acoustic radiation force-driven assessment of myocardial elasticity using the displacement ratio rate (DRR) method.,” Ultrasound Med. Biol. **37**(7), 1087–100 (2011).
[212] M. Urban, C. Pislaru, I. Nenadic, R. Kinnick, and J. Greenleaf, “Measurement of viscoelastic properties of in vivo swine myocardium using Lamb Wave Dispersion Ultrasound Vibrometry (LDUV),” IEEE Trans. Med. Imaging **32**(2), 247–261 (2013).
[213] C. Bellini, E.S. Di Martino, and S. Federico, “Mechanical behaviour of the human atria.,” Ann. Biomed. Eng. **41**(7), 1478–90 (2013).
[214] F.W. Prinzen, C.H. Augustijn, M. a Allessie, T. Arts, T. Delhaas, and R.S. Reneman, “The time sequence of electrical and mechanical activation during spontaneous beating and ectopic stimulation.,” Eur. Heart J. **13**(4), 535–43 (1992).
[215] J. Provost, S. Thiébaut, J. Luo, and E.E. Konofagou, “Single-heartbeat electromechanical wave imaging with optimal strain estimation using temporally unequispaced acquisition sequences.,” Phys. Med. Biol. **57**(4), 1095–112 (2012).
[216] T. Deffieux, G. Montaldo, M. Tanter, and M. Fink, “Shear wave spectroscopy for in vivo quantification of human soft tissues visco-elasticity.,” IEEE Trans. Med. Imaging **28**(3), 313–22 (2009).
[217] M. Couade *et al.*, “Quantitative assessment of arterial wall biomechanical properties using shear wave imaging.,” Ultrasound Med. Biol. **36**(10), 1662–76 (2010).
[218] E.S. Ebbini, H. Yao, and A. Shrestha, “Dual-Mode Ultrasound Phased Arrays for Image-Guided Surgery,” Ultrason. Imaging **28**(2), 65–82 (2006).
[219] F. Wu *et al.*, “Tumor Vessel Destruction Resuting From High-Intensity Focused Ultrasound in Patients With Solid Malignancies,” Ultrasound Med. Biol. **28**(4), 535–542 (2002).
[220] J.E. Kennedy *et al.*, “Contrast-enhanced ultrasound assessment of tissue response to high-intensity focused ultrasound.,” Ultrasound Med. Biol. **30**(6), 851–854 (2004).
[221] K. Nieman, F. Cademartiri, P.A. Lemos, R. Raaijmakers, P.M.T. Pattynama, and P.J. de Feyter, “Reliable Noninvasive Coronary Angiography With Fast Submillimeter Multislice Spiral Computed Tomography,” Circulation **106**(16), 2051–2054 (2002).
[222] T. Lockie *et al.*, “High-resolution magnetic resonance myocardial perfusion imaging at 3.0-tesla to detect hemodynamically significant coronary stenoses as determined by fractional flow reserve,” J. Am. Coll. Cardiol. **57**(1), 70–75 (2010).
[223] K. Wei *et al.*, “Detection of coronary stenoses at rest with myocardial contrast echocardiography,” Circulation **112**(8), 1154–1160 (2005).
[224] J. Bercoff *et al.*, “Ultrafast compound Doppler imaging: providing full blood flow characterization.,” IEEE Trans. Ultrason. Ferroelectr. Freq. Control **58**(1), 134–47 (2011).

[225] E. Macé, G. Montaldo, I. Cohen, M. Baulac, M. Fink, and M. Tanter, “Functional ultrasound imaging of the brain.,” Nat. Methods **8**(8), 662–664 (2011).
[226] E. Mace, G. Montaldo, B.-F. Osmanski, I. Cohen, M. Fink, and M. Tanter, “Functional ultrasound imaging of the brain: theory and basic principles.,” IEEE Trans. Ultrason. Ferroelectr. Freq. Control **60**(3), 492–506 (2013).
[227] C. Demené *et al.*, “Ultrafast Doppler reveals the mapping of cerebral vascular resistivity in neonates.,” J. Cereb. Blood Flow Metab. **34**(6), 1009–17 (2014).
[228] B.-F. Osmanski, D. Maresca, E. Messas, M. Tanter, and M. Pernot, “Transthoracic ultrafast Doppler imaging of human left ventricular hemodynamic function.,” IEEE Trans. Ultrason. Ferroelectr. Freq. Control **61**(8), 1268–75 (2014).
[229] B.-F. Osmanski, M. Pernot, G. Montaldo, A. Bel, E. Messas, and M. Tanter, “Ultrafast Doppler Imaging of Blood Flow Dynamics in the Myocardium,” IEEE Trans. Med. Imaging **31**(8), 1661–1668 (2012).
[230] C. Demene *et al.*, “Spatiotemporal clutter filtering of ultrafast ultrasound data highly increases Doppler and fUltrasound sensitivity,” IEEE Trans. Med. Imaging (2015).
[231] A. d’Avila, “Epicardial catheter ablation of ventricular tachycardia.,” Heart Rhythm **5**(6 Suppl), S73–5 (2008).
[232] K. Hynynen and J. Dennie, “Cylindrical ultrasonic transducers for cardiac catheter ablation,” IEEE Trans. Biomed. Eng. **44**(2), 144–151 (1997).
[233] J.S. Koruth *et al.*, “Safety and efficacy of high-intensity focused ultrasound atop coronary arteries during epicardial catheter ablation,” J. Cardiovasc. Electrophysiol. **22**(11), 1274–1280 (2011).
[234] Y. Hasebe *et al.*, “Development of a Novel Shock Wave Catheter Ablation System - The First Feasibility Study in Pigs-,” PLoS One **10**(1), 1–20 (2015).
[235] A. Natale *et al.*, “First Human Experience With Pulmonary Vein Isolation Using a Through-the-Balloon Circumferential Ultrasound Ablation System for Recurrent Atrial Fibrillation,” Circulation **102**(16), 1879–1882 (2000).
[236] W. Saliba *et al.*, “Circumferential ultrasound ablation for pulmonary vein isolation: analysis of acute and chronic failures.,” J. Cardiovasc. Electrophysiol. **13**(10), 957–61 (2002).
[237] H. Nakagawa *et al.*, “Initial experience using a forward directed, high-intensity focused ultrasound balloon catheter for pulmonary vein antrum isolation in patients with atrial fibrillation.,” J. Cardiovasc. Electrophysiol. **18**(2), 136–44 (2007).
[238] K. Neven *et al.*, “Fatal end of a safety algorithm for pulmonary vein isolation with use of high-intensity focused ultrasound.,” Circ. Arrhythm. Electrophysiol. **3**(3), 260–5 (2010).
[239] A. Metzner *et al.*, “Long-term clinical outcome following pulmonary vein isolation with high-intensity focused ultrasound balloon catheters in patients with paroxysmal atrial fibrillation.,” Europace **12**(2), 188–93 (2010).
[240] K.L. Gentry and S.W. Smith, “Integrated catheter for 3-D intracardiac echocardiography and ultrasound ablation.,” IEEE Trans. Ultrason. Ferroelectr. Freq. Control **51**(7), 800–8 (2004).
[241] K.L. Gentry, M.L. Palmeri, N. Sachedina, and S.W. Smith, “Finite-element analysis of temperature rise and lesion formation from catheter ultrasound ablation transducers,” IEEE Trans. Ultrason. Ferroelectr. Freq. Control **52**(10), 1713–1721 (2005).
[242] M. Carias and K. Hynynen, “The evaluation of steerable ultrasonic catheters for minimally invasive MRI-guided cardiac ablation,” Magn. Reson. Med. **72**(2), 591–598 (2014).

[243] E.S. Ebbini, J.C. Bischof, and J.E. Coad, “Lesion formation and visualization using dual-mode ultrasound phased arrays,” 2001 IEEE Ultrason. Symp. Proceedings. An Int. Symp. (Cat. No.01CH37263) **2**, 1351–1354 (2001).

[244] E.S. Ebbini, H. Yao, and A. Shrestha, “Dual-Mode Ultrasound Phased Arrays for Image-Guided Surgery,” Ultrason. Imaging **28**(2), 65–82 (2006).

[245] A.J. Casper, D. Liu, J.R. Ballard, and E.S. Ebbini, “Real-time implementation of a dual-mode ultrasound array system: In vivo results,” IEEE Trans. Biomed. Eng. **60**(10), 2751–2759 (2013).

[246] G. Bouchoux, C. Lafon, R. Berriet, J.Y. Chapelon, G. Fleury, and D. Cathignol, “Dual-mode ultrasound transducer for image-guided interstitial thermal therapy.,” Ultrasound Med. Biol. **34**(4), 607–16 (2008).

[247] N.R. Owen *et al.*, “In Vivo Evaluation of a Mechanically-Oscillating Dual-Mode Applicator for Ultrasound Imaging and Thermal Ablation,” IEEE Trans. Biomed. Eng. **1**(1), 1–14 (2009).

[248] T.D. Mast *et al.*, “Treatment of Rabbit Liver Cancer In Vivo Using Miniaturized Image-Ablate Ultrasound Arrays,” Ultrasound Med. Biol. **37**(10), 1609–1621 (2011).

[249] W. Kwiecinski *et al.*, “Quantitative evaluation of atrial radio frequency ablation using intracardiac shear-wave elastography,” Med. Phys. **41**(11), 112901 (2014).

[250] T. Deffieux, J.-L. Gennisson, J. Bercoff, and M. Tanter, “On the effects of reflected waves in transient shear wave elastography.,” IEEE Trans. Ultrason. Ferroelectr. Freq. Control **58**(10), 2032–5 (2011).

[251] V.Y. Reddy *et al.*, “The relationship between contact force and clinical outcome during radiofrequency catheter ablation of atrial fibrillation in the TOCCATA study.,” Heart Rhythm **9**(11), 1789–95 (2012).

[252] F. a Flachskampf *et al.*, “Recommendations for transoesophageal echocardiography: EACVI update 2014.,” Eur. Heart J. Cardiovasc. Imaging (2014).

[253] C.H. Siklódy *et al.*, “Cryoballoon pulmonary vein isolation guided by transesophageal echocardiography: novel aspects on an emerging ablation technique.,” J. Cardiovasc. Electrophysiol. **20**(11), 1197–202 (2009).

[254] L. Ottaviano *et al.*, “Cryoballoon ablation for atrial fibrillation guided by real-time three-dimensional transoesophageal echocardiography: a feasibility study.,” Europace **15**(7), 944–50 (2013).

[255] F.F. Faletra, F. Regoli, G. Nucifora, and A. Auricchio, “Real-time, fluoroless, anatomic-guided catheter navigation by 3D TEE during ablation procedures.,” JACC. Cardiovasc. Imaging **4**(2), 203–6 (2011).

[256] P. Song *et al.*, “Improved Shear Wave Motion Detection Using Pulse-Inversion Harmonic Imaging with a Phased Array Transducer.,” IEEE Trans. Med. Imaging (c), (2013).

[257] J.N. Hilberath, D. a. Oakes, S.K. Shernan, B.E. Bulwer, M.N. D'Ambra, and H.K. Eltzschig, “Safety of transesophageal echocardiography,” J. Am. Soc. Echocardiogr. **23**(11), 1115–1127 (2010).

[258] K. Kwong *et al.*, “Dynamic magnetic resonance imaging of human brain activity during primary sensory stimulation.,” Proc Natl Acad Sci U S A **89**(12), 5675–5679 (1992).

[259] S. Ogawa *et al.*, “Intrinsic signal changes accompanying sensory stimulation: functional brain mapping with magnetic resonance imaging.,” Proc. Natl. Acad. Sci. U. S. A. **89**(13), 5951–5955 (1992).

[260] a Villringer, J. Planck, C. Hock, L. Schleinkofer, and U. Dirnagl, “Near infrared spectroscopy (NIRS): a new tool to study hemodynamic changes during activation of brain function in human adults.,” Neurosci. Lett. **154**(1-2), 101–104 (1993).

[261] J. Provost, W.-N. Lee, K. Fujikura, and E.E. Konofagou, “Imaging the electromechanical activity of the heart in vivo.,” Proc. Natl. Acad. Sci. U. S. A. **108**(21), 8565–70 (2011).

[262] M. Pernot and E.E. Konofagou, “Electromechanical imaging of the myocardium at normal and pathological states,” Proc. - IEEE Ultrason. Symp. **2**(c), 1091–1094 (2005).

[263] J. Provost, W.N. Lee, K. Fujikura, and E.E. Konofagou, “Electromechanical wave imaging of normal and ischemic hearts in vivo,” IEEE Trans. Med. Imaging **29**(3), 625–635 (2010).

[264] M. Haissaguerre *et al.*, “Noninvasive panoramic mapping of human atrial fibrillation mechanisms: A feasibility report,” J. Cardiovasc. Electrophysiol. **24**(6), 711–717 (2013).

[265] H.U. Klemm *et al.*, “Catheter motion during atrial ablation due to the beating heart and respiration: impact on accuracy and spatial referencing in three-dimensional mapping.,” Heart Rhythm **4**(5), 587–92 (2007).

[266] F.E. Fox, K.F. Herzfeld, and G.D. Rock, *The Effect of Ultrasonic Waves on the Conductivity of Salt Solutions*, Phys. Rev. **70**(5 & 6), 329–341 (1946).

[267] J. Jossinet, B. Lavandier, and D. Cathignol, “The phenomenology of acousto-electric interaction signals in aqueous solutions of electrolytes,” Ultrasonics **36**(1-5), 607–613 (1998).

[268] R. Olafsson, S. Member, R.S. Witte, S. Huang, and M.O. Donnell, “Ultrasound Current Source Density Imaging,” IEEE Trans. Biomed. Eng. **55**(7), 1840–1848 (2008).

[269] R. Witte, R. Olafsson, S.-W. Huang, and M. O’Donnell, “Imaging current flow in lobster nerve cord using the acoustoelectric effect,” Appl. Phys. Lett. **90**(16), 163902 (2007).

[270] R. Olafsson, R.S. Witte, C. Jia, S.-W. Huang, K. Kim, and M. O’Donnell, “Cardiac activation mapping using ultrasound current source density imaging (UCSDI).,” IEEE Trans. Ultrason. Ferroelectr. Freq. Control **56**(3), 565–74 (2009).

[271] E. Candes, Ridgelets: theory and applications (Stanford University, 1998).

[272] D.L. Donoho and I.M. Johnstone, “Ideal Spatial Adaption by Wavelet Shrinkage,” Biometrika **81**(3), 425–455 (1994).

[273] D.L. Donoho, “De-noising by soft-thresholding,” IEEE Trans. Inf. Theory **41**(3), 613–627 (1995).

[274] C.E. Cook, “Pulse Compression-Key to More Efficient Radar Transmission,” Proc. IRE **48**(3), (1960).

[275] D.L.L. Donoho, “Compressed sensing,” IEEE Trans. Inf. Theory **52**(4), 1289–1306 (2006).

[276] E.J. Candès, J. Romberg, and T. Tao, “Robust uncertainty principles: Exact signal reconstruction from highly incomplete frequency information,” IEEE Trans. Inf. Theory **52**(2), 489–509 (2006).

[277] J. Provost and F. Lesage, “The application of compressed sensing for photo-acoustic tomography,” Med. Imaging, IEEE Trans. **28**(4), 585–594 (2009).

List of abbreviations

AAD: antiarrhythmic drugs

AE: acoustoelectric

AF: atrial fibrillation

ARFI: Acoustic Radiation Force Imaging

AV: atrio-ventricular

CE: Conformité Européenne

CEM: cumulative equivalent minutes

CT: Computed Tomography

ECG: Electrocardiogram

ECWT: Extracorporeal shock-wave therapy

FDA: Food and Drugs Administration

GPU: Graphics Processing Unit

HIFU: High-Intensity Focused Ultrasound

HMI: Harmonic Motion Imaging

ICE: intracardiac echocardiography

IVS: Interventricular Septum

MI: Mechanical Index

MR: Magnetic Resonance

MRE: Magnetic Resonance Elastography

MRI: Magnetic Resonance Imaging

PRF: pulse repetition frequency

PV: pulmonary vein

RF: Radio-Frequency

RFA: Radio-Frequency Ablation

RFCA: Radio-Frequency Catheter Ablation

SNR: Signal-to-Noise Ratio

SWE: Shear-Wave Elastography

TEE: Transesophageal Echocardiography

UAT: Ultrafast Acoustoelectric Tomography

VT: ventricular tachycardia

List of figures

List of tables